

**DESIGN AND ANALYSIS OF MICROWAVE COMPONENTS
FOR MIMO COMMUNICATION SYSTEM**

**A thesis submitted
In partial Fulfilment of the Requirements
For the degree of**

DOCTOR OF PHILOSOPHY

By

**GAURAV SAXENA
(Roll No. 2K14/Ph.D/EC/03)**

Under the Supervision of

**Dr. Priyanka Jain (Associate Professor)
Department of Electronics & Communication Engineering
Delhi Technological University, Delhi
&
Dr. Y K Awasthi (Professor)
Department of Electronics & Communication Engineering
Manav Rachna International Institute of Research and Studies,
Faridabad, Haryana**

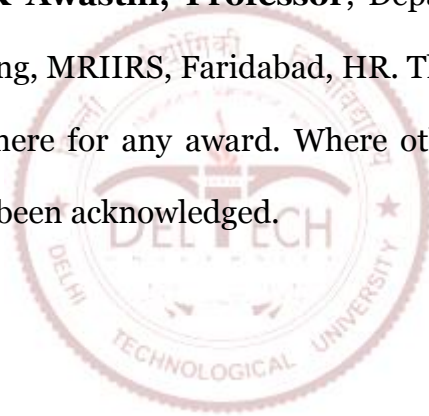


**DELHI TECHNOLOGICAL UNIVERSITY
NEW DELHI, INDIA**

November, 2020

DECLARATION

I hereby declare that the work which is being presented in the .thesis entitled “**Design and Analysis of Microwave Components for MIMO Communication System**” submitted to the Department of Electronics and Communication Engineering, Delhi Technological University, Delhi in partial fulfillment of the requirements for the award of the degree of **Doctor of Philosophy** is a bonafide work carried out during the period from 2014 to 2020 by me under the guidance of **Dr Priyanka Jain, Associate Professor**, Department of Electronics and Communication Engineering, Delhi Technological University, New Delhi, India and **Dr. Y K Awasthi, Professor**, Department of Electronics and Communication Engineering, MRIIRS, Faridabad, HR. The content of this thesis has not been submitted anywhere for any award. Where other sources of information have been used, they have been acknowledged.



A small rectangular image showing a handwritten signature in black ink on a light-colored background. The signature appears to read "Gaurav Saxena".

Date: November, 2020

Place: DTU, New Delhi

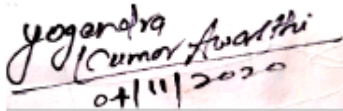
GAURAV SAXENA

2K14/PHD/EC/03

CERTIFICATE

Certified that **Gaurav Saxena (2k14/Ph.D/EC/03)** has carried out the research work presented in this thesis entitled “**DESIGN AND ANALYSIS OF MICROWAVE COMPONENTS FOR MIMO COMMUNICATION SYSTEM**”, for the award of **Doctor of Philosophy** from the Department of Electronics and Communication Engineering, **Delhi Technological University, New Delhi** is an authentic record of work carried out during Ph.D. under the supervision **Dr. Priyanka Jain (Associate Professor)** Department of Electronics and Communication Engineering, DTU, Delhi and Co-supervisor **Dr. Y K Awasthi (Professor)** Department of Electronics and Communication Engineering, MRIIRS, Faridabad, HR. The matter presented in this thesis has not been submitted by me for the award of any degree or diploma elsewhere.

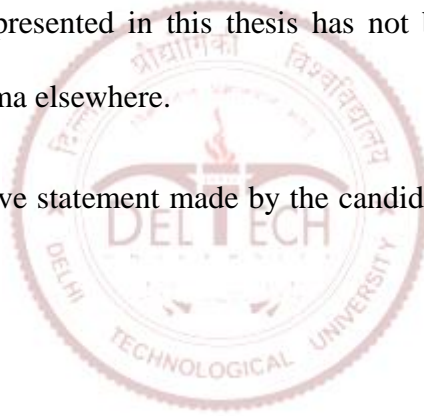
This is to certify that the above statement made by the candidate is correct to the best of my knowledge.



Yogendra Kumar Awasthi
04/11/2020

Sign of Co-Supervisor

Dr. Y K AWASTHI
Professor,
Department of ECE
MRIIRS, Haryana (INDIA)



Priyanka Jain
25/11/2020

Sign of Supervisor

Dr. PRIYANKA JAIN
Associate Professor,
Department of ECE
DTU, Delhi (INDIA)

Date:

The Viva Voice examination was successfully held at Delhi Technological University, New Delhi

On.....

Vice-Chancellor External Examiner Internal Examiner (1) Internal Examiner (2)

DRC Committee

ABSTRACT

Wireless communication demands better channel capacity with a high data rate in the modern era. To fulfill these demands, the MIMO-communication systems are developed that use manifold antennas for transmitter and receiver end. MIMO is a state-of-art technology that improves the reliability of the communication systems by utilizing the diversity technique to mitigate the multi-path fading issues, where signals may come together belligerently at the receiver. Improve spectral efficiency is achieved by the total transmitted power spreading over the antennas. Thus, MIMO can increase channel capacities as well as the reliability of the communication system without sacrificing extra transmitted power or power spectrum. Several MIMO antennas have been designed in the literature to improve their characteristics in terms of impedance bandwidth; miniaturization & isolation improvement. The MIMO-communication systems with THz range are required for high data speed in Terabit/sec (Tbps). Also, it is providing very high throughput per device (from multiple Gbps to several Tera-bps) including per area efficiency (bps/km²). It is also predicted that the world monthly traffic in smartphones will be about 40 Peta-bytes in 2021, so the demand for MIMO antennas will be increased in the future. In this thesis, various microwave components for the MIMO wireless communication system has been analyzed and designed. Three major components designed and analyzed in this thesis are

1. MIMO Antennas
2. Metamaterial Absorber
3. UWB Microwave Filter

MIMO Antennas: In this thesis, various MIMO antennas for UWB, SWB, and Multiband applications have been designed. Various decoupling techniques to avoid the

interference between antenna elements are designed which enhancing the diversity parameters with improved channel capacity for modern wireless applications. To mitigate the interference between bands and to improve the reliability of the signals, a notch characteristic has been introduced. SAR analysis also discusses in this thesis with the human head and confirms that proposed MIMO antennas are in the acceptable range with 1g and 10g of bio tissues given by FCC and EU for mobile and other near field applications. All the MIMO antennas with different frequency characteristics are discussed in [Chapter-2](#) to [Chapter-6](#).

Metamaterial Absorber: To improve the isolation level in MIMO antennas as well as to minimize the Radar Cross Section (RCS) and Electromagnetic Interference (EMI), a design of multiband metamaterial absorber (MMA) for X-band applications has been suggested. This MMA provides three high absorbance bands at 8.2GHz, 9.45GHz, and 12.45GHz with 99.4%, 96.4%, and 91.25% absorbance respectively. Proposed MMA is polarization insensitive in all three bands with minimum RCS -33.2dBm^2 . This absorber structure has designed on FR-4 (4.4) substrate having $\tan\delta = 0.02$ with unit cell dimension $20\times 20\times 1\text{mm}^3$. So the proposed absorber is found appropriate for stealth aircraft, RCS and EMC reduction, isolation in MIMO antenna, imaging, and sensing in the X-band applications, discussed in [Chapter-7](#).

UWB Microwave Filter: In this research work, the design of the UWB filter with extended stopband characteristics by using a parallel-coupled line, open-ended line, multi-mode resonator (MMR), and defected ground structure (DGS) has been presented. This filter provides good return and insertion loss in the passband (3.1-10.6GHz) as well as stopband (10.8-18GHz). The group delay of the filter is almost constant throughout the passband. Detailed analysis of supportive coupled, feeding, and the open-ended line is

verified with equivalent circuits. The prototype of the filter is compact as $22 \times 20 \text{mm}^2$ with a 109% fractional bandwidth. The proposed filter is suited for recent weather reporting Radar, Imaging, and Satellite receiver systems because simulated results have good agreement with measured results **as discussed in the Chapter-8.**

RESEARCH OBJECTIVES:

The major objectives of the research work are listed below:

1. To enhance the impedance bandwidth of the MIMO antenna and microstrip filter for various wireless applications.
2. To design and analyze the circularly polarized MIMO antenna for GPS, vehicular and 5G applications.
3. To enhance the isolation between the various elements of the MIMO antenna, to improve the various diversity parameters.
4. To enhance the specific absorption ratio (SAR) performance of the MIMO antenna for a handheld and mobile applications.
5. To design a Metasurface for stealth and isolation improvement in MIMO antenna applications.

ACKNOWLEDGMENTS

First of all, I would like to thank GOD for blessing me with courage, determination, and perseverance to keep working towards my goal, for making my bad day's bearable and good days wonderful. When I first stepped onto the unpaved path of research five years ago, I had an almost blank map in my hand, where only the largest tracks were drawn. I started walking, and during my journey, I managed to draw the map myself. Today, the map is almost complete and I hope it can be useful for other travellers. I have been down many frustrating sidings, but I have also found new useful paths that lead to discoveries, which is very rewarding and the source of my motivation several individuals have played an important role in the journey that led to this thesis.

I express my deepest sense of gratitude and thanks to my supervisor **Dr. Priyanka Jain** and Co-Supervisor **Dr. Y K Awasthi** for her/his generous help, continuous guidance, keen interest, constant encouragement, confidence, and support throughout my Ph.D. work at the **Department of Electronics and Communication Engineering, Delhi Technological University Delhi**. For me, my guides are one of those rare, extremely special people who not only advised me on recent advancements but also about life and research ethics. I would like to thank my guide and co-guide for allowing me to address some of the most off-putting challenges that the RF & Microwave industry is facing today.

First I thank Hon'ble vice-chancellor **Prof. (Dr.) Yogesh Singh**, Head **Prof. (Dr.) N S Raghava**, DRC Chairperson **Prof. (Dr.) Asok De** and **Prof. (Dr.) S Indu** Department of Electronics and Communication Engineering, Delhi Technological University, Delhi for making all facilities available to me during the research work and continuously encourage the research scholars for good publication.

My special thanks to Director GCET **Prof. (Dr.) Brijesh Singh**, HOD ECE, and **Prof. (Dr.) Lakshmanan M.** and my colleague **Dr. Madan Sharma, Mr. Ankit Sharma** for the kind supports of my research work. I am also thankful to **Prof. (Dr.) O P Verma, Mr. Padam**

Saini of GB Pant Engineering College, New Delhi for providing measurement facilities in his laboratory.

I also owe my thanks to my wife **Anchal Saxena**, my brother **Mr. Saurabh Saxena** and parents who always encouraged and supported me in all my decisions. I am thankful to my parents especially my mother **Smt. Sanju Rani Saxena** for unconditional love, sacrifice & for instilling in me the reverence for learning and the strength and belief, which have been pillars by my side throughout. This work would not have been possible without the blessings and affection of my daughter **Aradhya Saxena** and Son **Vivaan Saxena** who have helped and supported me to complete this thesis work. I would like to thank the rest of my family members & friends for being supportive, understanding, patience, and for shaping me into what I am.

Date: November 2020

Place: DTU, New Delhi



GAURAV SAXENA

Roll. No.2K14/PHD/EC/03

TABLE OF CONTENTS

DECLARATION.....	.ii
CERTIFICATE.....	.iii
ABSTRACT.....	iv
ACKNOWLEDGMENTS.....	vii
TABLE OF CONTENTS.....	ix
LIST OF TABLES.....	xii
LIST OF FIGURES.....	xv
LIST OF ACRONYMS.....	xxii
1. INTRODUCTION.....	1
1.1 Introduction.....	1
1.2 Diversity Parameters of MIMO Antenna.....	2
1.3 Literature Review.....	5
1.4 Thesis Organization.....	22
2. UWB MIMO ANTENNA WITH WLAN NOTCH BAND CHARACTERSTICS.....	26
2.1 Introduction of UWB MIMO Antenna.....	26
2.2 UWB MIMO Antenna Design Procedure.....	27
2.3 UWB MIMO Results and Discussion.....	31
2.4 UWB MIMO Diversity Performances.....	35
2.5 Summary.....	41
3. SUPER WIDEBAND (1.575-40GHZ) MIMO ANTENNA FOR WIRELESS APPLICATIONS.....	43
3.1 Introduction of SWB MIMO Antenna.....	43
3.2 SWB MIMO Antenna Design Procedures.....	44
3.3 SWB MIMO Antenna Results and Discussion.....	50

3.4 SWB MIMO Diversity Performances	56
3.5 Summary	63
4. HIGH ISOLATION MIMO ANTENNA FOR MULTIBAND APPLICATIONS	64
4.1 Introduction of Multiband Band MIMO Antenna	64
4.2 Design Procedure of Multiband MIMO Antenna.....	66
4.3 Results Discussion of Multiband MIMO Antenna	68
4.4 MIMO Antenna Diversity Performance.....	75
4.5 Summary.....	81
5.1 DESIGN OF METASURFACE ABSORBER FOR LOW RCS AND HIGH ISOLATION MIMO ANTENNA FOR RADIO LOCATION AND NAVIGATION..	82
5.1.1 Introduction	82
5.1.2 Absorber Design Analysis and Results	83
5.1.3 MIMO Antenna Design Analysis and Results	91
5.1.4 Diversity Performance of MIMO Antenna	95
5.1.5 Summary	98
5.2 TRIPLE BAND POLARIZATION INSENSITIVE ULTRA THIN METASURFACE ABSORBER FOR EMC AND RCS REDUCTION IN X-BAND APPLICATIONS ..	99
5.2.1 Introduction of Meta Absorber	99
5.2.2 Design of Proposed MMA Structure	99
5.2.3 Simulated Results of MMA	100
5.2.4 Summary of MMA	105
6. HIGH ISOLATION AND HIGH GAIN SUPER-WIDEBAND (0.33-10THZ) MIMO ANTENNA FOR THZ APPLICATIONS.....	106
6.1 Introduction of THz MIMO Antenna	106
6.2 Design Procedure of THz MIMO Antenna	107

6.3 Results and Discussion	108
6.4 THz Channel Model	113
6.5 Diversity Performance of THz MIMO.....	114
6.6 Summary	117
7. DESIGN AND ANALYSIS OF PLANAR UWB BANDPASS FILTER WITH STOPBAND CHARACTERISTIC	119
7.1 Introduction of UWB Filter.....	119
7.2 Filter Design Analysis.....	120
7.2.1 Design Equation of Parallel and Open-Ended Coupled Microstrip Line	122
7.2.2 Calculation of Microstrip Line Width (W)	124
7.2.3 Calculation of Length of Parallel Microstrip Coupled Line (L_{mcl})	124
7.2.4 Calculation & Analysis of MMR & DGS.....	125
7.2.5 Band- Stop Characteristic Analysis	126
7.3 Results and Discussion.....	128
7.4 Summary	132
8. CONCLUSION AND FUTURE SCOPE	133
8.1 Conclusion of the Thesis	133
8.2 Future Scope of Work.....	137
REFERENCES	139
LIST OF PUBLICATIONS.....	152
CURRICULUM VITAE	154

LIST OF TABLES

1.1	MIMO antenna and filter performance enhancement techniques	20
2.1	Parameters of the human head for calculation of specific absorption rate (SAR) by the proposed antenna at constant permeability (i.e. $\mu_r = 1$) . . .	35
2.2	SAR values near the human head at different resonant frequencies when the distance between the human head and MIMO antenna is 13mm . . .	35
2.3	Simulated MEG results of proposed MIMO antenna at various frequencies	39
2.4	Comparison of proposed UWB-MIMO antenna including WLAN notched band with existing references at various aspects	41
3.1	Performance comparison of the decoupling techniques over the proposed design	45
3.2	Proposed SWB MIMO antenna dimensions in mm	55
3.3	Parameters of the human head used for calculation of specific absorption rate by the proposed antenna at constant permeability	55
3.4	SAR values near the human head at the different resonant frequencies when the distance between the human head and MIMO antenna is 15mm	59
3.5	Simulated MEG results of proposed MIMO antenna at various frequencies	61
3.6	Comparison of designed SWB-MIMO antenna with existing references in various aspects	62

3.7	Performance comparison of the decoupling techniques over the proposed design	62
4.1	Simulated SAR at resonant frequencies for the human head at 6mm distance	74
4.2	Parameters of the bio tissues for skin, bone, and brain used for calculation of SAR of MIMO antenna with constant permeability	75
4.3	Simulated MEG results of penta-band MIMO antenna at various XPR and frequencies	79
4.4	Comparison of the performance of penta-band MIMO antenna with existing multiband MIMO antennas at diverse parameters ..	81
4.5	Comparison of the proposed isolation mechanism with the existing mechanism	81
5.1.1	Dimensions of designed metasurface shown in Fig 5.1 (a)	85
5.1.2	Meta surface position in MIMO antenna w.r.t ($X_{\min} = -35$, $X_{\max} = 20$) and ($Y_{\min} = -15$, $Y_{\max} = 25$), all dimensions in mm	90
5.1.3	Measured S-parameters of proposed 4-elements MIMO antenna with and without metasurface at 8.75-9.0GHz frequency band	92
5.1.4	Isolation and ECC comparison table of the proposed antenna with existing literature	97
5.1.5	Isolation and RCS comparison table of the proposed antenna with existing reference	97
5.2.1	Dimensions of designed MMA shown in Fig 8.1 (a) and 8.1(b)	100

5.2.2	Comparison table of proposed MMA with existing references	104
6.1	Comparison table of a designed THz MIMO antenna with existing references in various aspects for antenna performance	117
7.1	Elements value for optimum bandpass filter for ripple 0.5dB	123
7.2	Elements value for optimum bandstop filter for ripple less than 0.5dB	128
7.3	Results of the proposed UWB filter in the passband & stopband	129
7.4	Comparison of various parameters of the proposed filter with published articles	132



LIST OF FIGURES

1.1	UWB and other radio systems according to FCC	6
1.2	Structures offering –UWB MIMO antenna with notch characteristics	7
1.3	Structures offering SWB MIMO antenna with and without notch characteristics	9
1.4	Structures offering multiband MIMO antennas	11
1.5	Structures offering high isolation and low RCS antennas	14
1.6	Structures offering THz MIMO antennas	16
1.7	Various UWB bandpass filter with an extended notch	18
1.8	Various UWB and multiband band absorber	20
2.1	A generic block diagram of two-element UWB-MIMO antenna-based receiver station	26
2.2	Two-element UWB planar monopole MIMO antenna (a) Front view (b) Bottom view	27
2.3	Geometrical design steps of a designed antenna with WLAN band-notch characteristic	28
2.4	Simulated (using CST MWS) results of (a) Return loss (b) Isolation of the antennas shown in Fig.2.3	29
2.5	Simulated results of (a) Return loss and (b) Isolation of antenna with a variation of length of stubs (Ls) in the ground plane	29
2.6	Surface current distributions at (a) Notch band frequency i.e. 5.6GHz and (b) 4.1, 6.6 and 9.6GHz when port-2 terminated with 50Ω impedance and port-1 is excited	30
2.7	Simulated and measured results of (a) S-parameter (return & isolation) (b) Peak gain, radiation efficiency & total radiation efficiency of UWB-MIMO antenna	31
2.8	The 3D radiation pattern of MIMO antenna at (a) 4.1GHz (b) 6.6GHz (c) 9.6GHz only port-1 is excited and port-2 terminated by 50Ω load (d) Fabricated prototype (e) Antenna under test in an anechoic chamber for radiation pattern measurement	32

2.9	Measured & simulated 2D radiation pattern at 4.1, 6.6 and 9.6GHz for yz-plane (left) and xz-plane (right)	33
2.10	Calculation of specific absorption rate near the human head in presence of the proposed MIMO antenna	35
2.11	Simulated and measured results of the proposed antenna (a) Envelope correlation coefficient and diversity gain (b) Simulated result of multiplexing efficiency	36
2.12	Simulated and measured results of (a) Channel capacity loss (CCL) and total active reflection coefficient (TARC) (b) Simulated results of the mean effective gain (MEG) and group delay of proposed MIMO antenna	37
2.13	Simulated (a) Mean effective gain in Isotropic and Gaussian medium at various XPR values of proposed antenna applications (b) Power associated with proposed MIMO antenna for various diversity performances	40
3.1	Two-element SWB planar monopole MIMO antenna (a) Front view (b) Bottom view	45
3.2	Geometrical design steps of the proposed super-wideband MIMO antenna with band notch characteristics	46
3.3	Simulated (using CST MWS) results of (a) return loss (b) isolation of the antennas shown in Fig.3.2	47
3.4	Circuit analysis of electromagnetic band gap structures (a) Mushroom-shaped EBG designs near to the microstrip stepped feed line (b) Equivalent circuit model of EBG (c) Front cross-sectional view of EBG (d) Simulated results of the equivalent circuit model of EBG with its resonance frequency	48
3.5	Electromagnetic field analysis of stepped impedance feeding line and EBG structures (a) Simulated scattering results of stepped impedance feeding line only (b) Simulated scattering results of stepped impedance feeding line with EBG designs (c) Simulated FBR of SWB-antenna with and without EBG structures (d) Field distribution with and without EBG at 1.575, 3.4, 7.55, 15, 25, 35GHz frequency when port-1 excited and port-2 terminated with a matched load	50

3.6	Simulated and measured (a) S-parameters (return & isolation) (b) group delay and gain.	51
3.7	Simulated analysis (a) Parametric analysis of axial ratio in L1-band (b) Parametric analysis of axial ratio in K-band of SWB-MIMO antenna	52
3.8	Surface current density distribution at 1.575, 3.40, 3.45, 5.50, 7.55, 8.69, 15.0, 25.0, & 35.0GHz when antenna 1 (left) is energized and antenna 2 (right) terminated with match load	53
3.9	3D radiation pattern of designed MIMO antenna at (a) 1.575, 3.45, 3.50, 8.50, 15.0, & 37.9GHz (b) Fabricated prototype top and bottom view (c) Antenna under test in anechoic chamber for radiation pattern measurement	54
3.10	Measured & simulated 2D radiation patterns at 1.575, 3.45, and 28.0GHz for yz- plane (left) and xz- plane (right), antenna 1 is energized and antenna 2 is terminated by a matched load	55
3.11	Calculation of specific absorption rate near the human head in the presence of the designed MIMO antenna	55
3.12	Diversity performance of proposed SWB antenna (a) Measured and simulated results of envelope correlation coefficient (ECC) (b) Simulated results of ECC and DG with and without EBG	57
3.13	Comparison of channel capacity of 2 element antennas array with a maximum and permissible limit of a 2x2 MIMO antenna system	59
3.14	Simulated and measured results of channel capacity loss (CCL) and total active reflection coefficient (TARC) of proposed MIMO antenna	59
3.15	Simulated results of mean effective gain in Isotropic and Gaussian medium at different XPR values of the proposed antenna	60
3.16	Power level of 2 elements MIMO antenna in various states	60
4.1	A pictorial representation of the 4x4 MIMO antenna transceiver system	65

4.2	Proposed penta-band antenna (a) Step-by-step geometrical design procedure (b) Simulated return loss	66
4.3	The geometry of 4-element MIMO antenna including physical dimensions (a) Front view (b) Bottom view	67
4.4	Simulated and measured results of the proposed antenna in terms of (a) S_{11} (b) S_{21} , S_{31} , S_{41} (c) Axial ratio (d) Gain and radiation efficiency	69
4.5	Current density and Electric field distribution at (a) 2.2, 2.4GHz frequency for RHCP/LHCP (b) 2.2, 2.4, 2.6, 3.2, 3.4GHz when antenna 1 is energized and remaining antennas are terminated with matched 50 Ω load	71
4.6	3D radiation pattern of designed MIMO antenna at (a) 2.2, 2.4, 2.6, 3.2, & 3.4GHz when antenna 1 is excited only (b) Top and bottom view of a prototype (c) Antenna under test-AUT for radiation pattern measurement in the anechoic chamber	72
4.7	Simulated & measured 2D radiation patterns at 2.2, 2.4, 2.6, 3.2 and 3.4GHz for <i>E</i> -plane and <i>H</i> -plane, antenna 1 is energized and rests of antennas are terminated by a matched load	73
4.8	Specific absorption rate calculation of the designed MIMO antenna near the human head at a distance of 6mm	74
4.9	Measured and simulated results of the proposed MIMO antenna (a) Envelope correlation coefficient from radiated fields (b) Envelope correlation coefficient from S-parameters (c) multiplexing efficiency	76
4.10	The proposed 4-element antenna (a) Calculated average channel capacity (b) Simulated and measured results of channel capacity loss	77
4.11	Simulated results of mean effective gain of the proposed antenna in Isotropic, Laplacian and Gaussian medium for indoor and outdoor values	79
4.12	Power levels of the designed MIMO antenna in various states as power loss, power stimulated, power accepted, and power radiated, power absorbed, and power outgoing	79

5.1.1	The proposed geometry of the unit cell of metasurface with structural dimensions (a) Front view (b) Bottom view	84
5.1.2	A general equivalent circuit model of the proposed unit cell of metasurface structure.	85
5.1.3	Simulated return loss of proposed unit cell of metasurface at intended frequency	86
5.1.4	Simulated absorbance and reflectivity of the proposed unit cell of metasurface at intended frequency	86
5.1.5	Phase illustration of return loss and normalized input impedance of the proposed unit cell.....	87
5.1.6	Parametric study of return loss of the proposed unit cell with different values of used lumped resistance	84
5.1.7	Parametric study of the return loss of proposed metasurface with a variation of various incidence angles in TE-mode	85
5.1.8	Simulated (a) Current density (b) Electric field (c) RCS of proposed unit cell of metasurface at 8.78GHz frequency	85
5.1.9	Demo measurement setup of RCS (a) Anechoic chamber (b) Simulated and measured RCS of proposed metasurface at various incident angle- θ and polarization angle- ϕ ..	86
5.1.10	Top and bottom of the proposed four-element MIMO antenna with metasurface absorber	87
5.1.11	S-parameter measurement results (a) Return Loss (b) Isolation of 4-elements MIMO antenna with metasurface	91
5.1.12	(a) Setup an arrangement for measurement Co-polarization and Cross-polarization (b) E-plane simulated and measured (c) H-plane simulated and measured at 8.78GHz .	93
5.1.13	Simulated and measurement results of (a) Simulated Current density (b) Radiation efficiency and Gain (c) Simulated 3D radiation pattern measurement results of 4 elements MIMO antenna with MS	94
5.1.14	Simulated and measured results (a) ECC from S parameter and radiated field (b) MEG (c) TARC (d) CCL of proposed MIMO antenna with MS	95

5.2.1	Proposed triple band meta-material absorber structure (a) Front view (b) Bottom view	100
5.2.2	Simulated results of (a) Return loss of proposed triple-band absorber (b) Absorbance and reflectivity of proposed triple-band absorber at different frequencies	100
5.2.3	Simulated results (a) Return loss (phase) vs Frequency plot of proposed triple-band absorber (b) Parametric study of the return loss of proposed triple-band absorber with and without middle oval strips	101
5.2.4	Simulated response of return loss of proposed triple band MMA at various incidence angles	102
5.2.5	RCS vs Theta and Phi plot at (a) 8.2GHz (b) 9.45GHz (c) 12.45GHz	102
5.2.6	Simulated surface current density of proposed absorber at (a) 8.2GHz (b) 9.45GHz (c) 12.45GHz frequency respectively	103
5.2.7	Simulated electric field of proposed absorber at (a) 8.2GHz (b) 9.45GHz (c) 12.45GHz frequency respectively	104
6.1	Frequency spectrum with state-of-art THz communications	107
6.2	Two-element THz planar monopole MIMO antenna (a) Front view (b) Bottom view	108
6.3	Simulated results of (By using CST Microwave studio) (a) Return loss and isolation (b) Radiation and total efficiency (c) Gain and group delay of the antennas shown in Fig. 6.2	109
6.4	Surface current density distribution at frequencies 1THz, 2THz, 4THz, and 8THz when antenna-1 (left) is energized and antenna-2 (right) is terminated by a matched load (50ohm) and vice-versa	110
6.5	Simulated Far-Field patterns of designed MIMO antenna at frequencies 1THz, 2THz, 4THz, and 8THz (a) 3D radiation patterns (b) 2D field patterns at $\phi = 0^\circ$ and 90° ..	111
6.6	Simulated 2D radiation patterns at 1THz, 4THz, and 8THz for xz- plane (right) and yz- plane (left), when port-1 is energized and port-2 is terminated by a 50Ω matched the load.	112

6.7	Simulated results of the envelope correlation coefficient and diversity gain	115
6.8	Simulated results of (a) Maximum, threshold and proposed Average channel capacity (b) CCL and TARC of the proposed MIMO antenna	115
7.1	UWB Transmitter-Receiver block diagram with bandpass filters	119
7.2	The proposed geometry of filter (a) Front view (b) Back view	120
7.3	Step-by-step geometrical analysis of the proposed UWB bandpass filters (a) Geometrical steps (b) Return Loss (c) Insertion Loss	121
7.4	Transmission line model of the proposed UWB bandpass filter	122
7.5	Proposed DGS (a) Structure (b) Equivalent circuit (c) Equivalent circuit model of all DGS structure	125
7.6	The proposed UWB BPF/BSF (a) Return (S_{11}) & Insertion loss (S_{21}) results-simulated, measured, and equivalent circuit (b) Equivalent circuit model	129
7.7	Measured & simulated group delay of a proposed UWB BPF with stopband characteristics	131
7.8	The simulated current density of the designed filter at (a) 4.65GHz (b) 7.88GHz (c) 9.52GHz respectively (d) and prototype of a filter	131

LIST OF ACRONYMS

AUT	Antenna under Test
BPF	Band Pass Filter
BSF	Band Stop Filter
CCL	Channel Capacity Loss
CRR	Closed Ring Resonator
CST	Computer Simulation Technology
CSRR	Complementary Split Ring Resonator
DG	Directive Gain
DGS	Defected Ground System
EBG	Electromagnetic Band Gap
ECC	Envelope Correlation Coefficient
EM	Electromagnetic
EMC	Electromagnetic Compatibility
EMI	Electromagnetic Interference
FBR	Front to Back Ratio
FCC	Federal Communications Commission
IL	Insertion Loss
LOS	Line-of-Sight
LTE	Long Term Evaluation
LHCP	Left Hand Circular Polarization

MEG	Mean Effective Gain
MIMO	Multiple-Input and Multiple-Output
MS	Metasurface
MMA	Metamaterial Absorber
MMR	Multi Mode Resonator
RCS	Radar cross-section
RF	Radio Frequency
RHCP	Right Hand Circular Polarization
RL	Return Loss
ROC	Roll off Criteria
SAR	Specific Absorption Rate
SRR	Split Ring Resonator
SWB	Super Wide Band
TARC	Total Active Reflection Coefficient
UWB	Ultra Wide Band
VNA	Vector Network Analyser
WiMAX	Worldwide Interoperability for Microwave Access
WLAN	Wireless Local Area Network
XPR	Cross Polarization Ratio

CHAPTER-1

INTRODUCTION AND REVIEW OF THE STATE-OF-ART

1.1 INTRODUCTION:

The modern era of wireless communication demands a high data rate and better channel capacity. This drives the development of multiple-input-multiple-output (MIMO) communication systems that use multiple antennas on transmitter and receiver sides. MIMO is an up-coming technology that utilizes the diversity technique to improve the communication system's reliability by justifying the exposed multi-path fading problem, where signals may combine destructively at the receiver. This goal is achieved by spreading the total transmitted power over the antennas to improve spectral efficiency. Thus, MIMO can increase the data rate and the communication system's reliability without sacrificing extra transmitted power or power spectrum. Several MIMO antennas have been designed in the literature to improve their characteristics in terms of impedance bandwidth, miniaturization, and isolation improvement. MIMO antenna is extensively utilized in the modern wireless RF communication system to improve the diversity problem in a single input single output (SISO) antenna. Wireless communication demands better channel capacity with a high data rate. To fulfill these demands, the MIMO antenna is being used in GHz and THz range with high data speed in Giga-bits/sec to Tera-bit/sec (Tbps). MIMO antenna provides very high throughput per device (from multiple Gbps to several Tera-bps), including per area efficiency (bps/km²).

The performance of a MIMO antenna is evaluated by basic parameters such as impedance bandwidth, Gain, Radiation efficiency, and axial ratio apart from the diversity parameters which have been discussing in the next section-1.2.

1.2 DIVERSITY PARAMETERS OF MIMO ANTENNA:

The following terms evaluate the diversity performance of the MIMO antenna-

1. Envelope Correlation Coefficient (ECC):

ECC calculates the mutual coupling between two radiators and the amount of correlation between them. It is calculated through using S-parameters by following Equation (1.1) and this Equation is valid for measuring ECC when the antenna is lossless and radiated power is uniformly distributed along with the antennas.

$$ECC_{ij} = \frac{|S_{ii} * S_{ij} + S_{ji} * S_{jj}|^2}{(1 - |S_{ii}|^2 - |S_{ji}|^2)(1 - |S_{jj}|^2 - |S_{ij}|^2)} \quad (1.1)$$

But lossless is a hypothetical result that varies from empirical result so, computation of the ECC of a MIMO antenna can be obtained by Equation (1.2) in terms of radiated fields.

$$ECC = \frac{\left| \iint_{4\pi} [E_i(\theta, \phi) \times E_j(\theta, \phi)] d\Omega \right|^2}{\iint_{4\pi} |E_i(\theta, \phi)|^2 d\Omega \times \iint_{4\pi} |E_j(\theta, \phi)|^2 d\Omega} \quad (1.2)$$

where E_i & E_j are the radiated electric fields vector of the i^{th} and j^{th} elements of the MIMO antenna system. The ideal value of ECC is zero for uncorrelated MIMO antenna, but their acceptable value for practical MIMO antenna is less than 0.5.

2. Diversity Gain (DG):

MIMO channel fading performance is to be judge by DG. The ideal value of DG (at $ECC = 0$) of any MIMO antenna is 10dB and the practical value of DG is greater than 9.5dB and it is expressed in terms of ECC by $DG = 10 \times \sqrt{(1 - ECC^2)}$. If the value of DG closes to 10dB (i.e. less fading signals) reliability of received signals should be high.

3. Total Active Reflection Coefficient (TARC): TARC is the square root of the ratio of total reflected power to the total incident power. Hence, it gives information about the apparent return

loss of the MIMO antenna system. For side by side two-port radiated antenna system, it can be evaluated by Equation (1.3).

$$TARC = \frac{\sqrt{\sum_{i=1}^n |S_{i1} + \sum_{n=2}^n S_{in} e^{j\theta_{n-1}}|^2}}{2} \quad (1.3)$$

Its acceptable value for the MIMO antenna is greater than 0dB.

4. Multiplexing Efficiency (η_{MUX}):

Multiplexing efficiency (η_{MUX}) is the ratio of the power requirement for the test antenna to the reference antenna. The main feature of multiplexing efficiency is to shows the correlation and efficiency imbalance between MIMO antennas used in the wireless system. Multiplexing efficiency of the MIMO antenna and η_{MUX} is calculated by $\eta_{MUX} = \sqrt{(1 - |\rho_c|^2)} \eta_1 \eta_2$, where ρ_c is a complex correlation between two side by side antennas i.e. $ECC = \rho_c^2$ and η_1, η_2 is the total antenna efficiency of MIMO antenna elements. The practical value of multiplexing efficiency is greater than 0.5.

5. Mean Effective Gain (MEG):

Another parameter for evaluation of MIMO antenna performance is MEG, the mean effective gain (MEG) is the ratio of the mean received power (P_{rec}) by the i^{th} antenna to the mean incident power (P_{inc}) of the j^{th} antenna with the same route, $MEG_i = \mathcal{E}_{Total}/2$, where \mathcal{E}_{Total} is implying total effective efficiency of the i^{th} antenna, i.e. $\mathcal{E}_{Total}^i = \mathcal{E}_{mis}^i \times \mathcal{E}_{rad}^i$, where $\mathcal{E}_{mis}^i = 1 - \sum_{j=1}^N |S_{ij}|^2$, $\mathcal{E}_{rad}^i = \sum_{j=1}^N |S_{ij}|^2$ where \mathcal{E}_{mis}^i , and \mathcal{E}_{rad}^i are mismatch efficiency and radiation efficiency of the i^{th} antenna.

The MEG ratio for the MIMO antenna is to be extracted by Equation (1.4).

$$MEG_i = \frac{P_{rec}}{P_{inc}} = \oint \left[\frac{XPR \times G_{\theta i}(\Omega) + G_{\phi i}(\Omega) \times P_{\phi}(\Omega)}{1 + XPR} \right] d\Omega \quad (1.4)$$

Where, XPR is the cross-polarization ratio, $G_{\theta_i}(\Omega)$, $G_{\phi_i}(\Omega)$ and $P_{\phi}(\Omega)$ are the gain and power density function of the incident wave, Ω = beam area. The MEG of any practical MIMO antenna falls within the permissible limit ($\leq \pm 3\text{dB}$) for all bands.

6. Channel Capacity:

Channel capacity is an important parameter to judge the data speed of the MIMO communication system. It is expressed by Equation (1.5), where k denotes the no. of antenna elements proposed in the MIMO system and $[H][H^*]$ denotes the fading matrix. For a non-fading environment, the fading matrix is converted into an identity matrix $[I]$. If channel capacity increases then data speed also increases.

$$C_{\text{MIMO}} = k \left\{ \log_2 \left[\det \left([I] + \frac{\text{SNR}}{k} [H][H^*] \right) \right] \right\} \quad (1.5)$$

7. Channel Capacity Loss (CCL):

Channel capacity is dependent on the number of antenna elements used as well as on the correlation between two antenna elements. More the MIMO antennas are uncorrelated, the more the channel capacity *i.e.* the more correlation the more channel capacity loss (CCL); the diversity performance of MIMO antenna pretentious and channel capacity losses are calculated by the following Equation (1.6)-(1.8).

$$\text{CCL} = -\log_2(\psi^P) \quad (1.6)$$

$$\text{Where, } \psi^P = \begin{bmatrix} \rho_{11} & \rho_{12} & \rho_{13} & \rho_{14} \\ \rho_{21} & \rho_{22} & \rho_{23} & \rho_{24} \\ \rho_{31} & \rho_{32} & \rho_{33} & \rho_{34} \\ \rho_{41} & \rho_{42} & \rho_{43} & \rho_{44} \end{bmatrix}$$

$$\rho_{ii} = 1 - \left(\sum_{n=1}^N |S_{in}^* S_{ni}| \right) \quad (1.7)$$

$$\rho_{ij} = -\left(\sum_{n=1}^N |S_{in}^* S_{nj}|\right) \text{ Where } i, j, n=1, 2, 3... \quad (1.8)$$

The element matrix properly characterizes the performance of a MIMO system as it provides information about the phase and gain characteristic of the transmitting and receiving elements. However, in the presence of the correlation factor in MIMO antennas, the channel capacity losses are also increased. The ideal value of CCL should be zero and for satisfactory operation, CCL should be <0.35bps/Hz for the MIMO antenna.

In the next section, the literature review has been given where review has been divided into the following sections: UWB MIMO antenna, Super Wideband MIMO antenna, Multiband MIMO antenna, Metasurface for low RCS and high isolation MIMO antenna, THz MIMO Antenna and UWB bandpass filter. The literature review concerned with the above sections is discussed in the next sections 1.3.

1.3 LITERATURE REVIEW:

1.3.1 Ultra-Wideband (UWB) and Super-Wideband (SWB) MIMO Antennas:

FCC **has** introduced commercial communication applications like video imaging, ground-penetrating RADAR system, medical, and vehicular communication systems. According to FCC, revision of part 15 of the Commission's rules regarding Ultra-Wideband transmission, UWB frequency lies between 3.1-10.6GHz with 109% fractional bandwidth without licensing, the Effective Isotropic Radiated Power (EIRP) < -41.3dBm/MHz for indoor and outdoor operations. The most prominent advantage of UWB communication is the high data rate (>100Mbps) with low power consumption [1]. A complete UWB spectrum with other radio systems, according to FCC, is depicted in Fig.1.1. UWB antennas have many advantages, such as high data transmission rate, low power, and compact dimension. UWB MIMO antenna is used to improve diversity gain and reduce the multipath fading effect. Narrowband system like WLAN (5.15-5.185GHz) wireless local area network operates in UWB bandwidth and causes interference with

the UWB band. So designing of UWB MIMO antenna with the WLAN notch band characteristic is a very challenging task to avoid the interference WLAN band with the UWB spectrum. UWB MIMO antennas with band notch characteristics are discussed in the literature [2-24]. Two circular monopoles are placed orthogonally to achieve better isolation and ECC. Monopoles and fractal slots are used to achieve UWB bandwidth because they reduce the plate capacitance and decrease the Q factor, which provides UWB bandwidth.

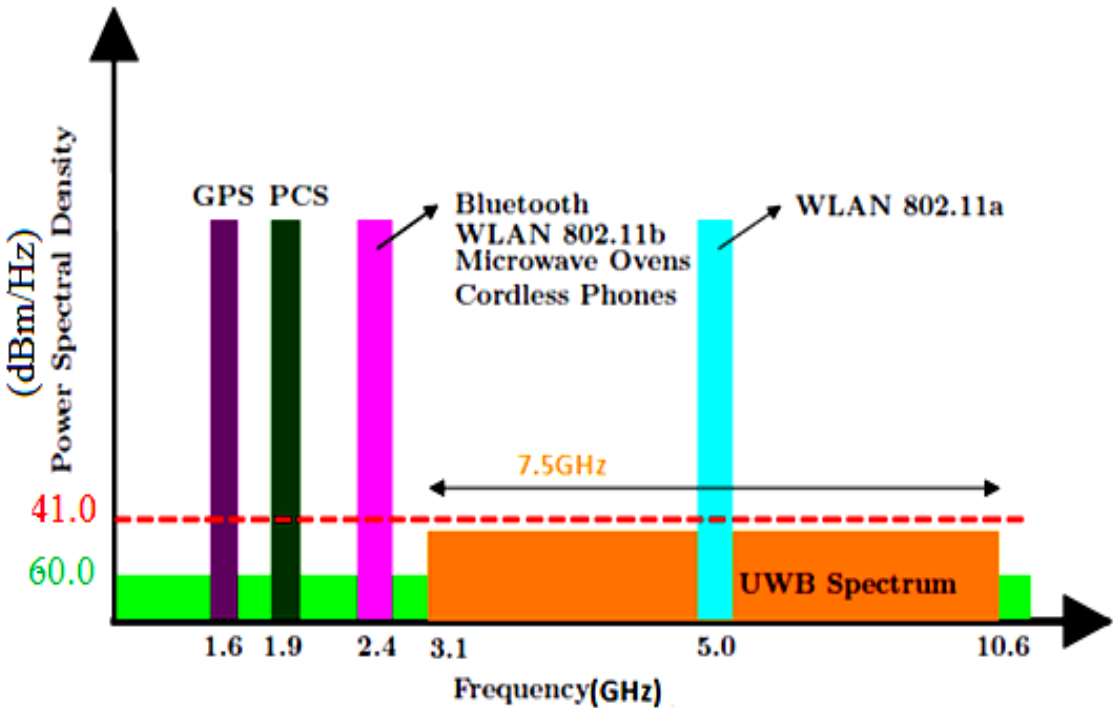


Fig. 1.1: UWB and other radio systems according to FCC

ESRR (Elliptical Split Ring Resonator) cuts on the patch provide the WLAN notch characteristics which mitigate the interference with UWB. Orthogonally placed MIMO antenna achieved good isolation because the electric field component from the radiated antenna to another antenna is zero [2-3] depicted in Fig.1.2 (a-b). U-shaped MIMO antenna with WLAN band-notched characteristics are achieved by using a circular slot on the patch which behaves like a band stop filter in 5.15-5.85GHz. A T and L-shaped decoupling structure is introduced between two radiators on the ground plane; accumulate the migrated current from the excited antenna to other antenna elements that provide high isolation in the UWB range [4-10].UWB

with reconfigurable notch characteristics MIMO antenna has been presented; reconfigurability is achieved by introducing the R.F. choke circuit with PIN diode [11-12] shown in Fig.1.2(c-d). A simple LC stub is designed on the ground plane to achieve the WLAN band's band-notched characteristics [13], shown in Fig.1.2 (e). Using line and rectangular slots on the ground decouple the radiated antenna's power to another antenna, which improves the isolation in the UWB band [14].

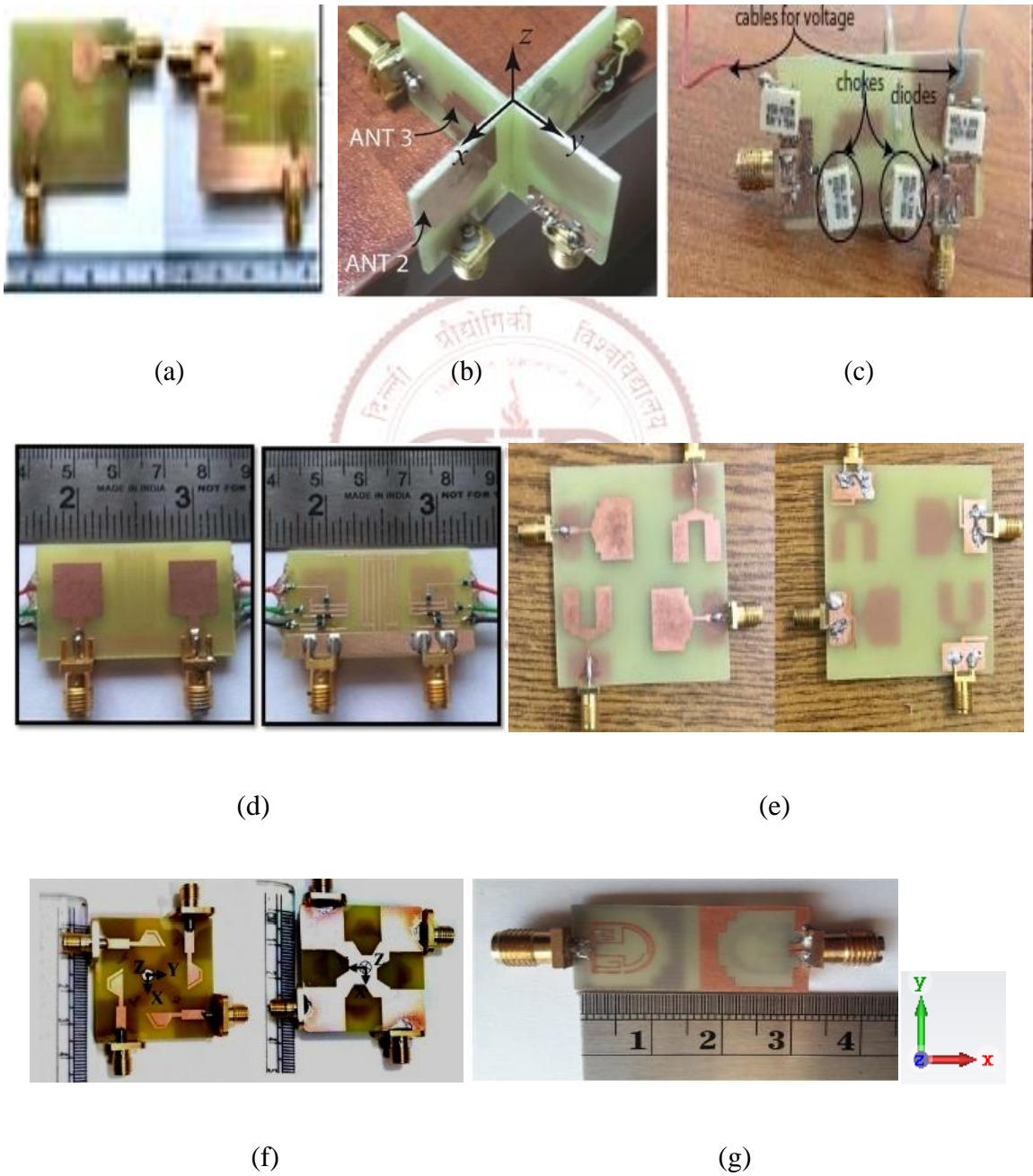
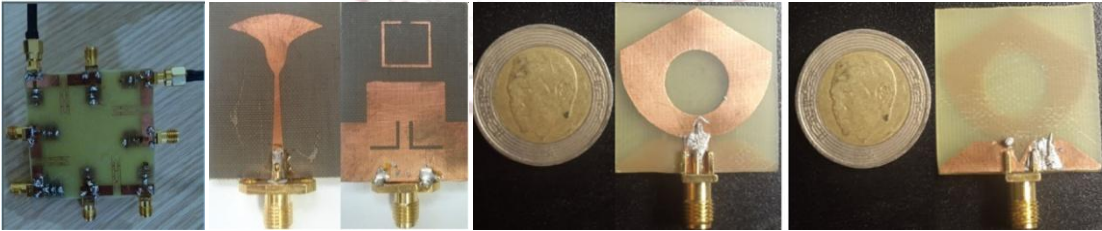


Fig.1.2: Structures offering UWB MIMO Antenna with Notch characteristics.

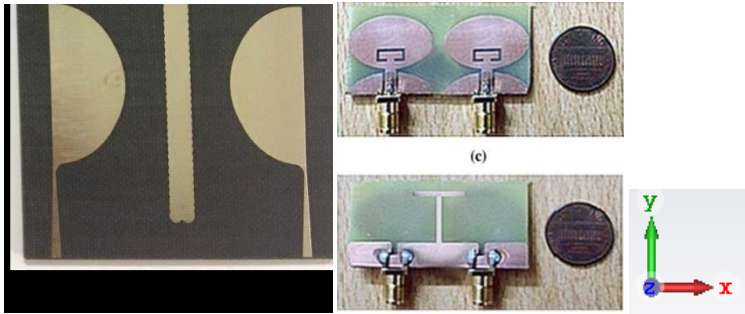
Monopole antenna with three modified rectangular slots provides the UWB bandwidth with high isolation, and G-shaped slots on the patch provide the WLAN notch band characteristics [15]. Four antennas are placed orthogonally, which provides enhanced isolation and 45% size reduction, in-ground LC (Hi-Low) based band stop filter characteristics is introduced to achieve WLAN notch characteristics [16-17]. An adaptive neuro-fuzzy interference system is applied to improve the isolation between two radiators [18] depicted in Fig.1.2 (g). EBG structure is also useful to enhance the MIMO system's isolation, which grounded the current to migrate from the radiated antenna to the rest of the antenna [19]. Triangular shaped radiators with tapered feed microstrip line produce UWB bandwidth. To enhance the isolation between two radiators, a funnel-shaped decoupling structure is introduced on the ground plane. A J-shaped slit cut on the patch provides band notch characteristics. The length of the slit is calculated by the formula, (Notch frequency) $f_n = \frac{c}{2 \times L_{\text{notch}} \times \epsilon_{\text{eff}}}$ where c = speed of light, L_{notch} = notch length and ϵ_{eff} = relative dielectric constant [20]. Fractal UWB MIMO antenna with modified DGS produces high isolation, and Split Ring Resonator (SRR) etched on the patch produces band notch characteristics [21]. A combination of modified T-shaped stub and complementary split-ring resonator (CSRR) is used to enhance the isolation and diversity parameters in the UWB range. This decoupling structure accumulates the radiated energy that is migrated from one antenna element to other elements [22]. I-shaped decoupling structure with orthogonally placed antenna elements is used to achieve good isolation and better diversity performance in the UWB range. A rectangular slot is cut on the patch for achieving notch band characteristics, which is helpful to avoid interference with indoor wireless electronic gadgets that have been reported in [23-24].

Microstrip antennas are narrowband antennas, but we enhance the antenna's impedance bandwidth without compromising antenna parameters by using some useful technique. The benefits of the SWB antenna is as a single antenna work in the entire bandwidth, so size and cost reduction point of view SWB antennas are popular in the communication market. If the fractional impedance bandwidth of any antenna is >150% or the antenna having a bandwidth

ratio 10:1, maintaining the return loss 10dB and VSWR is less than two over the entire range of frequency [25], then we say that the antenna works in an SWB frequency range. Prabhu Palanisamy *et al.* [26] provide the eight elements UWB/SWB MIMO antenna with WLAN notch characteristics by using parasitic notch structure on the patch. For isolation improvement, a hexagonal-ring type fencing decoupling structure is deployed between the two antenna radiators. This decoupling structure accumulates the electric field that migrated from one antenna element to the rest of the antenna shown in Fig.1.3 (a). Murli Manohar *et al.* [27] Design an SWB (0.9-100GHz) single notch antenna for multi wireless applications. A tapered feed microstrip feeding line is introduced for 111.1:1 bandwidth achievement. The maximum gain of this antenna is 7dBi. Inverted L-shaped slit cut on the ground plane for notching purpose, which stops the radiated power in the WLAN band, depicted in Fig.1.3 (b). A noble U-shaped with CRR (complementary Ring Resonator) based SWB antenna is described in Fig.1.3(c). Modified ground plane and U-shaped structure provide better resonance entire SWB with maximum gain 6dBi [28].



(a) (b) (c)



(d) (e)

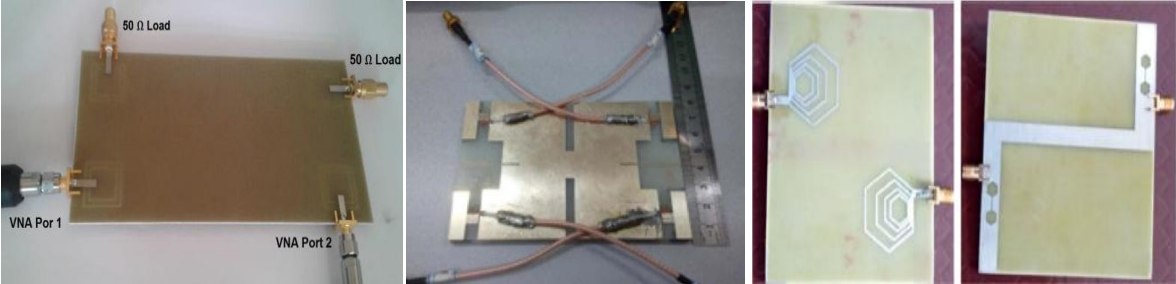
Fig.1.3: Structures offering SWB MIMO Antenna with and without Notch characteristics

Dinesh Kumar Raheja *et.al.* [29] Presents a compact coplanar waveguide (CPW)-fed quasi-elliptical-self complementary antenna (QESCA) exhibiting super-wideband (SWB) characteristics with dual-band notches for four-port multiple-input-multiple-output (MIMO) systems. Two slits are etched on the antenna radiators, provides the band stop characteristics in Wi-Max (3.5GHz) and WLAN (5.5GHz) band. Habib Ullah *et al.* [30] provide SWB bandwidth with a percent bandwidth of 187% and a 30.76:1 bandwidth ratio. The tapered feed line achieved this SWB bandwidth. The mutual coupling and diversity performance of antennas are improved by corrugated T-shape structure between two radiators in Fig.1.3 (d). In [31-33], the SWB MIMO antenna is discussed with notch band characteristics using an appropriate decoupling structure, which helps mitigate the interference and improved the quality of services with high SNR and low power requirements.

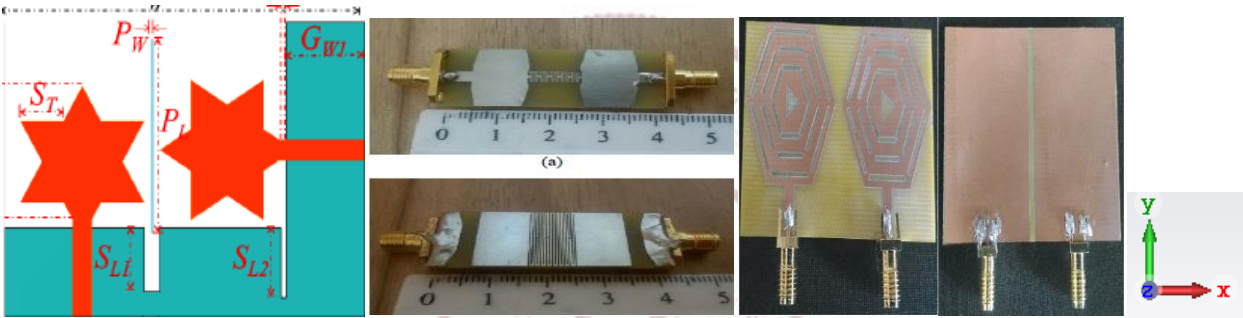
1.3.2 Multiband MIMO Antennas:

In [37-59] multiband MIMO antenna is discussed which is useful for WLAN, GSM850, GSM900, WiMAX, Bluetooth, WLAN, etc. wireless applications according to FCC. Jianfeng Zhu *et al.* design printed inverted F antenna (PIFA) is used to generate an additional band for GSM850 and GSM900 mobile application. To reduce the mutual coupling two “n” shaped strips are introduced between the antenna elements. Parallel folded strips placed at adjacent edges of the PIFA antenna provides the additional mode in a lower band (824-960MHz) used for mobile application [37]. Yaohui Yang *et al.* [38] design a multiband MIMO antenna for low-band (880–960 MHz), the middle-band (1800–2500 MHz), and the high-band (3400 MHz–5850 MHz) with 6dB return loss. This antenna is half surrounded by a long folded strip, provides low coupled power between two antenna elements. Naser Ojaroudi Parchin *et al.* and Ke Li, Yan Shi *et al.* design a multiband MIMO antenna for mobile phone 4G LTE, 5G applications [39-40] depicted in Fig.1.4 (a-b). In [39] two rectangle etched on the ground which provides better diversity performance and very less mutual coupling between two antenna radiators. K. Sumathi *et al.* [41] built a hexagonal-shaped fractal MIMO antenna with inset feed for GSM, PCS, WLAN, and Wi-

MAX for multiband operation. Hexagonal shaped dumbbell structure slits is etched on the ground plane to enhance the performance like isolation and diversity parameters. Four different fractal structures provide four different resonating bandwidth for multiband operations, depicted in Fig.1.4 (c).



(a) (b) (c)



(d) (e) (f)

Fig.1.4: Structures offering Multiband MIMO antennas

Jeet Banerjee et al., Negin POUYANFAR et al., and Pasumarthi S. Rao *et al.*[42-43] design a multiband MIMO antenna for C and X band applications. In [42], a star-shaped monopole antenna is designed with a modified ground plane for achieving multiband operation. These monopoles antenna is placed orthogonally for improving the isolation between two radiators as shown in Fig.1.4 (d). In [43] trapezoidal-shaped MIMO antenna is introduced, to improve the isolation between them a meander line-shaped DGS structure is deployed wisely which prevents the migrated current from excited antenna radiator to another antenna, depicted in Fig.1.4 (e). In [44], a Multiband MIMO antenna is designed, a DGS structure is deployed for avoiding the

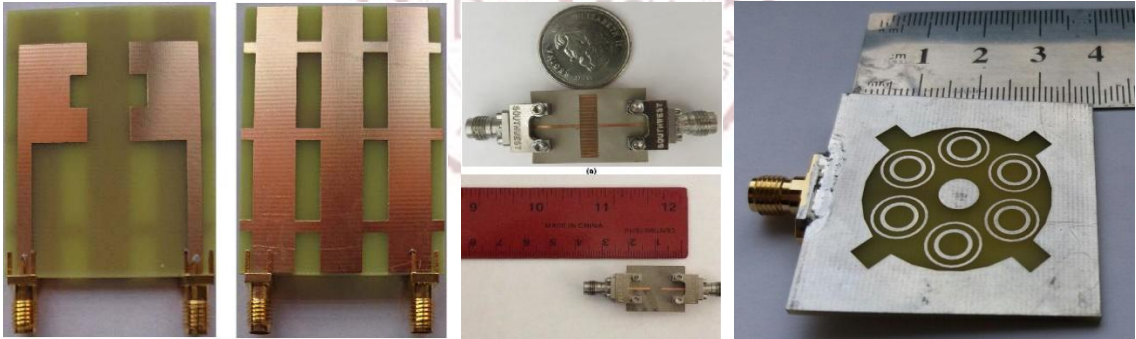
mutual coupling between two closely spaced MIMO antennas. In [45] frequency selective surface (FSS) multiband MIMO antenna is designed for Wi-MAX, WLAN, 5G Cellular, and 5G Wi-Fi applications. A grid of frequency selective surface provides the $>30\text{dB}$ isolation between antenna elements. Four resonance bands were achieved by a combination of T-shaped and rectangular slots, meander-line, and folded armatures. Loghman Asadpor et al. [46] offers CSRR based multiband MIMO antenna for global system for mobile (GSM) and 4G Long term evaluation (LTE) applications. CSRR does not allow the currents transfer from the radiated antenna to the rest of the antennas. In [47], Minkowski-shaped MIMO is discussed for multiband operation resonates at 2.5, 3.5, and 5.5GHz frequency with acceptable isolation in the working band. Jing Bai et al. [48], presents a multiband MIMO antenna for Time division (TD) LTE (2555-2575MHz, 2575-2635MHz and 2635-2655MHz) and WLAN 802.11a/b/g (2.4-2.4835GHz and 5.15-5.875GHz) applications. Tzu-Ling Chiu et al. [49], design a DRA based multiband MIMO antenna for automotive LTE application. Two improve the quality and reliability of the link two DRA's is placed upon the roof of the car. In [50-51], the Multiband MIMO antenna is discussed for mobile applications. For achieving good isolation and diversity performance parasitic elements are deployed. Amit Kumar et al.[52] designed CSRR based multiband MIMO antenna with isolation $>17\text{dB}$. In [53], a dual-polarized multiband MIMO antenna has been designed for near field LTE and Internet of Things (IoT) applications. This antenna provides high Q factor and narrowband matching in 1.9 and 2.4GHz frequency and for high isolation, two antennas are placed orthogonally that's why no components of the electric field are transferred to radiated antenna to 50ohm matched load termination antennas. Xin-Shuai Luo *et al.* [54], designed a multiband MIMO antenna by using the right/left-hand transmission line. Size Miniaturization is possible by using Zero-order theory for mobile application. D. Sarkar et al.[55], Ziyu Xu et al. [56] and Yingying Yang *et al.* [57], formed a multiband MIMO antenna loaded with SRR and decoupling structure for GSM900, PCS, LTE2300, and 5G bands with acceptable isolation and ECC. In [58], the Heptaband swastika arm shaped MIMO antenna is designed and discuss. The self-isolated structure is designed for better isolation in the

proposed band. This antenna offers stable radiation pattern and circular polarization at 3.66–3.7GHz and 5.93–6.13GHz and linear polarization at 0.95–1.02 GHz, 1.73–1.79 GHz, 2.68–2.85 GHz, 4.20–4.40 GHz, and 5.50–5.65 GHz bands. Gourab das et al. [59], presents a novel partial reflecting surface to improve the isolation and ECC between CDRA antennas. FSS is designed at 5.2GHz, 5.5GHz, and 5.8GHz bands to achieve multiband operations. This phase gradient FSS is utilized as a superstrate above each group of DR elements which provides different far-field pattern each group of antenna elements and achieve good diversity performance.

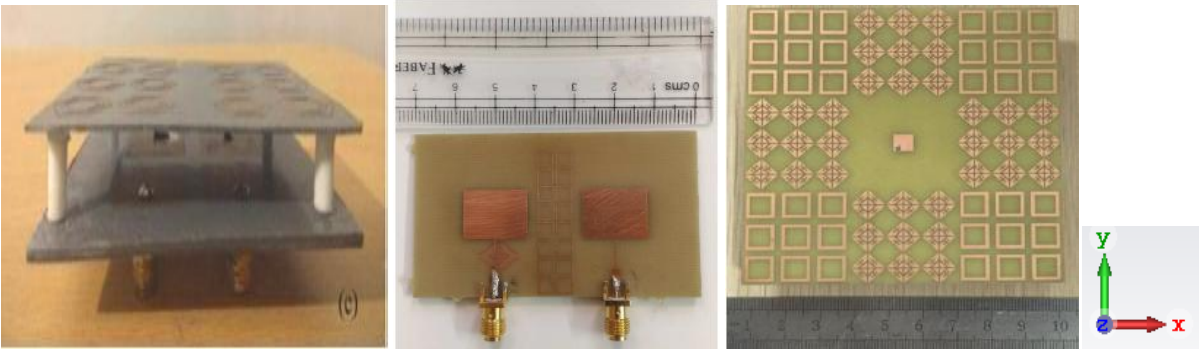
1.3.3 High Isolation and Low RCS MIMO Antennas:

MIMO (Multiple inputs multiple outputs) antennas play a vital role in modern wireless communication in enhancing the reliability and capacity of the network and become a major part of communications paradigms, such as LTE (long-term- evolution) future 5th-generation mobile communication network. Since mutual coupling between the MIMO antenna elements is an imperative metric when investigating the antenna's performance. In recent years, various isolation improvement techniques for multiple inputs and multiple outputs antennas have been reported as de-coupling networks, neutralization network technique, parasitic monopole elements, artificial magnetic conductor (AMC) reflector, negative group delay lines, ground plane modification method, or a combination of the above-mentioned methods but these techniques are tedious, occupied more space over the antenna, difficult to fabricate, and incomprehensible as six metallic pins near the two adjacent patches have engraved which provides orthogonal polarization to improve the isolation of the different antennas more than 20dB [60]. L and T-shaped decoupling structures on the ground plane are used to improve isolation by more than 30dB because the electric field doesn't migrate from one element to other elements [61-62]. A defected ground structure, substrate integrated waveguide (SIW), and fence type decoupling structures are better for enhancing isolation [63-64]. In other words, the isolation of adjacent antennas has been improved without any external decoupling structure by reducing ground current effects using a balanced open-slot mechanism in future smartphones. E-shaped

Unequal stubs and mushroom-shaped EBG structures are used to improve mutual decoupling of more than 20dB and front to back ratio (FBR) in super-wideband antenna [65-66] to minimize cross-polarization of the radiation pattern. E-shaped slot over a patch creating discontinuity is applied to improve isolation in ultra-wideband antenna. Modified array antenna decoupling surface (MAADS) reduces the migration of current density from one antenna to the rest of the antenna [67-68]. Elements of an antenna are positioned orthogonally to each other, and proper decoupling structure is introduced for isolation improvement [69-70]. Parasitic inverted neutralization line and two coupled feed loop antenna with conjoined capacitor embedded sections are provided high isolation [71-72]. Meanwhile, Radar cross-section (RCS) reduction is a severe problem in defense applications as detection, and stealth technology have currently gotten prominent attention. However, many more mechanisms have been proposed for RCS reduction in literature such as frequency selective surface, metamaterial absorber, and Electromagnetic Band Gap, etc. [73-86].



(a) (b) (c)



(d) (e) (f)

Fig.1.5: Structures offering high isolation and low RCS antennas

Low RCS is minimized the reflection coefficient of the sampling antenna [73]. Modified frequency selective surface (FSS) and EBG with choke absorber wall are designed and mounted between two antenna elements that provide good isolation as well as low RCS [74-75], depicted in Fig.1.5(a-b). A hexagonal polarization rotation surface has been fabricated for RCS reduction [76]. Modes cancellation method (MCM) is a popular technique that is used for RCS reduction in broadband [77]. Moreover, the fractal model [78] and hasted hexagonal-shaped metamaterial super-state [79], a flower-shaped metamaterial absorber [80], and AMC [81] are provided reduced RCS in specific bands shown in Fig.1.5(c-f). Polarization insensitive frequency selective surface, EBG, and MAAD techniques are also useful for the reduction of RCS along with high mutual decoupling [82-86]. Recently, the conventional microwave absorbers are to be replaced by low profile planar metasurface which is used in 5th-generation applications as an absorber. Planar metasurface (MS) is simpler in design and easily manufacturable by photolithography on printed circuit board (PCB) and has ample opportunity in state-of-art technology. Simultaneously, planar metasurface is also played a pivotal role to improve the de-coupling of MIMO antenna over and above RCS reduction in indispensable bands of frequency.

1.3.4 Multiband Metasurface Absorber:

A metamaterial absorber manipulates the loss components of metamaterial permittivity and permeability, to absorb a large amount of electromagnetic radiation. This is a useful feature for radar cross-section reduction, photo-detection, and solar photovoltaic applications. When a wave strikes on the surface of the absorber, it may be reflected, transmitted, scattered, or absorbed. If we assume negligible scattering due to roughness, then the absorbance $A(\omega)$ relationship can be given in Equation 1.8.

$$A(\omega) = 1 - |S_{11}(\omega)|^2 - |S_{21}(\omega)|^2 \quad (1.8)$$

S_{11} and S_{21} are return loss and insertion loss; respectively, a recent conventional microwave absorber is being replaced by low profile microstrip metamaterial absorber. These absorbers are used in the Stealth technology fifth-generation fighter plane to improve MIMO antenna's isolation, imaging, sensing, and RCS reduction. In a recent conventional microwave absorber to be replaced by low profile microstrip metamaterial absorber, which is used Stealth technology fifth-generation fighter plane, to improve the isolation in MIMO antenna, imaging, sensing, and RCS and EMC reduction. In [87-88] depicted in Fig.1.6 (a), ultra-thin CRR based wide-angle polarization-insensitive dual-band metamaterial absorber in C and X band is proposed with 90% absorbance is achieved in broadband. Mender line inspired seven-band Metamaterial absorber depicts in [89] with above 90% absorbance shown in Fig.1.6 (b).

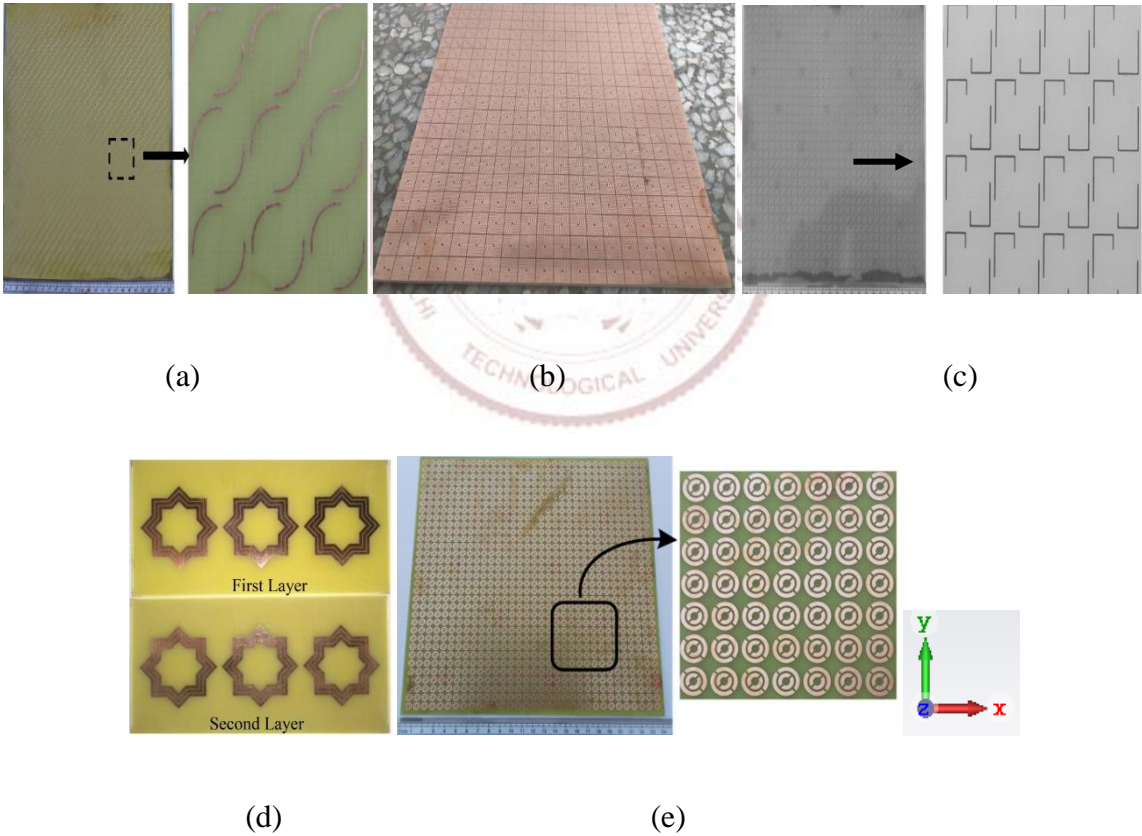


Fig. 1.6: Various UWB and Multiband Band Absorber

Symmetrical flower-shaped [90-91] structure with a wide incident angle polarization-insensitive structure is proposed in S and C band. Kong et al [92] show quad-band hexagonal-shaped MMA with above 90% absorbance is proposed. Somak et al. [93] proposed wideband MMA with high

absorbance at a very thin layer microstrip depicted in Fig.1.6 (c). Multilayer triple wide-angle polarization-independent Metamaterial absorber is discussed in Fig.1.6 (d) with >90% absorbance [94]. Ghosh, Saptarshi et al, design and demonstrate circular split ring based ultrathin UWB metamaterial absorber for stealth application depicted in Fig.1.6 (e) [95].

1.3.5 THz Antennas and Applications:

Wireless communication is demanded better channel capacity with a high data rate in the modern era. To fulfill these demands, the MIMO-communication systems with THz range are required for high data speed in Tera-bit/sec (Tbps). Also, it is providing very high throughput per device (from multiple Gbps to several Tera-bps) including per area efficiency (bps/km²). It is also predicted that the world monthly traffic in smartphones will be about 40 Peta-bytes in 2021 [96]. Gaurav Varshney *et al.* [97], Design a Graphene-based pattern diversity MIMO antenna with good diversity performance from 1.76THz to 1.87THz for Terahertz short-range communication depicted in Fig.1.7 (a). A Graphene-based MIMO antenna is also designed for reconfigurable applications by using a PIN diode [98]. Miao, Zhuo-Wei *et al.* [99], Design and simulate THz (400GHz) high-speed folded reflect-array antenna for high-density wireless communication and this is also useful to THz time-domain spectrometry to determine EM properties of dielectric materials [100] depicted in Fig.1.7 (b).

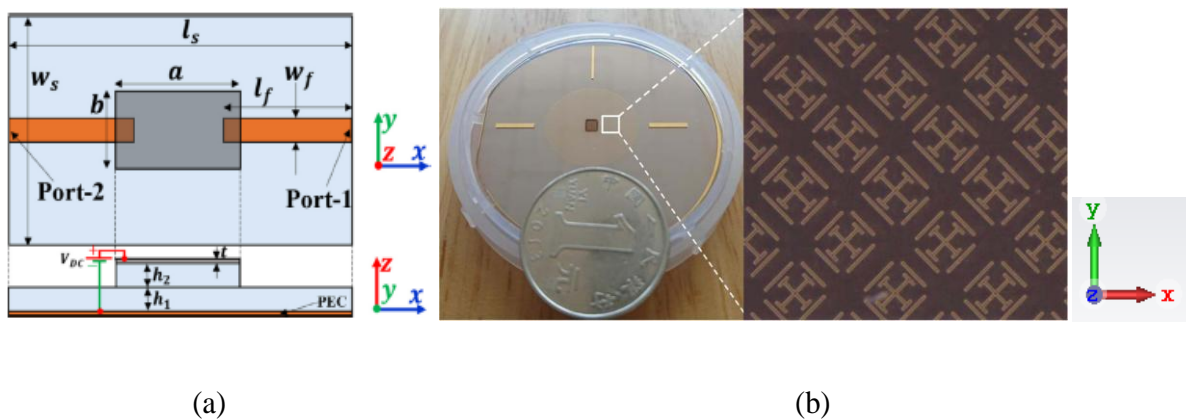


Fig.1.7: Structures offering THz MIMO antennas

For long and short distance communication, imaging, and screening of weapons an Elliptical-shaped THz microstrip ultra-wideband antenna with omnidirectional radiation pattern is designed with 12dB peak realized gain [101]. With the increasing demand for high bandwidth & speed, a plasmonic nano reconfigurable UM-MIMO antenna with beamforming capabilities is proposed which influences the properties of nano-materials and meta-materials [102]. Massive MIMO for beyond 5G (B5G) applications and 3D imaging RADAR is developed for THz range [103]. Antenna dispersion and distance problems and solution discussed [104-105] at THz frequency. Sub THz high gain DRA with integrated CMOS imager is demonstrated [106] for THz imaging. Graphene-based beam reconfigurable MIMO antenna for short-range communication with high isolation is developed in [107-108]. Antenna efficiency is an important parameter in THz frequency for astronomical radiometric applications; antenna radiation improvement technique is explained in [109].

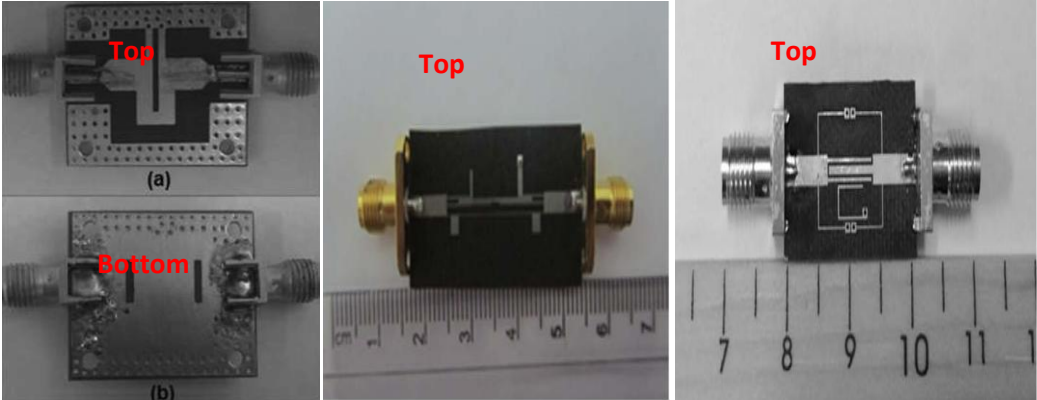
1.3.6 UWB Band Pass Filters:

In the current scenario, the UWB communication system offers numerous wideband applications such as microwave medical imaging, ground-penetrating radar (GPR), and radio frequency identification devices (RFID) tag for inventory control and asset management. A major advantage of a UWB system is transmitted a high transmission data rate, resist to jamming, low energy density, low transmission power requirement, and easy to retrieve error control coding. A UWB transceiver, where the information is first encoded, digitally modulated, and then converted into pulse using a pulse generator [110]. Impulse data is transmitted using the UWB antenna, and noise should be removed before transmission using the UWB bandpass filter. UWB bandpass filter is an essential component of the transceiver section. Compact bandpass filter design is extensively growing very fast from 2002 while the U.S. Federal Communication Commission (FCC) allowed commercial use of frequency with the range of 3.1-10.6GHz [111]. Compact and inexpensive UWB transceivers are always required for such wireless applications; therefore, UWB transceivers should be compact and affordable. Hence, UWB bandpass filter

with short-circuited meandered coupled line with rectangular shaped DGS on the ground plane, which improves the spurious response in stopband has been designed [112] depicted in Fig.1.8 (a). Besides, the UWB filter has been achieved by combining the spur line, DGS & SRR, and used to reduce the size and radiation loss of the Filter [113]. Moreover, the compactness of the Filter is achieved by using an arrowhead defected ground structure [114]. In continuation with a UWB bandpass filter by coupling two-stepped impedance resonator to the Filter with primary resonator and four short-circuited folded stubs are used to enhance the performance of selectivity of the Filter at lower and higher side cut-off frequency is reported [115]. Meanwhile, some techniques are discussed for enhancement of bandwidth of UWB filters as substrate integrated waveguide (SIW) technique with loading short and open-ended stubs at the middle then bandwidth to be improved [116]. Introducing a broadside coupled microstrip line/CPW structure that provides better bandwidth enhancement is also presented [117].

Similarly, the UWB bandpass filter is designed using the wave cancellation method, which first splitting then combining the signal, which provides signal zero characteristics at lower and higher cut-off frequency [118] shown in Fig.1.8(b).

Furthermore, to achieve a UWB-BPF, a three-mode resonator with one open stub is designed [119-120] including four folded shunt short circuit stubs separated from each other by quarter wavelength and used semicircle DGS structure to achieve good filter performance is presented [121] presented in Fig.1.8(c).



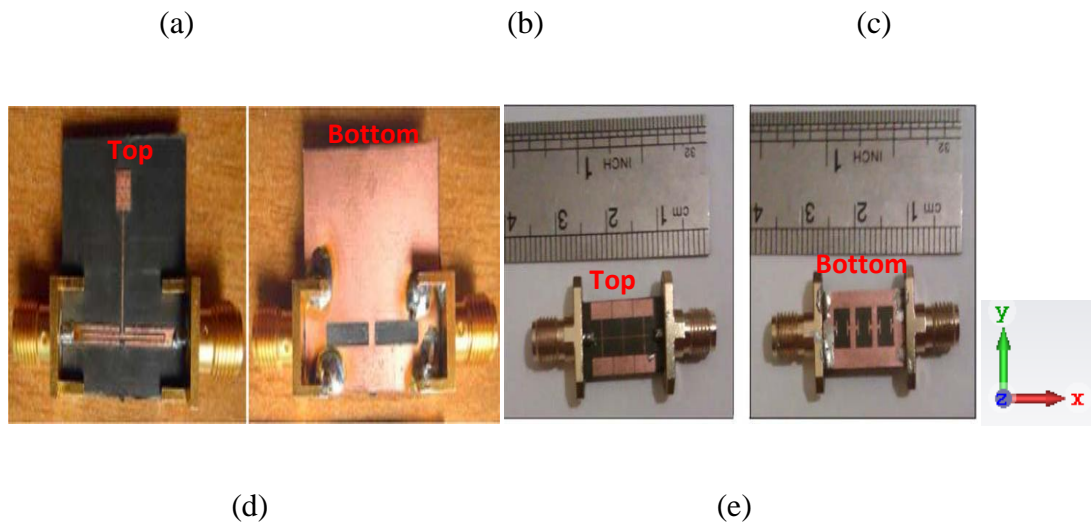


Figure 1.8: Various UWB bandpass filter with an extended notch

Another BPF is constructed by step impedance lowpass filter optimum distributed high pass filter with four rectangular shaped DGS slots in the ground plane and wire bounding interdigitized capacitance for obtaining strong wideband coupling and a UWB bandpass filter is also developed by using microstrip loaded stubs in which insertion loss of 0.02dB [122]. A DGS based UWB filter using DGS, including triple T-shaped slots and a pair of protruded T-shaped strips inside the triple rectangular slot, which present better bandwidth and good return loss in the UWB range is designed [123] depicted in Fig.1.8(d). Another novel microstrip line UWB bandpass filter has been reported using multiple-mode resonator (MMR) with an insertion loss of 2dB , and group delay varies from 0.28 to 0.43ns [124] shown in Fig.1.8(e). Introducing the DGS structure on the ground to enhance the performance of a filter in terms of selectivity and sharpness is designed [125]. The harmonic suppression technique is achieved in the same sequence by introducing a parallel-coupled stepped impedance resonator with a varactor load [126]. A hairpin structure is designed to achieve high fractional bandwidth, low Q to achieve UWB bandwidth [127]. Finally, a half-mode substrate integrated waveguide using a dumbbell-shaped DGS structure is proposed to improve filter performances [128-131].

In Table-1.1 we discuss various techniques to enhance the performance of the MIMO antennas.

Table 1.1: MIMO antenna and filter performance enhancement techniques

Parameters	Techniques
1. Bandwidth	<p>Step Impedance feeding line</p> <p>Monopole antenna</p> <p>Multimode resonator(In Filter)</p> <p>Metamaterial</p>
2. Size	<p>Complementary Split Ring Resonator(CSRR)</p> <p>Split Ring Resonator (SRR)</p> <p>Electromagnetic Band Gap(EBG)</p>
3. Isolation	<p>Decoupling Structure</p> <p>Neutralization Line</p> <p>EBG</p> <p>SIW(Substrate Integrated Waveguide)</p> <p>Metamaterial absorber</p> <p>Orthogonally placed antenna</p> <p>CSRR and SRR</p> <p>Defected Ground Structure</p>
5. ECC	<p>Decoupling Structure</p> <p>Neutralization Line</p> <p>EBG</p> <p>SIW(Substrate Integrated Waveguide)</p> <p>Metamaterial absorber</p> <p>Orthogonally placed antenna</p> <p>CSRR and SRR Loaded</p> <p>Defected Ground Structure</p> <p>Avoid charge accumulation on the patch</p> <p>Proper feeding</p>

6. Channel Capacity Loss	Increase the number of antenna elements Reduce Mutual Coupling
---------------------------------	---

Some of the MIMO components (antenna, Filter, Meta absorber) are discussed in different **Chapters**, shown in my thesis.

1.4 THESIS ORGANIZATION:

The thesis involves the various types of MIMO antennas for microwave and THz applications, which provide high channel capacity and high data rate without extra bandwidth and power. This thesis consists of nine **Chapters**, and **Chapter** wise summary is as follows:

Chapter -1: Introduction and Review States of Art:

This **Chapter** introduces MIMO antennas, Filters, and Meta absorbers with a detailed literature review of the critical manuscript used as references to this thesis. Mainly work has been focused on Gain, bandwidth, FBR, radiation efficiency, isolation, and diversity parameter improvement technique associated with MIMO antenna. We have also analyzed S11, S21, bandwidth, sharpness, and group delay enhancement technique for designing a suitable bandpass filter used in the MIMO communication system. Some Meta absorbers are also reviewed and discussed which is useful for enhancing antenna performance.

Chapter -2: UWB MIMO Antenna with WLAN Notch Band Characteristics:

In **Chapter** 2, an Ultra Wide Band (UWB) MIMO antenna with the wireless local area network (WLAN) band-notch (5.1–5.85 GHz) characteristic is offered. This antenna consists of two radiated patch. These radiating patches are fabricated on abundantly available FR-4 substrate with $36 \times 22 \times 1.6 \text{ mm}^3$. Results illustrate that the designed antenna produces an impedance bandwidth from 3.1 to 11.2 GHz and good isolation and diversity performance in the UWB range. Proposed antenna characteristics have the advantage of low-cost and more accessible

fabrication and are also found suitable for a human interface device. Simulated results of the proposed antenna are tested and verified by the experimental results.

Chapter-3: Super Wideband (1.575-40GHz) Single Band Notched MIMO Antenna for Multiple Wireless Applications:

Chapter-3 gives the details of the design and analysis of SWB (1.5-40GHz) MIMO antenna with single notch characteristics. This MIMO antenna is circularly polarized at 1.575GHz and 26.0GHz for GPS and mm 5G applications. The proposed MIMO antenna features SWB (Super Wide Band) bandwidth and compact size (55.6×50.5×1.6mm³) on the FR-4 substrate. This MIMO antenna is suitable for defense and handheld devices covering GPS/DCS/PCS/UMTS/WI-BRO/ISM/IRNSS/LTE (M/HB) /BLUETOOTH/IOT/SUB5G/WI-MAX / mm range 5G/X/Ku/K/Ka-band applications. Finally, this antenna is tested in a realistic application environment suitable for a human head interface device with acceptable SAR value.

Chapter-4: High Isolation MIMO Antenna for C, X, and Multiband Applications:

In Chapter-4, an EBG based circular MIMO antenna is presented for C-band (4.0-8.0GHz) applications with greater than 20dB isolation. The return loss of antenna, designed on the FR-4 substrate, is greater than 10dB by the size of 55×45×1.6mm³. The antenna's diversity performance is also permissible through ECC, and diversity gain is 0.0015 and 9.99dB, respectively. The proposed MIMO antenna is appropriate for wind profiler RADAR and weapon investing RADAR system.

In this Chapter, a high isolation electromagnetic bandgap (EBG) based MIMO antenna is also designed for X band (8-12GHz) applications. The proposed antenna is tailored on the FR-4 substrate with a size of 55×49×1.6mm³. This antenna has circular patches with extruded triangular and circular shapes, which provide better radiation efficiency (>0.45) in the X-band (8.0 to 12GHz). High isolation (22dB) is achieved in the entire bandwidth by using a mushroom-shaped EBG structure near the microstrip feeding line.

In this **Chapter**, meander line-shaped pentaband (2.165-2.48, 2.59-2.72, 2.89-2.97, 3.10-3.32, 3.38-3.46GHz) 4-elements multiple-input-multiple-output (MIMO) antenna is also presented. These frequency ranges are widely used for Microwave Service Switch (MSS) and Internet of things (IoT) applications. This antenna is designed on the FR-4 substrate with a compact size of $50 \times 70 \times 1.6 \text{mm}^3$. Simulated results show excellent diversity performance in pentaband, which is in the acceptable range. This antenna is appropriate for use in Mobile satellite services (MSS), ISM, Broadband Radio Services (BRS) and Educational Broadband Services (EBS), WiMAX Radio Location Services, and Amateur Radio Services respectively.

Chapter-5: Design of Metasurface Absorber for Low RCS and High Isolation MIMO Antenna for Radio Location and Navigation:

In this **Chapter**, a 4-elements MIMO antenna is designed using a novel metasurface absorber for isolation as well as RCS reduction. A unit cell of metasurface absorber is amalgamated by concentric circular and elliptical-shaped rings with four 300ohms lumped resistances. This MIMO antenna with an absorbing structure is fabricated on an existing FR4 substrate with dimensions of $55 \times 40 \times 1 \text{mm}^3$. The performance of the designed MIMO antenna is also judged by diversity parameters such as Envelope correlation coefficient (ECC), Directive gain (DG), Mean effective gain (MEG), Channel capacity loss (CCL), Total Active Reflection Coefficient (TARC), and channel capacity, etc. in the proposed frequency band. Simulated and measured ECC (calculate with the radiated field) of the proposed MIMO is less than 0.073 which exhibits that this antenna is suitable for military application in radiolocation and navigation.

In this **Chapter**, a triple-band polarization-insensitive metamaterial absorber (MMA) is also designed. MMA unit cell is proposed with a circular and oval ring-shaped structure. This absorber structure is designed on FR-4 substrate having $\tan \delta = 0.02$ with unit cell dimension $20 \times 20 \times 1 \text{mm}^3$. The absorbance of proposed triple-band MMA is 99.4%, 96.2%, and 91.25% at 8.2, 9.45, and 12.45GHz frequencies respectively. On the other hand, reflectivity is almost zero at the above-mentioned frequencies. Changing the incident and polarization angles of an

absorber, the absorbing characteristics are almost the same. So the proposed absorber is found appropriate for stealth aircraft, Radar Cross Section (RCS) and Electromagnetic Compatibility (EMC) reduction, and isolation in MIMO antenna, imaging, and sensing in the X-band applications.

Chapter-6: High Isolation and High Gain Super-Wideband (0.33-10THz) MIMO Antenna for THz Applications:

In this **Chapter**, an elliptical-shaped microstrip feed super-wideband (SWB) 2-elements MIMO antenna is proposed for high-speed terahertz (THz) applications. It has 2:1 VSWR operating bandwidth from 0.33-10THz (187%) with 19dBi peak gain. Radiation Efficiency is greater than 70% is achieved throughout the SWB bandwidth. The 2-element MIMO antenna is designed with a compact size of $1000 \times 1400 \times 101.29 \mu\text{m}^3$ on the RT5880 substrate having a relative permittivity of 2.2. Simulated results of antenna-like return loss, isolation, gain, efficiency, and diversity performance parameters (ECC, DG, and TARC) are in an acceptable range. Therefore, this antenna is useful for Sub 5G, vehicular communications, Imaging, 3D printing, Terahertz wave Radar, Health care, and Astronomical radiometric applications.

Chapter-7: Design and Analysis of Planar UWB Bandpass Filter with Stopband Characteristic:

In **Chapter-7**, a UWB bandpass with an extended stopband filter is also presented. Multi-Mode Resonator (MMR) techniques have been used for designing the filter. The proposed filter exhibits passband characteristics for the UWB range i.e. 3.1-10.6GHz with a return loss of **20dB** and stopband range from 10.8-20GHz with **0.4dB** return loss. The group delay and sharpness of the designed filter are $<0.30\text{ns}$ and 16dB/GHz at lower and higher cut-off frequency respectively in the passband. The dimension of the filter fabricated on the cost-effective substrate (FR-4) is $22 \times 20 \text{ mm}^2$ and the simulated frequency response is finally verified by the experimental results.

Chapter-8: Conclusion and Future Scope:

In **Chapter-8**, the main results of the thesis have been summarized and a critical review of the research work presented. The scope of further work and some of the specific problems that can be investigated in the area of MIMO antenna, Filters, and Metamaterial absorbers have also been identified.



CHAPTER-2

UWB MIMO ANTENNA WITH WLAN NOTCH BAND CHARACTERISTICS

2.1. INTRODUCTION

UWB wireless communications have various benefits such as highly secured communication, none interference with other communication systems, used for both LOS as well as non-LOS operation, high multipath immunity (If used as MIMO antenna), low cost, and low power requirement.

Numerous wideband applications such as microwave medical imaging, ground-penetrating radar (GPR), a RFID tag for inventory control, compact asset management, and inexpensive UWB-MIMO wireless transceivers. UWB-MIMO base station receiver architecture with different blocks is shown in Fig.2.1.

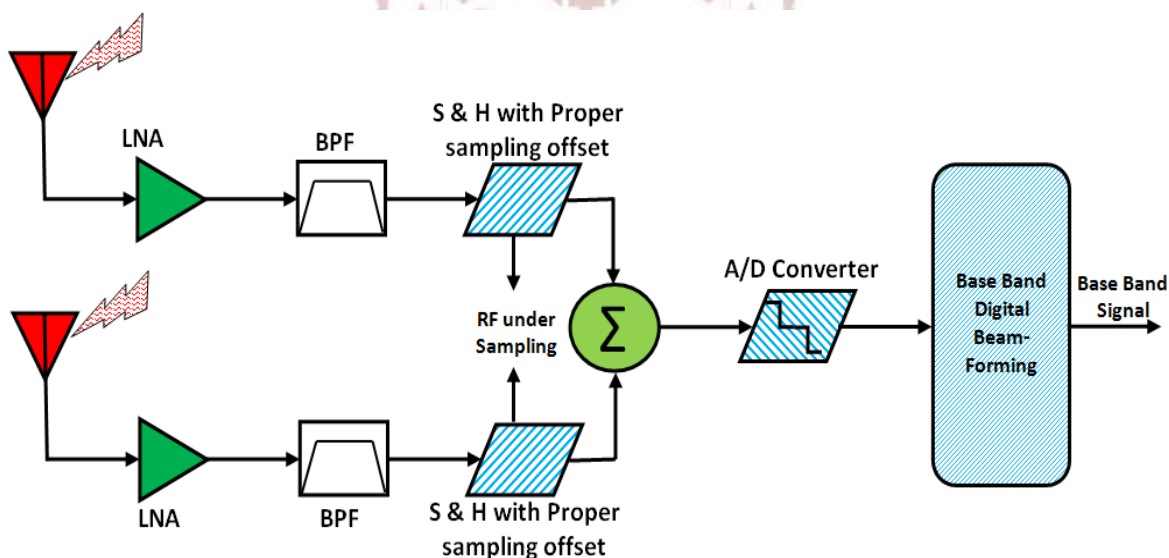


Fig.2.1. A generic block diagram of a two-element UWB-MIMO antenna-based receiver station

Impulse data is transmitted using the UWB-MIMO antenna and after that UWB-MIMO receiver antenna receives the data in a different path and produces the base-band signal, where the information is first encoded, digitally modulated, and then converted into pulse using a pulse

generator. Narrowband system like WLAN (5.15-5.85GHz) operates in UWB bandwidth and causes interference with the UWB band. So designing of UWB MIMO antenna with the WLAN notch band characteristic is a very challenging task to avoid interference.

In this Chapter, the MIMO antenna with a band notch characteristic at WLAN (5.1-5.85GHz) from UWB (3.1-10.6GHz) band is presented. Band notch characteristic is obtained through two open-ended stubs on the ground. Furthermore, the performance of the designed antenna has been studied in terms of the diversity characteristic of ECC, DG, TARC, “mean effective gain” MEGi/MEGj ratio, and channel capacity loss (CCL). Section-2.2 presents the proposed antenna design procedure. Section-2.3 shows the proposed antenna results and discussion, Section-2.4 proposed the diversity performance of the proposed antenna and, section-2.5 presents a summary of this Chapter.

2.2 DESIGNING OF UWB MIMO ANTENNA

This UWB-MIMO antenna has shown in Fig. 2.2 (a)-(b) with WLAN notch is fabricated on FR-4 substrate of height (h) 1.6mm with relative permittivity (ϵ_r) of 4.4, loss tangent ($\tan\delta$) of 0.02 by the dimension of 36mm×22mm. The antenna is designed by a circular with triangular notched patches and to enhance the isolation between two radiated patches, a T-I shaped slot in the ground is groomed, which improves the isolation better than 30dB in wished-for UWB bandwidth. The resonant frequency of a circular patch for TM_{11} mode is 7.15GHz which is used to calculate the patch radius to achieve the desired bandwidth (3.1-11.2GHz).

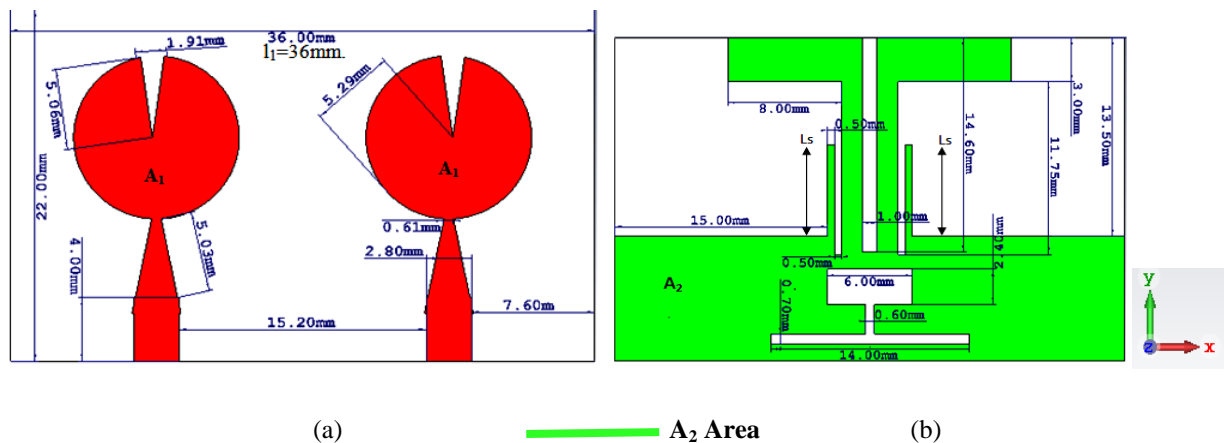


Fig.2.2. Two-element UWB planar monopole MIMO antenna (a) Front view (b) Bottom view

UWB bandwidth in MIMO antenna including notch band characteristic is achieved by using a tapered feed line together with the partially tailored ground plane. The fundamental resonance frequency of the monopole antenna is prearranged by Equation (2.1).

$$f_r = \frac{144}{l_1 + d_1 + h + \frac{A_1}{2\pi\sqrt{\epsilon_r + 1}} + \frac{A_2}{2\pi\sqrt{\epsilon_r + 1}}} = 7.1\text{GHz} \quad (2.1)$$

Where $A_1 = 87.87\text{mm}^2$, $A_2 = 370\text{mm}^2$ are the area of anticipated radiation patches and ground plane, $l_1 = 36\text{mm}$ length of the ground plane, $d_1 = 10.6\text{mm}$ diameter of circular radiated patches. Step by step procedure of the proposed UWB-MIMO antenna design is shown in Fig.2.3 and corresponding return loss and isolation are presented in Fig.2.4 (a)-(b) respectively. Antenna-1 provides unsatisfactory return loss 5 to 8dB in lower frequency range 3 to 4 GHz and isolation <10dB in 3.1-10.6GHz frequency range depicted in Fig.2.4 (a) and (b) respectively with black line. By changing the feeding line width of antenna-1, isolation is improved by 2dB in antenna-2 and the graph is showing in Fig.2.4 (b) with gray colour.

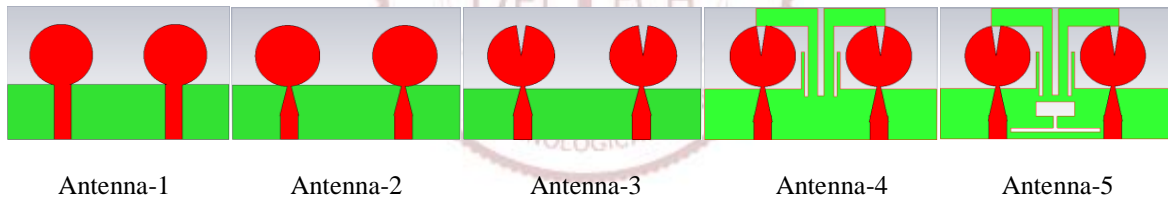


Fig.2.3. Geometrical design steps of a designed antenna with WLAN band-notch characteristic

In antenna-3, a triangular shape etched from patches which provide 4-12GHz bandwidth with >10dB return loss and >12dB isolation loss depicted in Fig.2.4 (a)-(b) with green colour. To mitigate the interference between WLAN band with UWB band, in an antenna-4, impart vertical stubs on the ground plane to get better return loss (>10dB) from 3.1 to 10.6GHz but poor isolation (>13dB) in UWB range and it also provides a notch band characteristics for WLAN (5.1-5.9GHz) shown in Fig.2.4 (a)-(b) with blue colour. Therefore, to improve isolation (>15dB) in Fig.2.4 (b) with saffron colour in 3.1-10.6GHz, engraved I and T-slot in the ground plane same shown in antenna-5in Fig. 2.3. The notched band can be achieved by varying the ground

stubs length (L_s) at the notch frequency $f_n = \frac{c}{2 \times L_s \times \sqrt{\epsilon_{\text{eff}}}}$, where c is the speed of the signal in a vacuum (3×10^8 m/sec), ϵ_{eff} is the effective relative permittivity [36] of the substrate and approximated length of L_s is 6.3mm at notched frequency.

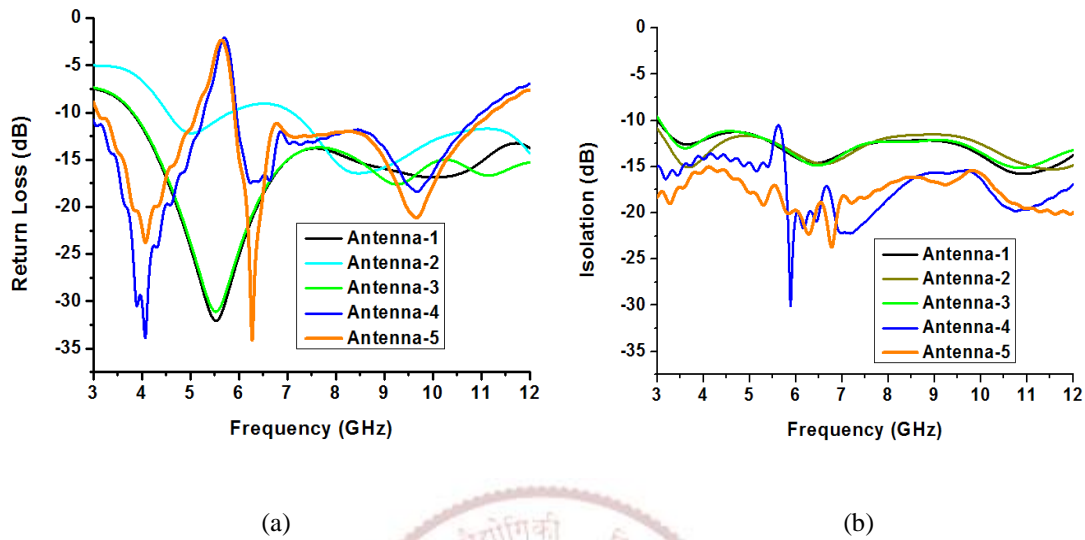


Fig.2.4. Simulated (using CST MWS) results of (a) Return loss (b) Isolation of the antennas shown in Fig.2.3

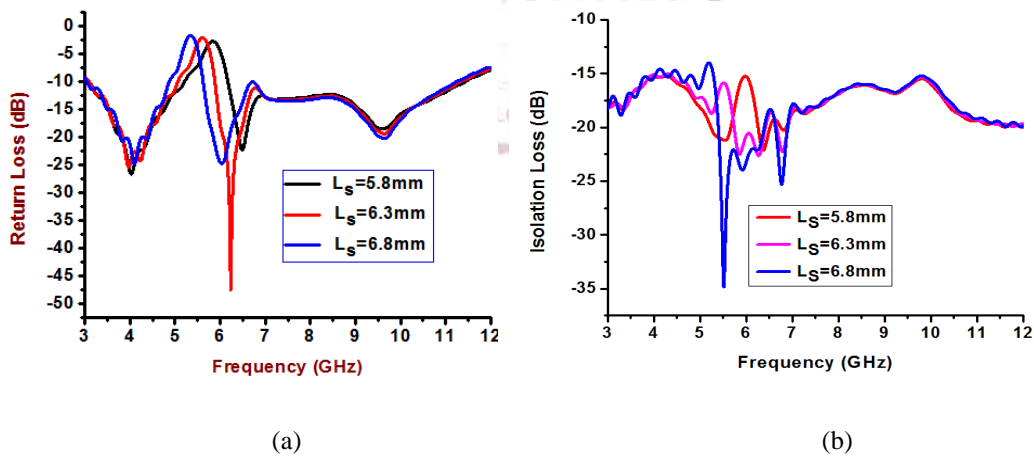


Fig.2.5. Simulated results of (a) Return loss and (b) Isolation of antenna with a variation of length of stubs (L_s) in the ground plane

Frequency selectivity of the rejection band is an important parameter to design a UWB antenna with a notched band. For selectivity of the notched band of the UWB-MIMO antenna, another ubiquitous parameter is ‘roll-off rate’ i.e. control required bandwidth of the WLAN band. Furthermore, RoC-Roll off Criteria is the ratio of the bandwidth at -5dB and -10dB, i.e. $RoC =$

BW_{-5dB}/BW_{-10dB} and the RoC of proposed antenna is 0.44, which is acceptable for practical design.

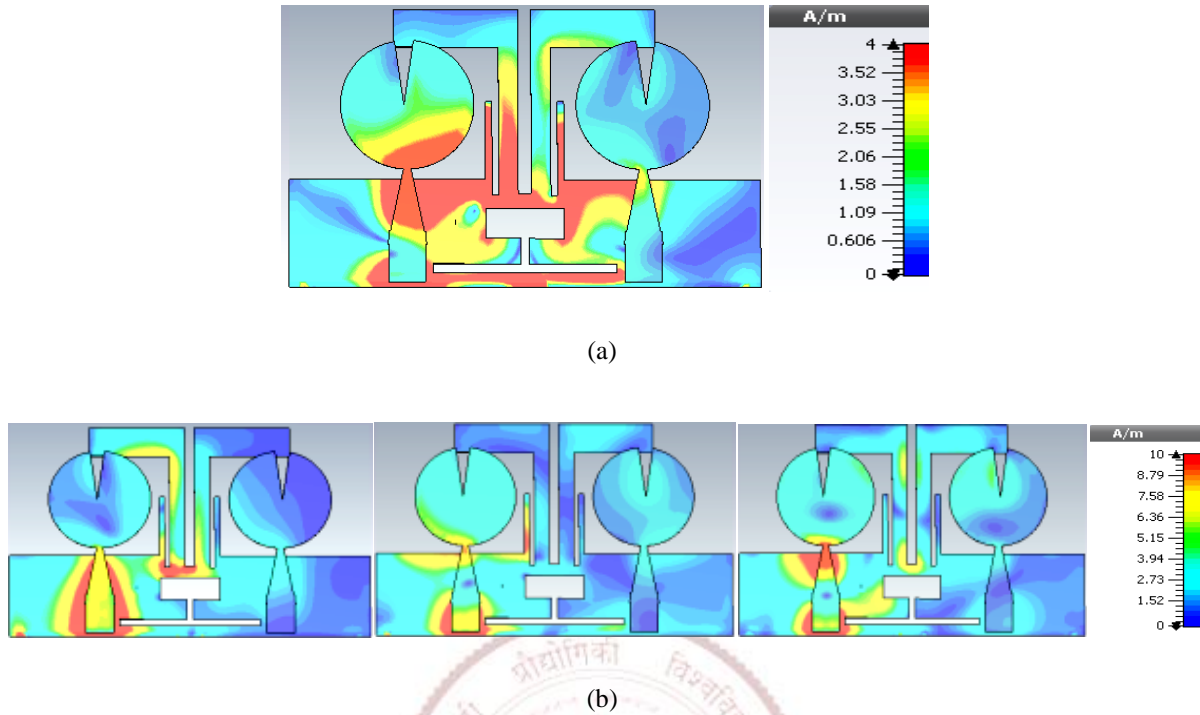


Fig.2.6. Surface current distributions at (a) notch band frequency i.e. 5.6GHz and (b) 4.1, 6.6, and 9.6GHz when port-2 terminated with 50Ω impedance and port-1 is excited

The bandwidth of the notched band is also controlled by the length of stubs (L_s) in-ground plane and the results of return loss, centered at 5.6GHz as made known in Fig.2.5. (a) & (b) By varying L_s from 5.8 to 6.8mm, the return loss curve shifts from higher to lower frequency, and the value of return loss at the intended notch (6.3mm) is 2.0dB. Impedance bandwidth is also maintained significantly, in the entire bandwidth throughout the optimization of L_s .

It is depicted from Fig.2.6 (a), where strong current accumulates around vertical stubs in the ground plane, which produces a notched for WLAN band in UWB bandwidth to mitigate interference. Fig.2.6 (b) shows the distribution of current on the antenna at various frequencies like 4.1, 6.6, and 9.6GHz respectively. It is too observed that the flows of current on the tapered feed line to circular element while a small current pours across the second element of MIMO. The slot in the ground plane works as an isolator between the two elements and this is preventing the coupling of electromagnetic energy.

2.3 RESULTS AND DISCUSSION:

The scattering parameter results (measured & simulated) are shown in Fig.2.7(a). Eventually, measured S_{12} shows better isolation than the simulation results, and isolation between two antenna radiators is $< 30\text{dB}$ for the entire UWB bandwidth. Results illustrate that the return loss of the proposed MIMO antenna is $\leq 10\text{dB}$ except for the notched band (WLAN) and the bandwidth of the antenna is 8.1GHz (from 2.1 to 11.2GHz), that fulfills the FCC requirement for UWB applications without interference.

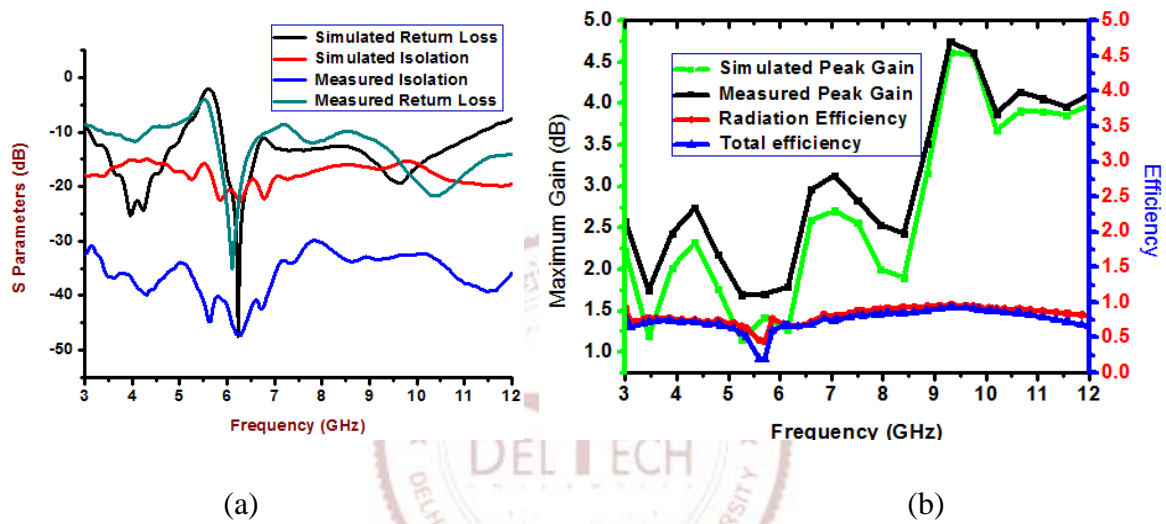
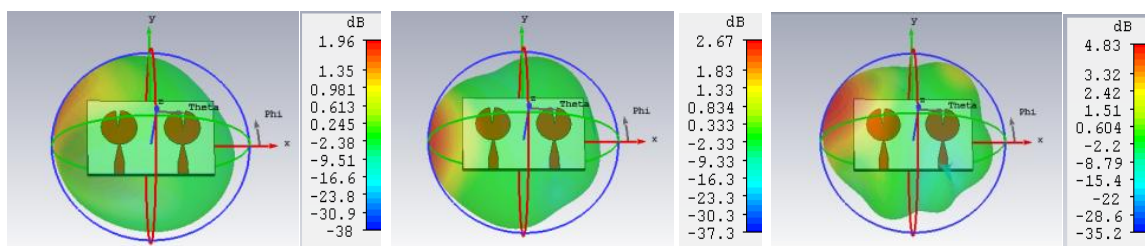


Fig.2.7. Simulated and Measured (a) S-parameter (Return & Isolation) (b) Peak gain, radiation efficiency & total radiation efficiency of UWB-MIMO antenna

The maximum peak gain of the antenna has revealed the better conformity between simulated and measured results and the maximum value of gain is 4.85dBi . The radiation efficiency of the antenna throughout the requisite band is higher than the permissible limit except for the notched band, which is centered at 5.6GHz . Consequently, the proposed MIMO can appropriate to work in the high interference surrounding as presented in Fig.2.7 (b).



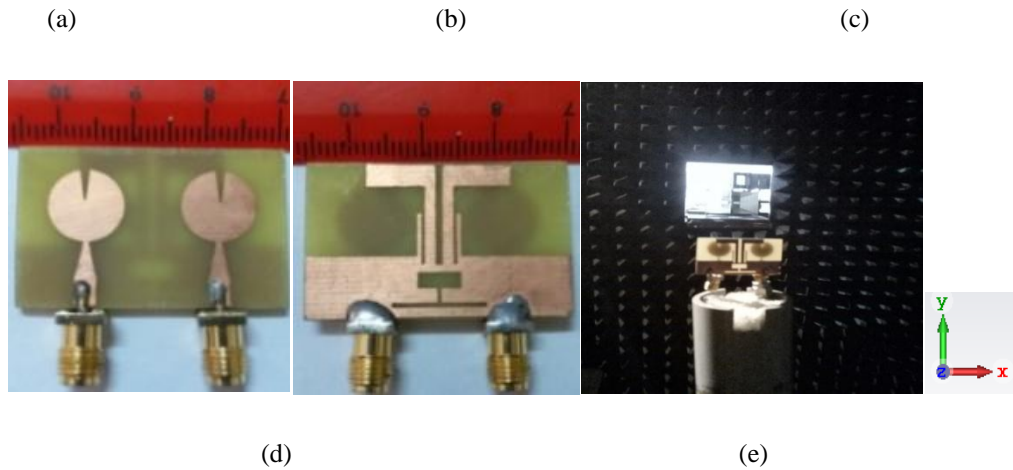
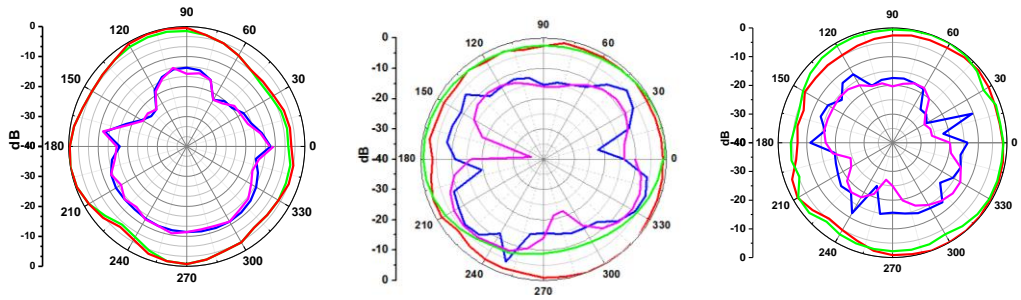
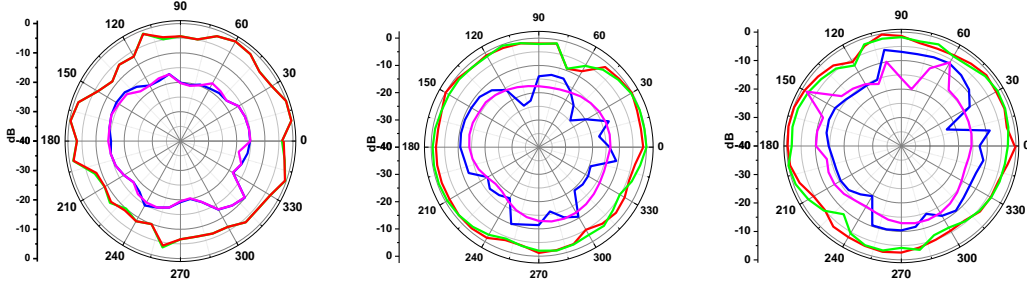


Fig.2.8. 3D radiation pattern of MIMO antenna at (a) 4.1GHz (b) 6.6GHz (c) 9.6GHz only port-1 is excited and port-2 terminated by 50 Ω load (d) Fabricated prototype (e) Antenna under test in an anechoic chamber for radiation pattern measurement

Fig.2.8 (a)-(c) shows the 3D radiation pattern of the proposed MIMO antenna at 4.1, 6.6, and 9.6GHz frequency correspondingly when port-1 is excited and port-2 is terminated with 50 Ω or vice-versa. Radiation patterns are slightly directional because power radiated towards the left of the yz-plane when port-1 is excited and when port-2 of the MIMO antenna is excited, the power is radiating towards the right of the yz-plane to achieved pattern diversity performance of an antenna. Co-polarization is the power level of an electromagnetic wave in an intended direction whilst cross-polarization is the power level of an electromagnetic wave in an un-intended direction due to interference at reception or transmission antenna. Co-polarization and Cross-polarization at different frequencies are calculated by the simulator (CST-Microwave studio) and validate these results by Vector Network Analyzer so we use two terms simulated, by CST-Microwave studio and measured by VNA. The prototype of the proposed MIMO antenna on the FR-4 substrate is fabricated by conventional printed circuit board design procedure and antenna under test in an anechoic chamber associated with VNA for measurement of radiation characteristics as shown in Fig.2.8 (d)-(e). Fig.2.9 shows the simulated/measured yz-plane (left) and xz-plane (right) radiation pattern of antenna at three different frequencies as 4.1, 6.5, and 9.6GHz respectively with an acceptable agreement.



yz-plane at 4.1GHz 6.6GHz 9.6GHz



xz-plane at 4.1GHz 6.6GHz 9.6GHz

— Co Polarization Simulated — Cross Polarization Simulated
— Co Polarization Measured — Cross Polarization Measured

Fig.2.9. Measured & simulated 2D radiation pattern of MIMO antenna at 4.1, 6.6, and 9.6GHz for yz-plane and xz-plane

Whereas the UWB-MIMO antenna consists of two indistinguishable radiated antenna elements and so the time of measurement of the 2D radiation pattern, port-1 is excited and port-2 is terminated by the 50Ω load. It is observed that at operating frequency band the radiation patterns are omnidirectional in H (xz)-plane and dipole like in E (yz)-plane except for the WLAN band. The splitting of the radiation lobes is also observed due to higher-order mode propagation at higher frequencies.

Specific absorption rate: SAR is a vital parameter in the antenna at which the human body is absorbed electromagnetic field energy when exposed, which means the power absorbed per mass of body/head tissue as shown in Fig.2.10. It is typically averaged either over a small sample volume (typically 1gm or 10gm of tissue) or over the entire body. The SAR value of any RF and

microwave electronic devices is obtained by penetration of electric field intensity in the human head tissue in a near field environment [34]. Furthermore, SAR estimation on the head at 4.1, 6.6, and 9.6GHz frequency, the skin radius, bone radius, and brain radius are 79.324mm, 75mm, and 65mm respectively are used and other parameters are also listed in **Table-2.1**. The calculated value of SAR is less than 1.6W/kg for the proposed antenna design as shown in table-2.2 but this SAR performance investigates without any plastic jacket or cover, thus when we wrap the proposed antenna into a plastic jacket or cover then SAR performance may be increased more. SAR for electromagnet energy is calculated by **Equation (2.2)**.

$$SAR = \frac{1}{V} \int \frac{\sigma(r) |E(r)|^2}{\rho(r)} dr \quad (2.2)$$

Where σ = thermal conductivity of sample in S/m, E_{rms} = electric field in V/m, ρ = sample density in kg/m³, V = volume of the sample in m².

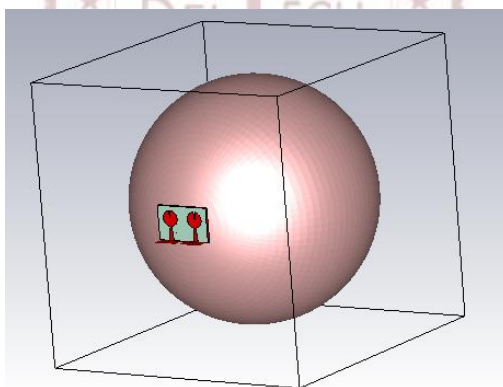


Fig.2.10. Calculation of specific absorption rate near the human head in the presence of the proposed MIMO antenna

Table 2.1. Parameters of the human head for calculation of specific absorption rate (SAR) by the proposed antenna at constant permeability (i.e. $\mu_r=1$).

Type	Density (ρ) kg/m ³	Thermal conductivity (σ) S/m	Heat capacity kJ/K/kg	Blood flow W/K/m ³	Metabolism rate W/m ³
------	--	--	-----------------------------	-------------------------------------	--

Bio-tissue skin	1100	0.293	2.5	9100	1620
Bio-tissue bone	1850	0.41	1.3	3400	610
Bio-tissue brain	1030	1.13	2.675	40000	7100

Table 2.2. SAR values near the human head at different resonant frequencies when the distance between the human head and MIMO antenna is 13mm.

Specific Absorption Rate (W/kg)					
4.1GHz		6.6GHz		9.6GHz	
1(gm)	10(gm)	1(gm)	10(gm)	1(gm)	10(gm)
1.28	0.86	1.39	0.93	1.49	1.04

2.4 MIMO DIVERSITY PERFORMANCE:

MIMO diversity performance of the proposed antenna is evaluated in terms of Envelope Correlation Coefficient, Total Active Reflection Co-efficient, Diversity Gain, Multiplexing Efficiency, and Group Delay. The mutual coupling between two radiation patches and the amount of correlation between them is examined by ECC. It is calculated through using \mathbf{S} -parameters by following Equation 2.3 (a) and this Equation is valid for measuring ECC when the antenna is lossless and radiated power is uniformly distributed along with the antennas.

$$ECC = \frac{|S_{11}^* S_{12} + S_{21}^* S_{22}|^2}{(1 - |S_{11}|^2 - |S_{21}|^2) \times (1 - |S_{22}|^2 - |S_{12}|^2)} \quad 2.3(a)$$

But lossless is a hypothetical result which varies from empirical result so, the computation of the ECC of the MIMO antenna by Equation 2.3 (b) in terms of radiated fields

$$ECC = \frac{\left| \iint_{4\pi} [E_i(\theta, \phi) \times E_j(\theta, \phi)] d\Omega \right|^2}{\iint_{4\pi} |E_i(\theta, \phi)|^2 d\Omega \times \iint_{4\pi} |E_j(\theta, \phi)|^2 d\Omega} \quad 2.3(b)$$

Where E_i & E_j are the radiated electric fields vector of the i^{th} and j^{th} elements of the MIMO antenna system and Ω denotes beam area.

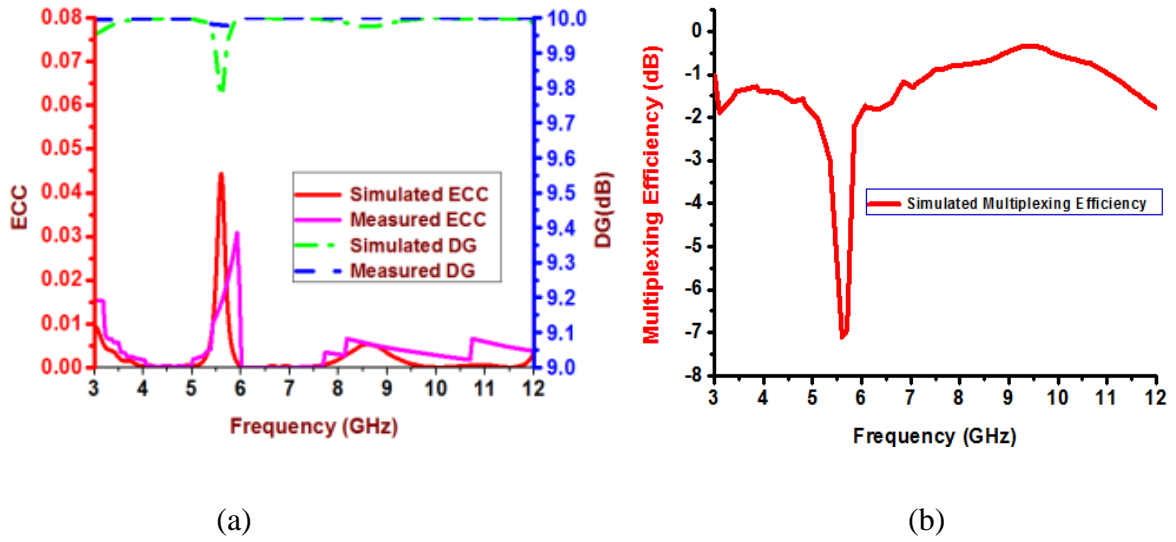


Fig.2.11. Simulated and measured results of the proposed antenna (a) envelope correlation coefficient and diversity gain (b) Simulated result of multiplexing efficiency

The ideal value of ECC is zero for uncorrelated MIMO antenna but their acceptable value for practical MIMO antenna is ≤ 0.5 and as per Fig.2.11 (a) the value of ECC of designed MIMO antenna is less than 0.01 in UWB bandwidth excluding notched band. Hence, the above result specifies a pretty low correlation between the two antenna ports, which shows excellent diversity performance. The diversity gain can be calculated by $DG = 10 \times \sqrt{(1 - ECC^2)}$ and for satisfactory operation of MIMO antenna diversity gain should be closed to 10dB and the value of diversity gain of UWB-MIMO antenna is 9.95dB apart from the notched band as depicted in Fig.2.11 (a).

Also, to optimize the antenna channel capacity, the multiplexing efficiency is a maneuver parameter which is not only explored the total antenna efficiency, but also the co-relation and efficiency disparity. Besides, multiplexing efficiency (η_{MUX}) is the ratio of the power requirement of an antenna to the reference antenna. Fig.2.11 (b) shows the multiplexing efficiency of the MIMO antenna and η_{MUX} is calculated by $\eta_{MUX} = \sqrt{(1 - |\rho_c|^2)} \eta_1 \eta_2$, where ρ_c

is a complex correlation between two side-by-side antennae i.e. $ECC = \rho_c^2$ and η_1, η_2 is the antenna total efficiency of MIMO antenna elements. The result shows that the total efficiency

(shown in Fig.2.7 (b)) and multiplexing efficiency are almost identical and its value goes downward at the notched WLAN band.

In the two-port antenna system, contiguous antenna elements impinge on each other and when working concurrently they influence the overall desirable gain, efficiency, and bandwidth. Actual MIMO antenna system performance will not be predicted by S-parameters only; therefore TARC has initiated this effect into account. It is the square root of the ratio of total reflected to total incident power and hence, it gives the information about the apparent return loss of the MIMO antenna system. For side by side two-port radiated antenna system, it can be evaluated by Equation (2.4).

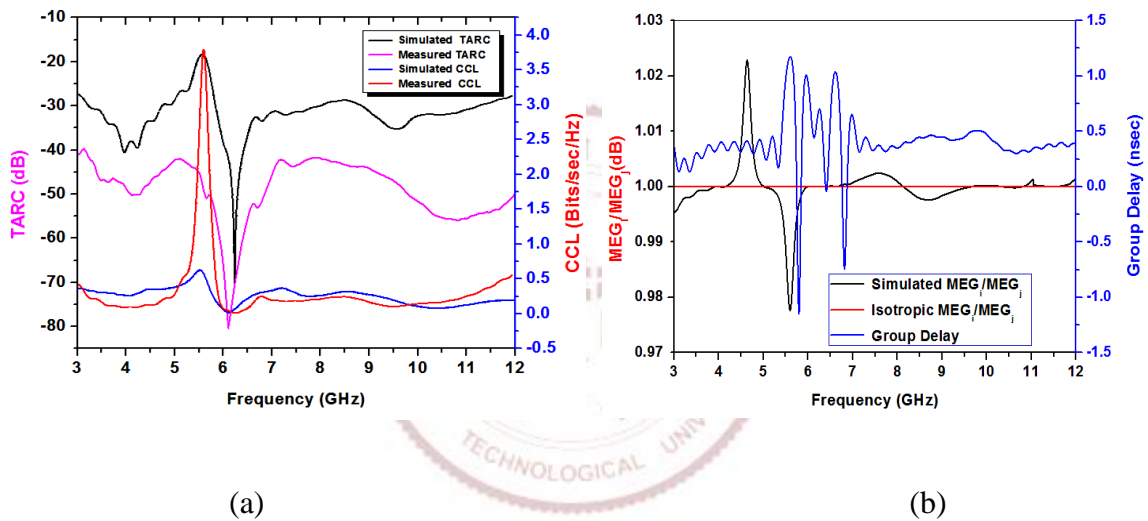


Fig.2.12. Simulated and measured results of (a) channel capacity loss (CCL) and total active reflection coefficient (TARC) (b) Simulated results of the mean effective gain (MEG) and group delay of proposed MIMO antenna

$$TARC = \sqrt{\frac{(S_{11} + S_{12})^2 + (S_{22} + S_{21})^2}{2}} \quad (2.4)$$

Ideally, the value of TARC should be less than 0dB for MIMO antenna-based system. Fig.2.12 (a) shows the simulated and measured TARC of the proposed MIMO antenna and it is observed that the value of TARC is less than -28dB and -50dB correspondingly in the entire UWB range except for the notched band, it shows the excellent diversity performance of the designed antenna. With increasing the number of elements, the channel capacity of the MIMO system is

linearly increased, so the element matrix properly characterizes the performance of a MIMO system as it provides the information about the phase and gain characteristics of the transmitting and receiving elements. However, in the presence of the correlation factor in MIMO antennas, the channel capacity losses are also increased. Therefore, diversity performance of proposed antenna pretentious and channel capacity losses are calculated by the following Equation (2.5)

$$\text{CCL(dB)} = -\log_2 \left[\det(\phi^R) \right] \quad (2.5)$$

Where ϕ^R is the 2×2 co-relation matrix in terms of S-parameter $\phi_{ii} = 1 - |S_{ii}|^2 - |S_{ij}|^2$, $\phi_{ij} = -(S_{ii} \times S_{ij} + S_{ji} \times S_{jj})$. Fig.2.12 (a) shows the CCL losses and it is less than 0.35bits/sec/Hz over the entire bandwidth except for the notch band, which offers better diversity results of the proposed MIMO antenna. Moreover, the mean effective gain (MEG) is the ratio of the mean received power by the i^{th} antenna to the mean incident power of the j^{th} antenna with the same route, $\text{MEG}_i = \mathcal{E}_{\text{Total}}/2$, where $\mathcal{E}_{\text{Total}}$ is implying total effective efficiency of the i^{th} antenna, *i.e.* $\mathcal{E}_{\text{Total}}^i = \mathcal{E}_{\text{mis}}^i \times \mathcal{E}_{\text{rad}}^i$, and where $\mathcal{E}_{\text{mis}}^i = 1 - \sum_{j=1}^N |S_{ij}|^2$, $\mathcal{E}_{\text{rad}}^i = \sum_{j=1}^N |S_{ij}|^2$ where $\mathcal{E}_{\text{mis}}^i$, and $\mathcal{E}_{\text{rad}}^i$ are mismatch efficiency and radiation efficiency of i^{th} antenna as shown in Fig. 2.12 (b). MEG ratio for the proposed MIMO antenna is to be extracted by Equation (2.6)

$$\text{MEG}_i = \frac{P_{\text{rec}}}{P_{\text{inc}}} = \oint \left[\frac{\text{XPR} \times G_{\theta i}(\Omega) + G_{\phi i}(\Omega) \times P_{\phi}(\Omega)}{1 + \text{XPR}} \right] d\Omega \quad (2.6)$$

Where, XPR is the cross-polarization ratio, $G_{\theta i}(\Omega)$, $G_{\phi i}(\Omega)$ and $P_{\phi}(\Omega)$ is the gain and power density function of the incident wave, Ω = beam width.

The acceptable ratio of mean effective gain of i^{th} and j^{th} antenna elements should be less than or equal to $\pm 3\text{dB}$ and as from Fig.2.12 (b), the MEG ratio of the projected MIMO antenna found in acceptable limit throughout the UWB range, which is a high-quality channel performance for wireless communication. Finally, to verify the time domain analysis of the intended MIMO antenna, two identical antennas have located in front of each other as a receiver and transmitter at a distance of 100cm and group delay (ns) is calculated. Group delay is the rate of change of

transmission phase angle with concerning frequency and it is almost constant in entire the intended band. Group delay in terms of return loss (S_{11}) is defined by the Equation $T_d(\omega) = -\delta\phi/\delta\omega$, where Φ = phase of S_{11} and ω = angular frequency in rad/sec. The group delay deviation of the proposed MIMO antenna is ≤ 0.3 ns entire the UWB frequency span excluding the notched band as shown in Fig.2.12 (b).

Table 2.3. Simulated MEG results of proposed MIMO antenna at various frequencies

Frequency (GHz)	MEG(dB) Isotropic medium		MEG(dB) Gaussian medium	
	XPR = 0dB	XPR = 6dB	XPR = 0dB	XPR = 6dB
4.1	-2.0	-4.4	-2.7	-6.1
6.6	-2.0	-4.5	-2.8	-4.9
9.6	-2.0	-5.1	-2.7	-5.6

The MEG is also represented in isotropic and Gaussian mediums, to investigate the diversity performance at XPR = 0dB (outdoor) and 6dB (indoor) as shown in Fig.2.13 (a) and Table 2.3 of the proposed antenna. The MEG for the isotropic medium at 0dB XPR is constant at -2.0dB and 6dB XPR is lies between -2.1 to -5.1dB for the entire UWB bandwidth. Similarly, the MEG for Gaussian medium at 0dB XPR and 6dB XPR is lies among -2.7dB to -2.7dB, and -4.6 to -6.5dB respectively for entire UWB bandwidth.

Fig.2.13 (b) shows the power loss, power accepted, power outgoing to all port, power radiated and power stimulated of proposed MIMO antenna, which is used to calculate all parameters as SAR, CCL, ECC, etc. Stimulated power is near 0.5W and diversity calculation associated with this power. Power loss in metal is extremely low and most of the power is radiated. Power accepted is all most same as stimulated power except notched band because in that region most of the power return back to the same port and power radiated is also high in UWB range but radiated power is always less than stimulated and accepted power due to dielectric, conductor, and surface wave loss in microstrip line except the notched band. Power going to all ports is

highly interfere with at the notched band (5.1-5.85GHz) so that the maximum power is correlated between ports and not used for radiation.

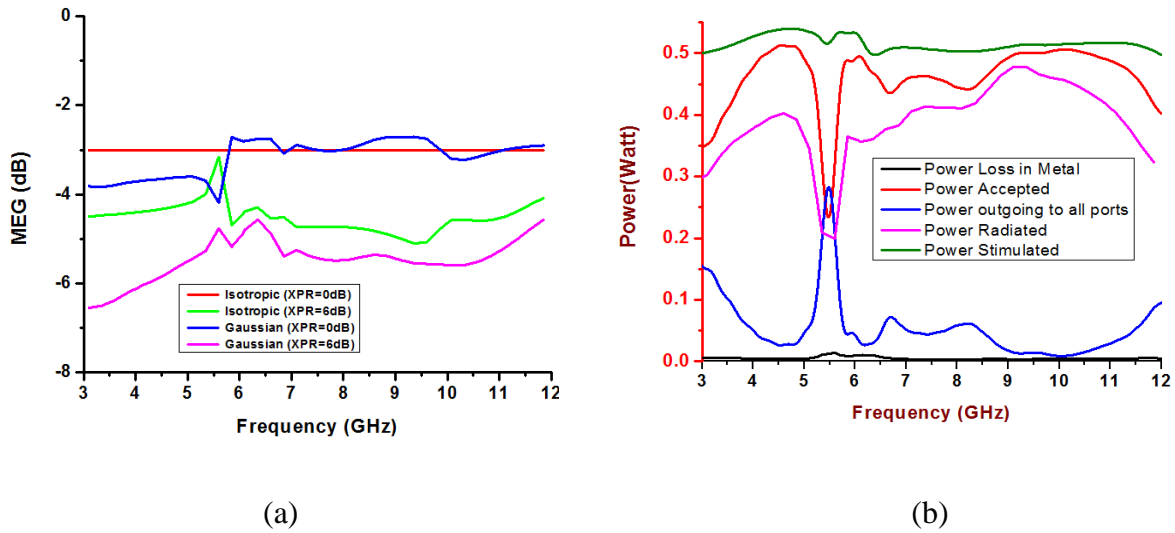


Fig.2.13. (a) A simulated mean effective gain in Isotropic and Gaussian medium at various XPR values of proposed antenna applications (b) Power associated with proposed MIMO antenna for various diversity performances

An evaluation of the proposed MIMO antenna with existing referred MIMO antennas is represented in Table 2.4. It is observed that the designed antenna achieves better results in comparison with most of the MIMO antennas at various specifications, which is highly appreciable as small in size, low in cost, improved radiation efficiency (0.75-0.97) with enhanced isolation, better ECC, and diversity gain (> 9.95dB).

Table 2.4. Comparison of proposed UWB-MIMO antenna including WLAN notched band with existing references at various aspects

Antenna Size (mm ²)	Isolation (dB)	Frequency (GHz)	ECC	DG (dB)	Material	Radiation Efficiency
29×38 [2]	21.5	2.5-19.0	0.01	9.50	FR-4	0.63
50×25 [3]	17.0	2.0-12.0	0.45	9.65	FR-4	0.70
26×40 [5]	15.0	2.1-10.6	0.04	9.79	FR-4	0.6-0.85
33×26 [6]	15.0	2.0-11.0	0.03	9.90	FR-4	0.70

22×29 [9]	15.0	2.5-12.0	0.003	9.95	Rogers RO4003	0.80
55×82 [10]	15.0	2.2-12.3	0.040	9.95	FR-4	0.60
40×20[12]	15.0	3.0-11.0	0.300	9.75	FR-4	0.85
50×50[13]	17.0	2.0-12.0	0.450	9.60	FR-4	0.73
50×39.8[14]	20.0	2.7-12.0	0.010	9.95	TMM4	0.82
36×22 [P]	30.0	3.1-11.2	0.008	9.95	FR-4	0.75-0.97

2.5 SUMMARY:

In this **Chapter**, a UWB-MIMO antenna with the WLAN band-notch (5.1GHz-5.85GHz) characteristic is offered. Results illustrate that the designed antenna has an impedance bandwidth from 2.1GHz to 11.2GHz as well as good isolation i.e. $S_{21} < -15\text{dB}$. Radiation efficiency is greater than 0.85 except the notched band is < 0.5 . Diversity performance is also set the new paradigm in terms of ECC (≤ 0.003), TARC ($\leq -25\text{dB}$), CCL ($\leq 0.3\text{bits/s/Hz}$), Mean effective gain ratio (MEGi) $\cong 1$, and directive gain ($\geq 9.95\text{dB}$) except the notched band. Proposed antenna characteristics are also found suitable with low SAR value at 1g and 10g of head bio tissue for a human interface device, low-cost, easily fabricated, and easy to work. This prototype antenna simulated results are tested and verified by the experimental results. The achieved results of measurement & simulation are in better concurrence. Apart from the above-mentioned antenna performance, the results of the antenna prototype are appropriate for UWB bandwidth at high interference surroundings in indoor or outdoor applications.

CHAPTER-3

SUPER-WIDEBAND (1.575-40GHz) MIMO ANTENNA FOR WIRELESS APPLICATIONS

3.1 INTRODUCTION:

With the entrance of new wireless communication services in recent years, super-wideband (SWB) MIMO antenna is highly demanded with small size, low cost, easy to fabrication, and SWB Omnidirectional radiation characteristics. To achieve different services like Global Position System (GPS), Industrial Science and Medical (ISM), WLAN, cognitive radio Bluetooth, WI-Max, Ultra-Wideband (UWB), sub/mm 5G, and many more wireless services SWB MIMO antenna will become more in demand. If the fractional impedance bandwidth of any antenna is greater than 163.36% or the antenna having a bandwidth ratio of 10:1, maintaining the 10dB return loss and VSWR is less than two over the entire range of frequency [7], the antenna is known as a super-wideband antenna. The Microstrip antenna provides narrow bandwidth but by using a monopole antenna and step impedance feeding line techniques bandwidth of the narrowband antenna can be increased up to the SWB range. SWB MIMO antenna has various advantages that are beneficial for a recent wireless system such as

1. SWB MIMO antenna provides high channel capacity, which is useful for transmitting and receiving voice and video data at a higher data rate.
2. SWB antenna can be used for spectrum sensing in cognitive radio
3. SWB antenna is useful for both long-range and short-range communication.
4. This type of antenna is resisted for jamming, low transmission power requirements, and multipath performance.

In this **Chapter**, the design, simulation, and fabrication of SWB two elements MIMO antenna is discussed. SWB MIMO antenna is working 1.5-40GHz frequency and covers L to Ka-band and

¹ Saxena, Gaurav, Priyanka Jain, and Y K Awasthi. "High diversity gain super-wideband single band-notch MIMO antenna for multiple wireless applications." *IET Microwaves, Antennas & Propagation* 14, no. 1 (2020): 109-119.

mitigates the frequency band 5.9-7.1GHz to avoid the interference with E-S satellite system. The proposed designed SWB MIMO antenna is circularly polarized in dual-band (1.575-3.00GHz; 25.75-26.50GHz). In designing a MIMO antenna, polarization is an important parameter. For GPS and vehicular communication and millimetre 5G applications, we required a circular polarization antenna as at least half power in need in any plane. In the MIMO antenna, when we transmitted power from an excited antenna at that time, no other antenna received that power at the transmitter end, so good isolation is required between antenna elements. The super-wideband (SWB) bandwidth of an antenna is attained by introducing a step impedance microstrip line to feed the radiator. Furthermore, two rectangular-shaped slots are etched on the ground plane to achieve band-notched characteristics. Unequal E-shaped stubs and mushroom-shaped EBG structure is used for obtaining high isolation. Circular-shape (Closed Ring Resonator-CRR) is etched on the patch to achieve circular polarization in two bands. Section 3.2 explains the SWB MIMO antenna design procedure. The proposed antenna is designed using a computer simulation technology-CST microwave studio simulation tool. Section 3.3 demonstrates the simulated and measured results. In section 3.4 diversity performance of the antenna, along with a comparison from literature has been discussed. Section 3.5 concludes the proposed work.

3.2 MIMO ANTENNA DESIGN PROCEDURE

The designed 2-element MIMO antenna, including notched band (5.9-7.1GHz) characteristic, is fabricated on the FR-4 substrate of height (h) 1.6mm with relative permittivity (ϵ_r) of 4.4 and loss tangent ($\tan\delta$) of 0.02 having an overall dimension of 55.5mm×50.6mm as shown in [Fig. 3.1 \(a\) - \(b\)](#). All dimensions of the proposed antenna are given in [Table 3.1](#) to achieve SWB impedance bandwidth (1.5-40GHz). This antenna consists of a circular patch, and a circular slot etched out of it to achieve circular polarization in dual-band. The current is accumulating along the circular radiator's periphery, affecting the bandwidth in a low-frequency range, therefore for

improving the low-frequency bandwidth, a "Closed Ring Resonator-CRR" of radius 5.3mm is etched at a circular patch without affecting the remaining antenna performance.

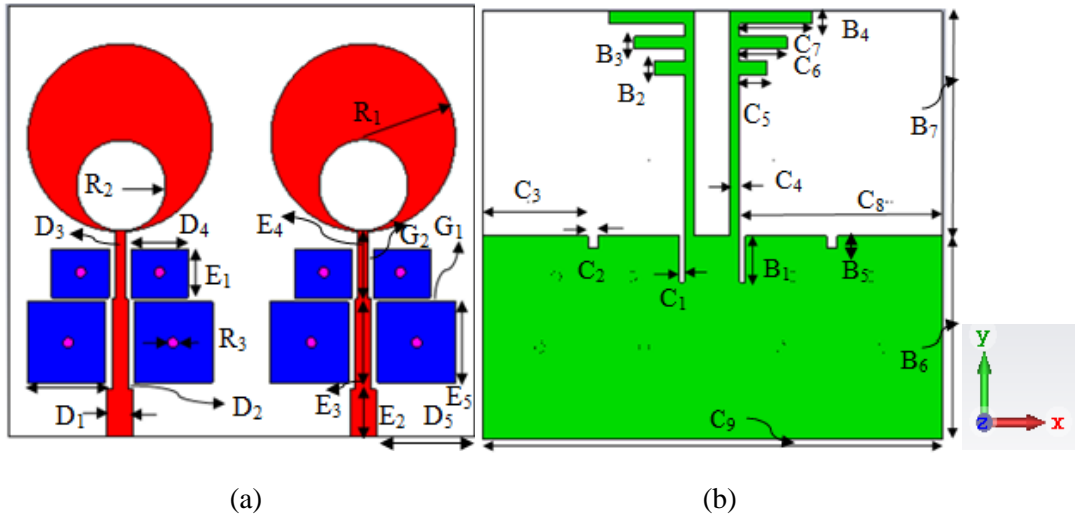


Fig.3.1. Two-element SWB planar monopole MIMO antenna (a) Front view (b) Bottom view

Table 3.1 Proposed SWB MIMO antenna dimensions in mm

R_1	R_2	D_1	D_2	D_3	D_4	D_5	E_1	E_2	E_3
11	5.3	3.2	1.9	1.2	6.85	11.7	5.8	5.5	10.6
E_4	E_5	G_1	G_2	C_1	C_2	C_3	C_4	C_5	C_6
7.92	9.35	0.45	0.6	0.6	1.3	13.7	1.2	3.3	5.7
C_7	C_8	C_9	B_1	B_2	B_3	B_4	B_5	B_6	B_7
8.7	24.3	55.6	5.5	1.5	1.5	1.5	1.5	24	26.5

The impedance feeding mechanism comprises of three feeding subsections having an impedance of 50, 65, and 81 Ω respectively with different lengths. Further, E-shaped stubs of unequal arm length are used to achieve the intended isolation between antennas as well as to extend bandwidth. E-shaped stubs of equal length cause poor isolation at a lower frequency. The number of stubs is optimized to provide maximum decoupling at a high frequency, so it cannot be improved further by increasing the number of stubs. Now, super-wideband, including band-notch characteristics, is obtained by using a stepped impedance feed line with a partially tailored ground plane and rectangular slots. The diameter of the EBG slots (R_3) is 1.2mm. The

fundamental resonance frequency (f_r) of the circular-shaped monopole antenna is calculated by the Equation (3.1)

$$f_r(\text{GHz}) = \frac{144}{C_0 + 2R_1 + h + \frac{A_1}{2\pi\sqrt{\epsilon_r + 1}} + \frac{A_2}{2\pi\sqrt{\epsilon_r + 1}}} = 20.85\text{GHz} \quad (3.1)$$

Where $A_1 = 291.79\text{mm}^2$, $A_2 = 1408\text{mm}^2$ is the area of anticipated radiation patch and ground plane, $C_0 = 55.6\text{mm}$ is the length of a ground plane, $2R_1 = 2 \times 11 = 22\text{mm}$ is a diameter of circular radiated patch depicted in Fig. 3.1 (a) - (b). The step by step design procedure of the proposed SWB-MIMO antenna is represented in Fig.3.2, and analogous return losses and isolations are presented in Fig.3.3 (a) - (b). Ant-1 provides unsatisfactory return loss ($<10\text{dB}$) and isolation ($<15\text{dB}$) in SWB bandwidth. By changing the feeding line width of Ant-1, return loss and isolation are improved as depicted in Ant-2 but return loss is not acceptable in the lower frequency range (1.5-6GHz). Since charges are accumulated on the etched portion of patches, the discontinuity is added to improve the return loss with compromised isolation in the intended band.

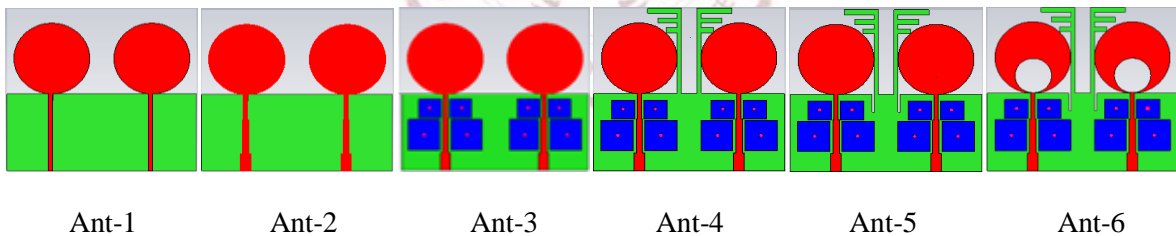
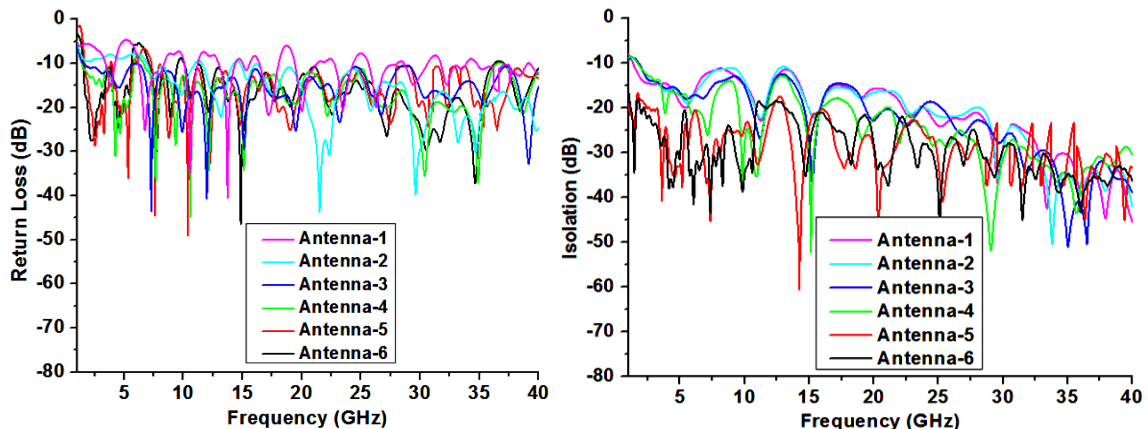


Fig.3.2. Geometrical design steps of the proposed super-wideband MIMO antenna with band notch characteristics



(a)

(b)

Fig.3.3. Simulated (using CST MWS) results of (a) Return loss (b) Isolation of the antennas shown in Fig.3.3

Therefore, in Ant-3, a mushroom-shaped EBG is introduced near the feed line which improves the return loss in the SWB range (>10dB) and isolation but isolation is not much improved in the frequency range (1.5-12GHz). Further, in Ant-4, an E-shaped decoupling structure is designed on the ground plane, which improves the isolation (>15dB) in the intended bandwidth. Further, in Ant-5 vertical slots are engraved in the ground plane to get better isolation in the frequency range of 3.1 to 4.8GHz (>20dB). To design a dual-band circularly polarized antenna a close ring resonator is etched on the patch in Ant-6. Ant-6 is finalized designed for giving 1.5-40GHz impedance bandwidth with notched characteristics and dual circular band. It also creates a notch band characteristic for avoiding interference from E-S satellite communication (5.9-7.1GHz), as shown in Fig.3.3. The bandwidth of the notched band can be controlled by changing the ground slot length (B_1) at the notch frequency, $f_n = c/(2 \times B_1 \times \epsilon_{\text{reff}})$, where c is the speed of the signal in a vacuum (3×10^8 m/sec) and ϵ_{reff} is the effective relative permittivity [36] of a substrate. The Center frequency of the intended notched-band is 6.5GHz at B_1 .

EBG structures, including a microstrip feed line and its equivalent circuit model with simulated results represented in Fig.3.4 (a) - (d) and center frequency of the designed EBG is calculated by

Equation (3.2)

$$f_{\text{EBG}} = \frac{1}{2\pi \sqrt{L_{\text{eq}}(C_{\text{gap eq}} + C_{\text{plate eq}})}} = 21.22\text{GHz} \quad (3.2)$$

C_{gap} is the gap capacitance between step impedance feeding line and square mushroom-shaped EBG structures having length E_1 & E_5 respectively and it is calculated by Equation 3.3(a)-(b).

$$C_{\text{gap1}} = \frac{E_1 \epsilon_0 (1 + \epsilon_r)}{\pi} \text{Cosh}^{-1} \left(\frac{E_1 + G_2}{G_2} \right) \text{F} = 49.69 \times 10^{-15} \text{ F} \quad 3.3(a)$$

$$C_{\text{gap3}} = \frac{E_5 \epsilon_0 (1 + \epsilon_r)}{\pi} \text{Cosh}^{-1} \left(\frac{E_5 + G_2}{G_2} \right) \text{F} = 143.74 \times 10^{-15} \text{ F} \quad 3.3(b)$$

As C_{gap1} & C_{gap2} are equal and parallel therefore the total $C_{\text{gap1, 2}}$ is $= C_{\text{gap1}} + C_{\text{gap2}} = 99.38 \times 10^{-15} \text{ F}$, similarly C_{gap3} & C_{gap4} are also equal and parallel so $C_{\text{gap3, 4}}$ is $= C_{\text{gap3}} + C_{\text{gap4}} = 287.49 \times 10^{-15} \text{ F}$. C_{plate} is the plate capacitance associated with EBG plate and ground plane, it is calculated by Equation 3.4 (a)-(b) respectively and $C_{\text{gapeq}} = C_{\text{gap1-2}} + C_{\text{gap3-4}} = 386.87 \text{ fF}$.

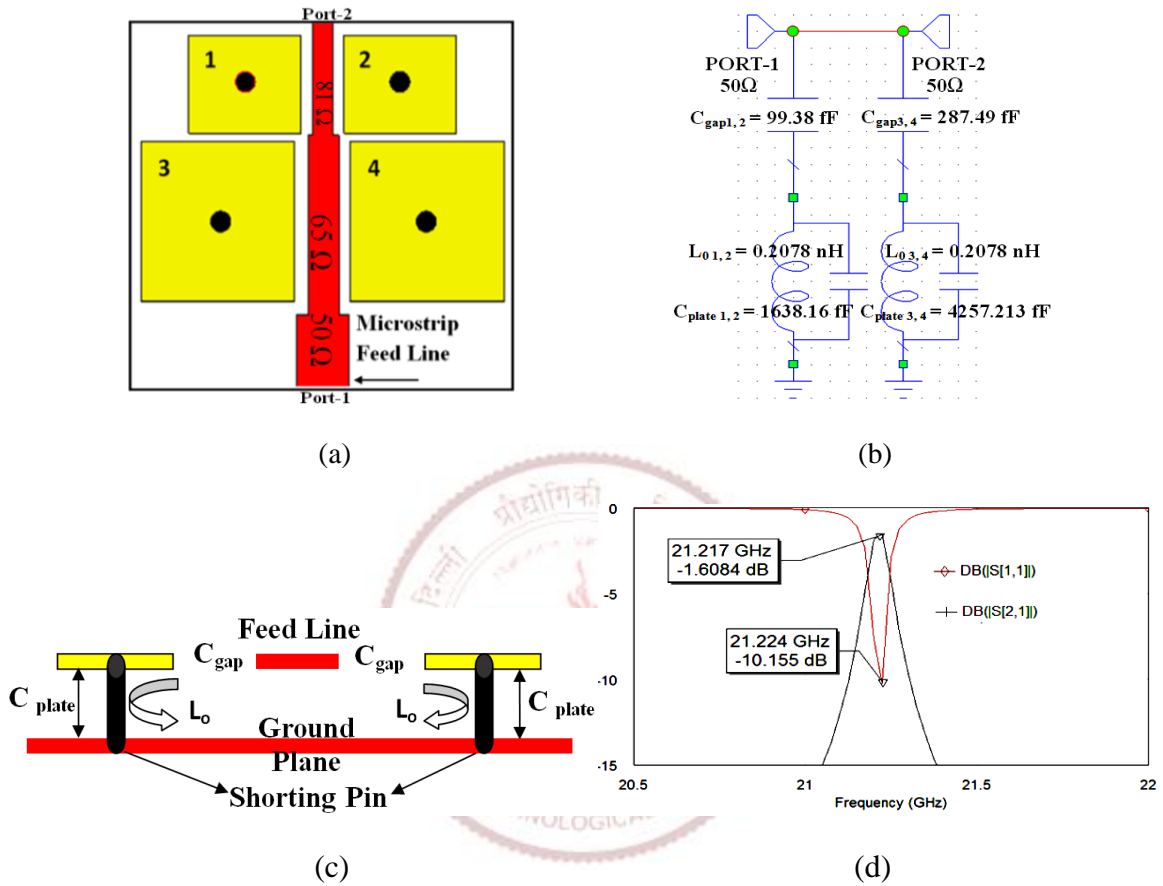


Fig.3.4. Circuit analysis of Electromagnetic Band Gap structures (a) Mushroom-shaped EBG designs near to the microstrip stepped feed line (b) Equivalent circuit model of EBG (c) Front cross-sectional view of EBG (d) Simulated results of the equivalent circuit model of EBG with its resonance frequency

$$C_{\text{plate1}} = \frac{\epsilon_0 \epsilon_r E_1 D_4}{h} \text{ F} = 819.08 \times 10^{-15} \text{ F} \quad 3.4(a)$$

$$C_{\text{plate3}} = \frac{\epsilon_0 \epsilon_r E_5^2}{h} \text{ F} = 2128.606 \times 10^{-15} \text{ F} \quad 3.4(b)$$

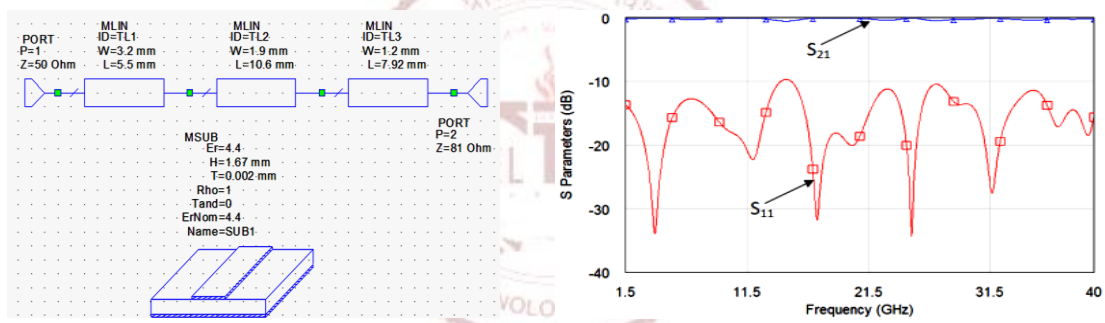
C_{plate1} & C_{plate2} are equal and parallel, therefore, $C_{\text{plate1,2}}$ is $= C_{\text{plate1}} + C_{\text{plate2}} = 1638.160 \text{ fF}$, similarly C_{plate3} & C_{plate4} are equal and parallel so $C_{\text{plate3, 4}}$ is $= C_{\text{plate3}} + C_{\text{plate4}} = 4257.213 \text{ fF}$ and $C_{\text{plateeq}} = C_{\text{plate1-2}} +$

$C_{\text{plate3-4}} = 5895.37\text{fF}$. L_O is the inductive loading of centrally located shorting pin in EBG structure and it is calculated by Equation (3.5)

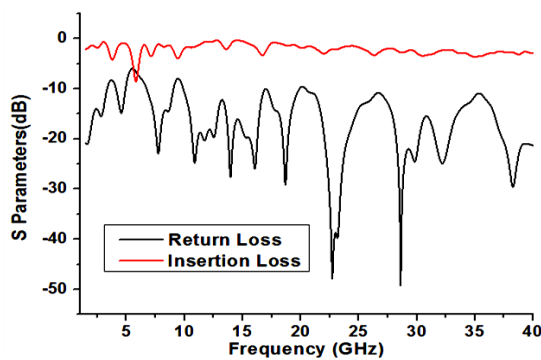
$$L_O = 2 \times 10^{-7} \times h \left[\ln \left(\frac{2 \times h}{R_3/2} \right) + 0.5 \left(\frac{R_3}{h} \right) - 0.75 \right] \text{H} = 0.4156 \times 10^{-9} \text{H} \quad (3.5)$$

Four equal and parallel shorting pins associated with four mushroom-shaped EBG structures, therefore total equivalent inductance ($L_{\text{eq}} = L_O/4$) is $0.1039 \times 10^{-9} \text{H}$. Hence, the calculated resonance frequency of the EBG structure is 21.224GHz by Equation (3.2).

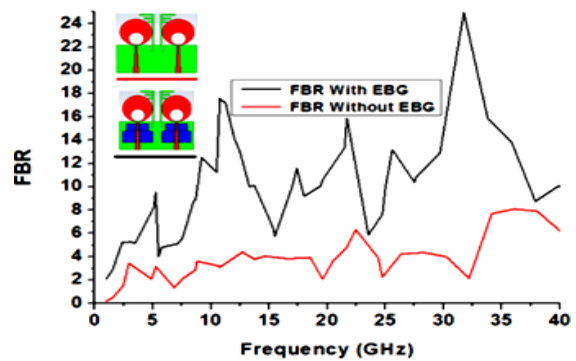
The proposed step quarter-wave impedance transformer technique without EBG is verified by a circuit simulation tool “Microwave Office” as shown in Fig. 3.5(a) Stepped impedance feed line with EBG, shown in Fig.3.4(a), provide permissible scattering results in the proposed antenna. The return loss is less than 10dB throughout the SWB (1.5GHz-40GHz), which means that maximum input power appears at port-2 as shown in Fig.3.5(b).



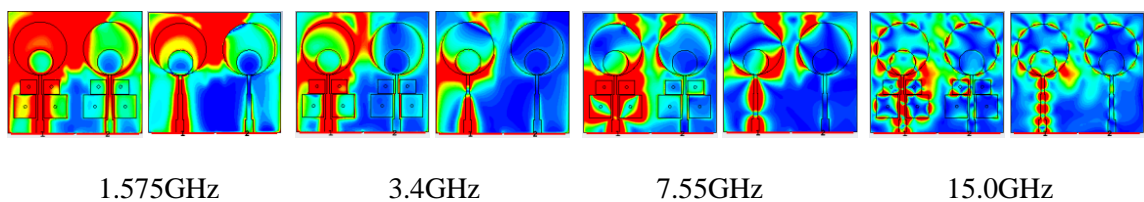
(a)



(b)



(c)



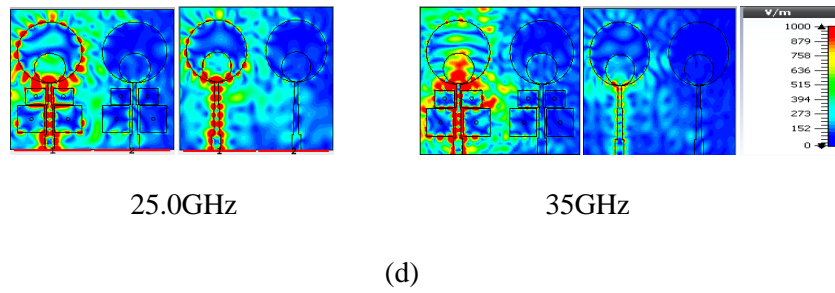


Fig.3.5. Electromagnetic field analysis of stepped impedance feeding line and EBG structures (a) Simulated scattering results of stepped impedance feeding line only (b) Simulated scattering results of stepped impedance feeding line with EBG designs (c) Simulated FBR of SWB-antenna with and without EBG structures (d) Field distribution with and without EBG at 1.575, 3.4, 7.55, 15, 25, 35GHz frequency when port-1 excited and port-2 terminated with a matched load

FBR (Front to Back Ratio) is calculated with and without EBG to represent the existence of EBG in the proposed antenna design, as shown in Fig.3.5(c). As EBG is used to prevent the surface wave loss and direct the radiated power in the intended direction, therefore, the FBR of the antenna with EBG is higher than that without EBG throughout the SWB bandwidth. Fig.3.5 (d) represents the electric field distribution over the antenna with EBG and without EBG. It is shown that more fields are confined around EBG, which improves the FBR in intended bandwidth.

3.3 RESULTS AND DISCUSSION

Measured and simulated return loss, isolation, constant group delay, and peak gain of the designed antenna, as represented in Fig. 3.6 (a) – (b), are less than 10dB, 20dB, almost 1.0ns, and 7.6dBi respectively, throughout the SWB bandwidth except for the notched band. The return loss begins to deteriorate at high frequencies, especially above 35GHz because, at high frequency, the inductance effect starts to dominate in the proposed impedance matching mechanism. The current is also confined on the surface of the conductor due to the skin effect, which creates impedance mismatch and provides low return loss. But the simulated return loss is still less than 10dB. Mobile phone and other movable handheld device antennas require at least half power in every plane for the effective communication link, so circular polarization of antenna for GPS and mm-wave 5G applications is planned. The proposed antenna is circularly polarized in dual-band,

which is achieved by etching a circular slot (Closed Ring Resonator: CRR) out of the radiating patch.

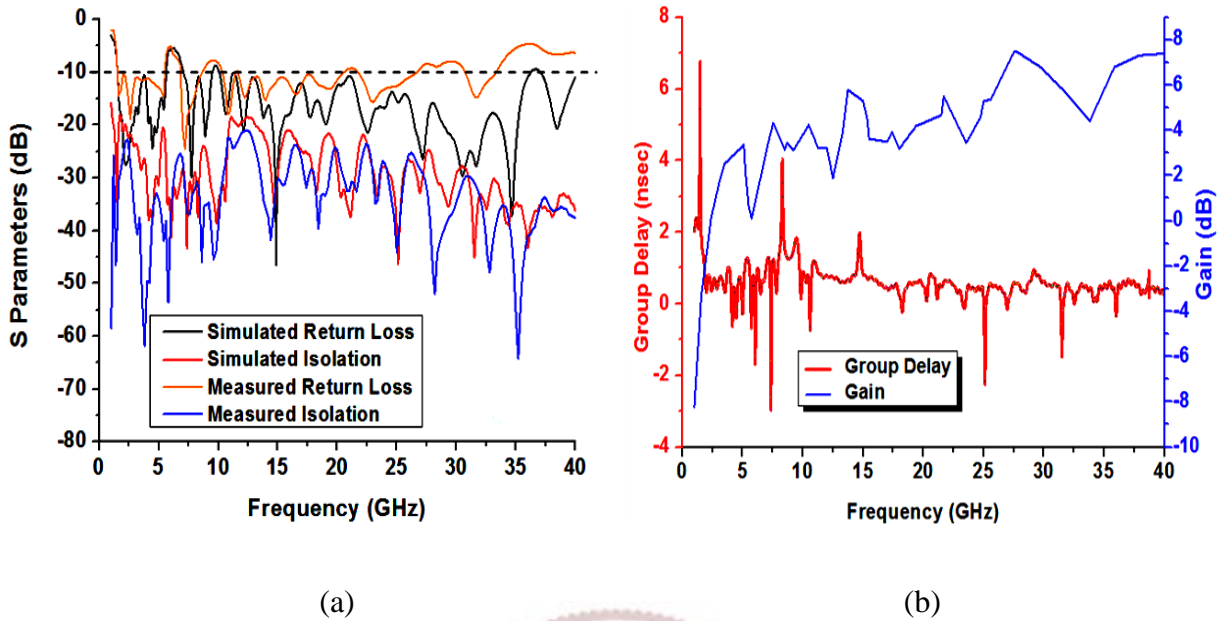


Fig.3.6. Simulated and measured (a) S-parameters (return & isolation) (b) Group delay and Gain

All steps of the proposed antenna design from linear to circular polarization are given in Fig.3.3 and the corresponding its axial ratio are shown in Fig. 3.7 (a)-(b). It is observed from the results of antennas (Ant-1 to Ant-5) that the axial ratio of antennas w.r.t. frequency is greater than 6dB throughout the Super wideband. Hence, all antenna designs (Ant-1 to Ant-5) are linearly polarized. The proposed Ant-6 with an etched CRR of the optimized radius produces circular polarization at 1.575GHz and 26.0GHz with an axial ratio of less than 3dB.

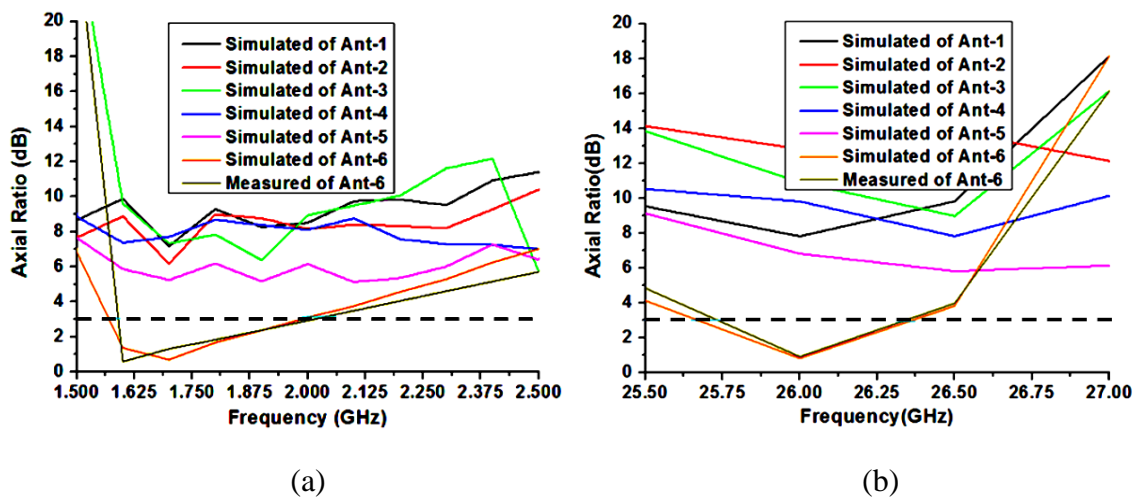


Fig.3.7. Simulated and measured (a) Parametric analysis of axial ratio in L₁-band (b) Parametric analysis of axial ratio in K-band of SWB-MIMO antenna

The optimized radius of the circular patch and etched CRR is 11.0mm (R₁) and 5.3mm (R₂), respectively. The simulated current density of antenna at 1.575, 3.40, 3.45, 3.50, 5.50, 8.69, 15.0, 25.0, 35.0GHz frequencies is represented in Fig.3.8. The main cause behind the mutual coupling between the adjacent antenna elements is the flow of surface current from the energized antenna-1 to antenna-3. Extremely low surface current on antenna-2 is observed due to the excitation of antenna-1, as shown in Fig.3.9. Hence, the level of mutual coupling between antenna-1 and antenna-2 is reduced. This proposed decoupling mechanism is useful in various antenna applications without affecting the adjacent antenna. In the present case, E-shaped stubs in a ground plane are used for achieving reduced mutual coupling between antennas. Therefore, better isolation is acquired in the intended frequency band.

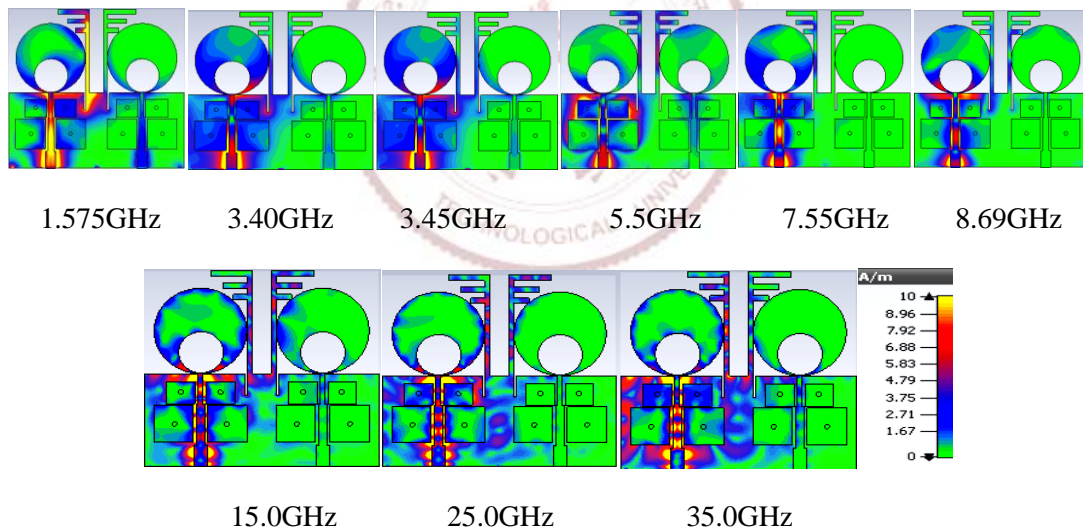


Fig.3.8. Surface current density distribution at 1.575, 3.40, 3.45, 5.50, 7.55, 8.69, 15.0, 25.0, & 35.0 GHz when antenna 1 (left) is energized and antenna 2 (right) terminated with match load

3D radiation patterns for antenna-1 (with antenna-2 is terminated with a matched load) are shown in Fig. 3.9 (a), where the peak of an antenna's radiation patterns is in one direction at all frequencies. When antenna-2 is excited, the power radiates towards the right of the yz- plane. Thus, the proposed antenna gets pattern diversity, which contributes to better isolation between

the two antennas. The designed MIMO antenna is fabricated on an FR4 substrate using a photolithography technique, shown in Fig.3.9 (b). The antenna under test is placed in an anechoic chamber associated with VNA (Vector Network Analyzer) to measure antenna characteristics, represented in Fig. 3.9 (c).

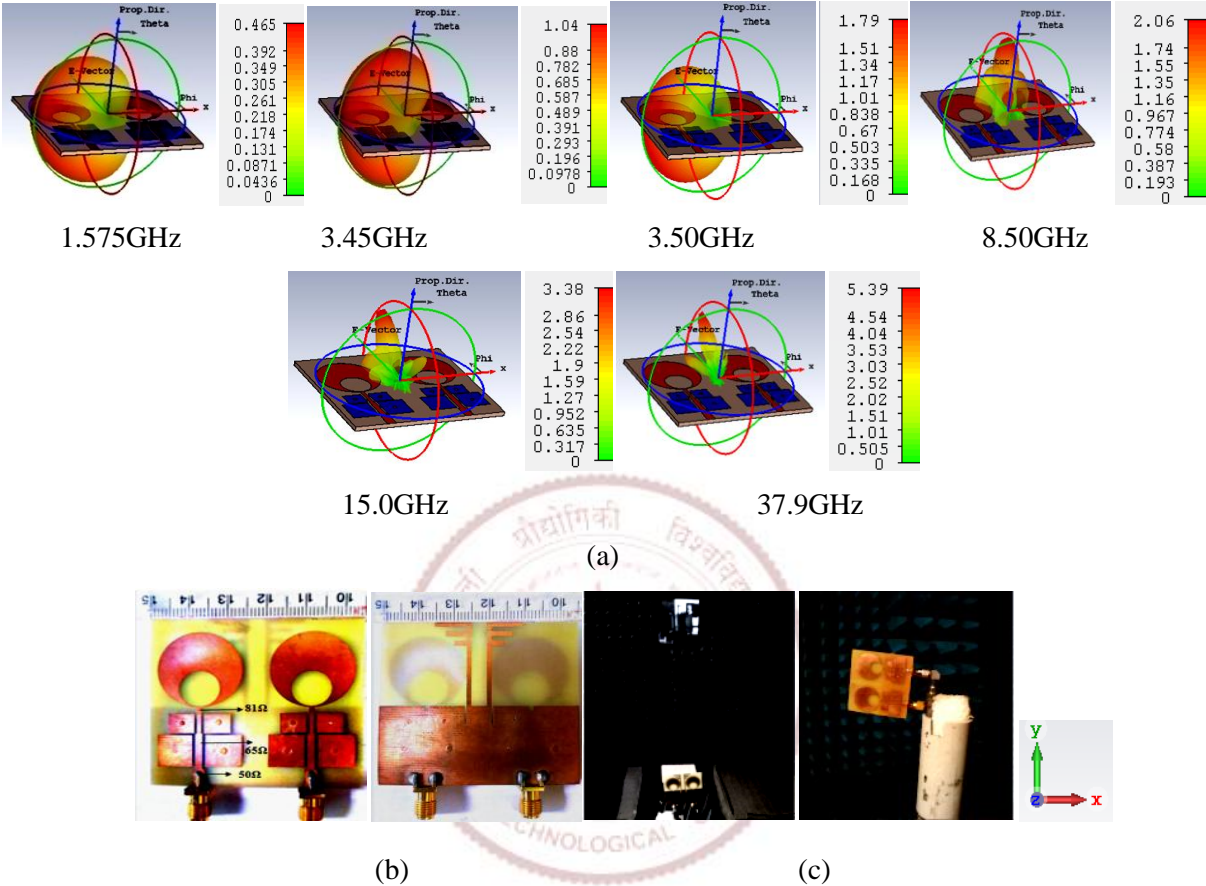
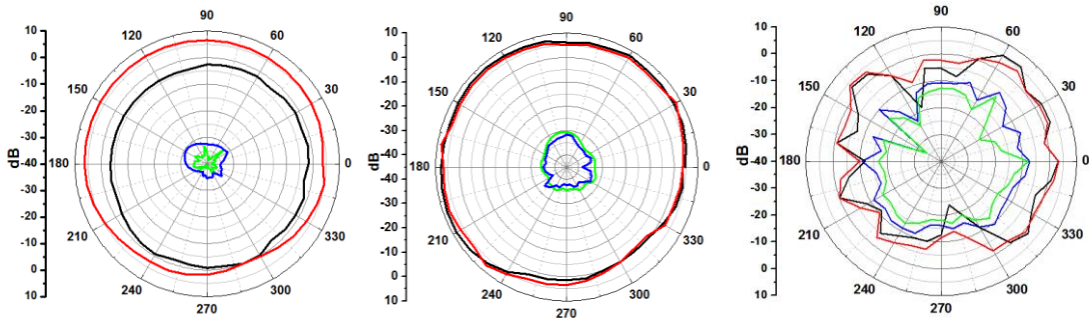
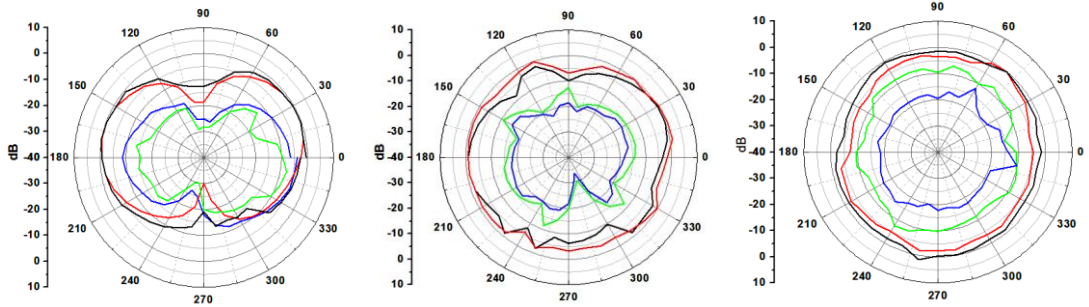


Fig.3.9. 3D radiation pattern of designed MIMO antenna at (a) 1.575, 3.45, 3.50, 8.50, 15.0, & 37.9GHz (b) Fabricated prototype top and bottom view (c) Antenna under test in anechoic chamber for radiation pattern measurement

Fig.3.10 presents the measured & simulated yz-plane (left) and xz-plane (right) 2D radiation patterns of the designed antenna at 1.575, 3.40, and 28.0GHz frequencies an acceptable agreement. It is noted that the patterns at the operating frequency band are omnidirectional at $\Phi = 0^\circ$ (xz)-plane and dipole like at $\Phi = 90^\circ$ (yz)-plane except notched band (5.9-6.9GHz). At higher frequency, the splitting of the radiation lobes is also noted due to higher-order mode propagation.



yz-plane at 1.575GHz, 3.45GHz, 28GHz



xz-plane at 1.575GHz, 3.45GHz, 28GHz

- Co- Polarization simulated — Cross- Polarization simulated
- Co- Polarization measured — Cross- Polarization measured

Fig.3.10. Measured & simulated 2D radiation patterns at 1.575, 3.45, and 28.0GHz when antenna-1 is energized and antenna-2 is terminated by a matched load

Specific Absorption Rate: SAR is a vital parameter in the antenna at which electromagnetic energy is consumed by the human body when exposed, as shown in Fig 3.11. SAR is explained as "the power absorbed per mass of tissue." SAR is usually averaged either over a small sample volume (typically 1g or 10g of tissue) or over the whole body.

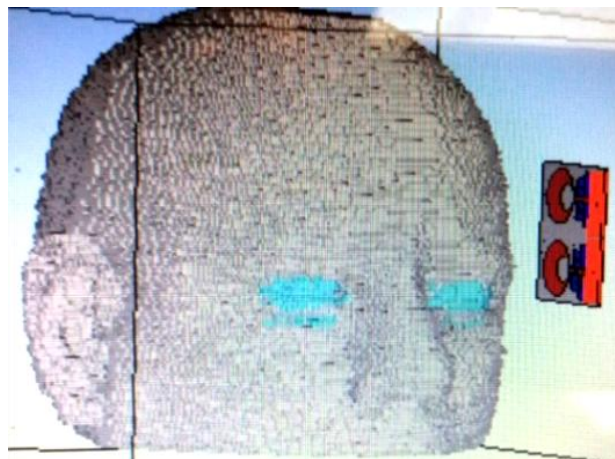


Fig.3.11. Calculation of specific absorption rate near the human head in the presence of the designed MIMO antenna

The SAR value of any RF and microwave electronic devices is obtained by penetrating electric field intensity in the human head tissue near the field environment [34]. Furthermore, the SAR estimation of the proposed antenna on the head at 1.575, 3.40, and 5.50GHz frequencies are listed in Table 3.3. For SAR analysis, the values used for the radius of skin, bone, and brain are 79.324, 75, and 65mm, respectively shown in Fig.3.11.

Table 3.2 Parameters of the human head used for calculation of specific absorption rate by the proposed antenna at constant permeability

Type	Density (ρ) kg/m ³	Thermal conductivity (σ) S/m	Heat capacity kJ/K/kg	Blood flow W/K/m ³	Metabolism rate W/m ³
Bio-tissue skin	1100	0.293	2.5	9100	1620
Bio-tissue bone	1850	0.41	1.3	3400	610
Bio-tissue brain	1030	1.13	2.675	40000	7100

Table 3.3 SAR values near the human head at the different resonant frequencies when the distance between the human head and MIMO antenna is 15mm

Specific Absorption Rate (W/kg)					
1.575GHz		3.4GHz		5.5GHz	
1(g)	10(g)	1(g)	10(g)	1(g)	10(g)
0.041	0.021	0.048	0.026	0.053	0.032

The calculated value of SAR is less than 1.6W/kg for the proposed antenna as shown in Table 3.3, for all parameters listed in Table 3.2. This SAR performance is investigated without any plastic jacket or cover. The SAR of electromagnetic energy is calculated by Equation (3.6)

$$\text{Specific Absorption Rate} = \frac{1}{V} \int \frac{\sigma(r)|E(r)|^2}{\rho(r)} dr \quad (3.6)$$

Where $\sigma(r)$ is the thermal conductivity of the model in S/m, $E_{\text{rms}}(r)$ is the root mean square electric field in V/m, $\rho(r)$ is sample density in kg/m^3 , and V is the volume of the sample in m^3 . SAR is the function of the input power, and 100mW power is used for calculation.

3.4 MIMO DIVERSITY PERFORMANCE

MIMO diversity performance of the designed antenna is evaluated in terms of Envelope Correlation Coefficient (ECC), Total Active Reflection Co-efficient (TARC), Diversity Gain (DG), Channel capacity loss (CCL). ECC calculates the mutual coupling between two radiators and the amount of correlation between them.

It is calculated through S-parameters by Equation 3.7 (a), and this Equation is only valid for lossless uniformly distributed power through antenna.

$$\text{ECC} = \frac{|S_{11}^* S_{12} + S_{21}^* S_{22}|^2}{(1 - |S_{11}|^2 + |S_{21}|^2) \times (1 - |S_{22}|^2 + |S_{12}|^2)} \quad 3.7(a)$$

ECC's ideal value is zero for uncorrelated MIMO antenna, but their acceptable value for practical MIMO antenna is ≤ 0.5 . In Fig.3.12 (a), ECC's value of designed MIMO antenna using s-parameters and radiated fields in super-wideband is observed to be less than 0.005 and 0.03, respectively, excluding the notched-band. Hence, the above results show a pretty low correlation between the two antennas, indicating excellent diversity performance.

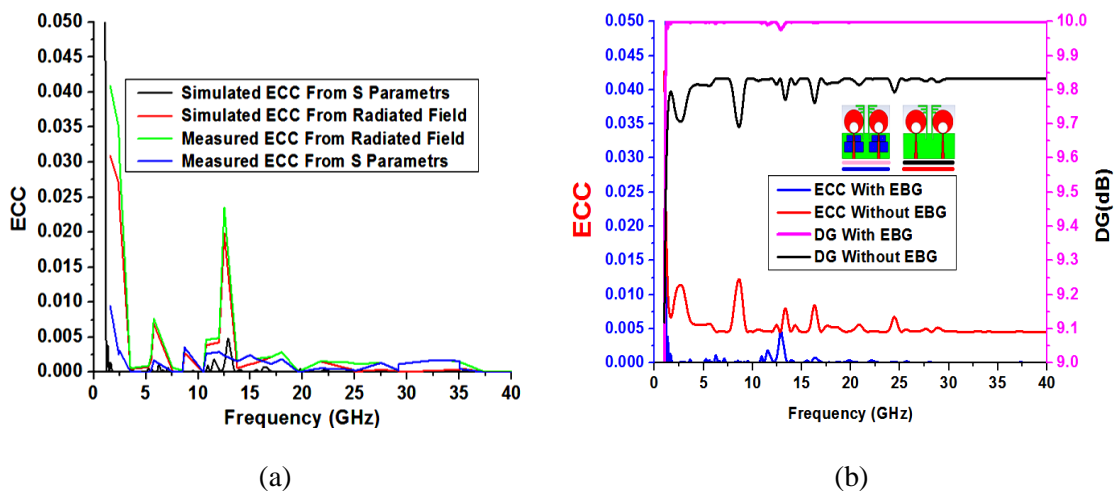


Fig.3.12. Diversity performance of proposed SWB antenna (a) Measured and simulated results of ECC (b) Simulated results of ECC and DG with and without EBG

But it provides a hypothetical result which varies from empirical result so, the computation of the ECC of the MIMO antenna by Equation 3.7 (b) in terms of radiated fields

$$\text{ECC} = \frac{\left| \iint_{4\pi} \left[E_i(\theta, \phi) \times E_j(\theta, \phi) \right] d\Omega \right|^2}{\iint_{4\pi} |E_i(\theta, \phi)|^2 d\Omega \times \iint_{4\pi} |E_j(\theta, \phi)|^2 d\Omega} \quad 3.7 (b)$$

Where E_i & E_j are the radiated electric fields vector of the i^{th} and j^{th} elements of the MIMO antenna system. The MIMO antenna's diversity gain is calculated approximately by the formula given by $\text{DG} = 10 \times \sqrt{1 - (\text{ECC})^2}$, and for satisfactory operation of MIMO antenna, diversity gain should be close to 10dB. The value of diversity gain of the designed super-wideband antenna is 9.99dB apart from the notched band. The ECC and DG with and without EBG structures vary from 0.0125 to 0.005 and 9.7dB to 9.99dB, respectively, as depicted in Fig.3.12 (b).

The designed two-element array SWB antenna channel capacity is verified by Ergodic MIMO channel capacity, and it is calculated by Equation 3.8. From Fig.3.14, the minimum and maximum channel capacity of the two-element array antenna system is 7.5bps/Hz and 11.34bps/Hz, respectively, through 20dB SNR in a uniform environment.

The correlation matrix of the MIMO system is $R_{xx}(\alpha) = (\alpha) [I] + (1-\alpha) [H][H^*]$, where, $0 < \alpha < k / (k-1)$ and k is the number of antenna elements, For minimum channel Capacity, the value of channel correlation coefficient (α) is zero, therefore, all channels are correlated to each other. Furthermore, the value of α is one for maximum channel capacity, hence all channel has no correlation and fading matrix $[H][H^*]$ is converted into an identity matrix. The maximum value of the channel capacity of the 2×2 MIMO antenna system is calculated by the Equation 3.8

$$C_{2 \times 2 \text{ MIMO Max.}} = k \left\{ \log_2 \left[\det \left([I] + \frac{\text{SNR}}{k} [H][H^*] \right) \right] \right\} \quad (3.8)$$

$$= 4 \times \log_2 (1+50) = 23.68 \text{ bits/sec/Hz}$$

Where, SNR is 20dB for Rayleigh fading environment i.e. $\text{SNR} = 100$. As the permissible limit of channel capacity of the 2×2 MIMO antenna system is 65% of its maximum value [35] (23.68

bits/sec/Hz) = $23.68 \times 0.65 = 14.74$ bits/sec/Hz by using Monte Carlo simulation for correlated Rayleigh channel.

The upper level of channel capacity of proposed 2 elements MIMO is calculated by Equation (3.8) $C_{2\text{-element MIMO}} = 2 \times \log_2(1+50) = 11.344$ bits/sec/Hz. Permissible level of channel capacity is 65% of its maximum value (11.344 bits/sec/Hz) = $11.344 \times 0.65 = 7.38$ bits/sec/Hz [35]. [I] is the identity matrix, SNR is the ratio of signals of device terminal and distributed channels (independent & identical) with Rayleigh fading environment i.e. SNR = 20dB. k is the number of transmitting antenna elements. [H] is the fading matrix and [H*] is the Hermitian transpose of a fading matrix.

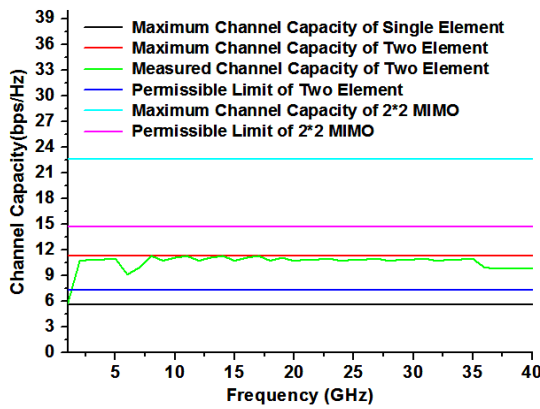


Fig.3.13. Comparison of channel capacity of 2 element antennas array with a maximum and permissible limit of a 2x2 MIMO antenna system

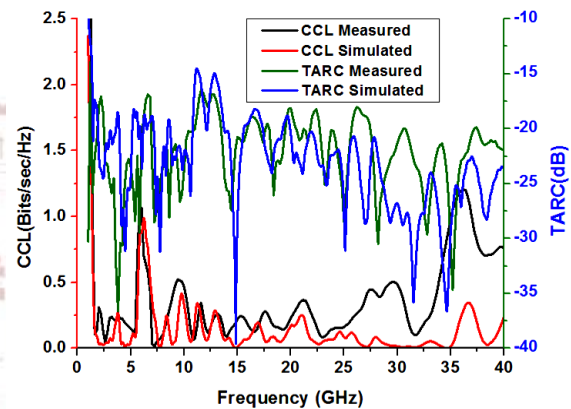


Fig.3.14. Simulated and measured results of channel capacity loss (CCL) and total active reflection coefficient (TARC) of proposed MIMO antenna

The channel capacity of the MIMO system is linearly increasing with increasing the number of elements; the element matrix properly characterizes the performance of a MIMO system as it provides the information about the phase and gain characteristic of the transmitting and receiving elements. However, in the presence of the correlation factor in MIMO antennas, the channel capacity losses are also increased. Therefore, the diversity performance of the proposed antenna is affected due to channel capacity losses. It is calculated by the Equation (3.9)

$$\text{CCL (dB)} = -\log_2 [\det (\varphi^c)] \quad (3.9)$$

Table 3.4 Simulated MEG results of proposed MIMO antenna at various frequencies

Frequency (GHz)	MEG(dB) Isotropic medium		MEG(dB) Gaussian medium	
	XPR = 1dB	XPR = 6dB	XPR = 1dB	XPR = 6dB
	1.575	-3.4	-4.7	-4.2
15	-3.1	-3.4	-3.4	-4.5
30	-3.0	-3.5	-4.3	-3.9
39	-3.0	-3.3	-3.8	-3.8

Where φ^c is 2×2 S-parameter correlation matrix $\varphi_{ii} = 1 - |S_{ii}|^2 - |S_{ij}|^2$, $\varphi_{ij} = -(S_{ii} \times S_{ij} + S_{ji} \times S_{ji})$. Fig.3.15 shows the CCLs, and it is less than 0.35bps/Hz over the entire bandwidth except for the notched band, which offers a better diversity result of the proposed MIMO antenna. In the two-port antenna system, contiguous antenna elements impinge on each other when they are working concurrently. This influences the overall desirable gain, efficiency, and bandwidth. Hence, the actual MIMO antenna system performance cannot be predicted by s-parameters only, so TARC is also calculated to account for this effect. For side by side two-port radiated antenna system, it can be evaluated by [Equation \(3.10\)](#).

$$\text{TARC} = \sqrt{\frac{(S_{ii} + S_{ij})^2 + (S_{ij} + S_{ji})^2}{2}} \quad (3.10)$$

Ideally, TARC should be less than 0dB for the MIMO antenna system. The simulated and measured TARC of the designed MIMO antenna is less than -15dB in the complete super-wideband bandwidth except for the notched band, again it shows the excellent diversity performance of a designed antenna shown in [Fig.3.14](#).

The MEG ratio for the proposed MIMO antenna is extracted by [Equation \(3.11\)](#).

$$\text{MEG}_i = \frac{P_{\text{rec}}}{P_{\text{inc}}} = \oint \left[\frac{\text{XPR} \times G_{\theta i}(\Omega) + G_{\phi i}(\Omega) \times P_{\phi}(\Omega)}{1 + \text{XPR}} \right] d\Omega \quad (3.11)$$

Where XPR is the cross-polarization ratio and $G_{\theta_i}(\Omega)$, $G_{\phi_i}(\Omega)$ & $P_{\phi}(\Omega)$ is the gain and power density functions of the incident wave, Ω is beam area. The acceptable ratio of mean effective gain of i^{th} and j^{th} antenna elements should be less than or equal to $\pm 3\text{dB}$. The MEG is also represented in isotropic and Gaussian mediums to investigate the diversity performance at XPR = 1.0dB (outdoor) and 6.0dB (indoor), as shown in Fig.3.15 and Table 3.4.

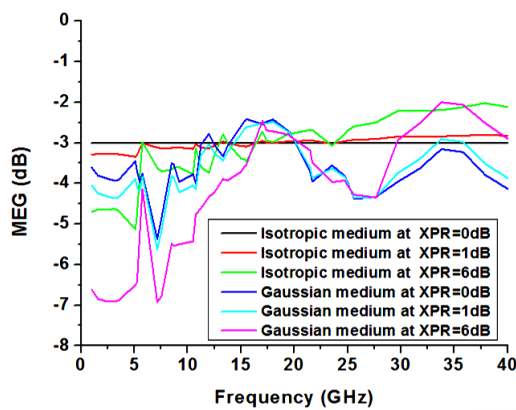


Fig.3.15. Simulated results of mean effective gain in Isotropic and Gaussian medium at different XPR values of the proposed antenna

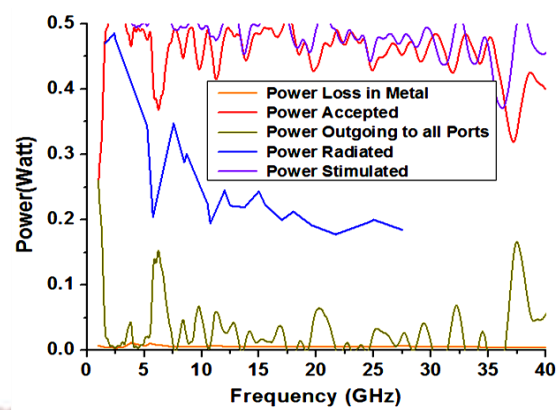


Fig.3.16. Power level of 2 elements MIMO antenna in various states

The MEG for the isotropic medium at 1.0dB XPR varies in the span of -3.4dB to -3.0dB, and at 6.0dB XPR is lying between -4.7 to -3.3dB. Similarly, the MEG for Gaussian medium at 1.0dB XPR and 6.0dB XPR is lying among -3.4dB to -4.2dB, and -6.6 to -3.8dB respectively for entire super-wideband bandwidth. From Fig.3.15, the MEG ratio of the proposed antenna is found in acceptable limits throughout the super-wideband bandwidth. Hence, it is as well a high-quality channel performance of antenna for wireless communication.

Fig.3.17 shows the power loss, power accepted, power outgoing to all ports, power radiated, and the proposed MIMO antenna for SAR calculations [34]. 0.5W stimulated power is used to calculate the diversity performance parameters. Power loss in metal is very less in mW order, so most of the power is radiated. Power accepted is almost the same as input power or stimulated power except for the notched band because, in that band, maximum power returns to the same ports. The radiated power is high in the super-wideband range except for the notch band. The radiated power is always less than stimulated and accepted power because of dielectric,

conductor, and surface wave loss in a microstrip line. Power going to all ports is highly interfere at notched-band (5.9-6.9GHz) due to the correlation shown in Fig.3.16.

Table 3.5 Comparison of designed SWB-MIMO antenna with existing references in various aspects

Antenna Size (mm ²)	Impedance B.W.(GHz)	Isolation (dB)	ECC	Max.Gain (dBi)
54×54 [26]	3.1-40	20	0.5	7.5
27.4×27.4 [29]	1.25-40	18	0.01	4
40×47[30]	1.3-40	20	0.02	3.6
58×58 [31]	2.9-40	17	0.04	13.5
33×26 [32]	1.3-40	20	0.01	5.8
20×36 [33]	1.21-34	20	0.25	3.5
55.6×50.5[Proposed]	1.5-40	20	0.005	7.5

It is noted from Table 3.5 and 3.6 that the designed antenna achieves better results in comparison with the referred MIMO antennas at various specifications, which is highly appreciable as the designed antenna is small in size with super-wideband impedance bandwidth. Group delay (ns) is also calculated to verify the time-domain characteristic of the MIMO antenna. The two identical antennas are aligned in front of each other as a receiver and transmitter kept 100cm apart to obtain group delay deviation. It is found to be almost constant in the super-wideband bandwidth, excluding the notched band.

Table 3.6 Comparison of SAR and CCL of designed SWB-MIMO antenna with existing references

Frequency (GHz)	Specific Absorption Rate (SAR)		Channel Capacity Loss (CCL)	
	1g (W/Kg)	10g (W/Kg)	Frequency (GHz)	CCL (bps/Hz)
3.45,5.8	0.246,0.122	0.124, 0.045 [132]	8-18	0.35 [135]
3.1,3.4,4.0	0.8,0.9,1.2	0.6,0.8, 0.8 [133]	0.95–6.13	0.50 [136]
3.4	0.0368	0.0138 [134]	3.08-10.98	0.35 [133]
1.575,3.4, 5.5	0.041,0.048, 0.053	0.021,0.026, 0.032 [P]	1.5-40	0.35 [P]

Table-3.7 shows the comparison of different decoupling techniques including the proposed one and concludes that Mushroom-shaped EBG including E-shaped decoupling structures provides greater than 20dB isolation in the SWB range (1.5-40GHz).

Table 3.7 Performance comparison of the decoupling techniques over the proposed design

Isolation Level (dB)/Refs	Isolation Techniques	Advantages	Disadvantages
16 [2]	Fractal Slots	Improved isolation and FBR	Complex structure with narrow bandwidth
15 [4]	T-shaped	Improved isolation	Limited to UWB only
15 [14]	Rectangular slits	Improved ECC, DG, MEG	Up to 6GHz only Poor isolation at low frequency (>2GHz)
20 [18]	F-shaped decoupling structure	Good isolation for UWB bandwidth	
20 [19]	EBG WITH FSS, Double-layer EBG, Mushroom-shaped EBG	Improved isolation, increased diversity gain	Complex geometry
24 [20]	Funnel-shaped decoupling	Provided good isolation for 173% bandwidth	Large in size
20 [21]	Defected Ground Structure (DGS)	Improved isolation at a lower frequency, compact structure	Complex structure
15 [22]	Complimentary Split-Ring Resonator (CSRR)	Compact structure and high isolation bandwidth	Limited to a wideband bandwidth
20 [25]	Flag-shaped stub on the ground plane	Good isolation for dual-band	Complex structure for the wideband only
20 [P]	Mushroom-shaped EBG including E-shaped decoupling structure	Improved isolation for 1-40GHz bandwidth with reduced cross-polarization	Complex structure

3.5 SUMMARY:

In this **Chapter**, A step impedance microstrip feed line structure is introduced to achieve a super-wideband impedance bandwidth (1.5-40GHz) of 185%. This antenna is designed to be circularly polarized at 1.575GHz (L₁-band) and 26.0GHz (K-band) by using a closed ring resonator on the radiating patch. The EBG structures improve FBR in lower (1.5-5GHz) and higher band (25-35GHz). The proposed antenna is designed with a compact size of 55.6×50.5×1.6mm³ on the FR-4 substrate, including exotic diversity performance. This MIMO antenna is suitable for defence and handheld devices covering GPS/ DCS/ PCS/ UMTS/ Wi-BRO/ ISM/ IRNSS/ LTE (M/HB)/ BLUETOOTH/ IoT/ WiMAX/ X/ Ku/ K/ Ka-band and it is also suitable for 5G (sub-6GHz/mm) applications with channel capacity of 11.34bps/Hz. Simulated results of MIMO antenna like radiated power based ECC and diversity parameters are also verified experimentally, which are in the acceptable range. Finally, this antenna is tested in a realistic environment for the

SAR application. A dual-band circularly polarized two-element MIMO antenna with band-notch characteristic has been evaluated for super-wideband applications having 20dB isolation. All simulated results of antenna have been verified with measured results to the entire impedance bandwidth, including the notched-band (5.9-7.1GHz), which mitigates the interference from E-S satellite communication. The antenna achieved 7.6dBi peak gain, including stable omnidirectional radiation patterns with excellent ECC, less than 0.005. The antenna's SAR performance is also demonstrated under the permissible limits, and the average channel capacity is 11.34bps/Hz. The performance of the proposed antenna proved that it is a good candidate in various portable wireless applications.



CHAPTER-4

HIGH ISOLATION MIMO ANTENNA FOR MULTIBAND APPLICATIONS

4.1 INTRODUCTION

Recently numerous wireless communication standards and protocols working at different frequencies have been developed and deployed worldwide. To meet the needs of all these services simultaneously, antennas in mobile phones and other wireless services that can cover multiple frequency bands are in increasing demand. This requirement is fulfilled by multiband MIMO antennas. The main advantage of multiband antennas is a small size, avoid interference from other bands, simple to integrate, and low cost.

The MIMO-communication system that uses numerous antennas on the transmitter as well as receiver ends, as shown in Fig. 4.1, fulfills the demand for enhanced channel capacity along with a high data rate. MIMO antenna improves the reliability and multi-path fading issues of the wireless communication systems, where signals may come together at the same time or different at the receiver end.

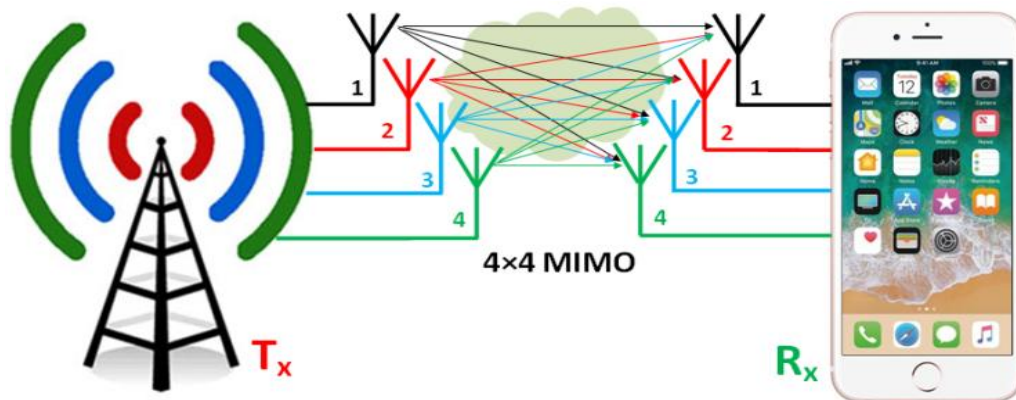


Fig.4.1. A pictorial representation of the 4x4 MIMO antenna transceiver system

In this **Chapter**, a compact multiband dual-polarized, meander line-shaped Penta-band (2.16-2.28, 2.38-2.42, 2.59-2.72, 3.10-3.32, 3.38-3.46 GHz) 4-elements multiple-input-multiple-output (MIMO) antenna is presented. A multiband characteristic is attained by introducing a L-shaped meander line as antenna radiators. Furthermore, four semi-circle-shaped slots and L-shaped stubs are introduced in the ground plane to improve isolation which is required for improving diversity performance. Radiation patterns of this antenna have shown the RHCP at port-1 & 3 and LHCP at port-2 & 4 at frequencies 2.2, 2.4GHz, which is widely used for MSS and IoT applications. This antenna is designed and fabricated with a compact size of $50 \times 70 \times 1.6 \text{ mm}^3$ on the FR-4 substrate with good diversity performance in pentaband. Simulated results of antenna-like return loss, isolation, and parameters related diversity have also tested experimentally in a controlled environment, which is within the permissible limit. The designed antenna will be appropriate for Mobile satellite services (MSS), ISM, Broadband Radio Services (BRS), Educational Broadband Services (EBS), WiMAX, Radio Location Services, and Amateur Radio Services respectively. Meanwhile, SAR of the designed antenna has been examined in an empirical environment for the Fresnel radiating near field applications. In section 4.2, an antenna design procedure is explained step by step for multiband characteristics with dual-band circular polarization. Section 4.3 demonstrates the antenna results like impedance bandwidth, isolation, gain, antenna radiation efficiency, and axial ratio, etc. Section 4.4 shows the results of the diversity performance like ECC, DG, TARC, CCL, and channel capacity of the antenna. The summary of this **Chapter** is discussed in section 4.5. This multi-band MIMO antenna has been simulated using a CST-microwave studio.

4.2.Design Procedure OF Mimo Antenna :

The geometrical design steps of the proposed pentaband antenna are represented in **Fig. 4.2(a)** along with its simulated return loss. Antenna-1 exhibits unacceptable return loss in intended bands, therefore to achieve anticipated bands, a meander line of optimized length is introduced in Antenna-

2. The results of Antenna-2 are somehow depicted pentaband characteristics with very poor return loss as shown in Fig.4.2 (b). To improve the return loss in requisite bands, a semi-circular shaped-slot is etched in a partial ground plane as shown in Antenna-3 and an L-shaped matching stub is also attached to the feeding line to improve input impedance as given in antenna-4. Hence, the requisite pentaband result is achieved by a very compact meandering antenna because the meander line is used for antenna size reduction. This antenna is made from continuously folded planar wire intended to reduce the resonant length. The meander line antenna tends to resonate at frequencies much lower than an ordinary antenna of equal length.

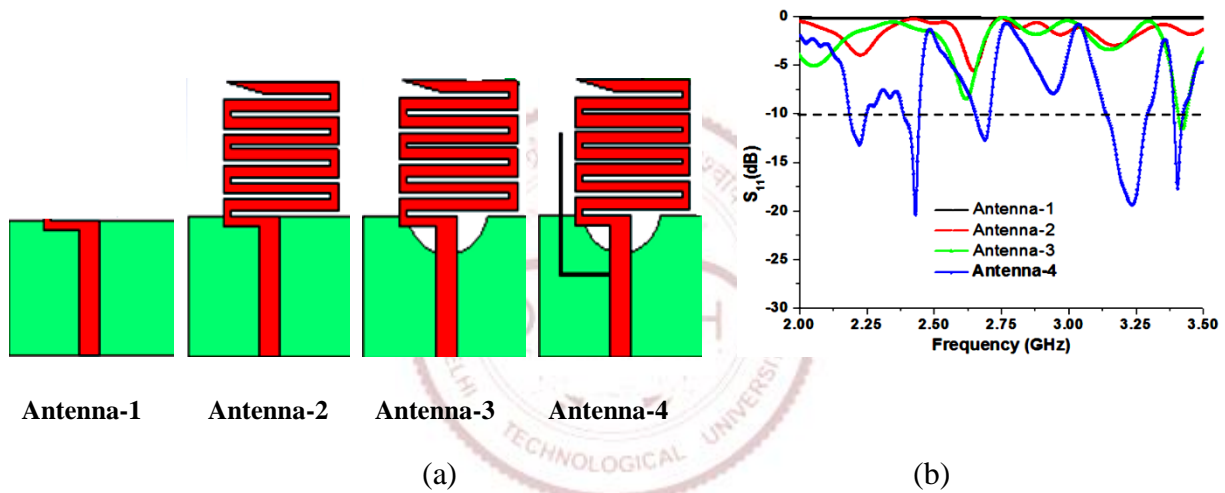
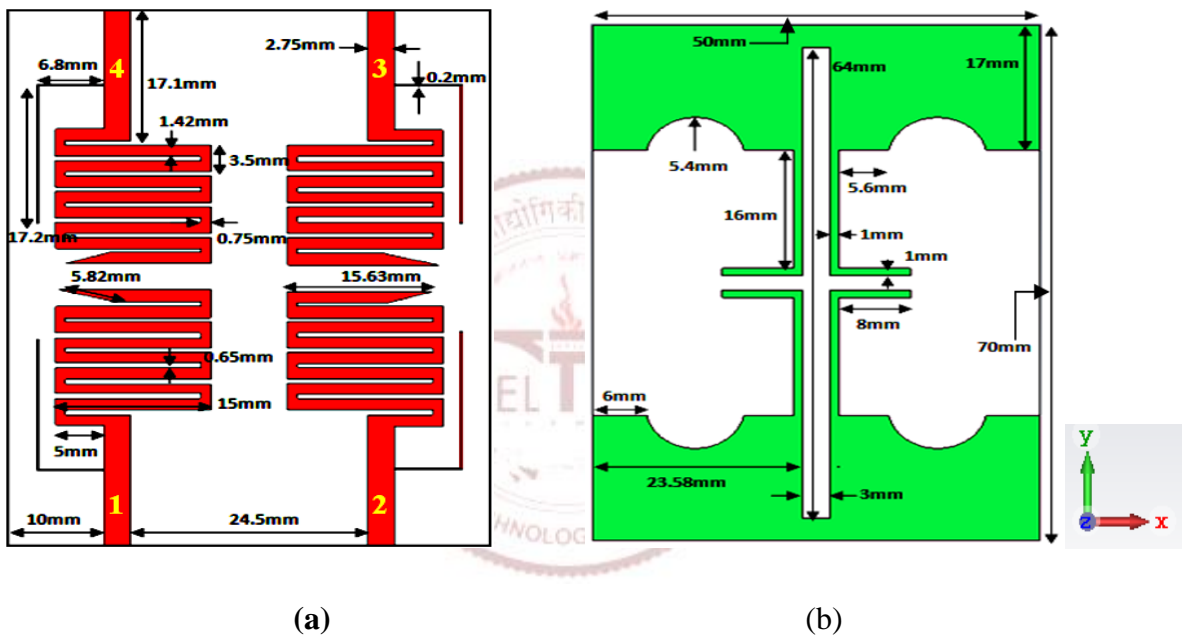


Fig.4.2. Proposed pentaband antenna (a) Step-by-step geometrical design procedure (b) Simulated return loss

The fundamental resonance frequency (f_{res}) of a meander-shaped monopole antenna is $= c/(2 \times L \times \sqrt{\epsilon_r})$ where, L is the length of the meandering antenna, and c is the velocity of light (3×10^8 m/sec) in free space. Therefore, the first, second, third, fourth and fifth resonating frequencies are 2.2, 2.4, 2.6, 3.2, and 3.4GHz at corresponding meander length of antenna 32.50, 29.73, 27.5, 22.34, 21.03mm respectively. Later on, the proposed antenna design is used for the 4-elements MIMO antenna with a suitable isolation mechanism. The proposed pentaband MIMO-antenna is fabricated by photolithography methods on the FR4 substrate with relative permittivity (ϵ_r) of 4.4 having loss

tangent 0.002 and substrate height (h) of 1.6mm. The overall dimension of the MIMO antenna (front and bottom) is 50mm×70mm as shown in Fig.4.3 (a)-(b). The proposed antenna has exhibited circular polarization in two-bands (2.2GHz and 2.4GHz) due to a ramp-shaped cut at the end of a meandering patch. This MIMO antenna also has dual-polarization (RH/LH) owing to the mirror image of antennas- 1 & 2 and 3 & 4 respectively. Therefore, Antennas 1 or 3 shows right-handed (RH) circular polarization, and antennas 2 or 4 shows left-handed (LH) circular polarization as shown in Fig.4.3 (a).



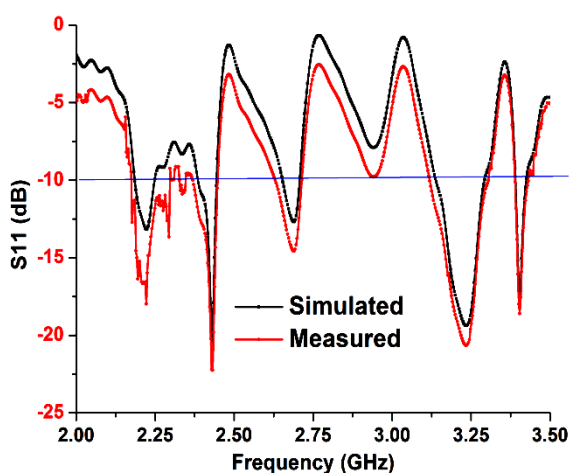
(b) Fig.4.3. The geometry of 4-element MIMO antenna including physical dimensions (a) Front view

(b) Bottom view

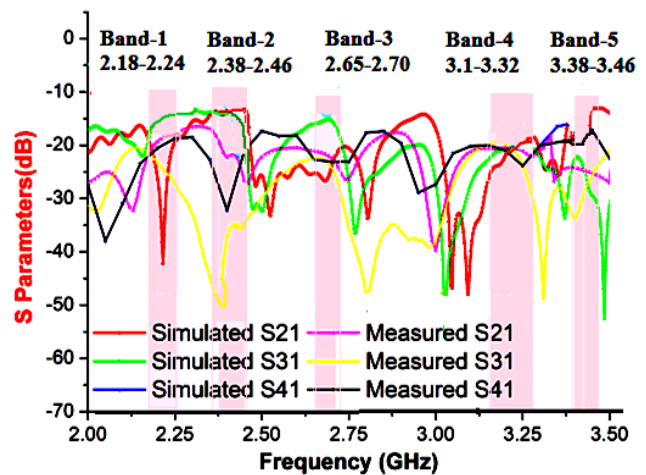
Mutual coupling happens due to the proximity of adjacent antenna elements with the energized element because the surface current is captured by adjacent antennas. A new isolation mechanism is proposed to encounter this problem in the proposed 4-elements antenna. It is found that low surface current density distribution on antennas 2, 3, and 4 when antenna 1 is excited due to the inverted L-shaped decoupling mechanism in the ground plane. Means, the migration of surface current between 4-elements is reduced.

4.3 DISCUSSION OF RESULTS

Results of the proposed pentaband antenna like return loss, isolation, peak gain, axial ratio, and radiation efficiency are represented in Fig.4.4 (a) to 4.4(d). The values of return loss in requisite bands are greater than 10dB and have a better agreement between simulated and measured results as depicted in Fig.4.4 (a). From Fig.4.4 (b), Isolation between the antenna elements is greater than permissible value, for this reason, the antenna exhibits a better diversity performance and it is also observed that the isolation between antenna 1 and 2 is high at 2.25GHz; because the inverted L-shaped stub structure in the ground plane is tuned at the same frequency. The axial ratio of the proposed MIMO antenna at 2.2 and 2.4GHz frequencies are less than 3dB which indicates that the antenna is circularly polarized at the above-mentioned frequencies as shown in Fig.4.4(c). A circularly polarized antenna is essentially important for mobile and vehicular devices to receive power in every orientation for establishing the desired communication link. Hence, the dual-band circular polarization of this antenna is useful for MSS & IoT applications. Gain and radiation efficiency of the antenna is depicted in Fig.4.4 (d) and radiation efficiency is almost greater than 70% in all indispensable bands.



(a)



(b)

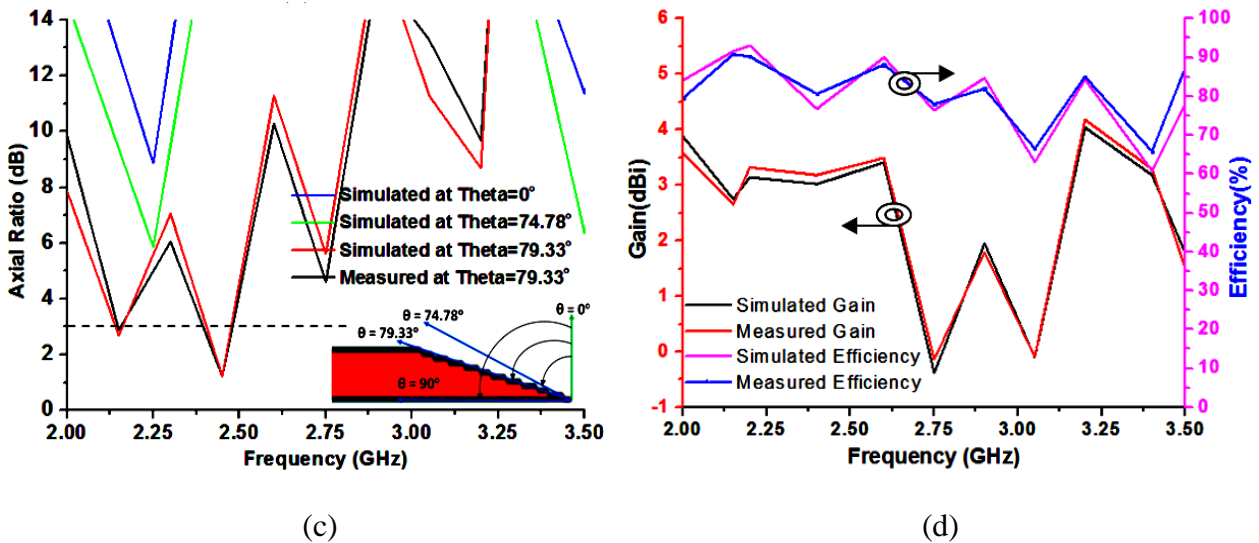
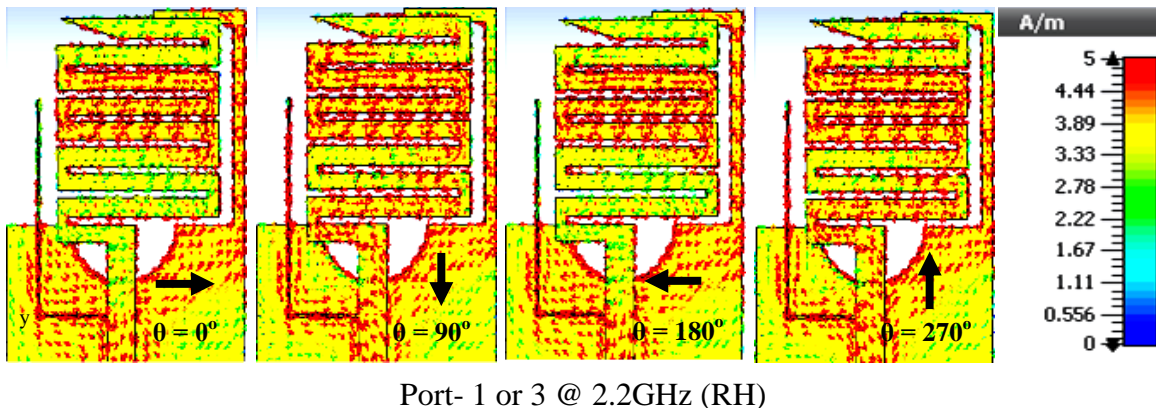


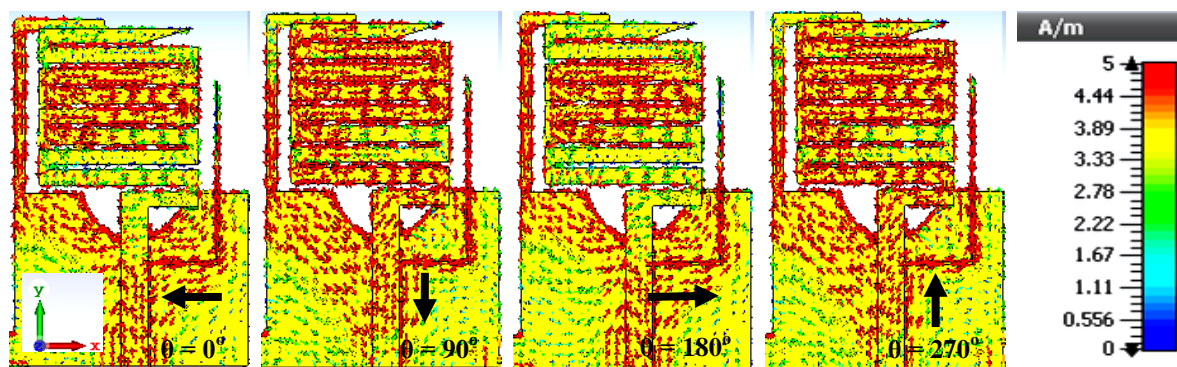
Fig.4.4. Simulated and measured results of the proposed antenna in terms of (a) S_{11} (b) S_{21} , S_{31} , S_{41} (c)

Axial ratio (d) Gain and radiation efficiency

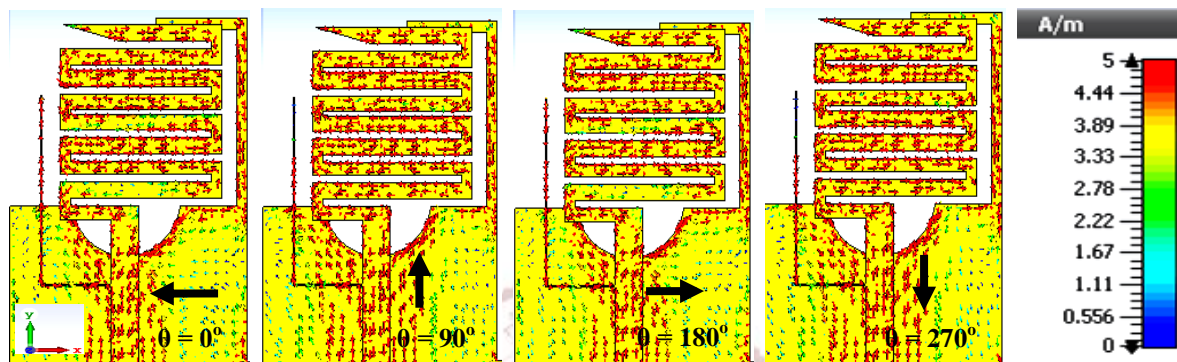
The distribution of the current density (A/m) at 2.2 and 2.4GHz frequency is rotating clockwise indicating by an arrow when at port 1 or 3 has excitation which indicates right-handed (RH) circular polarization of antennas. Similarly, when port 2 or 4 has excitation, The distribution of the current density is rotating anti-clockwise which indicates left-handed (LH) circular polarization of antennas as shown in Fig.4.5 (a). The simulated electric fields (V/m) of an antenna at 2.2, 2.4, 2.6, 3.2, 3.4GHz frequencies are represented in Fig.4.5 (b). Electric-field distribution over the single element provides better insight to understand which portion of the meandering line contributes to the specific bands and it is observed that at a lower frequency (2.2GHz) electric field cover the entire length of the meandering line.



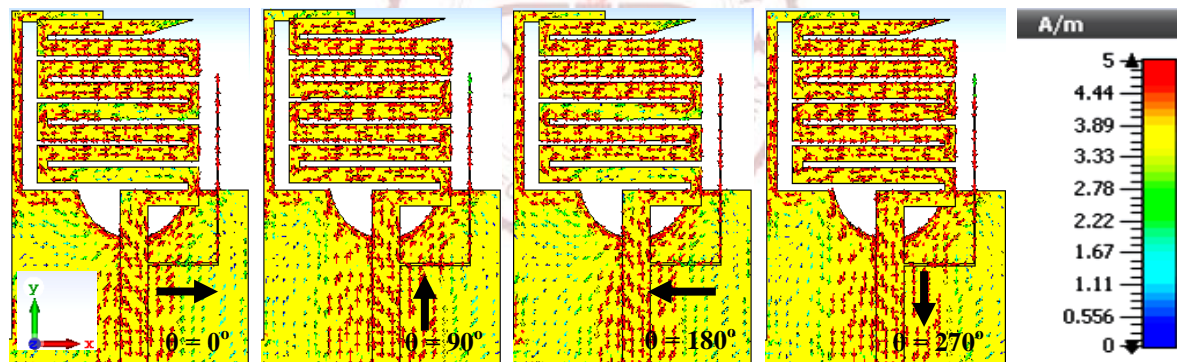
Port- 1 or 3 @ 2.2GHz (RH)



Port- 2 or 4 @ 2.2GHz (LH)

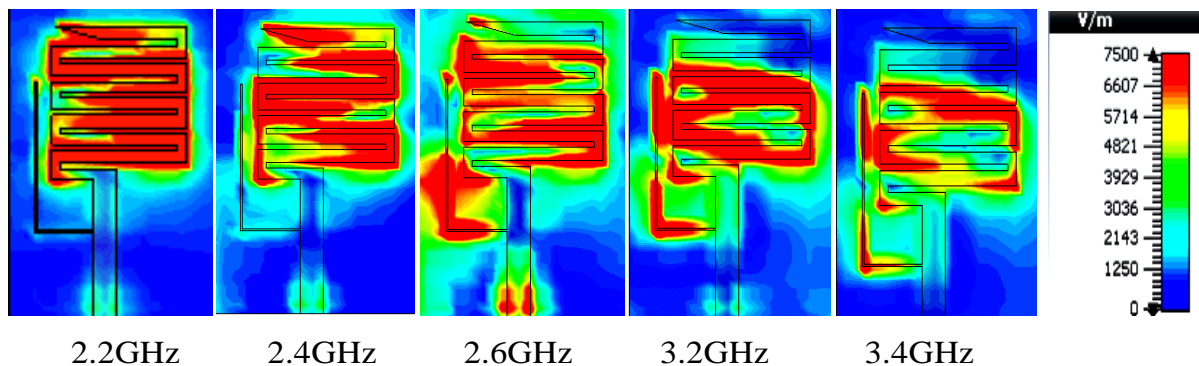


Port- 1 or 3 @ 2.4GHz (RH)



Port- 2 or 4 @ 2.4GHz (LH)

(a)



(b)

Fig.4.5. Current density and Electric field distribution at (a) 2.2, 2.4 GHz frequency for RHCP/LHCP (b) 2.2, 2.4, 2.6, 3.2, 3.4GHz when antenna 1 is energized and remaining antennas are terminated with matched 50Ω load

Therefore, the first, second, third, fourth, and fifth resonating frequencies are 2.2, 2.4, 2.6, 3.2, and 3.4GHz at corresponding meander length of antenna 32.50, 29.73, 27.50, 22.34, 21.03mm respectively. 3D radiation patterns are the spatial distribution of the electromagnetic field radiated from the transmitting antennas in vertical and horizontal planes as shown in Fig.4.6 (a), where the maximum radiation intensity of an antenna is observed in ± z-direction at intended frequencies.

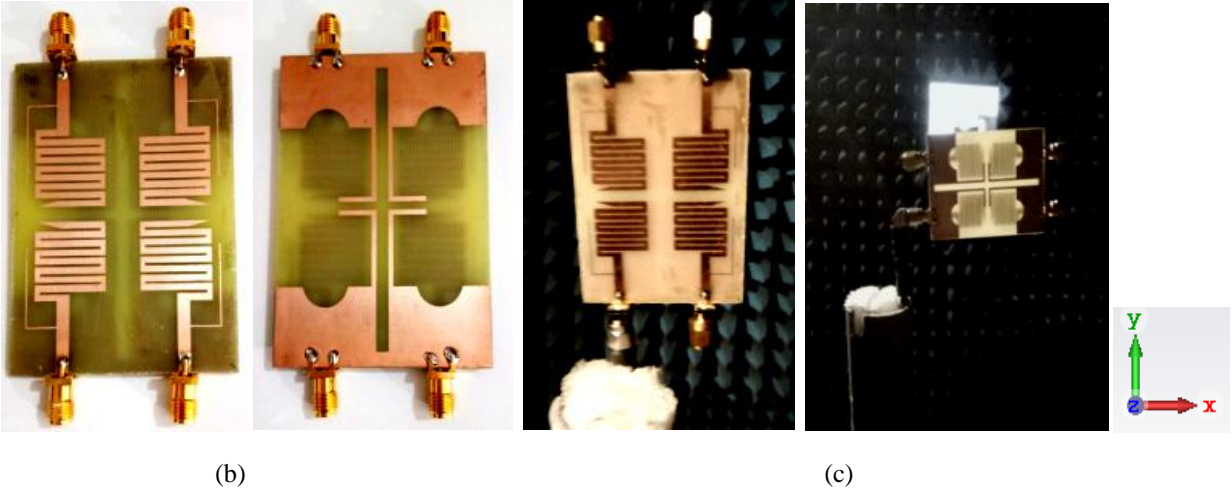
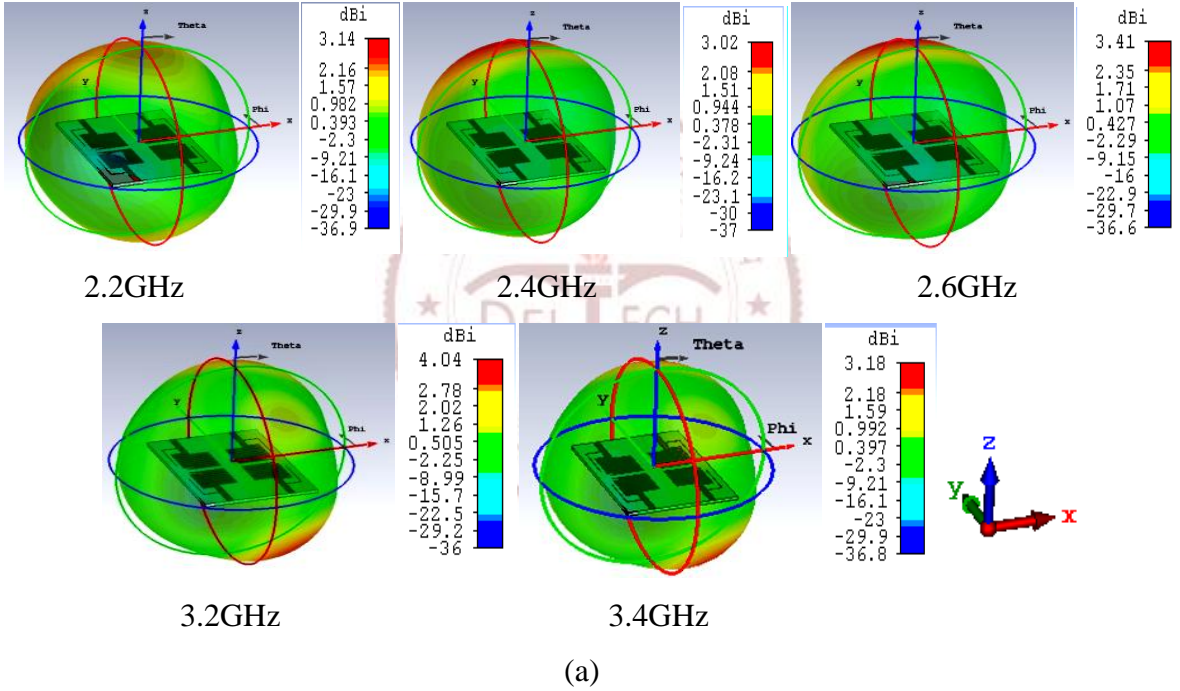


Fig.4.6. 3D radiation pattern of designed MIMO antenna at (a) 2.2, 2.4, 2.6, 3.2, & 3.4GHz when antenna-1 is excited only (b) Top and bottom view of a prototype (c) Antenna under test-AUT for radiation pattern measurement in the anechoic chamber

This MIMO antenna is fabricated on the FR4 substrate using double-sided 35 μ m copper peel by the double beam photolithography technique as exhibited in Fig.4.6 (b). The radiation performance of the antenna is also tested in an anechoic chamber associated with Vector Network Analyzer (VNA) as depicted in Fig.4.6 (c).

The radiation pattern in E and H-plane of the MIMO antenna is presented for pentaband applications in Fig.4.7. Co & cross-polarization of the antenna- 1 is simulated and measured when antennas- 2, 3, and 4 are terminated with a 50 Ω matched load. Fig.4.7 represents the measured & simulated radiation patterns of the proposed antenna at frequencies 2.2, 2.4, 2.6, 3.2, and 3.4GHz respectively in E-plane (yz) and H-plane (xz) within the satisfactory range.

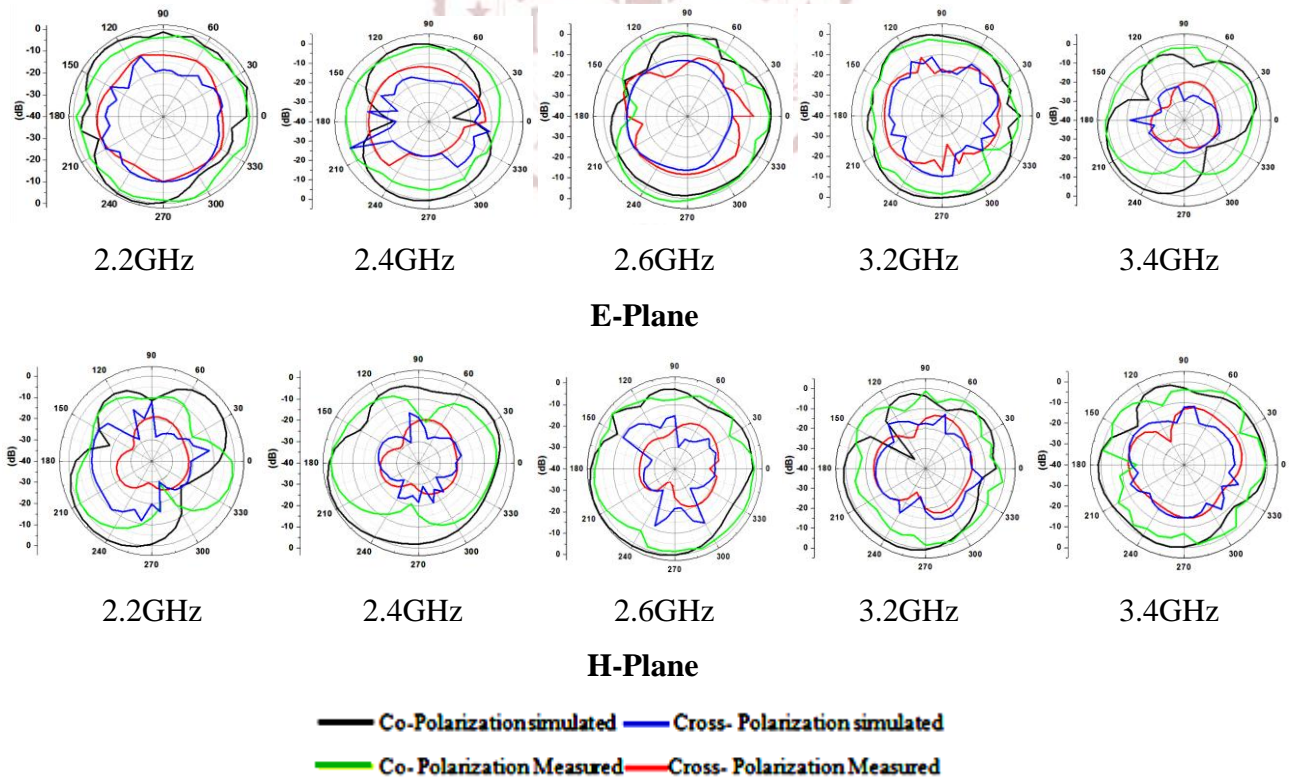


Fig.4.7. Simulated & measured 2D radiation patterns at 2.2, 2.4, 2.6, 3.2, and 3.4GHz for *E*-plane and *H*-plane, antenna-1 is energized and rests of antennas are terminated by a matched load

Here, authors have considered the right-hand polarization results at CST Microwave Studio as Co-polarization and left-hand polarization as Cross-polarization for E/H plane radiation patterns, and the same has been considered for measurement data also. It is noted that for the intended pentaband, the patterns are partially Omni-directional at $\Phi = 0^\circ$ (*H*-plane) and monopole like at $\Phi = 90^\circ$ (*E*-plane) and Co and Cross polarization level are well separated (i.e. 20dB) with each other.

Specific Absorption Rate: “the power absorbed per unit mass of tissue”, it is a vital component of an antenna when the antenna is used in near field applications of wireless communication. Radiated electromagnetic (EM) energy is absorbed by the human body as represented in Fig.4.8. SAR is generally calculated on a small bio tissue (usually 1gm or 10gm) or the entire body [34]. Furthermore, SAR estimation on the head for the proposed antenna at 2.2, 2.4, 2.6, 3.2, and 3.4GHz frequencies are represented in Table-4.1. For the assessment of SAR, the values of the thickness of the brain, bone, and skin are 66, 76, and 79.32mm respectively.

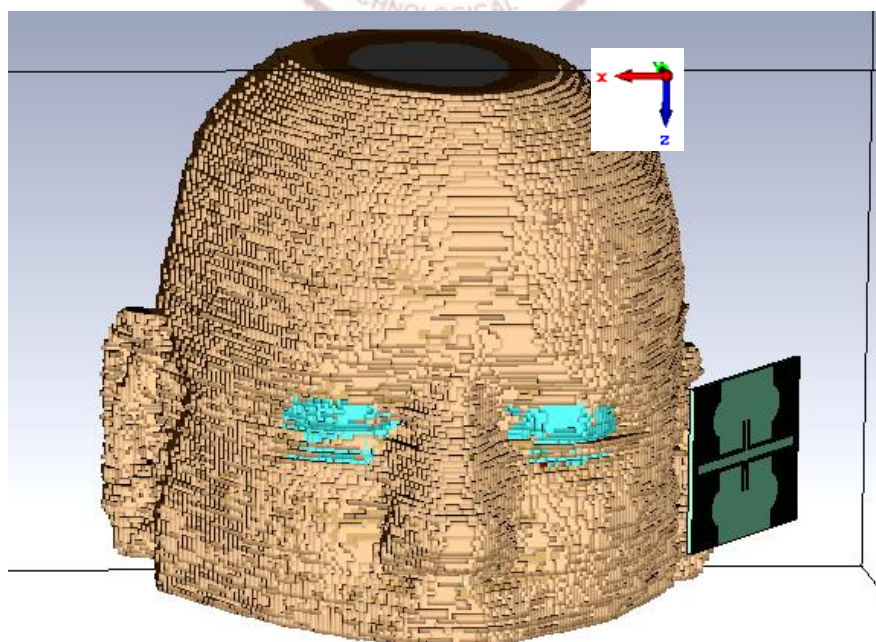


Fig.4.8. Specific absorption rate calculation of the designed MIMO antenna near the human head at a distance of 6mm

The simulated value of SAR for 1gm and 10gm of bio-tissue of the head is less than the permissible limit (i.e. 1.6W/kg) for the designed MIMO antenna as exhibited in Table-4.1 corresponding to all parameters scheduled in Table-4.2. The SAR results are calculated by CST microwave studio without any plastic-jacket or dielectric cover.

Table 4.1 Simulated SAR at resonant frequencies for the human head at a 6mm distance

Specific Absorption Rate (W/kg)									
2.2GHz		2.4GHz		2.6GHz		3.2GHz		3.4GHz	
1(g)	10(g)	1(g)	10(g)	1(g)	10(g)	1(g)	10(g)	1(g)	10(g)
1.08	0.98	1.10	1.17	1.13	1.23	1.16	1.27	1.19	1.29

Table 4.2 Parameters of the bio tissues for skin, bone, and brain used for calculation of SAR of MIMO antenna with constant permeability

Type Bio-tissue	Metabolism Rate W/m ³	Density (ρ) kg/m ³	Blood Flow W/K/m ³	Heat Capacity kJ/K/kg	Thermal Conductivity (σ) S/m
Brain	7100	1030	40000	3.675	1.13
Bone	610	1850	3400	1.30	0.41
Skin	1620	1100	9100	3.50	0.293

4.4 MIMO ANTENNA DIVERSITY PERFORMANCE:

The designed MIMO antenna diversity performance is examined in terms of various parameters like envelope correlation coefficient (ECC), multiplexing efficiency, channel capacity, channel capacity loss (CCL), and mean effective gain (MEG).

Envelope Correlation Coefficient: ECC is one of the diversity parameters to investigate the performance of the MIMO antenna system for wireless applications which shows how much antennas are correlated to each other.

The calculated and measured value of ECC between two antenna elements of a designed 4-elements antenna by S-parameters and radiated fields in all prescribed bands are observed less than 0.1 as exhibited in Fig.4.9 (a)-(b) respectively. Hence, This MIMO antenna shows less correlation between the two antennas in the MIMO system and gets excellent diversity performance.

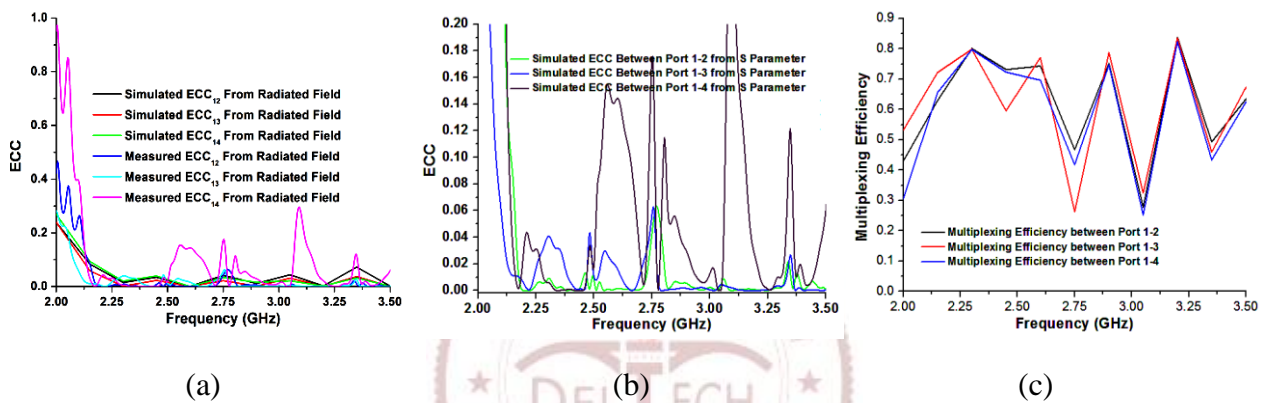


Fig.4.9. Measured and simulated results of the proposed MIMO antenna (a) Envelope correlation coefficient from radiated fields (b) Envelope correlation coefficient from S-parameters (c) Multiplexing efficiency

Directive gain: DG is also an important parameter of the MIMO antenna system. The diversity gain (DG) is an increment of signal-to-interference ratio due to some diversity scheme or to reduce the transmission power by using this scheme without compromising the performance of an antenna. Directive gain is depending on cross-correlation between the transmitted signals from the adjacent antennas and the relative mean power level. The calculated values of diversity gain in all intended bands are more than 9.8dB.

Multiplexing Efficiency: The main feature of multiplexing efficiency is to shows the correlation and efficiency imbalance between MIMO antennas used in a wireless system.

Hence, the values of total and multiplexing efficiency are more than (50%) and the value of efficiency goes down at the unintended bands as shown in Fig.4.9 (c).

Channel Capacity: Channel capacity of the MIMO antenna is investigate to know the data rate which is dependent on bandwidth and SNR (signal-to-noise ratio). The channel capacity of the 4-element pentaband MIMO antenna is verified with the average channel capacity of the standard MIMO system. The minimum and maximum threshold level of channel capacity of the 4-element antenna is varying between 14.85-22.68bps/Hz at 20dB SNR in a uniform environment as shown in Fig.4.10 (a).

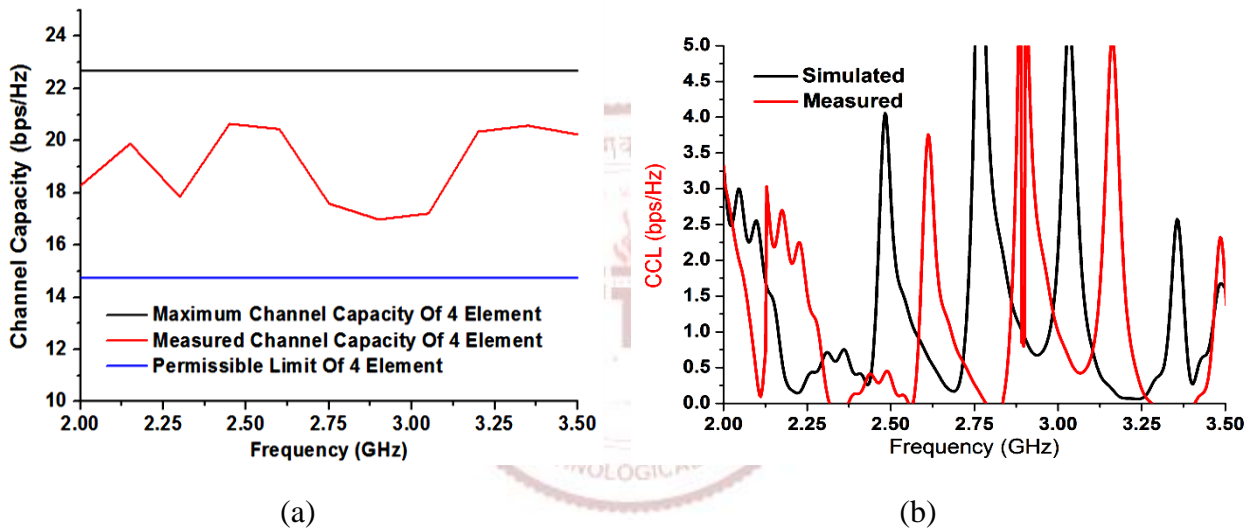


Fig.4.10. The proposed 4-element antenna (a) Calculated average channel capacity (b) Simulated and measured results of channel capacity loss

The value of SNR for the calculation of channel capacity is 20dB. Maximum channel capacity of the 4-element MIMO antenna system is 22.68bits/sec/Hz but the permissible limit is 65-70% of its maximum value ($22.68 \times 0.65 = 14.74$ bits/sec/Hz) [35]. The main factor behind the use of the MIMO antenna is to get an enhanced channel capacity at an appropriate level. However, the channel capacity of a wireless communication system is also dependent on the number of antenna elements used in the system and the correlation between antenna elements. Means, channel capacity will be increased with an increase of un-correlation between antenna elements.

Channel Capacity Loss: CCL is also related to the amount of correlation between antenna elements used in the MIMO system. The value simulated and measured CCL are below the prescribed (0.5bits/sec/Hz) limit for intended Penta-bands as shown in Fig.4.10 (b). CCL of the proposed multiband MIMO antenna is less than 0.35bps/Hz over the intended bands, which indicate a good diversity performance of the proposed pentaband MIMO antenna.

Total Active Reflection Coefficient: In a 4-port antenna system, adjacent antenna elements interrupt each other when they are excited at the same instant. This type of interruption affects the antenna performance parameters like overall gain, efficiency, and bandwidth of multi-band. Therefore, the actual performance of the MIMO antenna system will not be extracted by scattering-parameters only, it will also by the total active reflection coefficient (TARC). It is defined as “the square root of the sum of all incident powers at the ports minus radiation power, divided by the sum of all incident powers at the ports the TARC of the proposed 4-element MIMO system is calculated by Equation (4.1)-(4.3).

$$(\text{TARC}) \Gamma_A^t = \frac{\sum_{n=1}^N |b_n|^2}{\sum_{n=1}^N |a_n|^2} = \sqrt{\frac{(S_{11} + S_{22})^2 + (S_{22} + S_{33})^2}{n}} \quad (4.1)$$

Where a_i and b_i is an incident and reflected electromagnetic wave respectively and n denotes the number of antenna elements used in the MIMO system at transmitting or receiving ends.

$$[b] = [S][a] \quad (4.2)$$

Where $[S]$, $[a]$ and $[b]$ are scattering, incident, and reflected matrix of 4-port multiband MIMO antenna, respectively.

$$\begin{bmatrix} b_1 \\ b_2 \\ b_3 \\ b_4 \end{bmatrix} = \begin{bmatrix} S_{11} & S_{12} & S_{13} & S_{14} \\ S_{21} & S_{22} & S_{23} & S_{24} \\ S_{31} & S_{32} & S_{33} & S_{34} \\ S_{41} & S_{42} & S_{43} & S_{44} \end{bmatrix} \begin{bmatrix} a_1 \\ a_2 \\ a_3 \\ a_4 \end{bmatrix} \quad (4.3)$$

In general, TARC should be less than 0dB for better MIMO antenna performance, and TARC of the fabricated and simulated proposed MIMO antenna is less than -40dB in the intended bands. Hence, the designed antenna is depicted as the good diversity criteria for a MIMO wireless communication system.

Mean Effective Gain: MEG is an important parameter to investigate the diversity performance of the MIMO antenna it gives information about how much received mean power when input power is fed along the same route. The acceptable mean effective gain of i^{th} and j^{th} antenna elements is $\leq -3\text{dB}$.

The mean effective gain is calculated for the proposed antenna based on three propagation models where XPR has different values as 0dB, 1.0dB, and 6.0dB for isotropic, outdoor, and indoor with different mediums like Isotropic, Gaussian, and Laplacian as shown in Table 4.3 and Fig.4.11. The MEG of the proposed antenna is fall within the permissible limit ($\leq \pm 3\text{dB}$) for all bands. Hence, the proposed antenna has high-quality channel performance which applies to wireless communication.

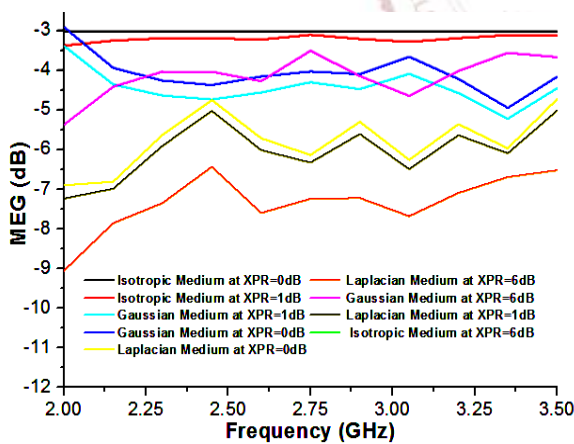


Fig.4.11. Simulated results of mean effective gain of the proposed antenna in Isotropic, Laplacian, and Gaussian medium for indoor and outdoor values

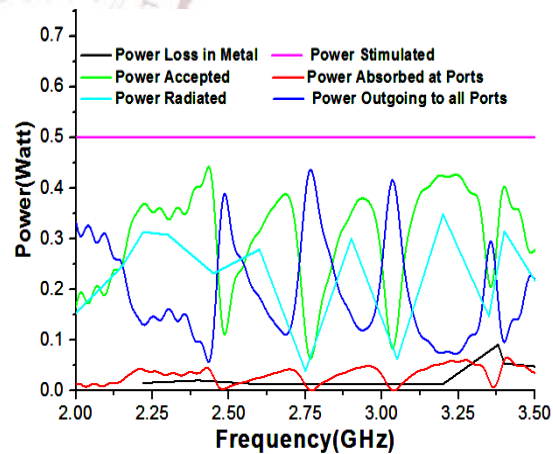


Fig.4.12. Power levels of the designed MIMO antenna in various states as power loss, power stimulated, power accepted, and power radiated, power absorbed, and power outgoing

Table 4.3 Simulated MEG results of pentaband MIMO antenna at various XPR and frequencies

Frequency (GHz)	MEG (dB) Laplacian medium		MEG (dB) Gaussian medium	
	XPR = 1dB	XPR = 6dB	XPR = 1dB	XPR = 6dB
	2.2	-6.9	-7.8	-4.5
2.4	-5.5	-7.3	-4.8	-4.1
2.6	-6.2	-7.6	-4.9	-4.5
3.2	-6.4	-7.1	-5.1	-2.8
3.4	-5.9	-6.8	-5.0	-3.8

The various power levels in terms of power loss, power accepted, power outgoing to all ports, and power radiated by the proposed antenna has been examined for SAR calculation as shown in Fig.4.12. Here, 0.5W stimulated power is used for the calculation of all powers and diversity parameters. In the proposed antenna, most of the power is radiated because this antenna has minimum power loss in intended bands. Power accepted is almost equal to stimulated power except unintended bands due to poor return loss means power returns back to the same ports. The radiated power is less than stimulated power because dielectric, conductor, and surface wave losses are associated with the proposed antenna. Powers going to all ports are highly interfere at other than the intended bands because at unintended bands most of the power is correlated between ports and power at the ports will not reach the antenna for radiation. Table-4.4 shows the comparison of the performance of the pentaband MIMO antenna with existing multiband MIMO antennas at diverse parameters. So, it is observed from Table-4.4 that the proposed antenna is having good radiation efficiency, ECC, and CCL including dual-band circular polarization characteristics. A lower value of ECC & CCL provides better channel capacity and less outage probability and circular polarization in two-band is applicable to immune the noise, produced due to Faraday rotation when the radiated field passes through the ionosphere

layer. Hence, the proposed MIMO antenna provides better performance in comparison with the existing references.

Table 4.4 Comparison of the performance of pentaband MIMO antenna with existing multiband MIMO antennas at diverse parameters

Size(m ²)	Frequency (GHz)	Efficiency	Max.Gain (dBi)	ECC	CCL (bits/sec/Hz)	CP Band	No. of Antenna Elements	DG (dB)	Isolation(dB)/References
90×60	0.81-0.97,1.36-2.8,3.4-3.75 (at 6dB)	0.5-0.75	-	0.15	0.5	-	2	9.75	13 [37]
125×75	0.75-0.96,1.7-3.60, (at 6dB)	0.75	4	0.5	0.35	-	4	9.80	15 [40]
60×70	1.9,2.9,3.2,5.0,5.6,7.74 (at 10dB)	0.7	8.69	0.02	0.30	-	2	9.57	20 [41]
60×70	0.89-0.97,1.88-1.98,2.2-2.4,2.5-2.9 (at 10dB)	0.73	2.8	0.01	0.35	-	2	9.75	15 [46]
60×40	2.3-2.6,3.3-3.8,5.7-5.85 (at 10dB)	-	3.6	0.04	0.34	-	2	9.80	40 [47]
115×65	1.90-3.21,3.51-3.71,25.7-30.5 (at 10dB)	0.7-0.8	9.9	0.16	0.35	2	6	9.85	15 [48]
50×70	2.18-2.24,2.38-2.46,2.65-2.70,3.10-3.32,3.38-3.46 (at 10dB)	0.81-0.95	4.04	0.005	0.35	2	4	9.90	17 [P]

Different isolation improving technique is discussed in Table-4.5 with refereed literature and discussed its limitations also which is useful to design a high isolation MIMO antenna.

Table 4.5 Comparison of the proposed isolation mechanism with the existing mechanism

Isolation Level (in dB)	Isolation Techniques	Advantages	Disadvantages
10 [54]	RH/LH Transmission Line	Improved isolation, increased diversity gain	Complex structure and used for only mobile application
40 [56]	Decoupling Structure	Limited to wideband	Not used in UWB and SWB
30 [57]	Nutrilazation Line	Good isolation for MB(Multiband) bandwidth	Complex structure

12 [59]	FSS	Good isolation for Multiband bandwidth	Limited isolation and size is bulky
18 [P]	Inverted L-shaped decoupling structure	Improved isolation in multiband for 4 elements	Limited to wideband only

4.5 SUMMARY

A dual-band circularly polarized 4-elements MIMO antenna has been proposed for pentaband applications as MSM, IoT, ISM, BRS, EBS, WLAN, and WiMAX. All the simulated results of the antenna had confirmed with measured results in the intended pentaband. The antenna has achieved 3.58dBi peak gain with stable omnidirectional radiation patterns with acceptable diversity performance like ECC, TARC, CCL, DG have values 0.005, -40dB, 0.35bits/sec/Hz and 9.5dB respectively as shown in [Table 4.5](#). The SAR performance of the proposed four ports MIMO antenna is calculated, it is also under the permissible limits for 1g and 10g of bio-tissue of the head. The diversity and antenna performance of the proposed antenna is excellent in all respect for wireless communications; this means this antenna is useful in various portable wireless applications with an average channel capacity of 14.68bps/Hz. Finally, the performance of the proposed antenna proved that it is a good candidate in multiple portable wireless applications.

CHAPTER-5

DESIGN OF METASURFACE ABSORBER FOR LOW RCS AND HIGH ISOLATION MIMO ANTENNA

5.1. INTRODUCTION:

MIMO (Multiple-input multiple-output) antennas are playing a vital role in modern wireless communication in enhancing the capacity and reliability of the network and become a major part of communications paradigms, such as LTE (long-term evolution) and forthcoming 5th-generation mobile communication network. Since mutual coupling between different elements of the MIMO antenna is an important metric when investigating the performance of the MIMO antenna. In recent years, various isolation improvement techniques for multiple inputs and multiple outputs antennas have been reported as decoupling networks, neutralization network technique, negative group delay lines, parasitic monopole elements, artificial magnetic conductor (AMC) reflector, ground plane modification method, or a combination of the above-mentioned methods but these techniques are tedious, occupied more space over the antenna and difficult to fabricate to improve the isolation between the different antennas. In this **Chapter**, a technique of improving isolation between MIMO antennas through Metasurface (MS) has been reported that absorbs all the current which couples from the excited antenna to the rest of the antennas.

Radar cross-section (RCS) has become increasingly important with the rapid development of stealth technology. RCS reduction can also be achieved by utilizing absorbing materials. RCS is mainly depending upon how much power reflected per unit beam solid angle. So this MS absorber can absorb incoming electromagnetic waves and convert the corresponding electromagnetic energy into heat energy and provides low RCS. Coating with radar absorbing materials (RAM), forming and using passive and active cancellation technology are normal methods in RCS reduction. In this **Chapter**, a novel metasurface based highly decoupled 4-

¹ Saxena, Gaurav, Priyanka Jain, and Yogendra Kumar Awasthi. "Design of Metasurface Absorber for Low RCS and High Isolation MIMO Antenna for Radiolocation and Aeronautical Radio Navigation." *AEU Journal Elsevier* (2020)

element MIMO antenna is designed at 8.78GHz frequency with reduced RCS. Section-5.1.2 shows the proposed metasurface absorber analysis and results. Section-5.1.3 depicts the results and analysis of the proposed antenna with and without metasurface. Section-5.1.4 is providing the results of the diversity performance of the proposed antenna in terms of ECC, MEG, TARC, and CCL. A summary of the proposed design work is summarized in section-5.1.5.

5.1.2 ABSORBER DESIGN ANALYSIS AND RESULTS

The top and bottom view of the proposed metasurface are presented in Fig.5.1.1 (a) and (b) including all dimensions of the top of the metasurface as mentioned in Table-5.1.1. The suggested metasurface can be viewed as an array which is shown in 5.1.1(c). The proposed metasurface is designed on FR-4 substrate with permittivity 4.3 and loss tangent ($\tan\delta$) = 0.02 of 1.0mm substrate height (h), while the bottom side is completely laminated by a copper sheet. The thickness of copper layers having conductivity (σ) $5.1.8 \times 10^7$ S/m on both sides is 0.035mm. The proposed unit cell of the metasurface is comprised of concentric circular and elliptical-shaped rings with four 300ohms lumped resistances. The design is simulated on EM simulation (CST Microwave Studio) using periodic boundary conditions and the Floquet ports excitation.

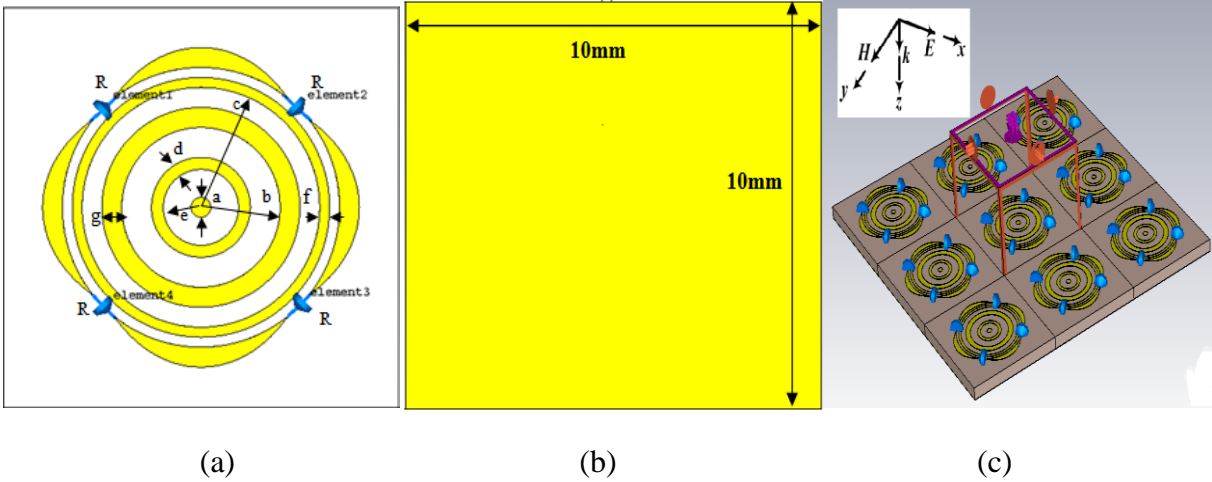


Fig.5.1.1. The proposed geometry of the unit cell of metasurface with structural dimensions (a) Front view (b) Bottom view(c) 3x3 MS array at normal incidence

Fig.5.1.1(c) shows a 3x3 MS array at normal incidence and all the calculations for Floquet port with this array.

Table-5.1.1 Dimensions of designed metasurface shown in Fig 5.1.1 (a)

a (mm)	b (mm)	c (mm)	d (mm)	e (mm)	f (mm)	g (mm)	R₁ (mm)
0.25	2	3	0.3	0.95	0.25	0.5	0.25

Transmission line theory-based mathematical analysis of absorber is comprised of a dielectric substrate with metasurface. Conforming to the response of metasurface in an external electromagnetic field, a general equivalent circuit of the metasurface is given in Fig. 5.1.2. The absorptivity $A(f)$ of any absorber structure is calculated by Equation (5.1.1).

$$A(f) = 1 - R(f) - T(f) = 1 - |S_{11}(f)|^2 - |S_{21}(f)|^2 \quad (5.1.1)$$

Where, $R(f) = |S_{11}(f)|^2$ is reflected power and $T(f) = |S_{21}(f)|^2$ is transmitted power. Since the bottom side of the metasurface is completely laminated by the copper, which prevents the transmission of incident EM waves and it makes transmitted power almost zero. So the Equation (5.1.1) becomes $A(f) = 1 - |S_{11}(f)|^2$. The absorption can be evaluated by Equation (5.1.2)

$$A(f) = 1 - \left| \frac{Z_{in} - Z_0}{Z_{in} + Z_0} \right|^2 = 1 - \text{Reflected Power} \quad (5.1.2)$$

Where $Z_0 = 377\Omega$ is the characteristics impedance of free space and Z_{in} is the input impedance of the proposed metasurface. Input Impedance (Z_1) of a dielectric medium of the proposed structure backed with a copper sheet is to be calculated by Equation (5.1.3) where c is the speed of light in free space i.e. 3×10^8 m/sec.

$$Z_1 = \frac{jZ_0}{\sqrt{\epsilon_r}} \tan \frac{2\pi f \sqrt{\epsilon_r}}{c} h \quad (5.1.3)$$

Meanwhile, the impedance (Z_2) of the top layer of the proposed structure which is in contact with free space is also calculated by Equation (5.1.4)

$$Z_2 = R + j \left(2\pi f L - \frac{1}{2\pi f C} \right) \quad (5.1.4)$$

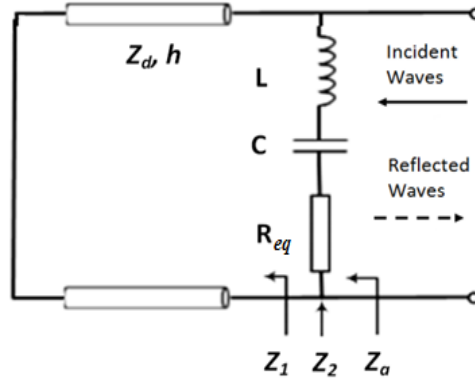


Fig.5.1.2. A general equivalent circuit model of the proposed unit cell of metasurface structure

The total input impedance of the proposed metasurface is obtained by Equation (5.1.5)

$$Z_a = \frac{Z_1 \times Z_2}{Z_1 + Z_2} \quad (5.1.5)$$

To match impedance with the free space means the total input impedance Z_a of the proposed metasurface is equal to the impedance of free space Z_0 . The value of R, L, and C are estimated by using Equations (5.1.2)-(5.1.5) at the intended frequency 8.78GHz.

The theoretical value of equivalent needed at intended frequency is given by Equation (5.1.6) while quantitative relation between the equivalent inductance (L) and equivalent capacitance (C) is suggested in Equation (5.1.7).

$$R_{eq} = \frac{Z_0 \tan^2 \left(\frac{2\pi f \sqrt{\epsilon_r} h}{c} \right)}{\epsilon_r + \tan^2 \left(\frac{2\pi f \sqrt{\epsilon_r} h}{c} \right)} \quad (5.1.6)$$

$$\left(2\pi f L - \frac{1}{2\pi f C} \right) = - \frac{\sqrt{\epsilon_r} Z_0 \tan \left(\frac{2\pi f \sqrt{\epsilon_r} h}{c} \right)}{\epsilon_r + \tan \left(\frac{2\pi f \sqrt{\epsilon_r} h}{c} \right)} \quad (5.1.7)$$

Using Equations (5.1.6) and (5.1.7), the value of $R = 13.76\Omega$, $L = 1.60\text{nH}$, and $C = 0.97\text{pF}$ for satisfying 99.8% absorbance at 8.78GHz frequency. Simulated return loss S_{11} of a unit cell of the proposed metasurface at 8.78GHz frequency is 39dB as shown in Fig.5.1.3 and 10dB

bandwidth of unit cell is 8.75-9.0GHz.

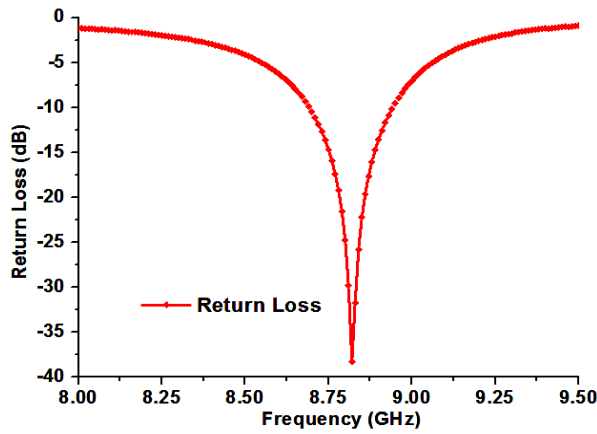


Fig. 5.1.3. Simulated return loss of a proposed unit cell of metasurface at the intended frequency

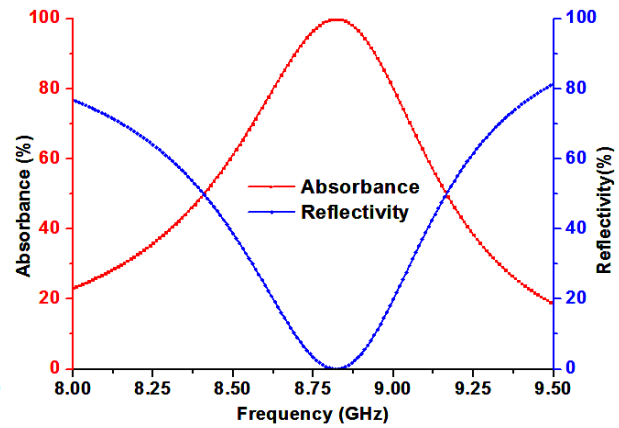


Fig. 5.1.4. Simulated absorbance and reflectivity of the proposed unit cell of metasurface at the intended frequency

Fig.5.1.4 shows the absorbance and reflectivity of the proposed unit cell at the frequency of interest (8.78GHz) that are 99.8% and almost zero respectively and the same is also comprehended by using Equations (5.1.1) and (5.1.2). Fig.5.1.5 shows the metamaterial properties of the unit cell that signify by the phase of return loss which is varying from -90° to $+90^\circ$ concerning 8.75-9.0GHz frequency band and concurrently normalized input impedance is constant at the unity that means input impedance Z_a of the proposed unit cell is matched with the intrinsic impedance Z_0 (377Ω) of free space in the same frequency band.

The parametric variation of return loss at the intended frequency of the proposed unit cell at different values of loaded lumped resistance is shown in Fig.5.1.6 which shows the adaptability of absorbance of the proposed design. At 300ohm lumped resistance, the return loss is 39dB which shows the best absorbance and reflectivity in the proposed design. If we not connected resistance at that instant proposed MS provides a minimum return loss of about 10dB and minimum absorbance. As the proposed unit cell is used to design a metasurface absorber which can be used in various applications in defense antennas therefore the electromagnetic signal can be analyzed for different incident angles (θ). So, the Fig.5.1.7 (a)-(b) depicts the variation of return

loss at different incidence angles and various polarization angles. It is also observed that the return loss depends on the incidence angle, hence this structure is polarization-sensitive metasurface for incidence angle but not change with various polarization angles (Φ) (0° to 60°) so this MS is polarization insensitive for Φ in TE mode.

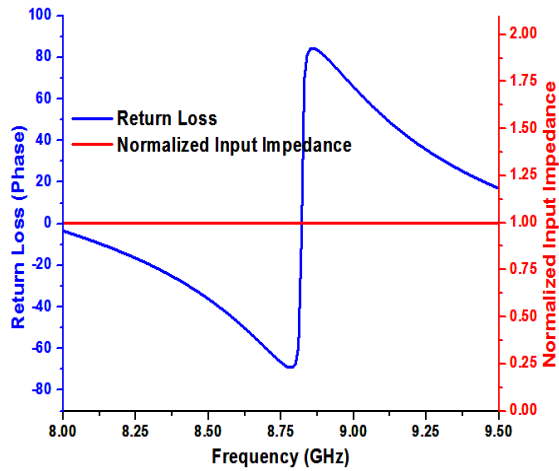


Fig. 5.1.5. Phase illustration of return loss and a normalized input impedance of the proposed unit cell

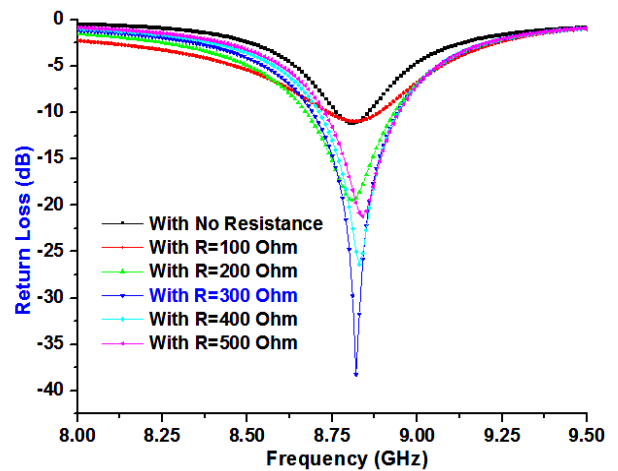
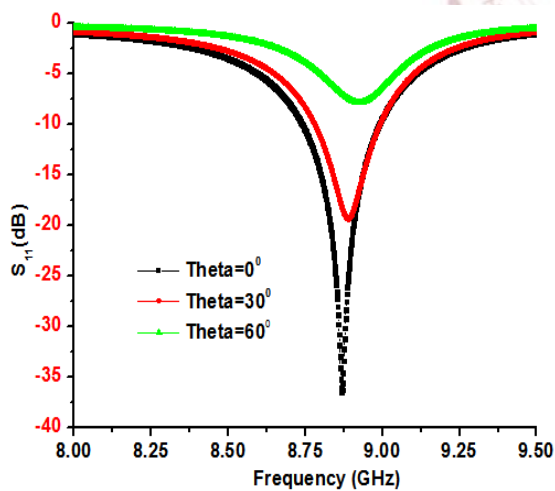
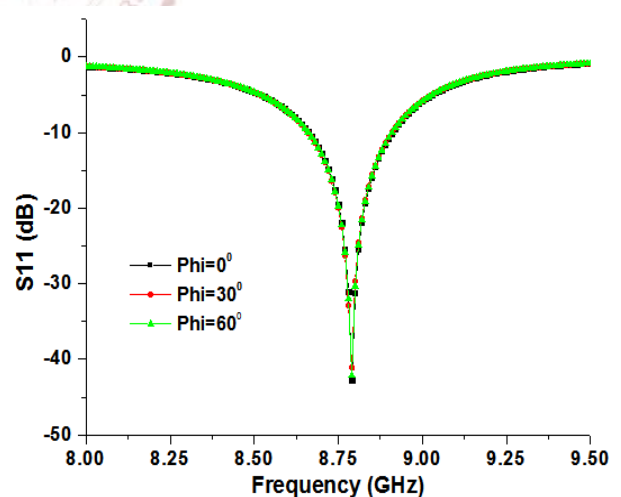


Fig.5.1.6. Parametric study of the return loss of the proposed unit cell with different values of used lumped resistance



(a)



(b)

Fig.5.1.7. Parametric study of the return loss of proposed metasurface with a variation of various incidence angles (a) various polarization angles (Phi) in TE-mode

Simulated current density, electric field, and RCS of the proposed unit cell of metasurface are shown in

Fig.5.1.8 and it is also clear from Fig.5.1.8 (a) and (b) that the total power density (W/m^2) incident normally at the surface of a unit cell is completely absorbed in intended frequency.

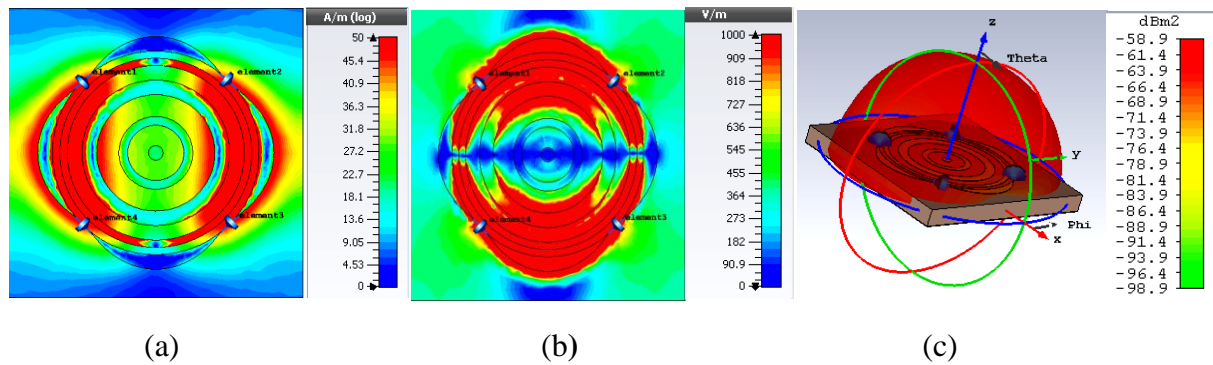


Fig.5.1.8. Simulated (a) Current density (b) Electric field (c) RCS of a proposed unit cell of metasurface at 8.78GHz frequency

In defense application, radar cross-section of any material is a very important parameter that needs to be maintaining as low as possible but the RCS antenna increased significantly as it is mostly backed by a ground conductor. To solve this problem in the proposed MIMO antenna, a metasurface is designed which has very low RCS as shown in Fig.5.1.8 (c). RCS is reduced up to 25dBsm by the proposed metasurface at the intended band of frequency as shown in Fig.5.1.9.

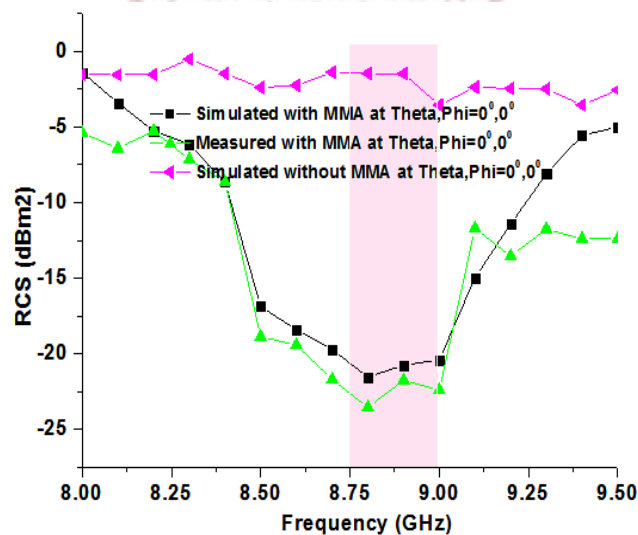


Fig.5.1.9. Simulated and measured RCS of proposed metasurface at various incident angle θ and polarization angle ϕ

To understand RCS theoretically, the ray theory has been explained in the following literature. The reflection coefficient (Γ_a) under zero incidence angle condition is defined by the Equation

(5.1.8)

$$\Gamma_a = \frac{Z_a - Z_0}{Z_a + Z_0} \quad (5.1.8)$$

Z_a is the intrinsic impedance of metasurface. The reflection coefficient of oblique incidence angle (Γ_0) can be defined by Equation (5.1.9)

$$\Gamma_0 = \frac{Z_a \cos \theta_i - Z_0 \cos \theta_t}{Z_a \cos \theta_i + Z_0 \cos \theta_t} \quad (5.1.9)$$

Where, θ_i and θ_t denotes the oblique incident angle and transmission angle. From Snell's Law

$$\frac{Z_0}{Z_a} = \frac{\sin \theta_t}{\sin \theta_i} \quad (5.1.10)$$

By Equations (5.1.9) and (5.1.10), calculate the condition for minimum reflection in TE-mode which is responsible for low RCS is given by Equation (5.1.11).

$$\Gamma_{\min_TE} = \mu_a \epsilon_a - \epsilon_a^2 \sin^2 \theta_i - \mu_a^2 \cos^2 \theta_i = 0 \quad (5.1.11)$$

Where μ_a and ϵ_a are permeability and permittivity of the metasurface. At $\mu_a = \epsilon_a$ and normal incidence $\theta_i = 0^\circ$ provides zero reflection and maximum absorbance for MS.

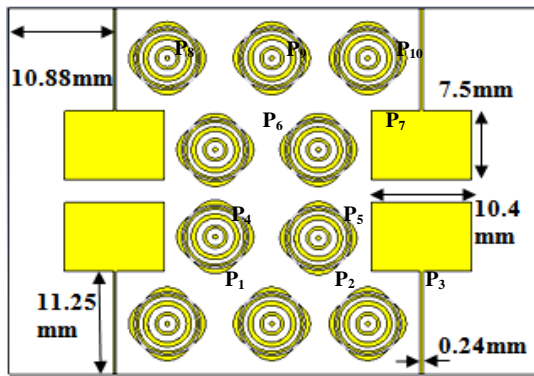
5.1.3. MIMO ANTENNA DESIGN ANALYSIS AND RESULTS:

Finally, the 4-elements MIMO antenna geometry is presented in Fig.5.1.10 with metasurface including all dimensions. This MIMO antenna is fabricated on FR-4 substrate ($\epsilon_r = 4.3$ and $\tan \delta = 0.02$) with 1.0mm substrate height including 0.035mm thick copper (conductivity $\sigma = 5.1.8 \times 10^7 \text{ S/m}$) clad on both side. Table-5.1.2 depicted the position of MS in microstrip.

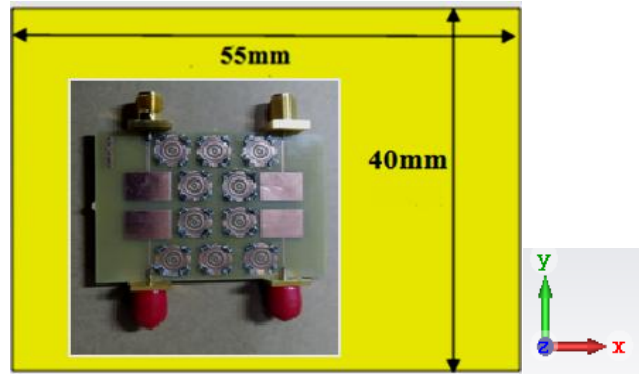
Table-5.1.2 Meta surface position in MIMO antenna w.r.t ($X_{\min} = -35$, $X_{\max} = 20$) and ($Y_{\min} = -15$, $Y_{\max} = 25$), all dimensions in mm

$P_1(x,y)$	$P_2(x,y)$	$P_3(x,y)$	$P_4(x,y)$	$P_5(x,y)$
(-18.5,-9.5)	(-7.6,-9.5)	(2.4,-9.5)	(-13.5,0)	(-2.75,0)
$P_6(x,y)$	$P_7(x,y)$	$P_8(x,y)$	$P_9(x,y)$	$P_{10}(x,y)$

(-13.5,9.5)	(-2.75,9.5)	(-18.5,19.5)	(-7.6,19.5)	(2.4,19.5)
-------------	-------------	--------------	-------------	------------



TOP



Fabricated MIMO antenna (Top view) and back view

Fig.5.1.10. Top view of the proposed four-element MIMO antenna with metasurface absorber

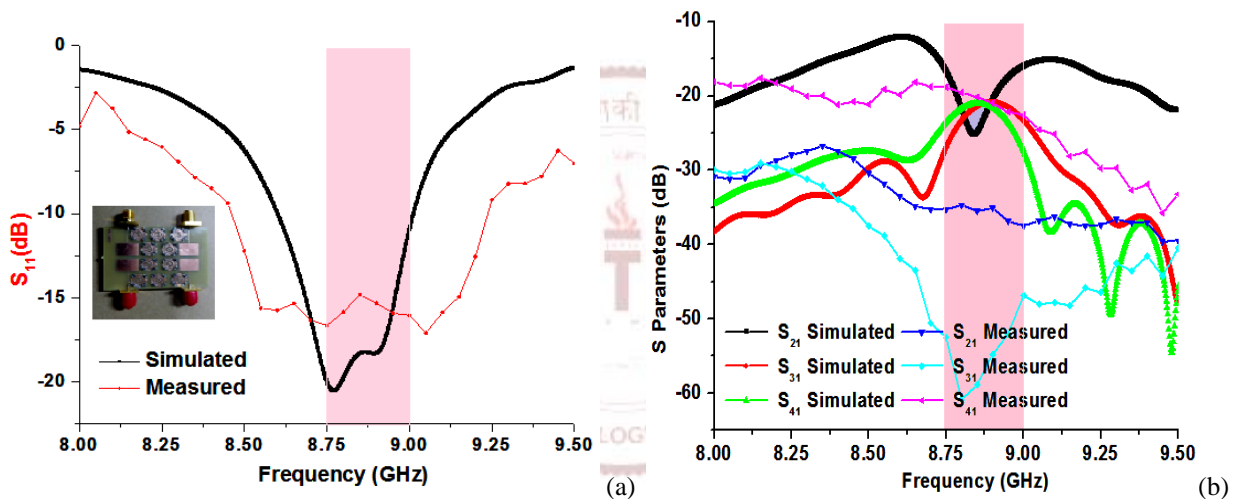


Fig.5.1.11. S-parameter measurement results (a) Return Loss (b) Isolation of 4-elements MIMO antenna with metasurface

Now from the simulated and fabricated MIMO antenna, various parameters have been measured.

Figs 5.1.11(a) and (b) represent return loss vs frequency plot and isolation plot for four elements MIMO antenna respectively. Where it is observed that return loss is less than between 8.75-9.0GHz frequency range and isolation level is greater than 20dB from 8.75-9.0GHz frequency which is highly acceptable without any decoupling, DGS and neutralization line structure introduce on it. Channel capacity also an important parameter for high-speed data transfer. Two common methods for increasing the channel capacity in MIMO system first one is increasing the

number of antenna elements and the second one to reduce the mutual coupling level, these two terms we improve in my proposed high isolation 4-elements metasurface based MIMO antenna. 4-elements metasurface based MIMO antenna has good S-parameter listed in Table-5.1.3. All S parameter is improved when MS is used with 4 element MIMO antenna as compared to without MS and concludes that return loss and isolation are improved by 9dB and 12dB respectively.

Table-5.1.3: Measured S-parameters of proposed 4-elements MIMO antenna with and without metasurface at the 8.75-9.0GHz frequency band

	$S_{11}(\text{dB})$	$S_{21}(\text{dB})$	$S_{31}(\text{dB})$	$S_{41}(\text{dB})$
Without MS	-9	-22	-21	-11
With MS	-18	-43	-33	-23

Fig.5.1.12 (a) shows the measurement setup of Co- & Cross-polarization and 2D simulated and measured radiation patterns of proposed antenna in E and H-plane at 8.78GHz frequency where Rx MIMO antenna is placed at a far-field distance with Tx horn antenna. Tx horn antenna is connected with a signal generator that transmits a microwave frequency and the R_x MIMO antenna is connected with a spectrum analyzer that measures the received power for Co and Cross power measurements with different theta. In co-polarization, the radiation pattern is almost omnidirectional which radiates the power in all directions but in the cross-polarization which is orthogonal to co-polarization provides the least radiated power which is depicted in Fig.5.1.12 (b) and the entire graph is stable for the best fit in the MIMO antenna. In the E-Plane, the Co-polarization power level lies between 0 to -10dB and the Cross-polarization level lies between -25dB to -35dB which shows a better separation between CO and Cross polarization level. In Fig.5.1.12(c), H-plane, Co- and Cross-polarization separation is almost 20dB down and shows a stable radiation pattern.

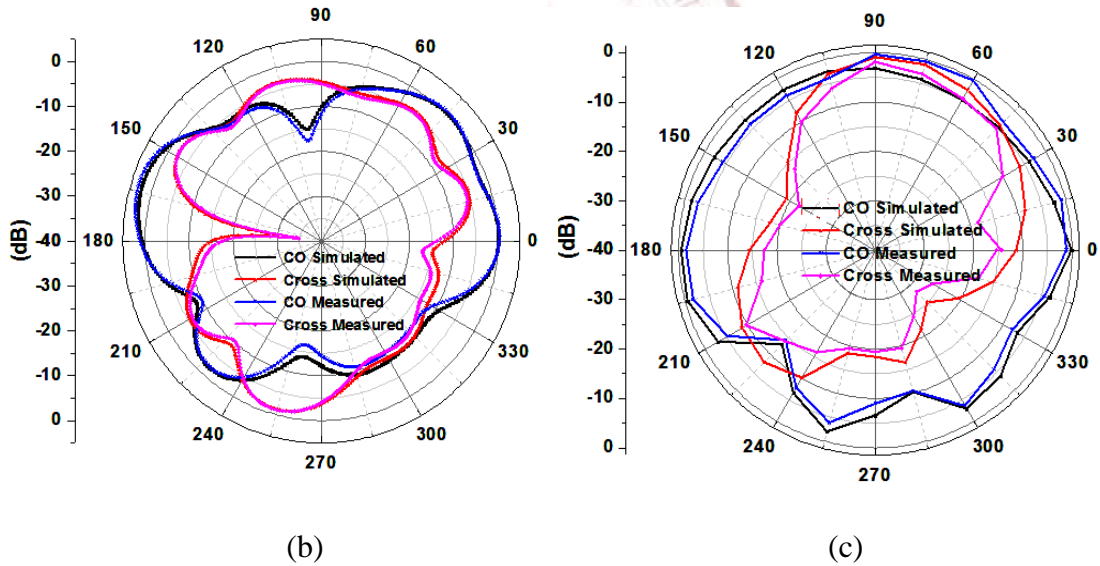
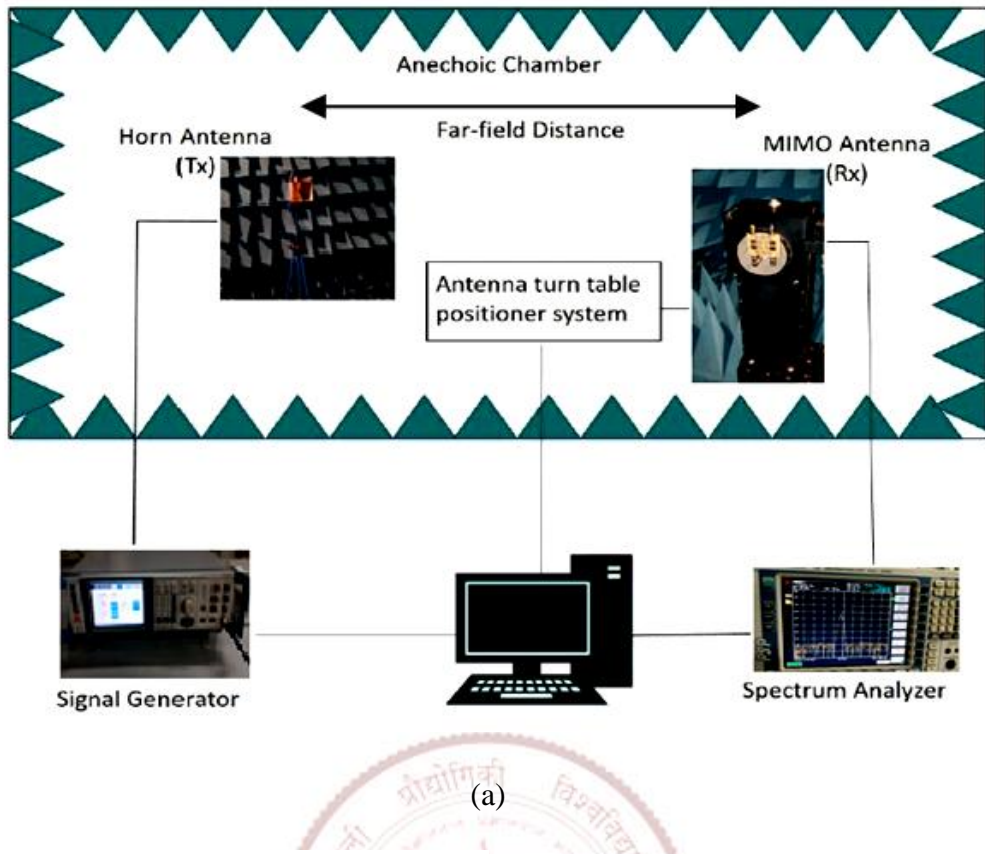


Fig.5.1.12. (a) Setup an arrangement for measurement Co-polarization and Cross-polarization (b) E-plane simulated and measured (c) H-plane simulated and measured at 8.78GHz

Fig.5.1.13(a) gives the information about the 3D radiation pattern of the proposed MIMO antenna and concludes that the maximum gain is 6.36dBi for the isotropic antenna (0dBi) depicted as red on the image.

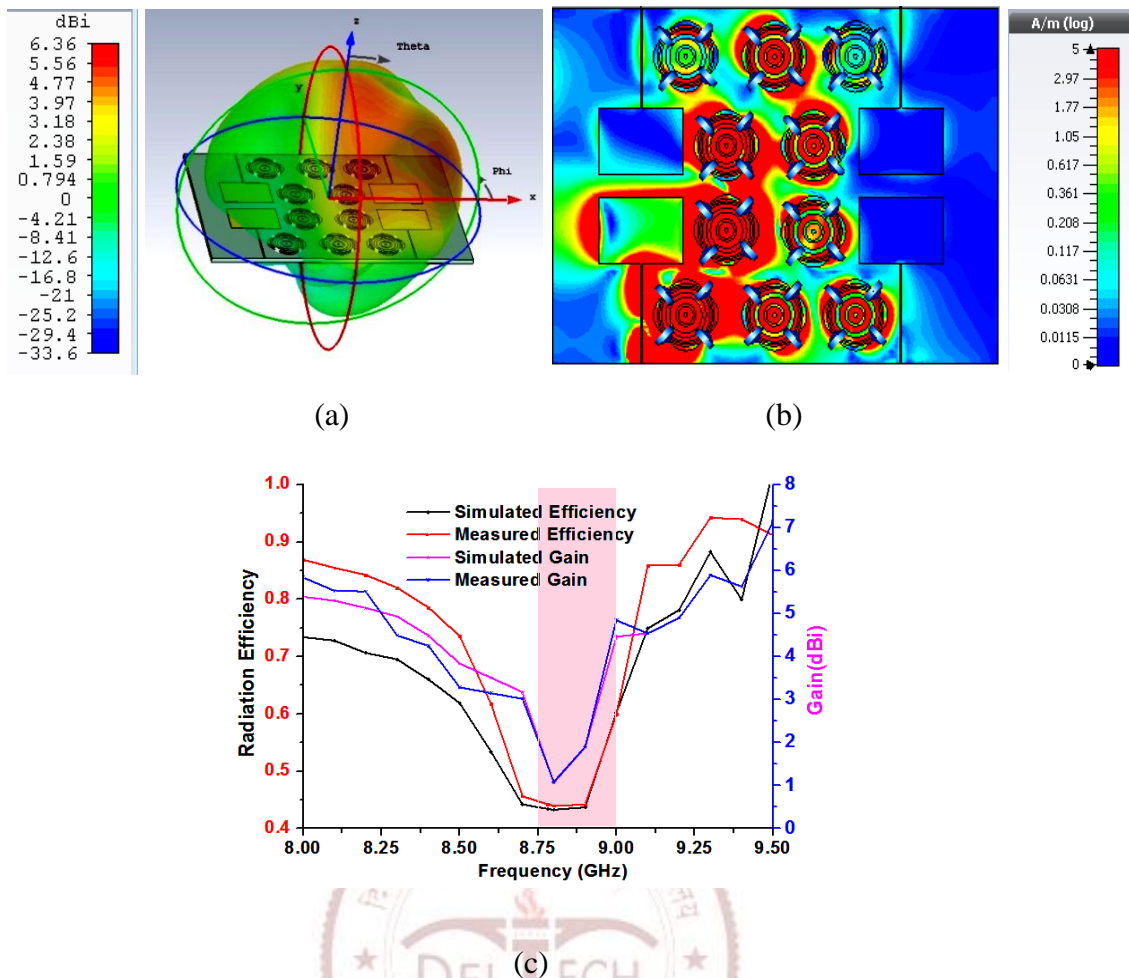


Fig.5.1.13. Simulated and measurement results of (a) Simulated 3D radiation pattern measurement results of 4 elements MIMO antenna with MS (b) Simulated Current density (c) Radiation efficiency and Gain

Fig.5.1.13 (b) we simulate a current density at 8.78GHz frequency and conclude that 99.58% of the current migrated from the excited antenna to the rest of the antenna is absorbed by MS. So, high isolation is achieved with MS. Antenna efficiency and gain with MS are shown in Fig.5.1.13 (c) and conclude that using metasurface, maximum gain and radiation efficiency in the intended band (8.75-9.0GHz) is 4.83dBi and 62% respectively.

5.1.4. DIVERSITY PERFORMANCE OF MIMO ANTENNA:

The diversity performance of the proposed MIMO antenna with metasurface is evaluated by ECC, TARC, MEG, and CCL. MIMO antenna is used for multipath reflections so 3D radiation pattern gives accurate results for judging diversity performance of MIMO antenna. So

measurement of ECC is done using radiated fields (for better accuracy) and s-parameters. In Fig.5.1.14 (a) we conclude that at 8.75-9.0GHz its value is less than 0.07(radiated fields) and less than 0.002 (S-parameters) which is far below the 0.1 practical threshold value for MIMO antenna designer point of view.

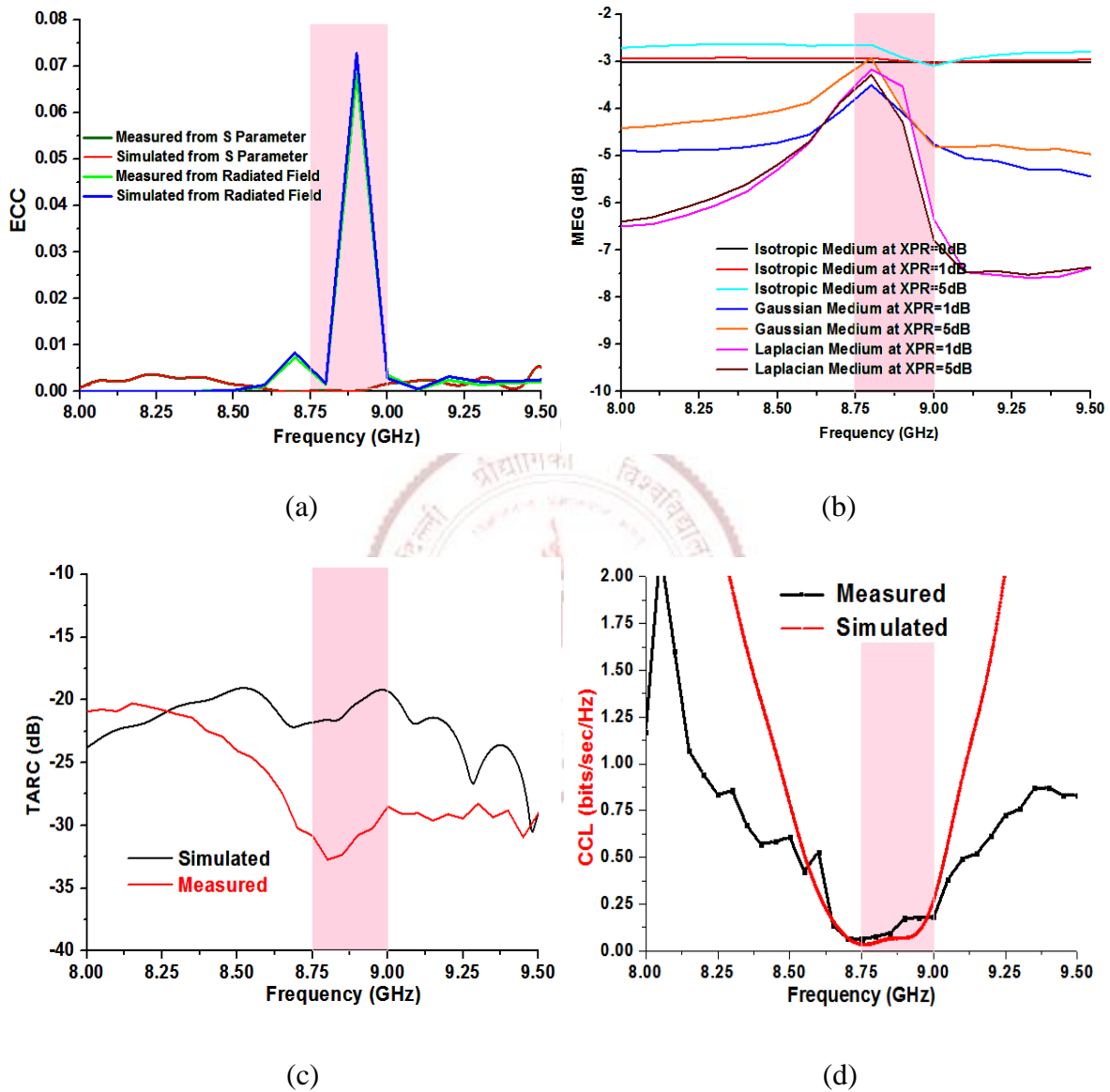


Fig.5.1.14. Simulated and measured results (a) ECC from S parameter and radiated field (b) MEG (c) TARC (d) CCL of proposed MIMO antenna with MS

Mean effective gain calculation for outdoor XPR = 0dB and indoor XPR = 6dB at isotropic Laplacian and Gaussian medium to be calculated and shown in Fig.5.1.14 (b). The TARC value of the proposed MIMO antenna is <math><-30\text{dB}</math> in the prescribed band shown in Fig.5.1.14(c). The

Fittest upper limit of information rate that can be broadcast in a wireless communication channel is judged by CCL and it should be $<0.5\text{bits/sec/Hz}$ for practical MIMO antenna but in the proposed MIMO antenna its value $<0.15\text{ bits/sec/Hz}$ depicted in Fig.5.1.14 (d). A comparative study is performed in the following Table 5.1.4 and 5.1.5 which shows better performance of the proposed MIMO antenna in terms of isolation, ECC, and RCS available in existing references. The proposed comparison table shows that the proposed MIMO antenna provides compact size, high isolation ($>23\text{dB}$), low ECC (<0.002), and low RCS ($<20\text{dBsm}$) provides good diversity performance and better signal quality.

Table-5.1.4: Isolation and ECC Comparison table of the proposed antenna with existing references

Size(mm^2)/Ref.	Isolation (dB)	ECC
30x55 [60]	20	-
36x22 [62]	30	0.008
23x12.5 [63]	12	0.018
50x35 [64]	25	0.004
50x37.4 [65]	19.5	-
150x80 [66]	17.5	0.05
55.1.6x50.5[67]	20	0.005
60.6x48.5[68]	25.1.9	-
55x45[P]	23,35,55	0.002

Table-5.1.5: Isolation and RCS Comparison table of the proposed antenna with existing references

Size (mm^2)/Ref.	Isolation (dB)	RCS reduction (dBsm)
48x48[75]	10	10
96x96[78]	-	10

90x90[82]	-	10
58x50[84]	20	15
30x30[85]	20	30
40x26[86]	25	-
25x25[87]	15	6
55x45[P]	23,35,55	20

5.1.5. SUMMARY

In this **Chapter**, a 4-elements MIMO antenna is designed using a novel metasurface absorber for isolation as well as RCS reduction. A unit cell of metasurface absorber is amalgamated by concentric circular and elliptical-shaped rings with four 300ohms lumped resistances. This MIMO antenna with an absorbing structure is fabricated on an abundantly available FR-4 substrate with dimensions of 55×40×1mm³. Absorbance at intended frequency i.e. 8.78GHz of metasurface absorber is 99.8% and its reflectivity is almost zero. Therefore, the isolation between antennas due to this absorbance is improved by 12dB at 8.78GHz and net isolation of the proposed antenna is achieved greater than 23dB. Similarly, RCS is also reduced by 25dBsm. The performance of the designed MIMO antenna is also judged by diversity parameters like ECC, DG, TARC, MEG, CCL and channel capacity, etc. at the proposed frequency. Simulated and fabricated results have good agreements at the intended frequency. The measured and simulated ECC of the proposed MIMO is less than 0.002 which shows that this antenna is suitable for radiolocation and aeronautical radio navigation applications.

TRIPLE BAND POLARIZATION INSENSITIVE ULTRATHIN METASURFACE ABSORBER

5.2.1 INTRODUCTION :

In this **Chapter**, A novel single layer triple-band MMA with polarization-insensitive has been

presented with high absorbance 99.4%, 96.4%, and 91.25% at three distinct frequencies 5.2.2, 9.45, and 12.45GHz frequency. The proposed structure is good absorbance in X-band and ultra-thin 0.013λ thickness with existing literature used in table-5.2.2. So this MMA used in many defense applications like stealth Fifth-generation stealth aircraft for RCS reduction, MIMO antenna isolation improvement, EMC reduction, Microwave imaging, and sensing in the intended band.

The whole of the Chapter is divided into three sections. Section-5.2.2 shows the design of the proposed MMA structure. Section-5.2.3 depicts the simulated results of the proposed MMA in terms of return loss, absorbance, reflectivity, current density, RCS, and electric field distribution. A summary of the proposed designing work is summarized in section-5.2.4.

5.2.2 DESIGN OF PROPOSED MMA STRUCTURE:

The front view and bottom view of the proposed MMA structure are presented in Fig.5.2.1 (a) and 5.2.1(b). 8 split ring and 1 oval ring is proposed for achieving triple-band absorbance.

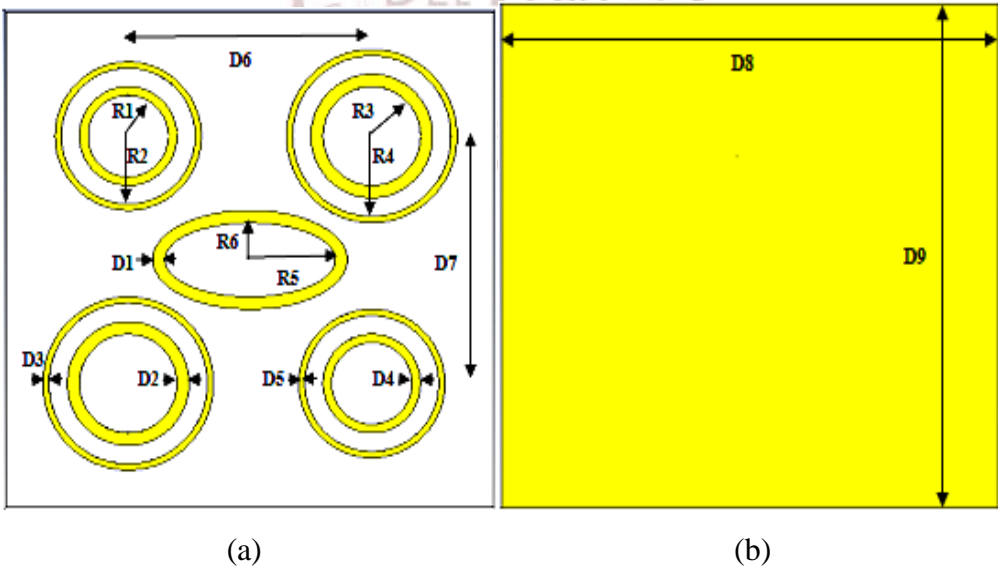


Fig.5.2.1. Proposed Triple band meta-material absorber structure (a) Front view (b) Bottom view

Table-5.2.1 Dimensions of designed MMA shown in Fig 5.2.1 (a) and 5.2.1(b)

R1 (mm)	R2 (mm)	R3 (mm)	R4 (mm)	R5 (mm)	R6 (mm)	D1 (mm)
------------	------------	------------	------------	------------	------------	------------

1.65	2.75	2	3.25	3.5	1.5	0.5	
D2	D3	D4	D5	D6	D7	D8	D9
(mm)	(mm)	(mm)	(mm)	(mm)	(mm)	(mm)	(mm)
0.5	0.25	0.35	0.25	10	10	20	20

The proposed MMA is designed on an FR-4 substrate with 1.0mm height (h) and 35 μ m copper conductor ($\sigma = 5.8 \times 10^7$ S/m) thickness. The backside is fully laminated with copper so that no transmission of the incident wave and thus minimizing the reflected wave which produces high absorbance. All dimensions of proposed MMA as mentioned in Table-5.2.1.

5.2.3 SIMULATED RESULTS:

The proposed Triple band MMA is simulated by a CST Microwave studio simulator with proper boundary condition and produces a return loss and absorptive curve depicted in Fig.5.2.2 (a) & 5.2.2(b).

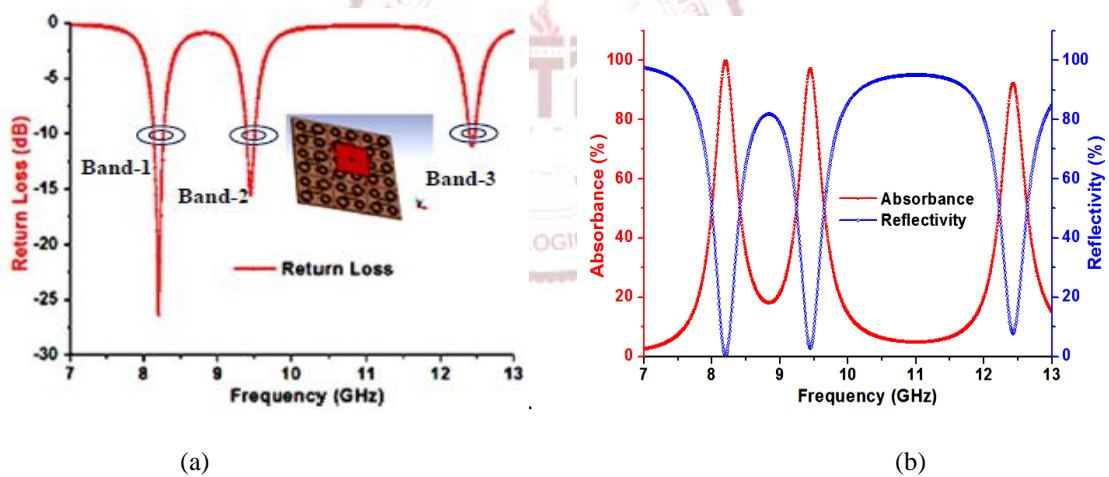


Fig.5.2. 2. Simulated Results of (a) Return loss of proposed triple-band absorber (b) Absorbance and Reflectivity of proposed triple-band absorber at different frequencies

Return loss at the intended band is 26.32dB, 15.42dB, and 11dB which depict its absorbance 99.4%, 96.2%, and 91.25% respectively. The absorption of the proposed MMA is calculated by Equation 5.2.1 [106-108] but the proposed MMA is fully ground conductor so no transmission occurs so S_{21} is assumed to be zero.

$$A(\omega) = 1 - |S_{11}(\omega)|^2 - |S_{21}(\omega)|^2 \quad (5.2.1)$$

Return loss (phase) vs frequency plot is shown in Fig.5.2.3(a) Its phase swing negative to positive in three different intended frequency bands which depicts metamaterial property. Fig. 5.2.3(b) depicts a parametric study of proposed MMA with and without oval strips. Black curve proposed intended MMA structure and red curve shows without middle oval strips. The band is shifted towards the left without oval strips and return loss also deteriorates. Fig.5.2.4 depicts the return loss phase response of proposed MMA at different incidence angles and concludes that at different incidence angles its return loss is not much affected so that proposed MMA shows the polarization-insensitive behavior.

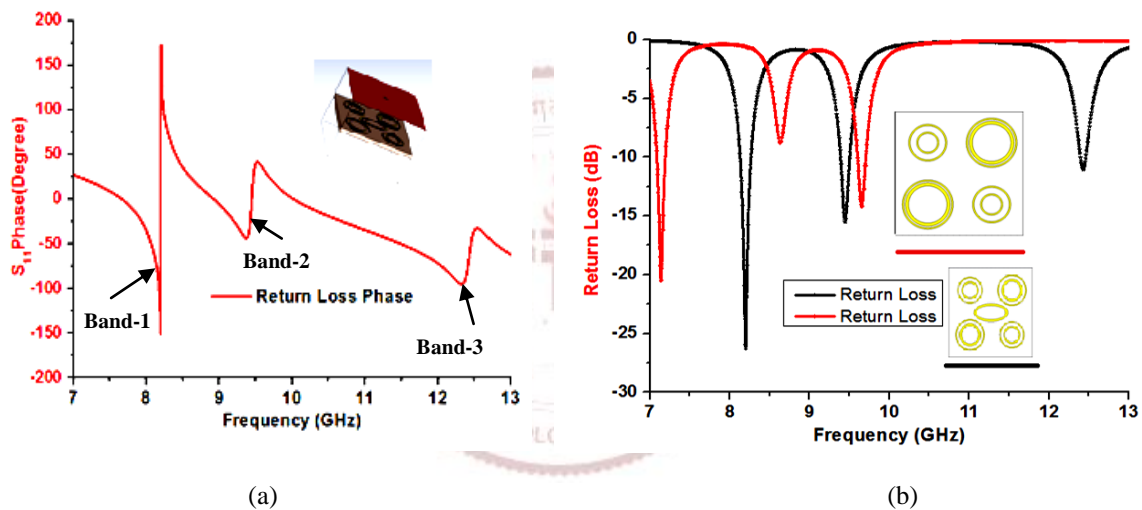


Fig.5.2.3. Simulated results (a) Return loss (phase) vs Frequency plot of proposed triple-band absorber (b) Parametric study of the return loss of proposed triple-band absorber with and without middle oval strips.

The design MMA is used in fifth-generation aircraft for the RCS reduction shown in Fig.5.2.5. The radar cross-section (RCS) of an object involving in stealth technology should be as low as possible. As a radar signature is proportional to the reflections from antenna surface, so metamaterial absorber used in stealth aircraft produces a low RCS signature to RADAR beacons in military applications as discussed in Ref [107-108].

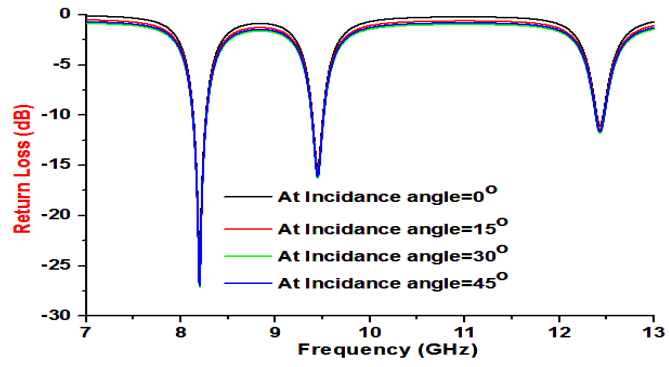
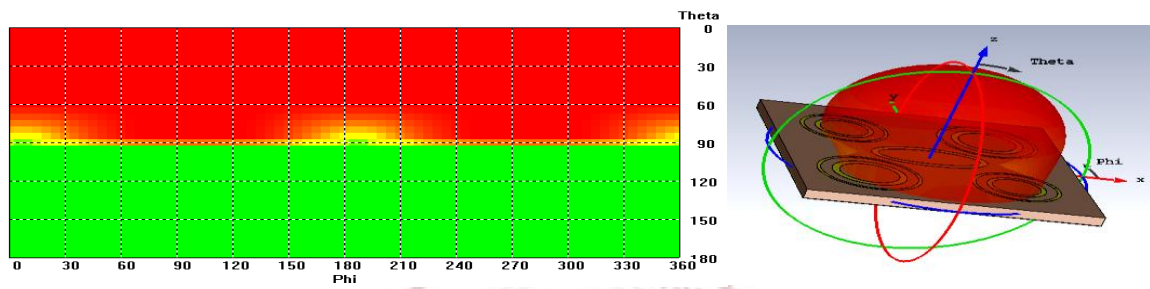
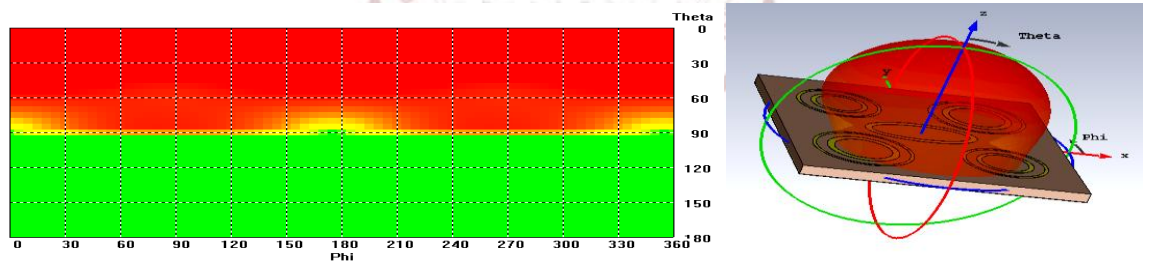


Fig.5.2.4. Simulated response of return loss of proposed triple-band MMA at various incidence angles

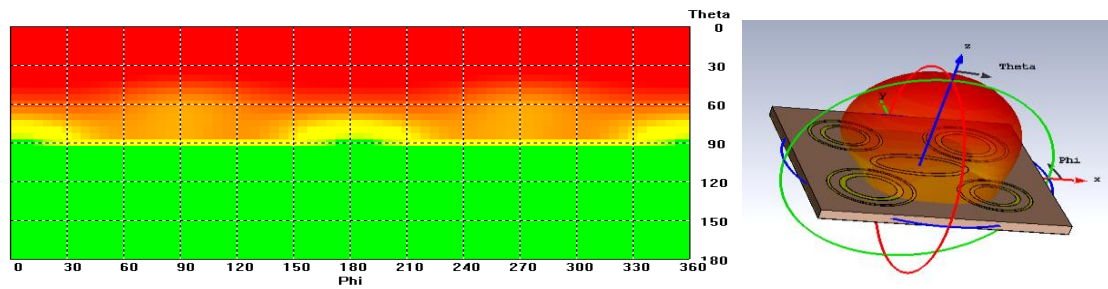


-76.2 -36.2 dBm2

(a)



(b)



-73.2 -33.2 dBm2

(c)

Fig.5.2.5 RCS vs Theta and Phi plot at (a) 5.2.2GHz (b) 9.45GHz (c) 12.45GHz

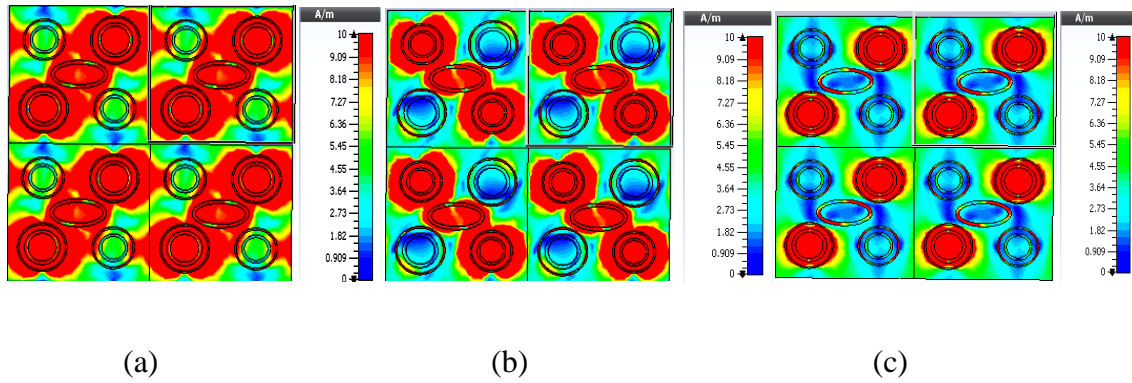


Fig.5.2.6. Simulated surface current density of proposed absorber at (a) 5.2.2GHz (b) 9.45GHz (c) 12.45 GHz frequency respectively.

Fig.5.2.6 shows the current density of proposed MMA at intended three different frequencies, It depicts that at high absorbance peak frequency charge is confined two big circular slots and a middle oval slot at 5.2.2GHz frequency Fig.5.2.6 (a), but in the case of a second resonant peak which occurs at 9.45GHz frequency Fig.5.2.6 (b), the charge accumulated only two small circular slot and middle oval slot. At 12.45GHz frequency Fig.5.2.6(c) charge is accumulated only two big circular slots only. The guided wavelength for different structures i.e. big and small circular slots and middle oval slots are different so they perform three different resonant frequencies to provide better absorbance.

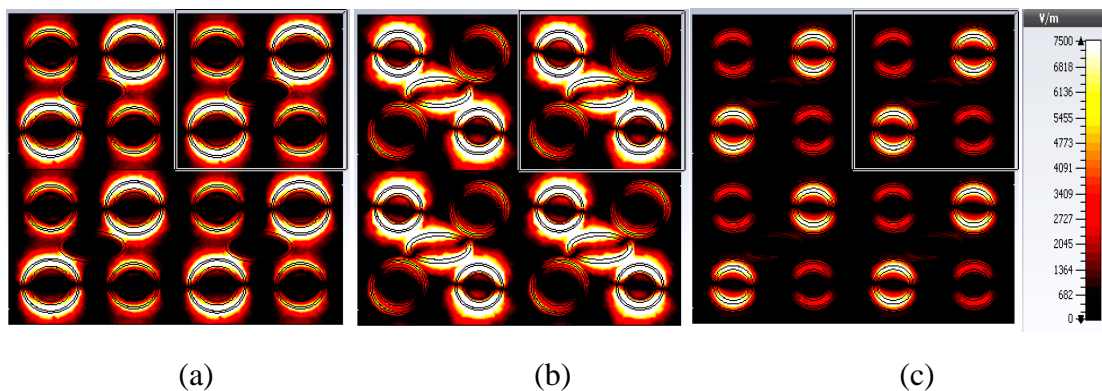


Fig.5.2.7. Simulated Electric field of proposed absorber at (a) 5.2.2GHz (b)9.45GHz (c) 12.45GHz frequency respectively

Electric field intensity at three intended bands which provide high return loss shows in Fig. 5.2.7

The electric field is confined in the big, small, and oval ring. At 5.2.2GHz frequency, big ring and the small ring is the main contributor for almost perfect absorbance, at 9.45GHz two small rings and the oval ring is responsible for high absorbance and two big slots are responsible at 12.45GHz shown in Fig.5.2.7 (a) (b) (c) respectively.

Table-5.2.2. Comparison table of proposed MMA with existing references

Unit Cell Periodicity	Absorbance Band	Absorbance (%)	Unit Cell Thickness	Polarization insensitivity/ Reference
12mm (0.169 λ)	2	>95.0	0.8mm (0.011 λ)	Yes [88]
0.37 λ	3	>90.0	3.2mm (0.12 λ)	Yes[89]
15.6mm	1	>80.0	0.085 λ	Yes[94]
0.209 λ	3	>99.0	2.4mm (0.029 λ)	Yes[95]
20 (0.27 λ)	3	>91.2	1.0mm (0.013 λ)	Yes [P]

Above Table-5.2.2 shows that proposed MMA provides good absorbance and low profile with above-referred articles.

5.2.4 SUMMARY

In this Chapter, a triple-band polarization-insensitive metamaterial absorber of fifth-generation is designed. A unique circular and oval ring-shaped structure are proposed. This absorber structure has designed on FR-4 (4.4) substrate having $\tan\delta=0.02$ with unit cell dimension $20\times 20\times 1\text{mm}^3$. The absorbance of proposed triple-band MMA is 99.4%, 96.2%, and 91.25% at 5.2.2, 9.45, and 12.45GHz frequencies respectively. On the other hand, reflectivity is almost zero at the above frequencies. Changing the incident and polarization angles of the absorber, the absorbing characteristics are almost the same. So the proposed absorber is found appropriate for stealth aircraft, RCS and EMC reduction, isolation in MIMO antenna, imaging, and sensing in the X-band applications.

CHAPTER-6

SUPER-WIDEBAND (0.33-10THz) MIMO ANTENNA FOR THz APPLICATIONS

6.1 INTRODUCTION

According to Edholm's law [96], the demand for data rates is doubled every 18 months and reached Tbps in the next few years. A terahertz frequency band is being applicable for state-of-art-communications because the requirement for higher data rates anytime anywhere is to be increased soon with an increase in the number of mobile-connected devices that will be never-ending. This spectrum provides numerous advantages like low interference probability, explosive and weapon investigating, imaging, sensing, and high data rate up to 10Gbps and low power requirement. As of now, research in millimeter-wave technology is reaching commercial deployments and is still motivated by the inadequate bandwidth; therefore the terahertz (THz) band is envisioned as the imminent frontier for wireless communication. THz Wireless communication is demanded better channel capacity with a high data rate in the modern era shown in Fig.6.1. To fulfill these demands, the MIMO-communication systems with THz range are required for high data speed in Tera-bit/sec (Tbps).

In this Chapter, the elliptical-shaped 2-element THz MIMO antenna is demonstrated with an L-shaped decoupling structure for achieving high isolation in SWB (0.33-10THz). It has 2:1 VSWR operating bandwidth from 0.33-10THz (187%) with 19dBi peak gain. Radiation Efficiency is also greater than 70% throughout SWB bandwidth. This 2-element MIMO antenna is designed with a compact size of $1000 \times 1400 \times 101.29 \mu\text{m}^3$ on the RT5880 substrate having a relative permittivity of 2.2. Simulated results of antenna-like return loss, isolation, gain, efficiency, and diversity

¹ Saxena, Gaurav, Priyanka Jain, and Yogendra Kumar Awasthi. "High Isolation and High Gain Super-Wideband (0.33-10THz) MIMO Antenna for THz Applications." *Optik journal Elsevier* (2020)

performance parameters (ECC, DG, TARC, etc.) are in an acceptable range. Therefore this antenna is useful for B5G, vehicular communications, Imaging, 3D printing, THz wave RADAR and Health care applications.

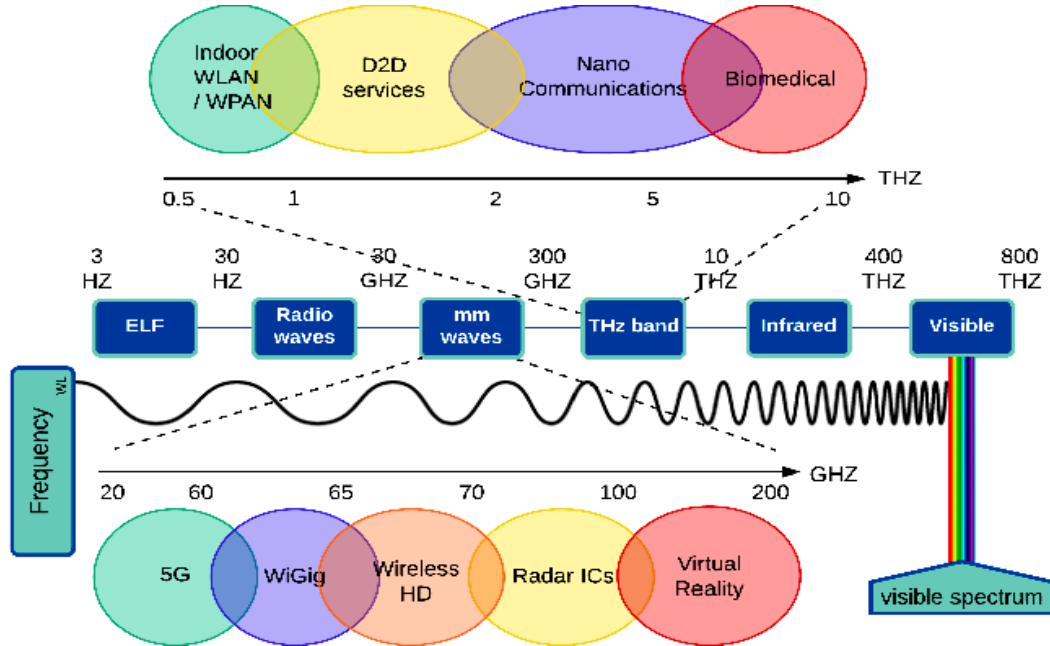


Fig.6.1 Frequency spectrum with state-of-art THz communications

All the detailed analysis and results are concluded in the following sections. In section-6.2, the THz MIMO antenna design procedure is discussed. In section-6.3 antenna results are discussed in terms of return loss, isolation, gain, efficiency, and group delay of proposed THz MIMO antenna. The THz channel model is discussed in section 6.4. The diversity performance parameters which are essential for MIMO antenna satisfactory operation is discussed in section 6.5. Section-6.6 finalizes the conclusion of this **Chapter** in terms of different parameters.

6.2 DESIGN PROCEDURE OF MIMO ANTENNA

The MIMO antenna with SWB characteristics is designed on RT5880 substrate of height (h) 101.29 μm with relative permittivity (ϵ_r) of 2.5 and loss tangent ($\tan\delta$) of 0.0009 having a size of 1000 μm ×1400 μm as shown in Fig.6.2 (a) - (b). This antenna is made by an elliptical patch with L-

shaped stubs in a ground plane to provide better isolation between two patches. The fundamental resonance frequency (f_r) of an elliptical-shaped monopole antenna is calculated by Equation 6.1 and its value approximate 4.9THz.

$$f_r(\text{THz}) = \frac{144}{400\mu\text{m} + 1400\mu\text{m} + h = 101.29\mu\text{m} + \frac{A_1 = 0.56\text{mm}^2}{2\pi\sqrt{2.2+1}} + \frac{A_2 = 0.38\text{mm}^2}{2\pi\sqrt{2.2+1}}} \approx 4.9\text{THz} \quad (6.1)$$

Equation 6.1 is valid if the entire dimension puts in mm. Area of the monopole elliptical patch antenna to be calculated by $A_1 = \pi \times 400\mu\text{m} \times 476\mu\text{m} = 0.56\text{mm}^2$ and ground conductor area (A_2) $= 0.38\text{mm}^2$. The separation between the two antennas is less than $\lambda/2$.

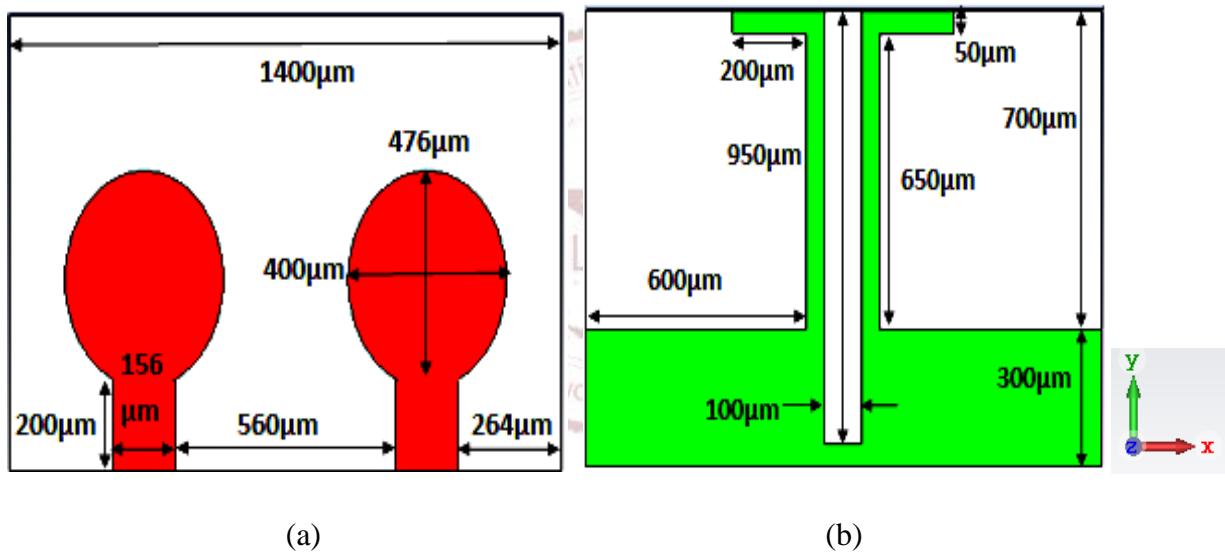


Fig.6.2 Two-element THz planar monopole MIMO antenna (a) Front view (b) Bottom view

6.3 RESULTS AND DISCUSSION

The design procedure of the proposed SWB THz MIMO antenna is depicted with its return loss and isolation as presented in Fig.6.3 (a). It is observed that the return loss is greater than 10dB and isolation is greater than 25dB in SWB bandwidth. The radiation efficiency of the proposed MIMO antenna is greater than 70% in intended bandwidth as depicted in Fig.6.3 (b). Group delay in terms

of return loss (S_{11}) is also calculated as this a super wideband antenna so the group delay in this bandwidth should be constant. Group delay is evaluated by Equation $T_d(\omega) = -\delta\phi/\delta\omega$, where Φ = phase of S_{11} and ω = angular frequency in rad/sec. The group delay deviation of the proposed MIMO antenna is less than 10ps in the SWB band. The average gain of the proposed antenna is almost more than 12dBi throughout the THz band; therefore, an antenna has high directivity in a particular direction as shown in Fig.6.3(c).

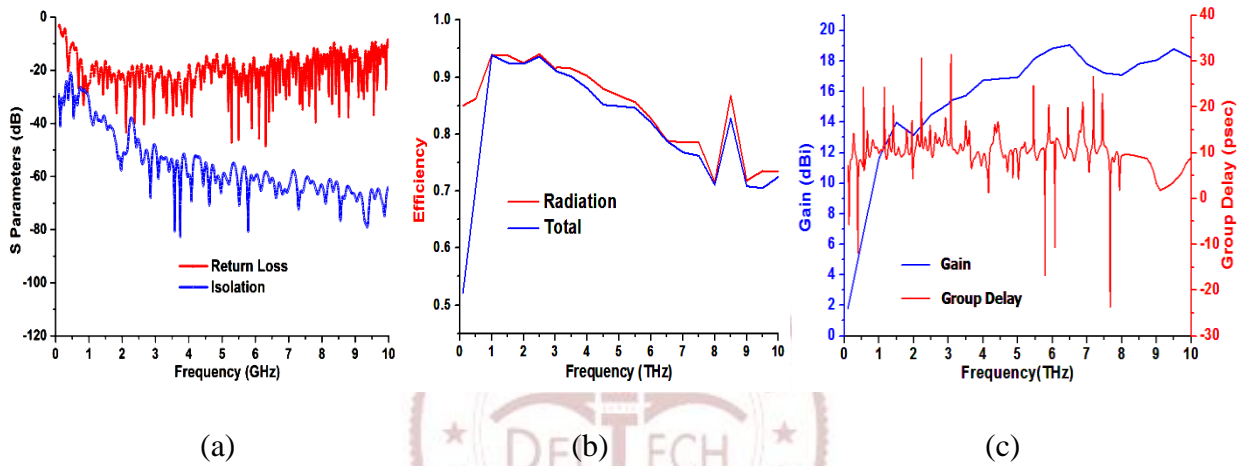


Fig. 6.3 Simulated results of (a) Return loss and isolation (b) Radiation and total efficiency (c) Gain and group delay of the antennas shown in Fig.6.2

The migration of surface current density from the energized antenna to the rest of the antennas is calculated by ECC. So, the simulated current density of the proposed antenna at frequencies of 1THz, 2THz, 4THz, and 8THz is represented in Fig.6.4. The surface current on antenna-2 is noted when antenna-1 is to be excited and vice-versa, as current density on antenna-2 is very less and hence, the mutual coupling will be deserted. Various decoupling techniques have been used by researchers to prevent the migration of surface current and here, a new approach is used to improve isolation between antenna elements. It is comprised of a rectangular L-shaped structure placed in a partial ground plane. Therefore, good isolation is achieved in the prescribed (0.33-10THz) SWB as it is also clear from Fig.6.3 (a).

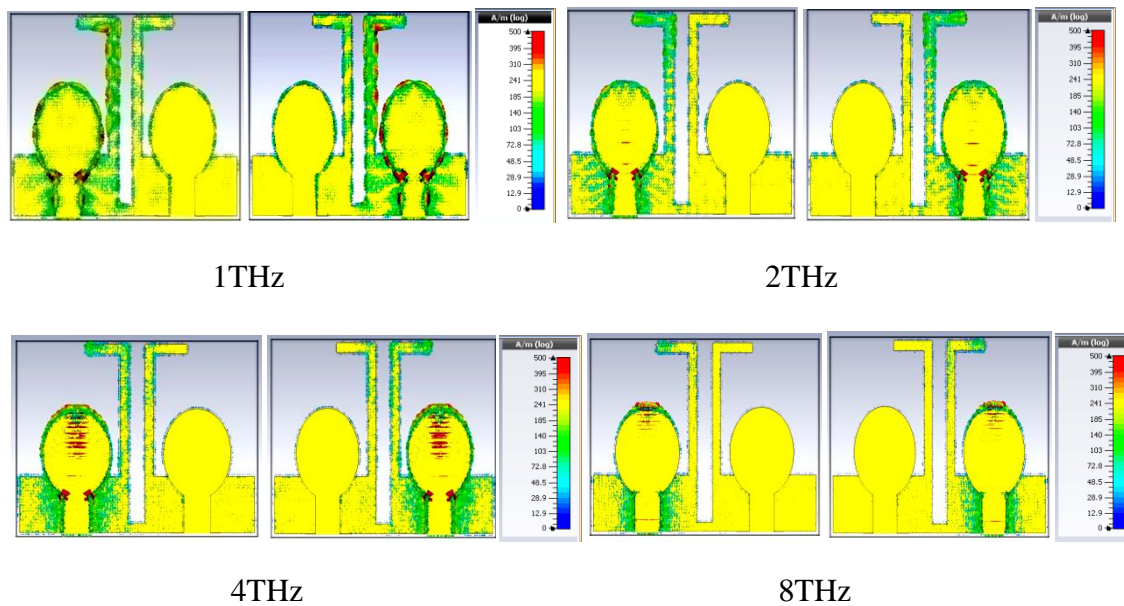
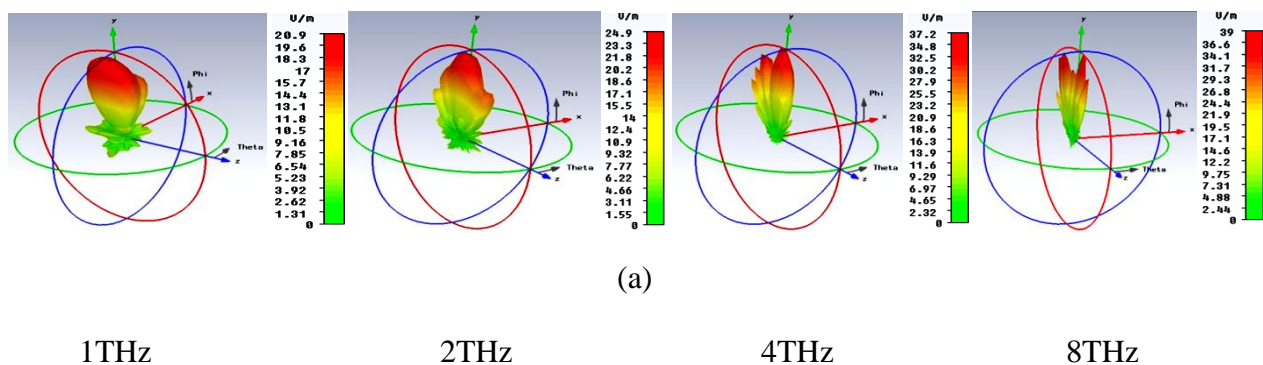
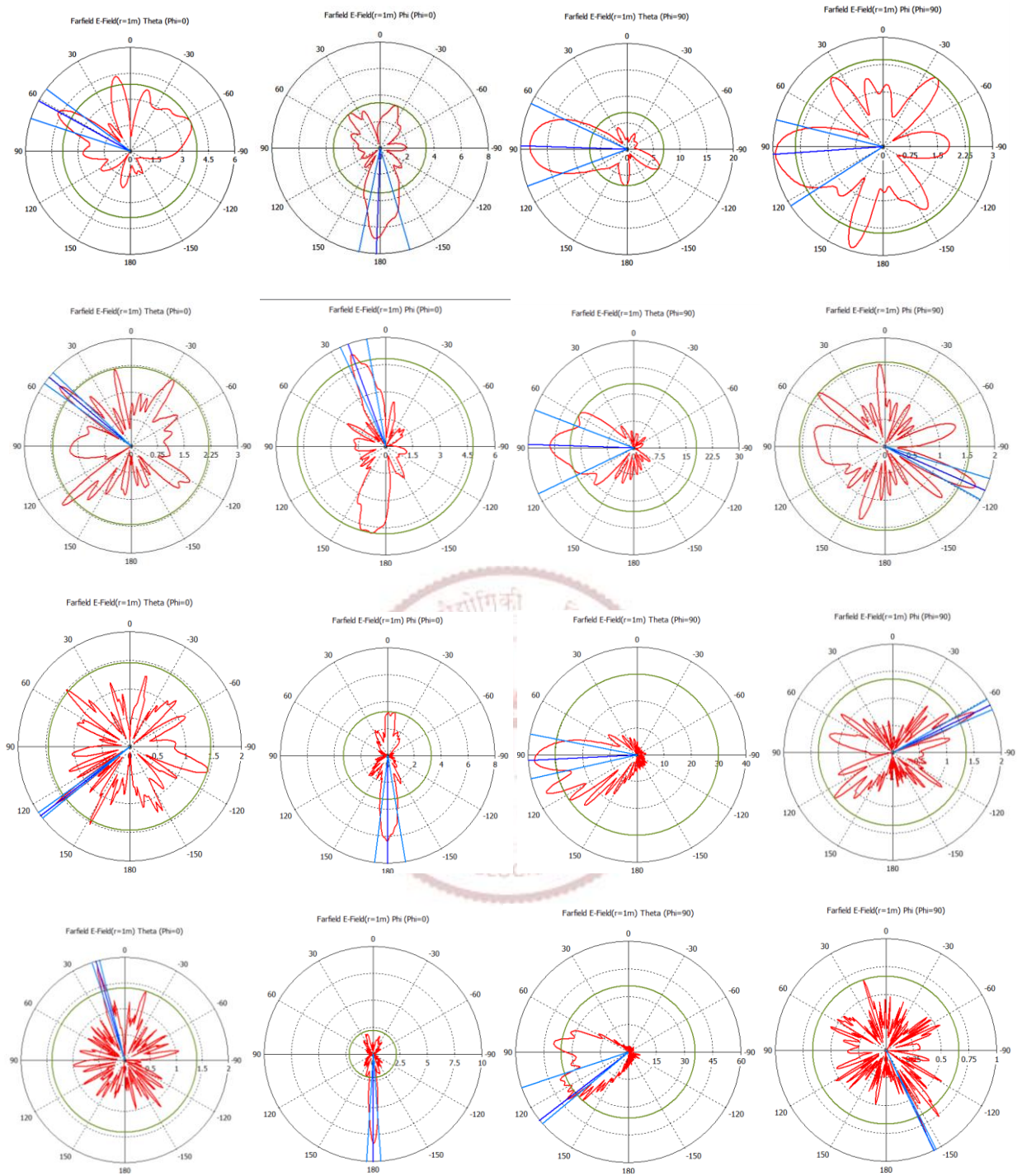


Fig.6.4 Surface current density distribution at frequencies 1THz, 2THz, 4THz, and 8THz when antenna-1 (left) is energized and antenna-2 (right) is terminated by a matched load (50ohm) and vice-versa

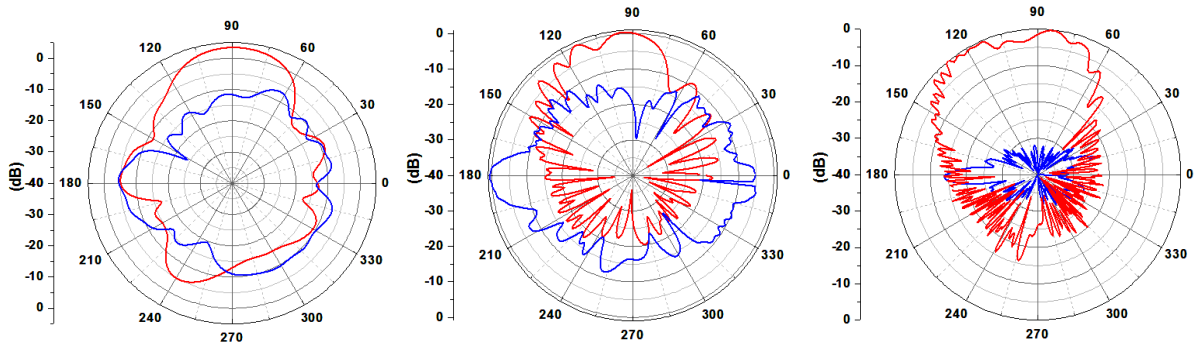
For the radiation pattern measurement of antenna-1, the antenna-2 is loaded with a 50Ω matched load and vice-versa. 3D and 2D electric field radiation patterns at different frequencies at 1THz, 2THz, 4THz, and 8THz respectively are shown in Fig.6.5 (a)-(b) where the radiation peak of the proposed antenna is in one direction at all intended frequencies means the antenna has highly directive.



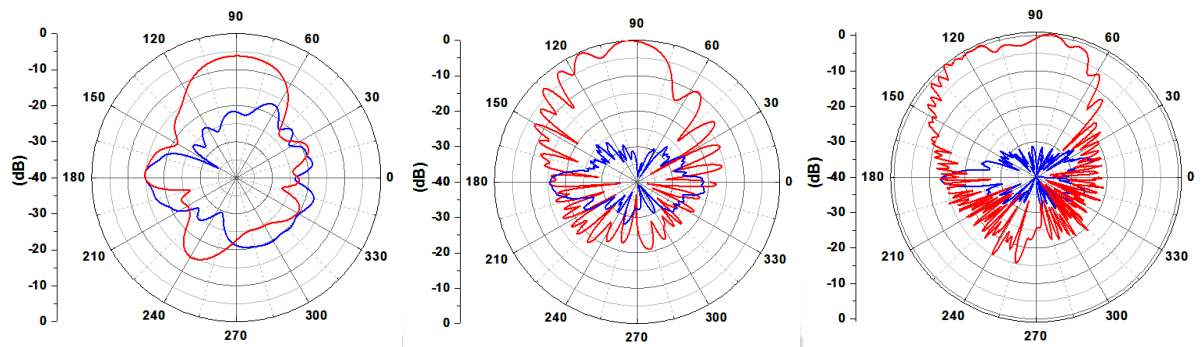


(b)

Fig.6.5 Simulated Far-Field patterns of designed MIMO antenna at frequencies 1THz, 2THz, 4THz, and 8 THz (a) 3D radiation patterns (b) 2D field patterns at $\phi = 0^\circ$, and 90°



yz- plane at 1THz, 4THz, 8THz



xz- plane at 1THz, 4THz, 8THz

— Co — Cross

Fig.6.6. Simulated 2D radiation patterns at 1THz, 4THz, and 8THz for xz- plane (right) and yz- plane (left), when port-1 is energized and port-2 is terminated by a 50Ω matched the load

The co cross-polarized radiation pattern in the E-plane and H plane at 1m distance is depicted in Fig.6.6. The simulated xz-plane (right) and yz-plane (left) 2D radiation patterns of the proposed antenna at 1THz, 4THz, and 8THz frequencies are also presented respectively as shown in Fig.6.6. It is noted that in an operating frequency band, the radiation patterns are highly directional at azimuth angle (Φ) = 0° (xz)-plane and at azimuth angle (Φ) = 90° (yz)-plane. In the directive field, Co and Cross polarization are more than 20dB separated with each other at 8THz in yz and xz plane.

6.4 THz CHANNEL MODEL

The THz signal is affected due to signal spreading loss and molecular absorption loss which is dominant at THz rather than GHz frequency. The total path loss ($L(f, d)$) associated with THz band is the addition of two losses and it is calculated by Equation (6.2) [102].

$$L(f, d) = L_{\text{Spread}}(f, d) + L_{\text{mabs}}(f, d) \quad (6.2)$$

Where $L_{\text{Spread}}(f, d)$ in dB is the spreading loss and $L_{\text{mabs}}(f, d)$ is the molecular absorption loss at a frequency (f) and distance (d) from the source. The same losses will be calculated using Equation 6.3 (a)-(b)

$$L_{\text{Spread}}(f, d) = 20 \log_{10} \left(\frac{4\pi fd}{c} \right) \text{dB} \quad 6.3(a)$$

$$L_{\text{mabs}}(f, d) = k(f) \times d \times 10 \times \log_{10} e \quad 6.3(b)$$

Where $k(f)$ denotes the medium absorption coefficient and it is a sum of the weighted coefficient of nitrogen, Oxygen, and water vapors. At THz frequency spreading $L_{\text{Spread}}(f, d)$ is dominant and its value reaches more than 60dB so the THz devices can be suitably used for applications of short-range communication. On the other hand, a surface that is considered smooth in GHz frequency, will be treated as rough in THz frequency therefore, the multipath fading factor is dominant in THz frequency, and multipath fading dependent upon the roughness factor which is calculated by Equation (6.4).

$$R = (r_0 + r_1) e^{\frac{-p}{2}} \quad (6.4)$$

$$\text{Where } p = \left(\frac{2\pi \cdot \Delta \cdot (\cos \theta_1 + \cos \theta_2)}{\lambda} \right)^2$$

r_0 , r_1 denotes the scattering coefficient related to the specular reflection & scattered field and Δ denotes the standard deviation of the surface roughness. λ denotes the corresponding signal wavelength. θ_1 and θ_2 denote the angle of incidence & reflection and both will be almost equal for the smooth surface. If the surface is rough ($p \gg 1$), θ_1 , θ_2 have different values. Hence, the receiving antenna gets the signal from a different position due to a rough surface, which produces multiple reflections spot than a smooth surface. If Antenna pattern behavior is Omnidirectional then only one path exists for a smooth surface while multiple paths exist for a rough surface. Highly directive antenna transmit and receive a signal in only one direction for a smooth surface and scattered a signal in multiple directions for rough surfaces as the non-specular reflection paths are strong enough to established a stable link.

6.5 DIVERSITY PERFORMANCE OF THz MIMO:

Diversity performance of the designed MIMO antenna is judged in terms of Envelope Correlation Coefficient (ECC), Diversity Gain (DG), Total Active Reflection Co-efficient (TARC), Channel Capacity and Channel Capacity Loss (CCL).

Envelope Correlation Coefficient ($\rho_{ecc,ij}$): The ECC is one of the important parameters to judge how much amount of electric field migrated from the excited antenna to the rest of the antenna in the MIMO system. It is calculated through S-parameters using [Equation 1.2](#).

For the uncorrelated MIMO antenna system, the value of ECC should be zero but their practical value for satisfactory operation in the MIMO communication system is less than 0.1. The numerical value of ECC of designed SWB THz MIMO antenna in SWB bandwidth is observed less than 0.0015 as shown in [Fig.6.7](#). Hence, the above results show a very low correlation between the two adjacent antennae, which shows good diversity performance in the proposed L-shaped decoupling structure designing.

Diversity Gain: The diversity gain of the MIMO antenna is calculated by the given formula $DG = 10 \times \sqrt{(1 - ECC^2)}$ and the acceptable value should be greater than 9.5dB. The value of diversity gain in SWB is 9.9999dB which is depicted in Fig.6.7.

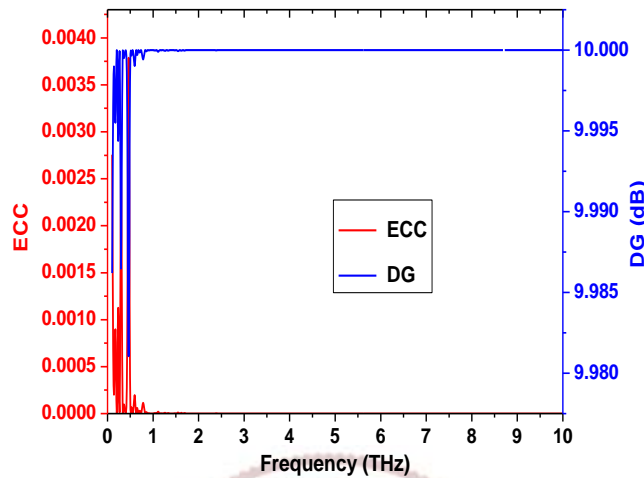


Fig.6.7. Simulated results of the envelope correlation coefficient and diversity gain

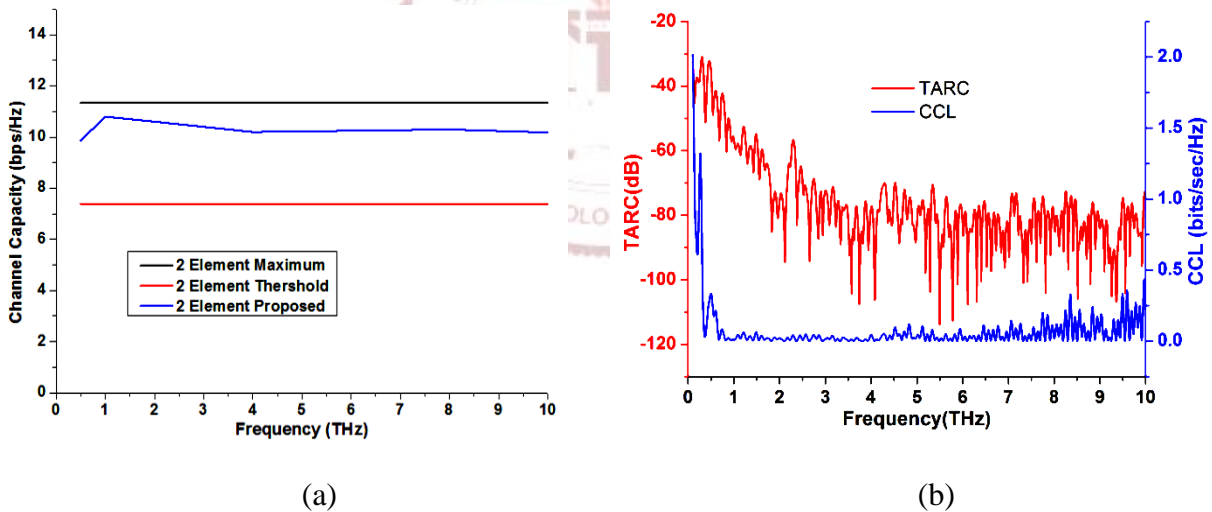


Fig.6.8. Simulated results of (a) Maximum, threshold and proposed Average channel capacity (b) CCL and TARC of the proposed MIMO antenna

Channel Capacity: The channel capacity is an important parameter to judge the data rate of the MIMO system. MIMO system is used to enhance the channel capacity and the performance of bandwidth and SNR (signal-to-noise) ratio compare with the SISO system. 2-element antenna

system provides a maximum channel capacity is 11.68bps/Hz at 20dB SNR in a uniform environment.

Where $[I]$ denote the identity matrix and number of transmitting and receiving antennas respectively, SNR is the ratio of signals feed at antenna port to the channels noise. For Rayleigh fading environment i.e. SNR = 20dB. The number of transmitting antenna elements is denoted by k . H & H^* are the channel matrix and its Hermitian transposing of a matrix. The maximum channel capacity of the proposed 2-elements MIMO is calculated.

$C_{2\text{-element MIMO}} = 2 \times \log_2(1+50) = 11.344 \text{ bits/sec/Hz}$. Monte Carlo provides the permission level of channel capacity for correlated Rayleigh channel. Permissible channel capacity is 65% of its maximum value ($11.344 \text{ bits/sec/Hz}$) = $11.344 \times 0.65 = 7.38 \text{ bits/sec/Hz}$ depicted in [Fig.6.8 \(a\)](#) [35].

Channel Capacity Loss: The main objective of the MIMO antenna system is to enhance the channel capacity as per the requirement. The channel capacity of the MIMO system is dependent upon the number of antenna elements involved in the MIMO system and the amount of correlation between antenna elements. If we increase the number of antenna elements then channel capacity increases linearly. But, the correlation factor and number of antenna elements in the MIMO system is increases then the channel capacity losses (CCL) is also increasing. The value of CCL for the proposed MIMO system is less than 0.3bps/Hz over the intended SWB bandwidth, which offers a better diversity result of the proposed MIMO antenna as shown in [Fig.6.8 \(b\)](#).

Total Active Reflection Co-efficient (TARC): In the 2-port antenna system, neighbouring antenna elements interrupt each other when they are working concurrently. This interruption influences the overall desirable gain, efficiency, and bandwidth of the proposed antenna. Hence, the actual MIMO antenna system performance will not be predicted by s-parameters only, so another important parameter (i.e. TARC) of the MIMO antenna system is explored to validate the

diversity performance. Ideally, TARC should be less than 0dB for the MIMO wireless communication system. The simulated TARC value of the designed THz MIMO antenna is less than -30dB in the intended THz SWB as shown in Fig. 6.8 (b), again it depicts the good diversity performance of a designed antenna. It is noted from Table-6.1 that the designed antenna achieves better results in comparison with the referenced MIMO antennas at various specifications. Proposed MIMO antenna having high bandwidth (0.33-10THz), high isolation (>25dB) with maximum gain 19dBi, and diversity parameters like ECC and CCL are quite below with accepted practical value which is suitable for less correlated and high data rate multiple THz applications.

Table 6.1 Comparison table of a designed THz MIMO antenna with existing references in various aspects for antenna performance

Frequency (THz)	Efficiency	Max.Gain (dBi)	ECC	CCL (bits/sec/Hz)	Isolation (dB)/References
1.76-1.87	-	-	0.015	-	- [97]
0.357-0.421	0.80	33.61	-	-	25[98]
0.46-6.96	0.14	12	-	-	- [103]
0.327-0.341	0.79	6.7	-	-	- [106]
1.1-1.7	-	3.6	0.01	-	- [108]
0.33-10	0.7	19	0.0015	0.25	25[P]

6.6 SUMMARY:

In this Chapter SWB THz, the MIMO antenna is designed with 187% fractional bandwidth and a good isolation level (>25dB) between two antenna elements. Radiation efficiency is greater than 70% entire SWB which is useful for high gain. This antenna has achieved a very high peak gain of 19dBi including stable directive radiation patterns with acceptable antenna and diversity performance. ECC of this antenna is very low 0.0015 that's mean very small power is coupled from the excited antenna to another antenna used in the MIMO system. CCL is also less than 0.35bps/Hz which provides high channel capacity for high-speed data transfer. The performances

of the proposed antenna have been proved that it is a good prototype for THz wireless communication and scanning networks.



CHAPTER-7

DESIGN AND ANALYSIS OF PLANAR UWB BANDPASS FILTER WITH EXTENDED STOPBAND CHARACTERISTIC

7.1 INTRODUCTION:

Modern wireless communication systems such as ultra-wideband (UWB) transceivers require miniaturized, wide pass-band filters with extended stop-band characteristics. In the current scenario, the UWB communication system offers numerous wideband applications such as microwave medical imaging, ground-penetrating radar (GPR), and radio frequency identification devices (RFID) tag for inventory control and asset management. The major advantages of a UWB system are to transmit data with a high rate, low energy density, low transmission power requirement, resist jamming, and easy to retrieve error control coding. A UWB transceiver with different blocks is shown in Fig.7.1, where the information is encoded first, digitally modulated, and then converted into pulse using a pulse generator and noise will be removed before transmission by using the UWB BPF. Compact planar BPF designs are growing very fast since 2002 while the US Federal Communication Commission (FCC) is allowed to commercial use of frequency range of 3.1GHz to 10.6GHz [1].

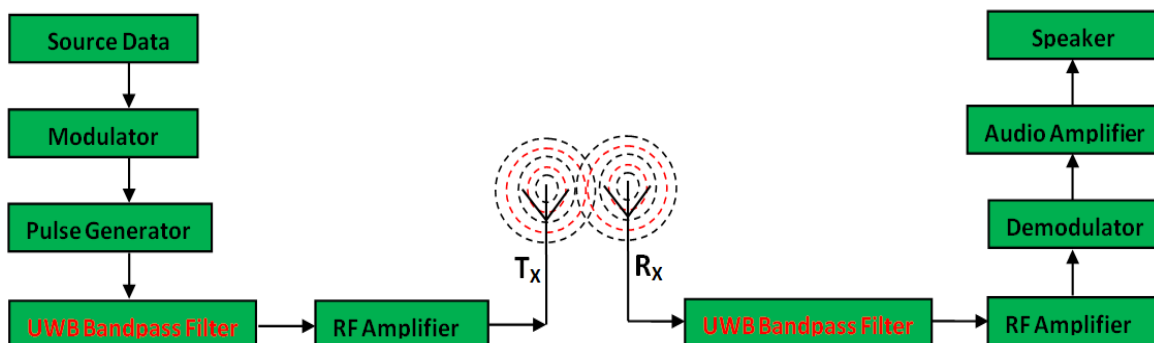


Figure 7.1. UWB Transmitter-Receiver block diagram with bandpass filters

¹ Saxena, Gaurav, Priyanka Jain, and Yogendra Kumar Awasthi. "Design Analysis of Compact Bandpass Filter with Stopband Characteristic for UWB Application using MMR Technique." *International Journal of Microwave and Wireless Technologies* (2020)

In this **Chapter**, a planer bandpass filter with extended stopband characteristics is achieved by using four combinations of circular/Mickey-shaped stubs (MMR), open-ended transmission line, parallel coupled-line sections, and DGS for UWB bandwidth. The designed filter is achieved better insertion loss and group delay in passband with a minimum value of 0.5dB and 0.30ns respectively. The proposed filter is fabricated over a cost-effective FR-4 substrate. In Section-7.2, the Filter design procedure and detailed analysis of the filter are explained. Section-7.3 represents S parameter results and current distribution analysis of MMR including group delay of the proposed Filter. The summary of the proposed design is mentioned in Section-7.4, which explains the utility of the UWB BPF in the empirical environment.

7.2 FILTER DESIGN PROCEDURE AND ANALYSIS:

The proposed UWB BPF is designed and fabricated over FR-4 substrate having a dielectric constant of 4.4 ($\tan\delta = 0.024$) with a substrate height of 1.6mm. The overall size of the filter is 22×20 mm² as depicted in **Fig.7.2** after multiple iterations and has been simulated using Computer Simulation Technology (CST) tool.

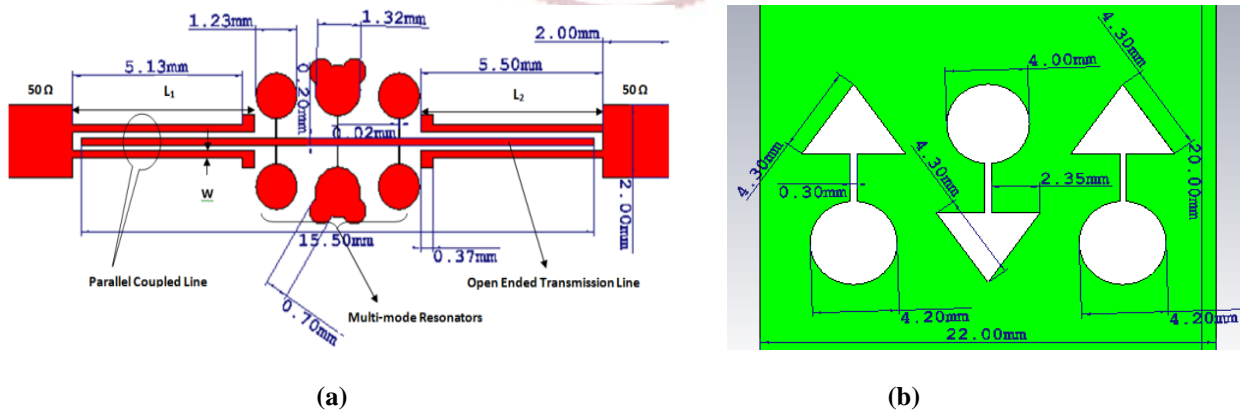


Fig. 7.2 Geometry of the proposed filter (a) Front view (b) Back view

The filter design has diversely shaped (arrow and circular head) DGS that enhance the pass bandwidth as well as a roll-off rate. This filter also has a multi-mode resonator (MMR) mechanism to enhance bandwidth in the passband, which includes two circular one Mickey-shaped stub

resonators over an open-ended transmission line coupled with parallel microstrip lines at two feeding ends of 50Ω as shown in Fig. 7.2.

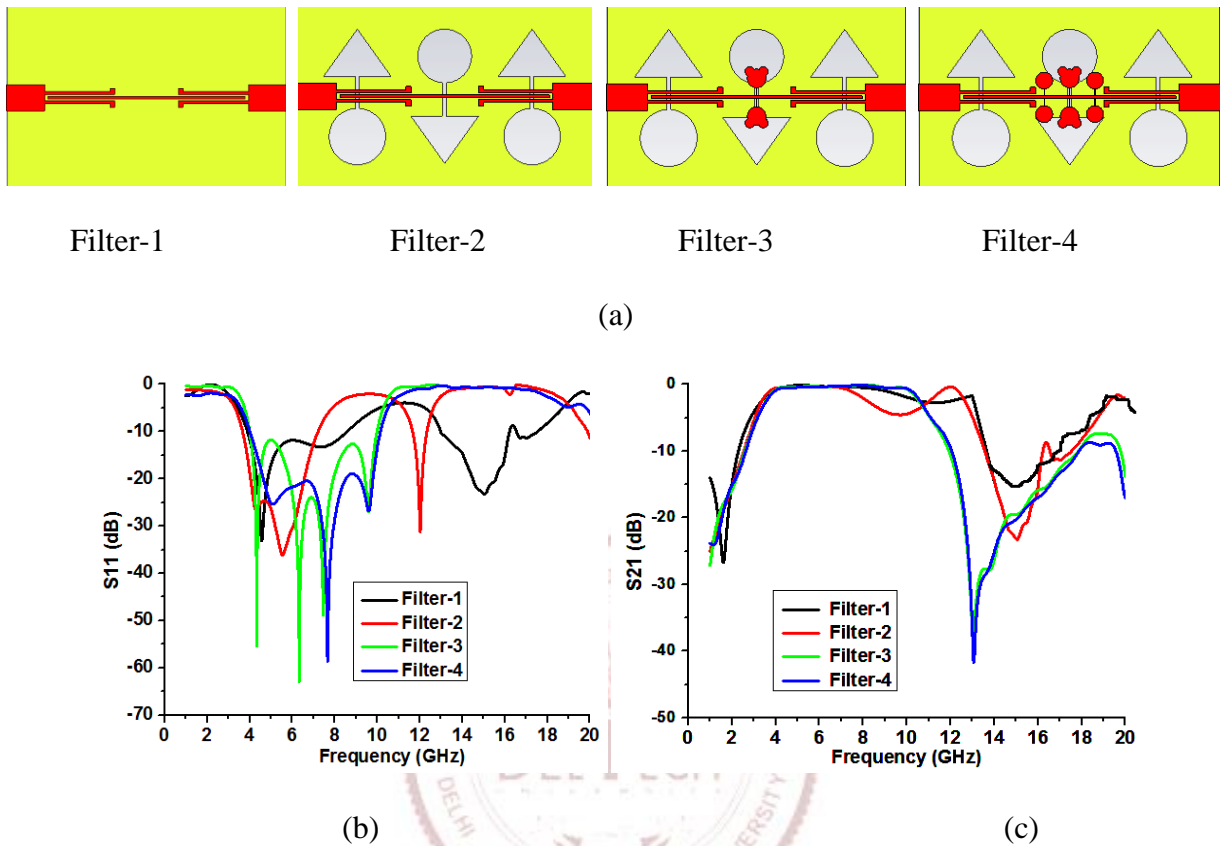


Fig.7.3 Step-by-step geometrical analysis of the proposed UWB bandpass filter (a) Geometrical steps
(b) Return Loss (c) Insertion Loss

Fig. 7.3 (a) represents the step-by-step geometrical analysis of the proposed UWB BPF with its s-parameters results as shown in Fig.7.3 (b). Filter-1 is designed with the combination of open-ended transmission line coupled with parallel transmission lines at feeding ends which provide bandpass characteristic in the range of 4 to 8GHz but it is not a good UWB bandpass filter in terms of S parameters as per the results shown in Fig. 7.3(b) & (c) respectively. To further improve the response in passband as well as in stopband, a periodic geometry of DGS is designed in the finite ground plane as shown in Filter-2 and corresponding results are shown in Fig. 7.3(b) & (c) with red colour. After the placement of the DGS, the results of Filter-2 are too far away from the intended

results, therefore, a Mickey-shaped open stub resonator is connected at the center of the open-ended transmission line as shown in Filter-3 and corresponding results are near to the intended UWB BPF with greater than 15dB return loss at 4-6GHz and 8-10GHz frequency band as shown in Fig. 7.3(b) & (c) with green colour. To further improve the return loss response, two circular-shaped open stub resonators are connected at an equal distance from port-1 and 2 over the open-ended transmission line as shown in Filter-4. Hence, the corresponding 3dB intended UWB (3.1-10.6GHz) bandwidth is achieved with greater than 20dB return loss and 0.5 dB insertion loss in passband as well as almost 18dB insertion loss and 0.4 dB return loss in stopband as shown in Fig. 7.3(b) & (c) with blue colour.

7.2.1 Design Equation of Parallel and Open-Ended Coupled Microstrip Line:

A half wavelength coupled transmission line resonators are used for a BPF design. These resonators are positioned parallel to each other to achieve maximum coupling by optimizing the space between resonators as illustrated in Fig.7.4. This structure provides a wider bandwidth to end coupled microstrip bandpass filter by suppression of harmonics. The proposed geometry of BPF is designed over a FR-4 substrate with 1.6mm thickness (h), relative permittivity (ϵ_r) = 4.4. The used substrate may be suitable for the TE mode propagation up to 25.89GHz as per the given relation $f_{TE} = c/(4 \times h \times [\sqrt{\epsilon_{eff}} - 1])$ where c is the speed of light (3×10^8 m/s) and ϵ_{eff} is the effective relative permittivity.

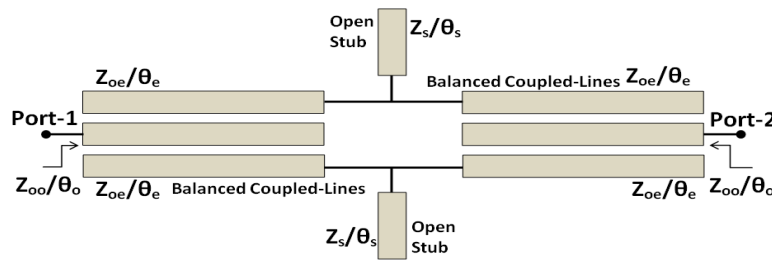


Fig.7.4. Transmission line model of the proposed UWB bandpass filter

Table -7.1 Elements value for optimum bandpass filter for ripple 0.5dB

FBW	$g_1 = g_5$	$g_2 = g_4$	g_3	$J_{1,2} = J_{4,5}$	$J_{2,3} = J_{3,4}$	N (order)
109%	1.7058	1.2296	2.5408	1.0016	0.7390	5

The design Equations of the filter are given as follows. All the values regarding bandpass analysis are shown in Table-7.1[137].

$$\frac{J_{01}}{Y_0} = \sqrt{\frac{\pi}{2} \times \frac{\text{FBW}}{g_0 g_1}} = 50.08 \quad (7.1)$$

$$\frac{J_{j,j+1}}{Y_0} = \frac{\pi \times \text{FBW}}{2} \times \frac{1}{\sqrt{g_j \times g_{j+1}}}, j = 1 \text{ to } n-1 \quad (7.2)$$

So, $J_{1,2}/Y_0 = J_{4,5}/Y_0 = 50.08\Omega$, $J_{2,3}/Y_0 = J_{3,4}/Y_0 = 39.65\Omega$

$$\frac{J_{n,n+1}}{Y_0} = \sqrt{\frac{\pi}{2} \times \frac{\text{FBW}}{g_n g_{n+1}}} \quad (7.3)$$

Where $g_0, g_1, g_2, \dots, g_n$ are the elements of a prototype bandpass filter with normalized cut-off $\Omega_c = 1$ and FBW is a fractional bandwidth of the filter. $J_{j,j+1}$ is the characteristic admittance of J-inverter and Y_0 is the characteristic admittance of the terminating transmission line. For the realization of J-inverter, Equations (7.1)-(7.3) [137], are used and characteristics impedance of parallel-coupled microstrip line resonators for even & odd-mode are obtained by Equations (7.4)-(7.5) as follows,

$$(Z_{oc})_{j,j+1} = \frac{1}{Y_0} \left[1 + \frac{J_{j,j+1}}{Y_0} + \left(\frac{J_{j,j+1}}{Y_0} \right)^2 \right] = 73\Omega, j = 0 \text{ to } n \quad (7.4)$$

$$(Z_{oo})_{j,j+1} = \frac{1}{Y_0} \left[1 - \frac{J_{j,j+1}}{Y_0} + \left(\frac{J_{j,j+1}}{Y_0} \right)^2 \right] = 35\Omega, j = 0 \text{ to } n \quad (7.5)$$

Where $Y_0 = 1/Z_0 = 1/50$ mho

The dimension of the filter can be determined by even & odd-mode characteristic impedance. The actual length of each coupled line can be determined by Equation (7.6).

$$L_j = \frac{\lambda_0}{4 \left(\sqrt{(\epsilon_{re})_j \times (\epsilon_{ro})_j} \right)} - \Delta L_j = 15.48 \text{mm} \quad (7.6)$$

Where, L_j is the equivalent length of open-ended microstrip line and, $(\epsilon_{re})_j = C_e/C_e^a = 4.08$, $(\epsilon_{ro})_j = C_o/C_o^a = 3.82$, C_e is the Even-mode capacitance of dielectric for parallel-coupled microstrip line. C_e^a is the Even-mode capacitance of air and C_o is the Odd-mode capacitance of dielectric. C_o^a is the Odd-mode capacitance in air, for coupled microstrip line.

7.2.2 Calculation of Microstrip Line Width (w):

Width of open-ended and parallel-coupled transmission lines by Equation (7.7) [137], as shown in Fig. 7.2(a)

$$\frac{w}{h} = \begin{cases} 8e^x \\ e^{2x} - 2 \end{cases}, w/h \leq 2 \quad (7.7)$$

The used width of the microstrip line (w) to design the proposed BPF is 1.89mm and the same is calculated by the following Equation.

$$\text{Where, } x = \frac{Z_0}{60} \sqrt{\frac{\epsilon_r + 1}{2} + \frac{\epsilon_r - 1}{\epsilon_r + 1} \left(0.23 + \frac{0.11}{\epsilon_r} \right)} = 1.39$$

Z_0 is the characteristic impedance of the microstrip transmission line i.e. 50Ω.

7.2.3 Calculation of Length of Parallel Microstrip Coupled Line (L_{mcl}):

The length of the line is calculated by using Equation (7.8). L_1 & L_2 is the length of open-ended parallel transmission lines which is optimized by simulation where L_1 is equal to L_2 due to symmetry as shown in Fig.7.2 (a).

$$L_{mcl} = 2L_1 + 2L_2 = \lambda_{eff} = 21.78\text{mm} \quad (7.8)$$

So individual length of a parallel-coupled line is $L_{mcl}/4 = 5.44\text{mm}$

Where the effective wavelength is $\lambda_{eff} = \frac{c}{f_{min} \sqrt{\epsilon_{eff}}} = 21.78\text{mm}$

and c is the speed of the light in a vacuum and ϵ_{eff} can be calculated [36] by Equation (7.9)

$$\epsilon_{eff} = \frac{\epsilon_r + 1}{2} + \frac{\epsilon_r - 1}{2} \frac{1}{\sqrt{1 + 12 \frac{h}{w}}} \approx 4.1 \quad (7.9)$$

7.2.4 Calculation & Analysis of MMR & DGS:

The multi-mode resonance techniques are offered low insertion loss as well as better matching with the transmission line. The proposed filter has mixed-shape resonators (circular & Mickey) and defected ground structures (arrowhead & circular) as shown in Fig. 7.5(a).

$$R_{dgs} \text{ (cm)} = \frac{P}{\sqrt{\left\{ 1 + \frac{2h}{\pi \epsilon_r P} \left[\ln \left(\frac{\pi P}{2h} \right) + 1.7726 \right] \right\}}} = 0.0209\text{cm} = 2.09\text{mm} \quad (7.10)$$

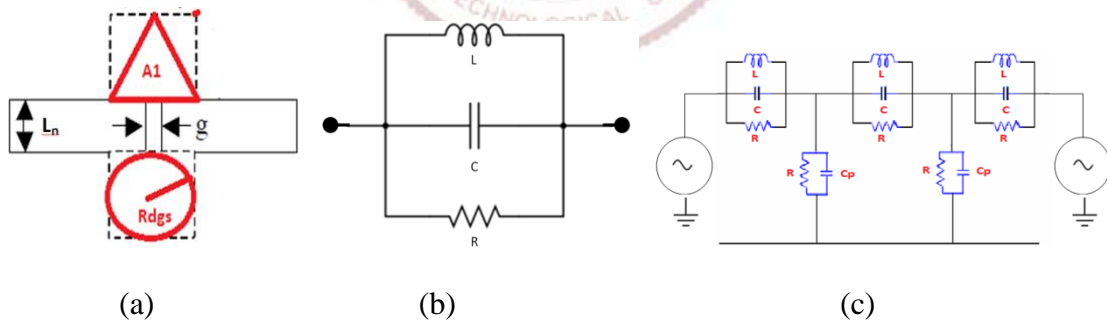


Fig.7.5. Proposed DGS (a) Structure (b) Equivalent circuit (c) Equivalent circuit model of all DGS structure

DGS provides a low profile and better degradation/sharpness (dB/GHz) in stopband to the filter. The radius of circular stubs and slots (R_{dgs}) is calculated from Equation (7.10) and approx the same area (A_1) is optimized for the triangular shape to increase required corner discontinuity [127].

Where, $p = \frac{8.791 \times 10^9}{f_{\min}} \times \frac{1}{\sqrt{\epsilon_r}} = 1.4$, f_{\min} is the lowest cut-off frequency of the proposed filter i.e. 3.1GHz.

The equivalent circuit of the proposed DGS structure is given in Fig.7.5 and values of resistance R (Ω), capacitance C(pF), and inductance L(nH) can be calculated by Equation (7.11)-(7.13) [137], respectively. The inductance and capacitance are mostly influenced by the width of the coupling gap (g) and the neck length (L_n) of the DGS slot. The resistance R (Ω) shows the loss in DGS structure which can be computed by Equation (7.11). Plate capacitance (C_p) is approximately 1835.68nF by calculation.

$$R(\Omega) = \frac{2 \times Z_0}{\sqrt{\left[\frac{1}{|S_{11}|^2} \left\{ 2 \times Z_0 \left(\omega_d C - \frac{1}{\omega_d L} \right) \right\}^2 - 1 \right]}} = 41.66 \Omega \quad (7.11)$$

Where, ω_d = design frequency of the filter i.e. 7.85GHz. The value of C(pF) and L(nH) can be computed by Equation (7.12) and (7.13).

$$C(\text{pF}) = 5 \left(\frac{f_c}{\pi} \right) (f_o)^2 (f_c)^2 = 2225.90 \text{pF} \quad (7.12)$$

$$L(\text{nH}) = \frac{250}{C} \left(\frac{\pi}{f_o} \right)^2 = 23.6 \text{nH} \quad (7.13)$$

7.2.5 BAND- STOP Characteristic Analysis:

Open-ended microstrip lines that are quarter wavelength length provide bandstop characteristics. Stopband filtering characteristic depends upon the characteristic impedance of the open-ended transmission line. This type of bandstop filter provides wide bandstop characteristics. The design procedure starts with a ladder-type bandpass prototype filter by using Equation (7.14) [137],

$$\Omega = \Omega_c \times \alpha \times \tan \left(\frac{\pi}{2} \times \frac{f}{f_o} \right) = 0.59 \quad (7.14)$$

Where $\alpha = \cot\left[\frac{\pi}{2}\left(1 - \frac{\text{FBW}}{2}\right)\right] = 1.63$

Ω and Ω_c are normalized frequency variable and cut-off frequency of prototype bandpass filter; f_0 and f are the mid-band frequency and frequency variable of the bandstop filter. FBW of the bandstop filter is defined by Equation (7.15)

$$\text{FBW} = \frac{f_2 - f_1}{f_0} = 0.6, \quad f_0 = \frac{f_1 + f_2}{2} = 15.3\text{GHz} \quad (7.15)$$

f_1 and f_2 are the lower and higher cut-off frequency of the bandstop filter. These types of bandstop characteristics periodically exist that's an odd multiple of frequency f_0 . At this frequency, open circuit stub length is an odd multiple of $\lambda_g/4$ where λ_g denotes the guided wavelength at frequency f_0 so they shorted with 50Ω line (port-1 and -2) provides bandstop characteristic. To design the n^{th} order optimum bandstop filter by using the optimum transfer function technique shown in Equation (7.16) at design frequency (7.75GHz) [137].

$$|S_{21}(f)|^2 = \frac{1}{1 + \varepsilon^2 \times F_n^2(f)} = 0.25 \quad (7.16)$$

Where ε denotes the ripple constant in passband and F_n is the filtering function which can be calculated by Equation (7.17)

$$F_n(f) = T_n\left(\frac{t}{t_c}\right) T_{n-1}\left(\frac{t\sqrt{1-t_c^2}}{t_c\sqrt{1-t^2}}\right) - U_n\left(\frac{t}{t_c}\right) U_{n-1}\left(\frac{t\sqrt{1-t_c^2}}{t_c\sqrt{1-t^2}}\right) = 2.25 \quad (\text{At design frequency} = 7.75\text{GHz}) \quad (7.17)$$

Where t is Richard's transform variable

$$t = j \tan\left(\frac{\pi}{2} \times \frac{f}{f_0}\right) = 0.879j \quad \text{and} \quad t_c = j \tan\left(\frac{\pi}{4} \times (2 - \text{FBW})\right) = 0.86j \quad (7.18)$$

$T_n(x)$ and $U_n(x)$ are Chebyshev's functions of order n and it is calculated by Equation (7.19) & (7.20) [137]

$$T_n(x) = \text{Cos}(n \times \text{Cos}^{-1} x) \quad (7.19)$$

$$U_n(x) = \text{Sin}(n \times \text{Cos}^{-1}x) \quad (7.20)$$

The characteristic impedance of each open-ended section can be determined by Equation (7.21), (7.22) & (7.23)

$$Z_{\text{Port1}} = Z_{\text{port2}} = Z_0 = 50\Omega \quad (7.21)$$

$$Z_i = \frac{Z_0}{g_i} \quad (7.22)$$

So that $Z_1 = Z_5 = 97.30\Omega$, $Z_2 = Z_4 = 53.32\Omega$ and $Z_3 = 50.14\Omega$

$$Z_{j,j+1} = \frac{Z_0}{J_{j,j+1}} \quad (7.23)$$

So that $Z_{1,2} = Z_{4,5} = 67.66\Omega$, $Z_{2,3} = Z_{3,4} = 69.95\Omega$

For bandstop lower cut-off frequency $f_1 = 10.6\text{GHz}$ and higher cut-off $f_2 = 20\text{GHz}$ then $f_0 = 15.4\text{GHz}$ and $\text{FBW} = 60\%$. By using Table-7.2 [137], value determines the characteristic impedance of the open-ended line to produce bandstop characteristics from 10.6GHz to 20GHz.

Table -7.2 Elements value for optimum bandstop filter for ripple less than 0.5dB

FBW	$g_1 = g_5$	$g_2 = g_4$	g_3	$J_{1,2} = J_{4,5}$	$J_{2,3} = J_{3,4}$	N (order)
60%	0.51385	0.93717	0.99711	0.75705	0.71472	5

7.3 UWB FILTER RESULTS AND DISCUSSION:

Simulated and measured results of the proposed filter have better agreement with the equivalent circuit(Fig.7.6(b)) results as depicted in Fig.7.6 (a) 3dB bandwidth of the filter throughout the passband is 3.1-10.6GHz and in stopband is 10.6-20GHz and the comparison of all requisite parameters is given in Table-7.3.

Table-7.3 Results of the proposed UWB filter in the passband & stopband

Parameters	S_{11} (Passband) (dB)	S_{21} (Passband) (dB)	S_{11} (Stopband) (dB)	S_{21} (Stopband) (dB)	Group Delay (ns)
Simulated	-20	-0.5	-0.4	-17	0.30
Measured	-19.5	-0.5	-0.5	-18	0.35

The group delay of S_{11} is defined by Equation $T_d(\omega) = -d\Phi/d\omega$, where Φ = phase of S_{11} and ω = angular frequency in rad/sec. The group delay of the coupled-line bandpass filter can be calculated directly from Equation (7.24) [137].

$$T_d(\omega) = \frac{d\phi}{d\omega} \times \frac{d\omega}{d\omega} \quad (7.24)$$

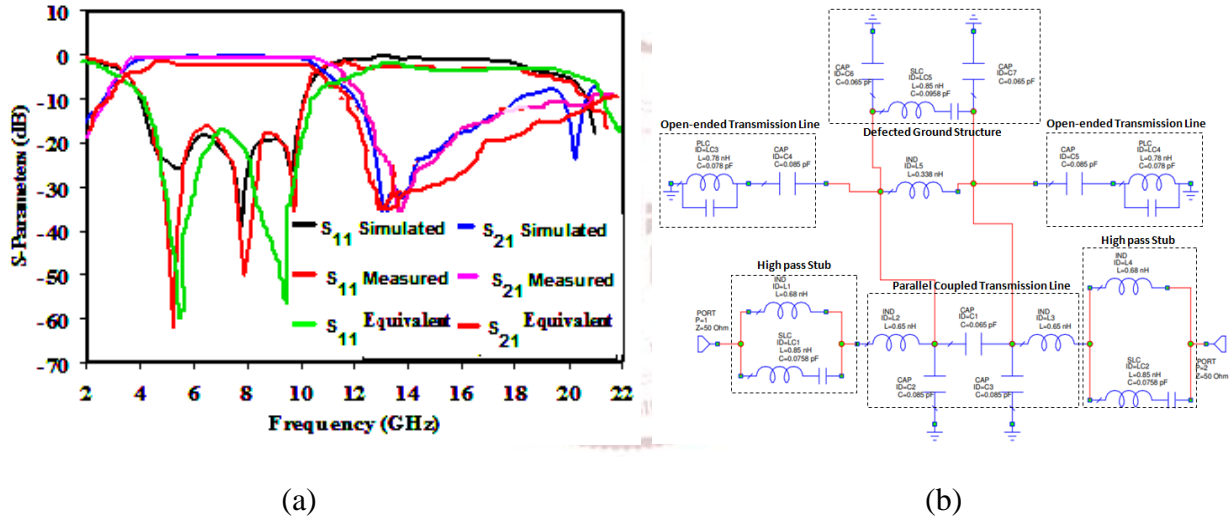


Fig.7.6 The proposed UWB BPF (a) Return (S_{11}) & Insertion loss (S_{21}) results- simulated, measured, and equivalent circuit (b) Equivalent circuit model

Where, ω' angular frequency of bandpass prototype filter and lowpass to bandpass transformation is given by Equation (7.25).

$$\omega' = \frac{\omega_0}{\omega_2 - \omega_1} \left(\frac{\omega}{\omega_0} - \frac{\omega_0}{\omega} \right) \quad (7.25)$$

Ideally at $\omega = \omega_0 = 7.75\text{GHz}$ $\omega' = 0$ and group delay of coupled line $T_{\text{dcpl}} = 0$ and calculated by

Equation (7.26)

$$T_{\text{dcpl}} = -\frac{\omega_0}{(\omega_2 - \omega_1)} \left(\frac{1}{\omega_0} + \frac{\omega_0}{\omega^2} \right) \frac{\delta\phi}{\delta\omega} \quad (7.26)$$

Now, $S_{11} = \frac{Z_{\text{in}} - Z_0}{Z_{\text{in}} + Z_0}$, where Z_{in} = purely imaginary and Z_0 = purely real quantity. So, $S_{11} = \frac{jX_{\text{in}} - Z_0}{jX_{\text{in}} + Z_0}$ and

$$\phi = -\tan^{-1} \left(\frac{X_{\text{in}}}{Z_0} \right) - \tan^{-1} \left(\frac{X_{\text{in}}}{Z_0} \right), \quad \phi = -2 \tan^{-1} \left(\frac{X_{\text{in}}}{Z_0} \right)$$

The transfer function of UWB BPF is given in terms of Bessel polynomial in **Equation (7.27)** [137]

and group delay is extracted from s-parameters as follows

$$S_{21}(j\omega) = \frac{B_0}{\sum_{k=0}^{k=n} \left\{ \frac{(2n-k)!}{2^{n-k}} \right\} (j\omega)^k (k \times (n-k))!} \quad (7.27)$$

Where B_0 is Bessel polynomial, which provides maximum flat group delay response in the passband, and “n” is several poles of the filter. Therefore, the calculated group delay at design frequency at 6.75GHz by **Equation (7.27)** is 0.278nsec in the passband which is near to the simulated group delay (0.3nsec). The simulated & measured results of group delay are 0.30nsec & 0.35nsec in UWB bandwidth respectively, which shows the permissible agreement as shown in **Fig.7.7**. The group delay should be constant from its definition like “the rate of change of transmission phase angle for frequency” and From **Fig.7.7**, it is obvious that group delay is almost constant in the entire passband and stopband respectively.

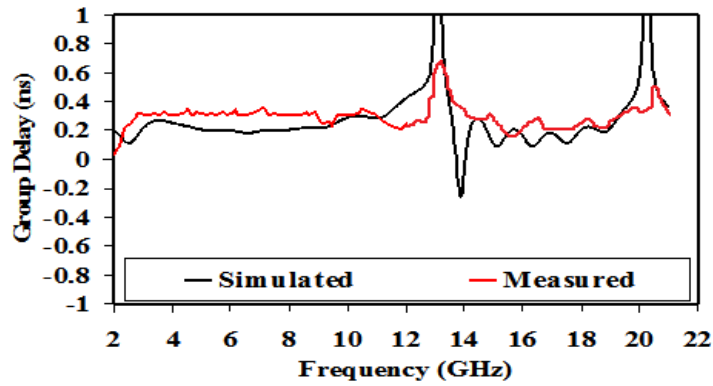


Fig.7.7. Measured & simulated group delay of a proposed UWB BPF with stopband characteristics

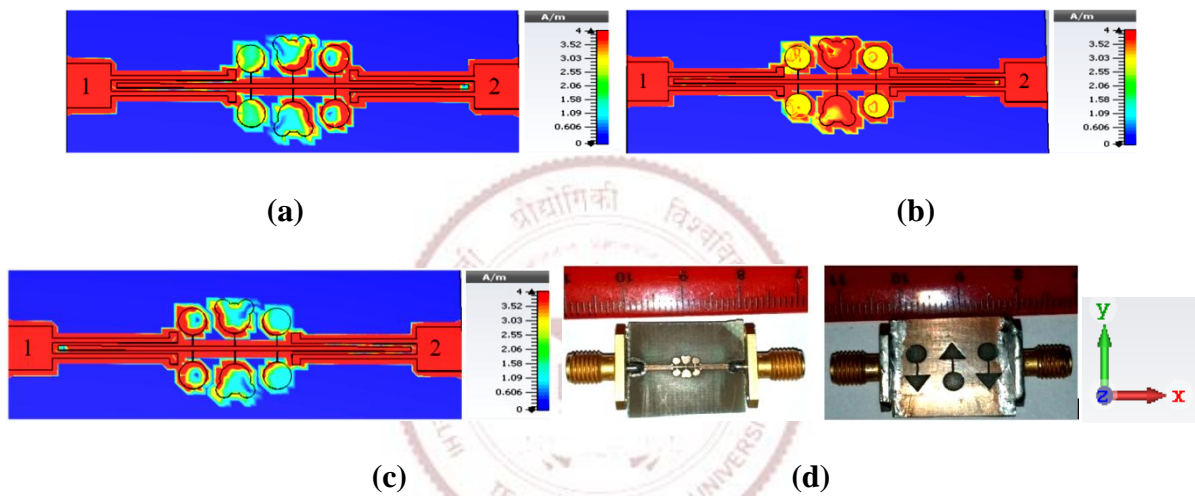


Fig.7.7. Simulated current density of the designed filter at (a) 4.65GHz (b) 7.88GHz (c) 9.52GHz respectively (d) Front and back view prototype of a filter

The simulated current density of the proposed filter is represented in Fig.7.8 including images of the prototype filter which is indicating the performance of open-ended stub resonators at various frequencies. Therefore, Fig. 7.8(a) shows that the filter is resonating at 4.65GHz due to the circular resonator which is nearest to the port-2 similarly Fig. 7.8(b) shows the filter is resonating at 7.88GHz due to the Mickey-shaped resonator, and Fig. 7.8(c) shows the filter is resonating at 9.52GHz due to the circular-shaped resonator nearest to port-1. Hence, these multi-modes resonators are playing a vital role to obtain UWB bandwidth. Table-7.4 shows a comparison of different UWB BPFs with the proposed filter like permissible return loss, smooth group delay variation in the

passband including stopband. The insertion loss of the proposed filter in the passband is 0.5dB i.e. only 1.12% power is a loss in passband 3.1-10.6GHz. The front and back view of the proposed fabricated prototype filter is shown in Fig.7.8(d).

Table 7.4 Comparison of various parameters of the proposed filter with published articles

S_{11} (Passband) (dB)	S_{21} (Passband) (dB)	Group Delay (ns)	Size (λ_g^2)	Material	Cost of Material
-20	-1.1	0.30	$0.74\lambda_g \times 0.74\lambda_g$	Carbon Tetra- chloride	High [110]
-18	-0.9	0.48	$0.58\lambda_g \times 0.69\lambda_g$	RT 5880	High [117]
-15	-1.0	0.50	$0.69\lambda_g \times 0.32\lambda_g$	RT 5880	High [121]
-20	-0.7	0.75	$0.73\lambda_g \times 0.73\lambda_g$	RT 6010	High [122]
-20	-1.0	0.65	$0.55\lambda_g \times 0.64\lambda_g$	ROGERS	High [130]
-20	-0.5	0.30	$0.74\lambda_g \times 0.67\lambda_g$	FR-4	Low [P]

7.4 SUMMARY:

In this Chapter, a UWB bandpass filter with stopband characteristics is presented via a multi-mode resonator technique. MMR is formed by loading three dumbbell-shaped (Mickey & circular) shunt stubs placed in the center and two symmetrical locations from ports respectively. Three circular and arrowhead DGS structures on the ground plane are introduced to achieve UWB bandwidth including a better roll-off rate. The proposed filter exhibits stopband characteristics from 10.8-20GHz with 0.4dB return loss. The group delay and roll-off rate of the designed filter are less than 0.30ns in the passband and 16dB/GHz at lower and higher cut-off frequency respectively. The dimension of the filter is $22 \times 20 \text{mm}^2$ and fabricated on a cost-effective substrate. All simulated results are verified through the experimental results. A bandpass filter with wide stopband characteristics has been designed and analyzed for UWB application using the MMR technique. The designed filter has

achieved good insertion loss less than 0.5dB and 0.3ns group delay in the intended passband. The prototype of the filter is compact as $22 \times 20 \text{mm}^2$ with a 109% fractional bandwidth. From [Table-7.4](#), it is observed that this filter has better responses although it is fabricated over FR-4 substrate than referred filters. The proposed filter is suited for recent weather reporting Radar, Imaging, and Satellite receiver systems because simulated results have good agreement with measured results.



CHAPTER-8

CONCLUSION AND FUTURE SCOPE

8.1 CONCLUSION:

This thesis presents designing and analysis of microwave components i.e. antenna, metasurface absorber, and filter which are used in MIMO wireless communication systems. The proposed structures are low profile, high efficiency, super-wideband, and high gain with acceptable diversity performance used in a microwave and THz communication system. It is validated that each component (prototype) designs are suitable for microwave/THz communication.

Following conclusions are derived from the research carried out in the thesis:

8.1.1. High Isolation Super Wideband WLAN Notched Dual Polarized MIMO Antenna For Multiple Applications:

1. A super wideband microstrip MIMO antenna with mushroom type EBG with an E-shaped decoupling structure on the ground is presented for high isolation and high front to back ratio (FBR).
2. To achieve super wideband impedance bandwidth (185%), a step impedance microstrip feeding structure is introduced.
3. This MIMO antenna is circularly polarized at 1.575GHz and 26.0GHz by using the circular slot on the radiating patch.
4. The EBG structure reduces the back radiations and improves the FBR in lower (1.5-5GHz) and higher band (25-40GHz).
5. The proposed MIMO antenna features SWB (Super Wide Band) bandwidth and compact size ($55.6 \times 50.5 \times 1.6 \text{mm}^3$) on the FR-4 substrate.
6. This MIMO antenna is suitable for defense applications and handheld device covering

GPS/ DCS/ PCS/ UMTS/ WI-BRO/ ISM/ IRNSS/ LTE (M/HB)/ BLUETOOTH / IOT/SUB 5G/WIMAX/mm range 5G/X/Ku/K/Ka-band.

7. The 3D radiation pattern based ECC and diversity parameters of the MIMO antenna is also verified by simulation and experimental results in the prescribed range. Finally, this antenna is tested in a realistic application environment.

8.1.2. High Diversity Gain MIMO Antenna for UWB Application With WLAN Notch

Band Characteristic Including Human Interface Devices:

1. A UWB–MIMO antenna with the WLAN band-notch (5.1–5.85 GHz) characteristic is offered.
2. This antenna consists of two radiated patch feeding with a tapered line and fabricated on FR-4 substrate having the size of $36 \times 22 \times 1.6 \text{ mm}^3$.
3. A notched-band response is achieved by introducing an open-ended stub on the ground plane which mitigates the WLAN (5.1-5.85GHz) band to avoid interference from the UWB band.
4. Proposed antenna has an impedance bandwidth from 3.1 to 11.2GHz as well as high isolation i.e. S_{21} is less than -30dB . Radiation efficiency is greater than 0.75 except for the notched band (< 0.5).
5. Diversity performance are also set the new paradigm in terms of ECC (≤ 0.008), TARC ($\leq -25 \text{ dB}$), CCL ($\leq 0.3 \text{ bits/s/Hz}$), Mean effective gain ratio (MEGi) $\cong 1$, and Directive gain ($\geq 8.95 \text{ dB}$) except the notched band.
6. Simulated results of the proposed antenna are tested and verified by the experimental results. Proposed antenna characteristics are also found suitable for a human interface device, low-cost, and easily fabricated.

8.1.3. Meander Line Inspired Penta-Band MIMO Antenna for Wireless Applications:

1. A meander line-shaped penta band (2.165-2.48, 2.59-2.72, 2.89-2.97, 3.10-3.32, 3.38-3.46GHz) 4-elements multiple-input-multiple-output (MIMO) antenna is presented.
2. Radiation patterns of the antenna shows Right Handed Circular Polarization (RHCP) at port-1 and 3 and Left Handed Circular Polarization LHCP at port-2 and 4 at frequencies 2.2, 2.4GHz. These frequency ranges are widely used for MSS and IoT applications.
3. This antenna is designed with compact size $50 \times 70 \times 1.6 \text{mm}^3$ on the FR-4 substrate with excellent diversity performance in pentaband.
4. Simulated results of antenna-like return loss, isolation, and diversity parameters have also been verified experimentally, which are in the acceptable range.
5. This antenna is tested in a realistic environment for the SAR application. This antenna is appropriate for Mobile satellite services (MSS), ISM, Broadband Radio Services (BRS) and Educational Broadband Services (EBS), WiMAX Radio Location Services, and Amateur Radio Services respectively.

8.1.4 Design of Metasurface Absorber for Low RCS and High Isolation MIMO Antenna for Radiolocation and Aeronautical Radio Navigation Applications:

1. This MIMO antenna and absorber structure design on FR-4 substrate with $55 \times 40 \times 1$ and $10 \times 10 \times 1 \text{mm}^3$ respectively.
2. At 8.78GHz and 12.52GHz Metamaterial absorber absorbance is 98.89% and 98.16% respectively and its reflectivity is almost zero.
3. The MIMO antenna performance is judged by antenna parameters and diversity performance i.e. return loss, isolation, maximum gain, ECC, DG, TARC, MEG, CCL, and Channel capacity. At 8.78GHz proposed MIMO antenna achieved isolation greater than 28dB and ECC is less than 0.002 which concludes that this MIMO antenna is suitable for radiolocation and aeronautical radio navigation applications.

8.1.5. High Isolation and High Gain Super-Wideband (0.33-10THz) MIMO Antenna for THz Applications:

1. An elliptical-shaped microstrip feed super-wideband (SWB) 2-elements MIMO antenna is proposed for high-speed terahertz (THz) applications. It has 2:1 VSWR operating bandwidth from 0.33-10THz (187%) with 19dBi peak gain.
2. Radiation Efficiency is also greater than 70% throughout SWB bandwidth. The 2-element MIMO antenna is designed with a compact size of $1000 \times 1400 \times 101.29 \mu\text{m}^3$ on the RT5880 substrate having a relative permittivity of 2.2.
3. Simulated results of antenna-like return loss, isolation, gain, efficiency, and diversity performance parameters (ECC, DG, TARC, etc.) are in an acceptable range. Therefore, this antenna is useful for Sub 5G, vehicular communications, Imaging, 3D printing, Terahertz wave Radar, Health care, and Astronomical radiometric application.

8.1.6 Compact Bandpass Filter with Extended Stopband Characteristic for UWB application using MMR Technique:

1. UWB bandpass with an extended stopband filter is presented by using multi-mode resonator techniques. MMR is formed by loading three dumbbell-shaped (Micky & circular) shunt stubs placed in the center and two symmetrical locations from ports, respectively.
2. Filter performance is enhanced by introducing three circular and arrowhead, DGS structures on the ground to achieved UWB bandwidth including better sharpness of the filter. The proposed filter exhibits passband characteristics for the UWB range i.e. 3.1-10.6GHz with a return loss of **20dB** and stopband range from 10.8-20GHz with **0.4dB** return loss.

3. The group delay and sharpness of the designed filter are $<0.30\text{ns}$ in the passband and 16dB/GHz at lower and higher cut-off frequency respectively. The dimension of the filter fabricated on the cost-effective substrate (FR-4) is $22\times 20\text{mm}^2$ and the simulated frequency response is finally verified by the experimental results.

8.2. FUTURE SCOPE OF WORK:

Based on the work done during the Ph.D., Some important research problem is identified which can be investigated in the future:

8.2.1 MIMO Antennas:

1. Massive MIMO antenna can be designed by placing more antennas for attaining high channel capacity and a high data rate for 5G communication.
2. Multiple user MIMO antenna and Smart antenna can be designed with high throughput, better channel capacity, and high data rate. Beamforming and splitting will also be used for designing Multiple Users (MU) MIMO antenna.
3. Quantum MIMO Antenna is a very emerging field for the future, so, Graphene-based THz range quantum MIMO antenna for B5G wireless communication can also be designed.
4. AOC (Antenna on-chip) also plays a very important role in future 5G and B5G wireless communication so in the future work can be extended in this emerging technology.
5. Reconfigurability (frequency, pattern, and polarization) to be added in the future for MIMO and Massive MIMO antennas.
6. Massive MIMO antenna works as a wireless sensor for the biomedical field (detection of the brain tumour and breast cancer tissue) can be designed.

8.2.2 Microwave and THz Filters:

1. SIW based reconfigurable filter can be made for enhancing the performance.
2. Graphene and vanadium oxide-based THz filters can also be investigated in the future.
3. Active filters may also be explored.

8.2.3 Metamaterial Absorber (MMA):

1. UWB MMA can be investigated.
2. Vanadium oxide-based reconfigurable wideband THz MMA can be made in the future.

All the above-mentioned structures can be investigated in the real-world for wireless communication systems.



REFERENCES

- [1] F. Government and N. Telecommunications, “Federal Communications Commission Before the Federal Communications Commission Washington, D .C. 20554 In the Matter of Revision of Part 15 of the Commission’s Rules Regarding Ultra-Wideband Transmission Systems Petition for Waiver of the Part 15 UWB,” vol. 24558, no. 98, 2010.
- [2] S. Tripathi, A. Mohan, and S. Yadav, “A compact MIMO/diversity antenna with WLAN band-notch characteristics for portable UWB applications,” *Progress In Electromagnetics Research C*, vol. 77, no. April, pp.29–38, 2017.
- [3] M. S. Khan, S. A. Naqvi, A. Iftikhar, S. M. Asif, A. Fida, and R. M. Shubair, “A WLAN band-notched compact four element UWB MIMO antenna,” *International Journal of RF and Microwave Computer-Aided Engineering*, vol. 30, no. 9, pp. 1–10, 2020.
- [4] D. Yadav, M. P. Abegaonkar, S. K. Koul, V. Tiwari, and D. Bhatnagar, “Two element band-notched UWB MIMO antenna with high and uniform isolation,” *Progress In Electromagnetics Research M*, vol. 63, no. November 2017, pp. 119–129, 2018.
- [5] J. P. Kumar, “Ultra Wideband MIMO Notched Antenna for WLAN and Mobile Applications,” vol. 118, no. 9, pp. 929–934, 2018.
- [6] G. Liu, Y. Liu, and S. Gong, “Compact uniplanar UWB MIMO antenna with band-notched characteristic,” *Microwave and Optical Technology Letters*, vol. 59, no. 9, pp. 2207–2212, 2017.
- [7] A. S. Fazal *et al.*, “A compact UWB CPW-fed antenna with inverted L-shaped slot for WLAN band notched characteristics,” *2017 11th European Conference on Antennas and Propagation, EUCAP 2017*, pp. 981–984, 2017.
- [8] T. Rao, A. Sudhakar, and K. Raju, “Novel Technique of Mimo Antenna Design for UWB Applications Using Defective Ground Structures,” *Journal of Scientific and Industrial Research*, vol. 77, no. 1, pp. 66–69, 2018.
- [9] Malekpour, N., Amin Honarvar, M., Dadgarpur, A., Virdee, B.S. and Denidni, T.A., Compact UWB mimo antenna with band-notched characteristic. *Microwave and Optical Technology Letters*, Vol.59, no.(5), pp.1037-1041, 2017.
- [10] A. Toktas, “G-shaped band-notched ultra-wideband MIMO antenna system for mobile terminals,” *IET Microwaves, Antennas and Propagation*, vol. 11, no. 5, pp. 718–725, 2017.
- [11] M. S. Khan *et al.*, “Ultra-compact reconfigurable band reject uwb MIMO antenna with four radiators,” *Electronics (Switzerland)*, vol. 9, no. 4, pp. 1–13, 2020.

- [12] R. Mathur and S. Dwari, "Compact planar reconfigurable UWB-MIMO antenna with on-demand worldwide interoperability for microwave access/wireless local area network rejection," *IET Microwaves, Antennas & Propagation*, vol. 13, no. 10, pp. 1684–1689, 2019.
- [13] M. S. Khan, A. Iftikhar, R. M. Shubair, A. D. Capobianco, B. D. Braaten, and D. E. Anagnostou, "A four element, planar, compact UWB MIMO antenna with WLAN band rejection capabilities," *Microwave and Optical Technology Letters*, vol. 62, no. 10, pp. 3124–3131, 2020.
- [14] Y. Zhang, X. Wu, Y. Li, and Z. Liu, "A compact printed UWB MIMO antenna with WLAN band rejection," *2016 Progress In Electromagnetics Research Symposium, PIERS 2016 - Proceedings*, vol. 2, pp. 2464–2466, 2016.
- [15] T. S. Sun, J. S. Hong, and J. Cheng, "A Compact Miniaturized UWB-MIMO Antenna with WLAN Band-Notched Function," *2019 International Conference on Microwave and Millimeter Wave Technology, ICMMT 2019 - Proceedings*, pp. 10–13, 2019.
- [16] M. S. Khan, A. D. Capobianco, S. Asif, A. Iftikhar, B. Ijaz, and B. D. Braaten, "Compact 4×4 UWB-MIMO antenna with WLAN band rejected operation," *Electronics Letters*, vol. 51, no. 14, pp. 1048–1050, 2015.
- [17] J. Aquil, D. Sarkar, and K. V. Srivastava, "A quasi self-complementary UWB MIMO antenna having WLAN-band notched characteristics," *Applied Electromagnetics Conference, AEMC 2017*, vol. 2018-January, pp. 1–2, 2018.
- [18] M. A. Layegh, C. Ghobadi, J. Nourinia, Y. Samoodi, and S. N. Mashhadi, "Adaptive Neuro-Fuzzy Inference System approach in bandwidth and mutual coupling analyses of a novel UWB MIMO antenna with notch bands applicable for massive MIMOs," *AEU - International Journal of Electronics and Communications*, vol. 94, no. July, pp. 407–417, 2018.
- [19] W. Wu, B. Yuan, and A. Wu, "A quad-element UWB-MIMO antenna with band-notch and reduced mutual coupling based on EBG structures," *International Journal of Antennas and Propagation*, vol. 2018, 2018.
- [20] A. K. Gautam, S. Yadav, and K. Rambabu, "Design of ultra-compact UWB antenna with band-notched characteristics for MIMO applications," *IET Microwaves, Antennas and Propagation*, vol. 12, no. 12, pp. 1895–1900, 2018.
- [21] A. Bhattacharya, B. Roy, S. K. Chowdhury, and A. K. Bhattacharjee, "Computational and experimental analysis of a low-profile, isolation-enhanced, band-notch UWB-MIMO antenna," *Journal of Computational Electronics*, vol. 18, no. 2, pp. 680–688, 2019.

- [22] S. Kumar, R. Kumar, R. Kumar Vishwakarma, and K. Srivastava, "An improved compact MIMO antenna for wireless applications with band-notched characteristics," *AEU - International Journal of Electronics and Communications*, vol. 90, pp. 20–29, 2018.
- [23] E. Thakur, N. Jaglan, S. D. Gupta, and B. K. Kanaujia, "A compact notched UWB MIMO antenna with enhanced performance," *Progress In Electromagnetics Research C*, vol. 91, no. March, pp. 39–53, 2019.
- [24] P. Palanisamy and M. Subramani, "Closely Mounted UWB MIMO Antenna with Notch Characteristics for Short-Range Wireless Video Transmission Application," *IETE Journal of Research*, vol. 2063, no. May, 2020.
- [25] W. Balani *et al.*, "Design Techniques of Super-Wideband Antenna-Existing and Future Prospective," *IEEE Access*, vol. 7, pp. 141241–141257, 2019.
- [26] P. Palanisamy and M. Subramani, "Design and Experimental Analysis of Miniaturized Octa-Port UWB/SWB-MIMO Antenna with Triple-Band Rejection Characteristics," *IETE Journal of Research*, vol. 0, no. 0, pp. 1–15, 2020.
- [27] M. Manohar, R. S. Kshetrimayum, and A. K. Gogoi, "Super wideband antenna with single band suppression," *International Journal of Microwave and Wireless Technologies*, vol. 9, no. 1, pp. 143–150, 2017.
- [28] M. Elhabchi, M. N. Srfi, and R. Touahni, "A novel modified U-shaped microstrip antenna for super wide band (SWB) applications," *Analog Integrated Circuits and Signal Processing*, vol. 102, no. 3, pp. 571–578, 2020.
- [29] D. K. Raheja, S. Kumar, and B. K. Kanaujia, "Compact quasi-elliptical-self-complementary four-port super-wideband MIMO antenna with dual band elimination characteristics," *AEU - International Journal of Electronics and Communications*, vol. 114, p. 153001, 2020.
- [30] H. Ullah, S. U. Rahman, Q. Cao, I. Khan, and H. Ullah, "Design of SWB MIMO Antenna with Extremely Wideband Isolation," *Electronics*, vol. 9, no. 1, p. 194, 2020.
- [31] C. Yu *et al.*, "A Super-Wideband and High Isolation MIMO Antenna System Using a Windmill-Shaped Decoupling Structure," *IEEE Access*, vol. 8, pp. 115767–115777, 2020.
- [32] P. Kumar, S. Urooj, and F. Alrowais, "Design of quad-port MIMO/diversity antenna with triple-band elimination characteristics for super-wideband applications," *Sensors (Switzerland)*, vol. 20, no. 3, pp. 1–13, 2020.

- [33] A. Bhattacharya, B. Roy, and A. K. Bhattacharjee, "Compact, Isolation Enhanced, Band-Notched SWB-MIMO Antenna Suited for Wireless Personal Communications," *Wireless Personal Communications*, no. 0123456789, 2020.
- [34] T. Iyama, T. Onishi, Y. Tarusawa, S. Uebayashi, and T. Nojima, "Novel specific absorption rate (SAR) measurement method using a flat solid phantom," *IEEE Transactions on Electromagnetic Compatibility*, vol. 50, no. 1, pp. 43–51, 2008.
- [35] S. L. Loyka, "Channel capacity of MIMO architecture using the exponential correlation matrix," *IEEE Communications Letters*, vol. 5, no. 9, pp. 369–371, 2001.
- [36] Y. K. Awasthi, H. Singh, M. Sharma, S. Kumari, and A. K. Verma, "Computer-aided design-based circuit model of microstrip line for terahertz interconnects technology," *The Journal of Engineering*, vol. 2017, no. 9, pp. 512–526, 2017.
- [37] Zhu, J., Feng, B., Peng, B., Deng, L. and Li, S., Multiband printed mobile MIMO antenna for WWAN and LTE applications. *Microwave and Optical Technology Letters*, vol.59, no. (6), pp.1446-1450, 2017.
- [38] Y. Yang, Z. Zhao, and Z. Nie, "Closely spaced multi-band MIMO antenna for mobile terminals," *Progress in Electromagnetics Research Symposium*, pp. 1222–1226, 2017.
- [39] N. O. Parchin, H. J. Basherlou, Y. I. A. Al-Yasir, A. Ullah, R. A. Abd-Alhameed, and J. M. Noras, "Multi-band MIMO antenna design with user-impact investigation for 4G and 5G mobile terminals," *Sensors (Switzerland)*, vol. 19, no. 3, pp. 1–16, 2019.
- [40] Li, K., Shi, Y. and Liang, C.H., Quad-element multi-band antenna array in the smart mobile phone for LTE MIMO operations. *Microwave and Optical Technology Letters*, vol.58, no. (11), pp.2619-2626, 2016.
- [41] K. Sumathi and M. Abirami, "Hexagonal shaped fractal MIMO antenna for multiband wireless applications," *Analog Integrated Circuits and Signal Processing*, vol. 104, no. 3, pp. 277–287, 2020.
- [42] J. Banerjee *et al.*, "An Orthogonally Oriented Multiband MIMO Antenna for WLAN, C-Band and X-Band Wireless Applications," *2020 IEEE Calcutta Conference, CALCON 2020 - Proceedings*, pp. 328–332, 2020.
- [43] N. Pouyanfar, C. Ghobadi, J. Nourinia, K. Pedram, and M. Majidzadeh, "A compact multi-band MIMO antenna with high isolation for C and X bands using defected ground structure," *Radioengineering*, vol. 27, no. 3, pp. 686–693, 2018.
- [44] P. S. Rao, K. J. Babu, and A. M. Prasad, "Compact multi-band MIMO antenna with improved isolation," *Progress In Electromagnetics Research M*, vol. 62, no. November, pp. 199–210, 2017.

- [45] R. Saleem, M. Bilal, H. T. Chattha, S. Ur Rehman, A. Mushtaq, and M. F. Shafique, "An FSS Based Multiband MIMO System Incorporating 3D Antennas for WLAN/WiMAX/5G Cellular and 5G Wi-Fi Applications," *IEEE Access*, vol. 7, pp. 144732–144740, 2019.
- [46] L. Asadpor and M. Rezvani, "Multiband microstrip MIMO antenna with CSRR loaded for GSM and LTE applications," *Microwave and Optical Technology Letters*, vol. 60, no. 12, pp. 3076–3080, 2018.
- [47] K. V. Babu and B. Anuradha, "Design of multi-band minkowski MIMO antenna to reduce the mutual coupling," *Journal of King Saud University - Engineering Sciences*, vol. 32, no. 1, pp. 51–57, 2020.
- [48] J. Bai, R. Zhi, W. Wu, M. Shangguan, B. Wei, and G. Liu, "A novel multiband MIMO antenna for TD-LTE and WLAN applications," *Progress in Electromagnetics Research Letters*, vol. 74, no. March, pp. 131–136, 2018.
- [49] T. L. Chiu, L. Huitema, O. Pajona, and T. Monediere, "Compact and multiband MIMO dielectric resonator antenna for automotive LTE communications," *International Journal of Antennas and Propagation*, vol. 2018, 2018.
- [50] Fu, Y. and Yang, G.M., Design of compact multiband MIMO antenna for the mobile handsets. *Microwave and Optical Technology Letters*, vol.58, no. (10), pp.2411-2415, 2016.
- [51] M. Ikram, M. S. Sharawi, A. Shamim, and A. Sebak, "A multiband dual-standard MIMO antenna system based on monopoles (4G) and connected slots (5G) for future smart phones," *Microwave and Optical Technology Letters*, vol. 60, no. 6, pp. 1468–1476, 2018.
- [52] A. Kumar, A. Q. Ansari, B. K. Kanaujia, and J. Kishor, "High isolation compact four-port MIMO antenna loaded with CSRR for multiband applications," *Frequenz*, vol. 72, no. 9–10, pp. 415–427, 2018.
- [53] N. K. Maurya and R. Bhattacharya, "Design of compact dual-polarized multiband MIMO antenna using near-field for IoT," *AEU - International Journal of Electronics and Communications*, vol. 117, p. 153091, 2020.
- [54] X. S. Luo, Z. Bin Weng, W. J. Zhang, and L. Yang, "Compact planar multiband MIMO antenna based on composite right/left-handed transmission line for mobile phone applications," *Microwave and Optical Technology Letters*, vol. 60, no. 6, pp. 1505–1511, 2018.

- [55] D. Sarkar and K. V. Srivastava, "Compact four-element SRR-loaded dual-band MIMO antenna for WLAN/WiMAX/WiFi/4G-LTE and 5G applications," *Electronics Letters*, vol. 53, no. 25, pp. 1623–1624, 2017.
- [56] Z. Xu, Q. Zhang, and L. Guo, "A printed multiband MIMO antenna with decoupling element," *International Journal of Microwave and Wireless Technologies*, vol. 11, no. 4, pp. 413–419, 2019.
- [57] Y. Yang, Q. Chu, and C. Mao, "Multiband MIMO Antenna for GSM, DCS, and LTE Indoor Applications," *IEEE Antennas and Wireless Propagation Letters*, vol. 15, no. c, pp. 1573–1576, 2016.
- [58] S. Rajkumar, N. Vivek Sivaraman, S. Murali, and K. T. Selvan, "Heptaband swastik arm antenna for MIMO applications," *IET Microwaves, Antennas & Propagation*, vol. 11, no. 9, pp. 1255–1261, 2017.
- [59] G. Das, A. Sharma, R. K. Gangwar, and M. S. Sharawi, "Performance improvement of multiband MIMO dielectric resonator antenna system with a partially reflecting surface," *IEEE Antennas and Wireless Propagation Letters*, vol. 18, no. 10, pp. 2105–2109, 2019.
- [60] M. Abdullah, Q. Li, W. Xue, G. Peng, Y. He, and X. Chen, "Isolation enhancement of MIMO antennas using shorting pins," *Journal of Electromagnetic Waves and Applications*, vol. 33, no. 10, pp. 1249–1263, 2019.
- [61] Roshna, Thazhe Koralath, Unmimadhavan Deepak, and Pezhohil Mohanan. "Compact UWB MIMO antenna for tridirectional pattern diversity characteristics." *IET Microwaves, Antennas & Propagation* 11, no. 14 (2017): 2059-2065.
- [62] Katie, Mohannad Obaid, Mohd Faizal Jamlos, Abdulrahman Shueai Mohsen Alqadami, and Mohd Aminudin Jamlos. "Isolation enhancement of compact dual-wideband MIMO antenna using flag-shaped stub." *Microwave and Optical Technology Letters* 59, no. 5 (2017): 1028-1032.
- [63] J. Duan, K. Xu, X. Li, S. Chen, P. Zhao, and G. Wang, "Dual-band and enhanced-isolation MIMO antenna with L-shaped meta-rim extended ground stubs for 5G mobile handsets," *International Journal of RF and Microwave Computer-Aided Engineering*, vol. 29, no. 8, pp. 1–8, 2019.
- [64] L. Wang *et al.*, "Compact UWB MIMO Antenna with High Isolation Using Fence-Type Decoupling Structure," *IEEE Antennas and Wireless Propagation Letters*, vol. 18, no. 8, pp. 1641–1645, 2019.
- [65] B. J. Niu and J. H. Tan, "Compact SIW cavity MIMO antenna with enhanced bandwidth and high isolation," *Electronics Letters*, vol. 55, no. 11, pp. 631–632, 2019.

- [66] Y. Li, C. Y. D. Sim, Y. Luo, and G. Yang, "High-Isolation 3.5 GHz Eight-Antenna MIMO Array Using Balanced Open-Slot Antenna Element for 5G Smartphones," *IEEE Transactions on Antennas and Propagation*, vol. 67, no. 6, pp. 3820–3830, 2019.
- [67] V. Bhanumathi and G. Sivaranjani, "High isolation MIMO antenna using semi-circle patch for UWB applications," *Progress In Electromagnetics Research C*, vol. 92, no. April, pp. 31–40, 2019.
- [68] Niu, Z., Zhang, H., Chen, Q. and Zhong, T., Isolation enhancement in closely coupled dual-band MIMO patch antennas. *IEEE Antennas and Wireless Propagation Letters*, vol. 18, no. (8), pp.1686-1690, 2019.
- [69] Z. Tang, X. Wu, J. Zhan, S. Hu, Z. Xi, and Y. Liu, "Compact UWB-MIMO Antenna with High Isolation and Triple Band-Notched Characteristics," *IEEE Access*, vol. 7, pp. 19856–19865, 2019.
- [70] S. Rajkumar, A. Anto Amala, and K. T. Selvan, "Isolation improvement of UWB MIMO antenna utilising molecule fractal structure," *Electronics Letters*, vol. 55, no. 10, pp. 576–579, 2019.
- [71] A. Mohanty and S. Sahu, "High isolation two-port compact MIMO fractal antenna with Wi-Max and X-band suppression characteristics," *International Journal of RF and Microwave Computer-Aided Engineering*, vol. 30, no. 1, pp. 1–11, 2020.
- [72] K. L. Wong, B. W. Lin, and S. E. Lin, "High-isolation conjoined loop multi-input multi-output antennas for the fifth-generation tablet device," *Microwave and Optical Technology Letters*, vol. 61, no. 1, pp. 111–119, 2019.
- [73] Z. Niu, H. Zhang, Q. Chen, and T. Zhong, "Isolation Enhancement in Closely Coupled," *Ieee Antennas and Wireless Propagation Letters*, vol. 18, no. 8, pp. 1686–1690, 2019.
- [74] J. Wu, Y. Qi, W. Yu, L. Liu, and F. Li, "An absorber-integrated taper slot antenna," *IEEE Transactions on Electromagnetic Compatibility*, vol. 59, no. 6, pp. 1741–1747, 2017.
- [75] S. R. Thummaluru, R. Kumar, and R. K. Chaudhary, "Isolation Enhancement and Radar Cross Section Reduction of MIMO Antenna with Frequency Selective Surface," *IEEE Transactions on Antennas and Propagation*, vol. 66, no. 3, pp. 1595–1600, 2018.
- [76] M. Al-Hasan, I. Ben Mabrouk, E. R. F. Almajali, M. Nedil, and T. A. Denidni, "Hybrid Isolator for Mutual-Coupling Reduction in Millimeter-Wave MIMO Antenna Systems," *IEEE Access*, vol. 7, pp. 58466–58474, 2019.
- [77] Z. H. Deng, F. W. Wang, Y. H. Ren, K. Li, and B. J. Gao, "A Novel Wideband Low-RCS Reflector by Hexagon Polarization Rotation Surfaces," *IEEE Access*, vol. 7, pp. 131527–131533, 2019.

- [78] Y. Shi, Z. K. Meng, W. Y. Wei, W. Zheng, and L. Li, "Characteristic Mode Cancellation Method and Its Application for Antenna RCS Reduction," *IEEE Antennas and Wireless Propagation Letters*, vol. 18, no. 9, pp. 1784–1788, 2019.
- [79] M. A. Rad, M. R. Soheilifar, and F. B. Zarrabi, "Compact microstrip antenna based on fractal metasurface with low radar cross section and wide bandwidth," *AEU - International Journal of Electronics and Communications*, vol. 98, pp. 74–79, 2019.
- [80] R. Mark, N. Rajak, K. Mandal, and S. Das, "Isolation and gain enhancement using metamaterial based superstrate for MIMO applications," *Radioengineering*, vol. 28, no. 4, pp. 689–695, 2019.
- [81] P. Garg and P. Jain, "Isolation Improvement of MIMO Antenna Using a Novel Flower Shaped Metamaterial Absorber at 5.5 GHz WiMAX Band," *IEEE Transactions on Circuits and Systems II: Express Briefs*, vol. 67, no. 4, pp. 675–679, 2020.
- [82] Y. Ge, Y. Zhao, and J. Chen, "Wideband RCS reduction and gain enhancement for a patch antenna with broadband AMC structure," *Radioengineering*, vol. 27, no. 1, pp. 45–52, 2019.
- [83] Z. Liu, S. Jie, H. Ma, X. Zhang, and B. Xing, "A novel dual-passband net-shaped FSS structure used for MIMO antennas," *Progress In Electromagnetics Research C*, vol. 90, no. December 2018, pp. 29–39, 2019.
- [84] S. R. Thummaluru and R. K. Chaudhary, "Reducing the RCS of MIMO antenna using angularly stable FSS," *2019 URSI Asia-Pacific Radio Science Conference, AP-RASC 2019*, no. March, pp. 5–8, 2019.
- [85] P. Ranjan, M. Patil, S. Chand, A. Ranjan, S. Singh, and A. Sharma, "Investigation on dual-port printed MIMO antenna with reduced RCS for C-band radar application," *International Journal of RF and Microwave Computer-Aided Engineering*, vol. 30, no. 3, 2020.
- [86] Z. Wang, L. Zhao, Y. Cai, S. Zheng, and Y. Yin, "A Meta-Surface Antenna Array Decoupling (MAAD) Method for Mutual Coupling Reduction in a MIMO Antenna System," *Scientific Reports*, vol. 8, no. 1, pp. 1–9, 2018.
- [87] M. Agarwal and M. K. Meshram, "Metamaterial-based dual-band microwave absorber with polarization insensitive and wide-angle performance," *AIP Advances*, vol. 8, no. 9, 2018.
- [88] S. Bhattacharyya, "A Broadband Microwave Metamaterial Absorber with Octave Bandwidth," *Mapan - Journal of Metrology Society of India*, vol. 31, no. 4, pp. 299–307, 2016.

- [89] S. Bhattacharyya, S. Ghosh, D. Chaurasiya, and K. V. Srivastava, "Wide-angle broadband microwave metamaterial absorber with octave bandwidth," *IET Microwaves, Antennas and Propagation*, vol. 9, no. 11, pp. 1160–1166, 2015.
- [90] Y. Cheng, Y. Zou, H. Luo, F. Chen, and X. Mao, "Compact Ultra-Thin Seven-Band Microwave Metamaterial Absorber Based on a Single Resonator Structure," *Journal of Electronic Materials*, vol. 48, no. 6, pp. 3939–3946, 2019.
- [91] S. Ghosh, S. Bhattacharyya, D. Chaurasiya, and K. V. Srivastava, "An ultrawideband ultrathin metamaterial absorber based on circular split rings," *IEEE Antennas and Wireless Propagation Letters*, vol. 14, no. c, pp. 1172–1175, 2015.
- [92] N. T. Q. Hoa, T. S. Tuan, L. T. Hieu, and B. L. Giang, "Facile design of an ultra-thin broadband metamaterial absorber for C-band applications," *Scientific Reports*, vol. 9, no. 1, pp. 1–9, 2019.
- [93] N. T. Q. Hoa, P. D. Tung, N. D. Dung, H. Nguyen, and T. S. Tuan, "Numerical study of a wide incident angle- and polarisation-insensitive microwave metamaterial absorber based on a symmetric flower structure," *AIP Advances*, vol. 9, no. 6, 2019.
- [94] K. P. Kaur and T. Upadhyaya, "Wide-angle and polarisation-independent triband dual-layer microwave metamaterial absorber," *IET Microwaves, Antennas and Propagation*, vol. 12, no. 8, pp. 1428–1434, 2018.
- [95] Y. H. Ren, J. Ding, C. J. Guo, Y. Qu, and Y. C. Song, "Design of a Quad-Band Wide-Angle Microwave Metamaterial Absorber," *Journal of Electronic Materials*, vol. 46, no. 1, pp. 370–376, 2017.
- [96] S. Mumtaz, J. M. Jornet, J. Aulin, W. H. Gerstacker, X. Dong, and B. Ai, "Terahertz Communication for Vehicular Networks," *IEEE Transactions on Vehicular Technology*, vol. 66, no. 7, pp. 5617–5625, Jul. 2017.
- [97] G. Varshney, S. Gotra, V. S. Pandey, and R. S. Yaduvanshi, "Proximity-coupled two-port multi-input-multi-output graphene antenna with pattern diversity for THz applications," *Nano Communication Networks*, vol. 21, Sep. 2019.
- [98] Z. Xu, X. Dong, and J. Bornemann, "Design of a reconfigurable MIMO system for THz communications based on graphene antennas," *IEEE Transactions on Terahertz Science and Technology*, vol. 4, no. 5, pp. 609–617, 2014.
- [99] Z. W. Miao, Z. C. Hao, Y. Wang, B. B. Jin, J. B. Wu, and W. Hong, "A 400-GHz High-Gain Quartz-Based Single Layered Folded Reflectarray Antenna for Terahertz Applications," *IEEE Transactions on Terahertz Science and Technology*, vol. 9, no. 1, pp. 78–88, Jan. 2019.

- [100] S. Singhal, "Ultrawideband elliptical microstrip antenna for terahertz applications," *Microwave and Optical Technology Letters*, 2019.
- [101] I. F. Akyildiz and J. M. Jornet, "Realizing Ultra-Massive MIMO (1024×1024) communication in the (0.06-10) Terahertz band," *Nano Communication Networks*, vol. 8, pp. 46–54, Jan. 2016.
- [102] IEEE Communications Society and Institute of Electrical and Electronics Engineers, *2019 IEEE International Conference on Communications (ICC): proceedings: Shanghai, China, 20-24 May 2019*. .
- [103] B. Cheng *et al.*, "340-GHz 3-D imaging radar with 4Tx-16Rx MIMO array," *IEEE Transactions on Terahertz Science and Technology*, vol. 8, no. 5, pp. 509–519, Sep. 2018.
- [104] I. F. Akyildiz, C. Han, and S. Nie, "Combating the Distance Problem in the Millimeter Wave and Terahertz Frequency Bands," *IEEE Communications Magazine*, vol. 56, no. 6, pp. 102–108, Jun. 2018.
- [105] L. E. Garcia Munoz, "Comments on 'THz time-domain sensing: The antenna dispersion problem and a possible solution,'" *IEEE Transactions on Terahertz Science and Technology*, vol. 4, no. 1, pp. 125–126, Jan-2014
- [106] C. H. Li and T. Y. Chiu, "340-GHz Low-Cost and High-Gain On-Chip Higher Order Mode Dielectric Resonator Antenna for THz Applications," *IEEE Transactions on Terahertz Science and Technology*, vol. 7, no. 3, pp. 284–294, May 2017.
- [107] Y. Luo *et al.*, "Graphene-Based Multi-Beam Reconfigurable THz Antennas," *IEEE Access*, vol. 7, pp. 30802–30808, 2019.
- [108] B. Zhang, J. M. Jornet, I. F. Akyildiz, and Z. P. Wu, "Mutual coupling reduction for ultra-dense multi-band plasmonic nano-antenna arrays using graphene-based frequency selective surface," *IEEE Access*, vol. 7, pp. 33214–33225, 2019.
- [109] O. Yurduseven, J. Bueno, S. Yates, A. Neto, J. Baselmans, and N. Llombart, "Incoherent Detection of Orthogonal Polarizations via an Antenna Coupled MKID: Experimental Validation at 1.55 THz," *IEEE Transactions on Terahertz Science and Technology*, vol. 8, no. 6, pp. 736–745, Nov. 2018.
- [110] Wang, Hang, Lei Zhu, and Wolfgang Menzel, Ultra-wideband bandpass filter with hybrid microstrip/CPW structure, *IEEE Microwave and Wireless Components Letters* 15 (12) (2005): 844-846.
- [111] Li, Rui, and Lei Zhu, Compact UWB bandpass filter using stub-loaded multiple-mode resonator, *IEEE Microwave and Wireless Components Letters* 17, (1) (2007): 40-42.

- [112] Packiaraj D, Vinoy K J, Ramesh M, Kalghatgi AT, Miniaturized ultra wideband filter with extended stop band, *Microwave and Optical Technology Letters* 55(4) (2013): 703-705.
- [113] Zhou XY, Zheng SY, Chan WS, HoD, Compact bandpass filter with controllable bandwidth based on low radiation spur-line defected ground structure, *Microwave and Optical Technology Letters*, 58 (12) (2016): 2966-2968.
- [114] Shaman, Hussein, and Jia-Sheng Hong, Ultra-wideband (UWB) bandpass filter with embedded band notch structures, *IEEE Microwave and Wireless Components Letters* 17 (3) (2007): 193-195.
- [115] Nouri S, Nourinia J, Ghobadi C, Alizadeh F, Mohammadi B, Design and analysis of compact BPF with dual notch bands based on stepped-impedance resonator for UWB applications, *Microwave and Optical Technology Letters*, 59 (3) (2017): 672-674..
- [116] Li CS, Ho MH, Hong W, Design of UWB BPF using SIR with open-and short-circuit stubs for bandwidth enhancement, In *Antennas and Propagation (APCAP), IEEE 3rd Asia-Pacific Conference on* (2014): 1123-1126.
- [117] Luo X, Ma JG, Ma K, Yeo KS, Compact UWB bandpass filter with ultra narrow notched band. *IEEE Microwave and Wireless Components Letters*, 20 (3) (2010): 145-147.
- [118] Gholipour M, Amin Honarvar M, Virdee BS, UWB bandpass filters with triple notched band characteristics implemented using wave cancellation technique, *Microwave and Optical Technology Letters*, 58 (8) (2016): 1875-1879.
- [119] Ishii, Hiroyuki, Toru Kimura, Naotaka Kobayashi, Atsushi Saito, Zhewang Ma, and Shigetoshi Ohshima, Development of UWB HTS bandpass filters with microstrip stubs-loaded three-mode resonator, *IEEE Transactions on Applied Superconductivity* 23 (3) (2013): 1500204-1500208.
- [120] Zhu, Lei, Sheng Sun, and Wolfgang Menzel, Ultra-wideband (UWB) bandpass filters using multiple-mode resonator, *IEEE Microwave and Wireless components letters* 15 (11) (2005): 796-798.
- [121] Wei F, Li WT, Huang QL, Shi XW. Super compact UWB BPF with one narrow notched band and wide stopband. *Microwave and Optical Technology Letters*. 57 (3) (2015): 763-765.
- [122] L. Han, K. Wu, and X. Zhang, Development of packaged ultrawideband bandpass filters, *IEEE Trans. Microw. Theory Techn.*, 58 (1) (2010): 220–228.
- [123] A. Taibi, M. Trabelsi, A. Slimane, M. T. Belaroussi, and J.-P. Raskin, A novel design method for compact UWB bandpass filters, *IEEE Microw. Wireless Compon. Lett.*, 25, (1) (2015): 4–6.

- [124] Faraghi A, Ojaroudi M, Ghadimi N, Compact microstrip low-pass filter with sharp selection characteristics using triple novel defected structures for UWB applications, *Microwave and Optical Technology Letters*, 56 (4) (2014): 1007-1010.
- [125] Kamma, Anil, G. Shrikanth Reddy, and Jayanta Mukherjee, Band notch UWB bandpass filter with additional GSM1800 band, *IEEE, In Progress in Electromagnetic Research Symposium (PIERS)*, (2016): 4481-4481.
- [126] Kumar A, Kartikeyan MV. Design and realization of microstrip filters with new defected ground structure (DGS). *Engineering Science and Technology, an International Journal* 20 (2) (2017): 679-86.
- [127] Kumar A, Pathak NP. Harmonic suppressed coupled stepped-impedance resonator based dual-band tunable bandpass filter. *Engineering science and technology, an international journal* 20 (5) (2017): 1460-5.
- [128] Tripathi S, Pathak NP, Parida M. Microwave front-end subsystems design for ITS/GPS applications. *Engineering Science and Technology, an International Journal* 19 (4) (2016): 1815-25.
- [129] Noura, A., Benaissa, M., Abri, M., Badaoui, H., Vuong, T.H. and Tao, J. —Miniaturized half-mode SIW band-pass filter design integrating dumbbell DGS cells|. *Microwave and Optical Technology Letters*, 61(6), (2019):1473-1477.
- [130] Chen, H., Jiang, D. and Chen, X., 2016. Wideband bandstop filter using hybrid microstrip/CPW-DGS with via-hole connection. *Electronics Letters*, 52(17), pp.1469-1470.
- [131] Zhong, Y., Yang, Y., Zhu, X., Dutkiewicz, E., Shum, K.M. and Xue, Q. —An on-chip bandpass filter using a broadside-coupled meander line resonator with a defected-ground structure|. *IEEE Electron Device Letters*, 38(5), (2017): 626-630.
- [132] Singh, H.S., Pandey, G.K., Bharti, P.K. and Meshram, M.K., 2015. A compact dual-band diversity antenna for WLAN applications with high isolation. *Microwave and optical technology letters*, 57(4), pp.906-912.
- [133] S. Chouhan, D. K. Panda, V. S. Kushwah, and P. K. Mishra, “Octagonal-shaped wideband MIMO antenna for human interface device and S-band application,” *International Journal of Microwave and Wireless Technologies*, vol. 11, no. 3, pp. 287–296, 2019.
- [134] A. Y. I. Ashyap *et al.*, “Compact and Low-Profile Textile EBG-Based Antenna for Wearable Medical Applications,” *IEEE Antennas and Wireless Propagation Letters*, vol. 16, no. c, pp. 2550–2553, 2017.

- [135] A. Kumar, A. Q. Ansari, B. K. Kanaujia, J. Kishor, and S. Kumar, "An ultra-compact two-port UWB-MIMO antenna with dual band-notched characteristics," *AEU - International Journal of Electronics and Communications*, vol. 114, p. 152997, 2020
- [136] S. P. Biswal and S. Das, "A low-profile dual port UWB-MIMO/diversity antenna with band rejection ability," *International Journal of RF and Microwave Computer-Aided Engineering*, vol. 28, no. 1, pp. 1–11, 2018.
- [137] J. S. Hong and M. J. Lancaster, "Microstrip Filters for RF/Microwave Applications," John Wiley & Sons, Inc., Vol. 25, No. 3, p.p.285-346 New York, 2001.



LIST OF PUBLICATIONS

❖ Journals:

1. Saxena, Gaurav, Priyanka Jain, and Yogendra Kumar Awasthi. "High diversity gain super-wideband single band-notch MIMO antenna for multiple wireless applications." *IET Microwaves, Antennas & Propagation* 14, no. 1 (2020): 109-119. (SCI Journal with Impact Factor: 2.036), DOI-[10.1049/iet-map.2019.0450](https://doi.org/10.1049/iet-map.2019.0450)
2. Saxena, Gaurav, Priyanka Jain, and Yogendra Kumar Awasthi. "High Diversity Gain MIMO-Antenna for UWB Application with WLAN Notch Band Characteristic Including Human Interface Devices." *Wireless Personal Communications* (2020): 1-17. (SCI Journal with Impact Factor: 1.031), DOI-<https://doi.org/10.1007/s11277-019-07018-1>
3. Saxena, Gaurav, Priyanka Jain, and Yogendra Kumar Awasthi. "High Isolation and High Gain Super-Wideband (0.33-10THz) MIMO Antenna for THz Applications." *Optik journal Elsevier* (2020), (SCI Journal with Impact Factor: 2.186), DOI-<https://doi.org/10.1016/j.ijleo.2020.165335>
4. Saxena, Gaurav, Priyanka Jain, and Yogendra Kumar Awasthi. "Pentaband MIMO Antenna with Dual Polarization for Wireless Applications." *International Journal of Microwave and Wireless Technologies* (2020): Accepted with revision. (SCI Journal with Impact Factor:0.976)
5. Saxena, Gaurav, Priyanka Jain, and Yogendra Kumar Awasthi. "Design of Metasurface Absorber for Low RCS and High Isolation MIMO Antenna for Radiolocation and Aeronautical Radio Navigation." *AEU Journal Elsevier* (2020): Communicated. (SCI Journal with Impact Factor: 2.924)
6. Saxena, Gaurav, Priyanka Jain, and Yogendra Kumar Awasthi. "Design Analysis of Compact Bandpass Filter with Stopband Characteristic for UWB Application using MMR Technique." *International Journal of Microwave and Wireless Technologies* (2020): Accepted with revision. (SCI Journal with Impact Factor:0.976)

❖ International Conferences:

1. Saxena, Gaurav, Priyanka Jain, and Y. K. Awasthi. "High Isolation EBG Based MIMO

- Antenna for X-Band Applications."** In *2019 6th International Conference on Signal Processing and Integrated Networks (SPIN)* pp. 97-100. IEEE, 2019, DOI-[10.1109/SPIN.2019.8711602](https://doi.org/10.1109/SPIN.2019.8711602)
2. Saxena, Gaurav, Priyanka Jain, and Y. K. Awasthi "**High Isolation EBG Based MIMO Antenna for C-Band Applications**" *Proceeding of International Conference on Signal Processing, VLSI and Communication Engineering (ICSPVCE-2019)*, March 28-30, 2019, DTU, New Delhi, India.
 3. Saxena, Gaurav, R. L. Yadava, Priyanka Jain, and Y. K. Awasthi. "**Triple Band Polarization Insensitive Ultra Thin Metamaterial Absorber for EMC and RCS Reduction in X-Band Applications.**" In *2020 7th International Conference on Signal Processing and Integrated Networks (SPIN)* pp. 772-775. IEEE, 2020, DOI-[10.1109/SPIN48934.2020.9071128](https://doi.org/10.1109/SPIN48934.2020.9071128)



CURRICULUM VITAE



Gaurav Saxena received his Bachelor of Technology(b.Tech.) degree in Electronics and Communication Engineering, from Uttar Pradesh Technical University Lucknow, India, in 2007, M. Tech degree in Microwave Electronics, from University of Delhi, South Campus, Delhi, India, in 2012. He has also received a meritorious scholarship from July 2010 to July 2012 given by the University of Delhi. From Dec.2011 to May 2012 he has worked as an internship trainee at CSIR, NPL Delhi where he established traceability of the VNA and received an appreciation certificate given by Mr. P S Negi (Senior Principal Scientist). Currently, he is working as an Assistant Professor in Galgotia College of Engineering and Technology, Greater Noida, Uttar Pradesh and Pursuing Ph.D. from Delhi Technological University, Delhi, India. His recent research interest includes Modelling of passive microwave components like filters Power divider/combiner, Microwave antenna for 5G and Wireless applications, Meta-material absorber, MIMO receiver/transmitter, THz MIMO antenna and absorbers and LNA etc.

Permanent Address: House No.280, Rani Ram Kali Bagh Subhash Road Chandausi Dist. Sambhal U.P.

Email address: gauravsaxena.engg@gmail.com

Mobile No.: 9971948625, 8920877725